UNIVERSITÀ DEGLI STUDI DI TRIESTE

DOTTORATO DI RICERCA IN FISICA

XV CICLO

Preliminary measurement of Transversity at COMPASS experiment

Candidato:
Dott. Paolo Pagano

Tutore:
Chiar.mo Prof. Franco Bradamante
Università degli studi di Trieste

Coordinatore:
Chiar.ma Prof.ssa Maria F. Matteucci
Università degli studi di Trieste

Anno Accademico 2001-2002

Abstract

In the COMPASS physics program a particular attention is devoted to the spin dependent Parton Distribution Functions.
The observables related to Transversity are the subject of this work.
As a first hint for these measurements, the data collected during year 2002 run have been analyzed. This sample, taken with a transverse polarized deuteron target, consists of about 15 days of smooth data taking.
In this thesis, after a phenomenological introduction to the physics case, a detailed description of the COMPASS spectrometer is given, pointing the attention to the RICH detector and its performance.
The analysis algorithms are fully described. Preliminary results on Transversity, obtained via the so-called Collins effect, are shown.

Nel programma di fisica di COMPASS si presta particolare attenzione alle funzioni di struttura del nucleone.
Le osservabili connesse alla Trasversità sono l'argomento di questo lavoro.
I dati acquisiti durante il run del 2002 sono stati analizati per dare una prima valutazione di queste misure. Il campione statistico, preso con il bersaglio di deutoni polarizzato trasversalmente, consiste di circa 15 giorni di presa dati stabile.
In questa tesi, dopo una introduzione fenomenologia all'argomento di fisica, si dà una descrizione dettagliata dello spettrometro, soffermandosi sul rivelatore RICH e sulle sue prestazioni.
Gli algoritmi di analisi sono descritti interamente. Si presentano i risultati preliminari sulla Trasversità, ottenuti attraverso l'effetto Collins.

A papà, mamma e Licia

Don Lolò: "Eh, caro mio, con me, chi vuol aver da fare - guarda - (cava di tasca un libro di piccolo formato, legato in tela rossa) c'è questo. Lo sai che è? Ti sembra un libriccino da messa? È il Codice Civile! Me l'ha regalato il mio avvocato, che ora è qua, a villeggiatura da me. E ho imparato a leggerci, sai, in questo libriccino, e a me non me la fa più nessuno, neppure il Padreterno! Contemplato tutto, qua: caso per caso. E me lo pago ad anno, io, l'avvocato!"

— *La Giara*, Luigi Pirandello, *1925*

Acknowledgments

I would like to thank those who have made possible the work described in this thesis.
I thank Franco and Massimo whose interest has been a powerful source of ideas and questions to answer.

Thanks also to Benigno, Renato and Vinicio for the technical support and to Andrea B. who has let me not to lose the contact with RICH-1 group and its activities. Thanks to Anna for the sharing of her ideas and the achieved results. Thanks to Silvia and Fulvio for their attention. I thank every single member of Trieste COMPASS group for his human/scientific support.

Thanks to Fritz-Herbert, Horst, Kenneth, Laura, Martin for their help and all the Coral Weekly mailing list members who have solved the many technical problems which arise in a delicate Physics measurement as that for Transversity.

Thanks to Licia who has thought me how the life flows in the opposite direction with respect to the Physics predictions. Thanks to my family and, in a special way, to my mother and my sister Maria for their constant presence in my life though the distance which separates each other. Thanks to Matilde and my granny for their love. Thanks to auntie Alma, Annalisa's and Roby's families to have let me feel at home so far away from my native land.

Special thanks to Ciccio M., Isabelle, Marco V. and Turi because they are a treasure. Thanks to Amorino, Andrea D., Cate, Capy, Cinzia, Claribelle, Davide D., Elvie, Francisca, fr. Hugh, Ina, Luca C., Luciana, Marco S., Ornella, Pierre, Sylvain, Tony, Victor and to all those who feel to be my friends.

Contents

List of Tables

List of Figures

Introduction

Since the time of my Diploma thesis (Trieste, 1999) I've been involved in Experimental High Energy Physics in the framework of the COMPASS experiment at CERN.

My activities have been devoted first to learning and understanding the physics of the spin structure of the nucleon, secondly to the construction, setting up and commissioning of the RICH-1 detector, and finally to the physics data taking and analysis.

In the first two chapters of this thesis, I present the physics case of transversity (the measurement of which is one of the main goals of COMPASS) and the present status of the measurements.

The following chapter describes in details the COMPASS experimental apparatus: the muon beam line and its features, the polarized target, the two-stages spectrometer, the calorimetry, the trigger and the DAQ system.

A dedicated chapter describes the RICH-1 detector and its performances from the preliminary analysis of data collected in the year 2002 run. I have been personally involved in the Photon Detectors setting up and commissioning.

Chapter 5 is dedicated to the COMPASS data organization. Here there is a general description of Objectivity/DB, the Data Base that COMPASS has adopted until 2002. A detailed description of the COmpass Reconstruction and Analysis Libraries (CORAL) introduces the data processing and DST production. I've processed most of the data collected with transversely polarized target in year 2002.

Chapter 6 is a collection of tests and measurements I did with the data collected in year 2001 (commissioning run) in order to contribute to the delevopment of the CORAL code and to test the spectrometer performance. In the last section the present status of the reconstruction is shown using some examples, obtained by the collaboration, as V^0 reconstruction and particle identification.

In the last chapter the preliminary analysis on 2/3 of the available statistics collected in transverse polarization is presented. My search of the Collins effect (still in progress) is described in detail and the values for the experimental asymmetries are compared to recent theoretical predictions.

Chapter 1

The structure of the nucleon

1.1 The Physics case

Spin Physics has represented in the last 30 years a powerful tool of investigation for the nucleon's structure. The spin puzzle, arisen in the late 80's with the EMC experiment at CERN, is still unsolved and many open questions might find their solution in the light of the data that new experiments are collecting.

Since last year, the COMPASS experiment at CERN is running at the SPS accelerator facility. The collaboration points to the direct measurement of gluon polarization Δg via charmed quark pairs production in Photon-Gluon Fusion (PGF) reaction. The experiment will also measure the complete set of real functions, known as Parton Distribution Functions (PDF), fully describing the structure of the nucleon at the leading order, including $h_1(x)$ the function related to transversity which hasn't yet been measured.

COMPASS, a "third generation" experiment[1], will measure for the first time Δg and $h_1(x)$, and will reduce the error of the already known PDFs opening up a "new age" resolution in the PDFs' measurement.

Historically the measurements of the PDFs have been done probing the nucleons by an energetic leptonic flux. The e.m. reaction taking place between the lepton and one of the nucleon's constituents is known as Deep Inelastic Scattering (DIS) and will be theoretically described in this chapter. The particular case of the polarized DIS will be discussed in

[1]The diction "generation" distinguishes the type of reactions measured in the experiment: the first generation has measured the inclusive, unpolarized DIS, the second has measured the inclusive polarized DIS, the third the seminclusive polarized DIS with full PID and calorimetry.

detail.

1.2 Kinematics of DIS

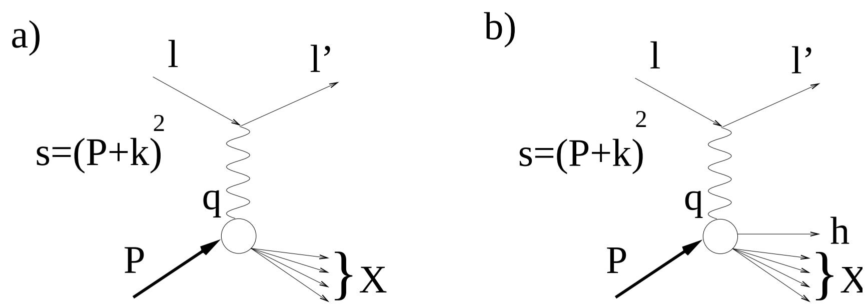

Figure 1.1: Inclusive (a) and semi-inclusive (b) DIS at tree level.

In a DIS reaction one can be interested in calculating all the observables referring to the incident and scattered lepton without paying attention to the other products. Such a reaction:

$$\ell\ (k) + N\ (P) \rightarrow \ell'\ (k') + X$$

is sketched in figure 1.1/a. Its cross section, called inclusive (referring to the fact that no attention has been paid to the products), can be written as:

$$\frac{d\sigma}{dx\ dy} = \frac{\pi\ \alpha_{\text{em}}^2}{Q^4}\ y\ L_{\mu\nu}\ 2MW^{\mu\nu}. \tag{1.1}$$

where $L_{\mu\nu}$ and $W^{\mu\nu}$ are the leptonic and hadronic tensors, Q^2 is the opposite of the virtual photon mass, x and y are the Lorenz-scalar Bjorken variables defined as:

$$x = \quad \tfrac{-q^2}{2pq} = \tfrac{Q^2}{2M_N\nu} \qquad 0 \leq x \leq 1 \tag{1.2}$$

$$y = \tfrac{pq}{pk} = \tfrac{\nu}{E} = 1 - \tfrac{E'}{E} \quad 0 \leq y \leq 1 \tag{1.3}$$

where ν is the virtual photon's energy. The Bjorken variables specify the inelasticity and the energy transfer of the reaction. Their boundary values define the deep inelastic and elastic limits.

The leptonic tensor has a well known structure deriving from the lepton nature of point-like, e.m. interacting particle. Instead the hadronic tensor is in principle not known because of the inner structure of the nucleon. It will be defined through a set of independent, real (and consequently measurable) functions, the PDFs.

In case one wants to measure at least one hadron produced in the reaction, *i.e.* to explore the semi-inclusive case sketched in figure 1.1/b:

$$\ell\ (k) + N\ (P) \rightarrow \ell'\ (k') + h\ (P_h) + X$$

the corresponding cross section:

$$\frac{d\sigma}{dx\, dy\, dz_h\, d^2\mathbf{q}_T} = \frac{\pi\, \alpha_{\rm em}^2}{2Q^4}\, y\, z_h\, L_{\mu\nu}\, 2MW^{\mu\nu} \tag{1.4}$$

where $\mathbf{q}_T$ is the virtual photon transverse momentum in the frame in which the nucleon and hadron momenta are collinear. The cross-section defined in 1.4 depends on the hadron momentum through another Lorenz-scalar defined as the ratio of the hadron momentum over its maximum possible value, i.e. the energy of the virtual gamma:

$$z_h \equiv \frac{P \cdot P_h}{P \cdot q} \approx -\frac{2P_h \cdot q}{Q^2} = \frac{E_h}{\nu} \tag{1.5}$$

In case of polarized DIS, both the hadronic ($W_{\mu\nu}$) and leptonic ($L_{\mu\nu}$) tensors can be splitted into a real and an imaginary (spin dependent) part, symmetric and antisymmetric under $\mu - \nu$ interchange:

$$L_{\mu\nu} = L_{\mu\nu}^{(\mathrm{S})}(\ell, \ell') + \mathrm{i}\, L_{\mu\nu}^{(\mathrm{A})}(\ell, s_l; \ell')\,, \tag{1.6a}$$

$$W_{\mu\nu} = W_{\mu\nu}^{(\mathrm{S})}(q, P) + \mathrm{i}\, W_{\mu\nu}^{(\mathrm{A})}(q; P, S)\,. \tag{1.6b}$$

where s_l and S the spin vectors of the lepton and the nucleon.

1.2.1 The hadronic tensor and the inner structure of the nucleon

Reducing the degrees of freedom by the e.m. gauge invariance ($q_\mu W^{\mu\nu} = 0 = q_\nu W^{\mu\nu}$), the symmetric and the antisymmetric parts are expressed in terms of two pairs of structure functions, W_1, W_2 and G_1, G_2, as

$$\begin{aligned}\frac{1}{2M}\,W^{(\mathrm{S})}_{\mu\nu} &= \left(-g_{\mu\nu} + \frac{q_\mu q_\nu}{q^2}\right) W_1(P{\cdot}q, q^2) \\ &+ \frac{1}{M^2}\left[\left(P_\mu - \frac{P{\cdot}q}{q^2}\,q_\mu\right)\left(P_\nu - \frac{P{\cdot}q}{q^2}\,q_\nu\right)\right] W_2(P{\cdot}q, q^2)\,, \qquad (1.7\mathrm{a})\\ \frac{1}{2M}\,W^{(\mathrm{A})}_{\mu\nu} &= \varepsilon_{\mu\nu\rho\sigma}\,q^\rho \left\{ M S^\sigma\, G_1(P{\cdot}q, q^2) \right.\\ &\left. + \frac{1}{M}\left[P{\cdot}q\, S^\sigma - S{\cdot}q\, P^\sigma\right] G_2(P{\cdot}q, q^2) \right\}. \qquad (1.7\mathrm{b})\end{aligned}$$

Using (1.6a, 1.6b) the inclusive DIS cross-section becomes:

$$\frac{d\sigma}{dE'\,d\Omega} = \frac{\alpha^2_{\mathrm{em}}}{2MQ^4}\,\frac{E'}{E}\left[L^{(\mathrm{S})}_{\mu\nu} W^{\mu\nu\,(\mathrm{S})} - L^{(\mathrm{A})}_{\mu\nu} W^{\mu\nu\,(\mathrm{A})}\right]. \qquad (1.8)$$

The unpolarised cross-section is then obtained by averaging over the spins of the incoming lepton (s_l) and of the nucleon (S) reads:

$$\frac{d\sigma^{\mathrm{unp}}}{dE'\,d\Omega} = \frac{1}{2}\sum_{s_l}\frac{1}{2}\sum_{S}\frac{d\sigma}{dE'\,d\Omega} = \frac{\alpha^2_{\mathrm{em}}}{2MQ^4}\,\frac{E'}{E}\,L^{(\mathrm{S})}_{\mu\nu} W^{\mu\nu\,(\mathrm{S})} \qquad (1.9)$$

and only depends on the symmetric component of the two tensors.

Making use of the explicit expressions for the symmetric component of the leptonic tensor[1] and for the hadronic tensor in eq. 1.7a, one can rewrite eq. 1.9 to obtain the formula:

$$\frac{d\sigma^{\mathrm{unp}}}{dE'\,d\Omega} = \frac{4\alpha^2_{\mathrm{em}}E'^2}{Q^4}\left[2W_1\,\sin^2\frac{\vartheta}{2} + W_2\,\cos^2\frac{\vartheta}{2}\right]. \qquad (1.10)$$

Moreover, from eq. 1.8, if we take the difference in the cross-sections when the target spins are opposite ($\pm S$), we get:

$$\frac{d\sigma(+S)}{dE'\,d\Omega} - \frac{d\sigma(-S)}{dE'\,d\Omega} = -\frac{\alpha_{\rm em}^2}{2MQ^4}\,\frac{E'}{E}\,2L_{\mu\nu}^{({\rm A})}W^{\mu\nu\,({\rm A})}\,. \tag{1.11}$$

which only depends on the anti-symmetric components.

In the target rest frame, the polarized cross-sections can be expressed as function of the polar coordinates of hadron spin vector (assuming $|\vec{S}| = 1$) and scattered muon. Taking the direction of the incoming lepton to be the z-axis, denoting by ϑ the lepton scattering angle and by φ its azimuthal deviation, we have:

$$\begin{aligned} \ell^\mu &= E(1,0,0,1)\,, \\ \ell'^\mu &= E'(1,\,\sin\vartheta\cos\varphi,\,\sin\vartheta\sin\varphi,\,\cos\vartheta)\,, \end{aligned} \tag{1.12}$$

In the same way, the target spin in polar coordinates can be written as:

$$S^\mu = (0,\vec{S}) = (0,\,\sin\alpha\cos\beta,\,\sin\alpha\sin\beta,\,\cos\alpha)\,. \tag{1.13}$$

For the two specific cases of longitudinal ($\alpha = 0$) and transverse ($\alpha = \pi/2$) polarized target[2] one gets:

$$\frac{d\sigma^{\Rightarrow}}{dE'\,d\Omega} - \frac{d\sigma^{\Leftarrow}}{dE'\,d\Omega} = -\frac{4\alpha_{\rm em}^2 E'}{Q^2 E}\left[(E + E'\cos\vartheta)\,M\,G_1 - Q^2\,G_2\right]. \tag{1.14a}$$

$$\frac{d\sigma^{\Uparrow}}{dE'\,d\Omega} - \frac{d\sigma^{\Downarrow}}{dE'\,d\Omega} = -\frac{4\alpha_{\rm em}^2 E'^2}{Q^2 E}\,\sin\vartheta\left[M\,G_1 + 2E\,G_2\right]. \tag{1.14b}$$

The real functions appearing in eqs. 1.10, 1.14a, 1.14b completely describe the polarized DIS. In order to evaluate the weight of each structure function w.r.t. the momentum transferred in the reaction (Q), it's useful to extract from the structure functions its dimensionless component:

$$\begin{aligned} F_1(x,Q^2) &\equiv M\,W_1(\nu,Q^2) \qquad & g_1(x,Q^2) &\equiv M^2\nu\,G_1(\nu,Q^2)\,; \\ F_2(x,Q^2) &\equiv \nu\,W_2(\nu,Q^2) \qquad & g_2(x,Q^2) &\equiv M\nu^2\,G_2(\nu,Q^2)\,. \end{aligned} \tag{1.15}$$

[2]The adjectives longitudinal and transverse refer to the incoming beam momentum.

In the Bjorken limit:

$$\nu, Q^2 \to \infty\,, \quad x = \frac{Q^2}{2M\nu} \quad \text{fixed,} \tag{1.16}$$

due to the point-like nature of partons, these dimensionless functions are supposed to scale, i.e. to depend only on x. In terms of F_1, F_2, g_1 and g_2, the hadronic tensor reads:

$$\begin{aligned}
W_{\mu\nu}^{(\mathrm{S})} &= 2\left(-g_{\mu\nu} + \frac{q_\mu q_\nu}{q^2}\right) F_1(x, Q^2) \\
&\quad + \frac{2}{P{\cdot}q}\left[\left(P_\mu - \frac{P{\cdot}q}{q^2}\, q_\mu\right)\left(P_\nu - \frac{P{\cdot}q}{q^2}\, q_\nu\right)\right] F_2(x, Q^2)\,, && (1.17\text{a}) \\
W_{\mu\nu}^{(\mathrm{A})} &= \frac{2M\,\varepsilon_{\mu\nu\rho\sigma}\, q^\rho}{P{\cdot}q}\left\{S^\sigma\, g_1(x, Q^2) + \left[S^\sigma - \frac{S{\cdot}q}{P{\cdot}q}\, P^\sigma\right] g_2(x, Q^2)\right\}. && (1.17\text{b})
\end{aligned}$$

The unpolarised cross-section then becomes (as a function of x and y):

$$\frac{d\sigma^{\mathrm{unp}}}{dx\,dy} = \frac{4\pi\alpha_{\mathrm{em}}^2 s}{Q^4}\left\{xy^2\, F_1(x, Q^2) + \left(1 - y - \frac{xym_N^2}{s}\right) F_2(x, Q^2)\right\}, \tag{1.18}$$

being s the Mandelstam variable.

The fermionic nature of the quarks leads to a close relation between the two unpolarized distribution functions known as Callan Gross relation:

$$F_2(x) = 2x \cdot F_1(x)\,, \tag{1.19}$$

meaning that the measurement of cross section 1.18 will probe the only-degree of freedom of such unpolarized states.

The spin asymmetries (1.14a - 1.14b), in terms of g_1 and g_2, take on the form:

$$\begin{aligned}
\frac{d\sigma^{\Rightarrow}}{dx\,dy\,d\varphi} - \frac{d\sigma^{\Leftarrow}}{dx\,dy\,d\varphi} &= -\frac{4\alpha_{\mathrm{em}}^2}{Q^2} \cdot (2-y)\, g_1(x, Q^2) && (1.20\text{a}) \\
\frac{d\sigma^{\Uparrow}}{dx\,dy\,d\varphi} - \frac{d\sigma^{\Downarrow}}{dx\,dy\,d\varphi} &= -\frac{4\alpha_{\mathrm{em}}^2}{Q^2}\left\{\frac{2Mx}{Q}\sqrt{1-y}\,\left[g_1(x, Q^2) + g_2(x, Q^2)\right]\cos\varphi\right\} && (1.20\text{b})
\end{aligned}$$

where we have neglected contributions of order M^2/Q^2. Equation 1.20a suggests that g_1 is strictly connected to longitudinal polarization whereas equation 1.20b demonstrates that, in transverse polarization mode, a linear combination of the two polarized structure functions can be probed.

1.3 The theoretical approach

1.3.1 The naive parton model and the Parton Distribution Functions

In the parton model, the nucleon is thought as a bound state of “quasi-free” elementary, point-like fermions known as “partons”. Each parton carries a fraction x of the parent nucleon momentum and has a spin either parallel $(+)$ or antiparallel $(-)$ w.r.t. the parent's spin.

Let's say that we have a probability $f_+(x)$ to find a parton with momentum xP polarized as the parent nucleon and a probability $f_-(x)$ to find it polarized in the opposite direction. Within this terminology, the probability to find a parton with momentum x independently of its polarization is the first theoretical functions characterizing the nucleon state starting from its components, and can be defined as:

$$f(x) = f_+(x) + f_-(x)\,. \tag{1.21}$$

The second “theoretical” function refers to the difference in partons' probability to have positive and negative helicity:

$$\Delta f(x) = f_+(x) - f_-(x)\,. \tag{1.22}$$

The last function, $\Delta_T f(x)$, although less familiar, also has a very simple meaning: it's the number density of partons with momentum fraction x and polarisation parallel to the transverse component of the nucleon's spin, minus the number density of quarks with the same momentum fraction and antiparallel polarisation, *i.e.*,[3]

$$\Delta_T f(x) = f_\uparrow(x) - f_\downarrow(x)\,. \tag{1.23}$$

1.3.2 The helicity conservation

The quark - nucleon scattering phenomena can be described [2] by the absorption and re-emission of a quark by the nucleon.

[3]Throughout this thesis the subscripts $\pm$ will denote helicity whereas the subscripts $\uparrow\downarrow$ will denote transverse polarisation.

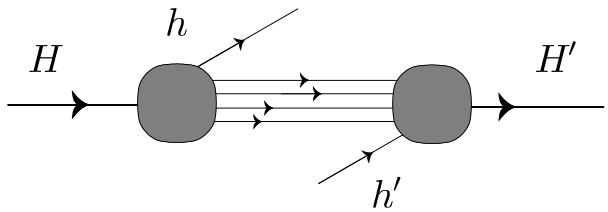

Figure 1.2: Emission of a quark with helicity h from a nucleon of helicity H, and reabsorption of the quark with helicity h' to give a hadron of helicity H'.

Let's consider the reaction sketched in figure 1.2:

$$H \; + \; h' \rightarrow H' \; + \; h \tag{1.24}$$

The quark $(h,\ h')$ and nucleon $(H,\ H')$ helicities take on the values $\pm 1/2$. Helicity conservation requires $H+h' = H'+h$. Parity sends $h \rightarrow -h$ and $H \rightarrow -H$, and time-reversal interchanges initial (H, h') and final (H', h) helicities. Because of helicity conservation law, the only three possibilities for reaction 1.24 are the following:

$$\begin{array}{cccccc} \frac{1}{2} & \frac{1}{2} & \longrightarrow & \frac{1}{2} & \frac{1}{2} \\ \frac{1}{2} & -\frac{1}{2} & \longrightarrow & \frac{1}{2} & -\frac{1}{2} \\ \frac{1}{2} & -\frac{1}{2} & \longrightarrow & -\frac{1}{2} & \frac{1}{2} \end{array} \tag{1.25}$$

Each of the three possibilities (sketched in figure 1.3) is proportional to one of the PDF described in 1.3.1:

$$\begin{array}{lcl} f(x) & \longleftrightarrow & \left(\frac{1}{2} \;\; \frac{1}{2} \;\; \rightarrow \;\; \frac{1}{2} \;\; \frac{1}{2} \right) + \left(\frac{1}{2} \;\; -\frac{1}{2} \;\; \rightarrow \;\; \frac{1}{2} \;\; -\frac{1}{2} \right) \\ \Delta f(x) & \longleftrightarrow & \left(\frac{1}{2} \;\; \frac{1}{2} \;\; \rightarrow \;\; \frac{1}{2} \;\; \frac{1}{2} \right) - \left(\frac{1}{2} \;\; -\frac{1}{2} \;\; \rightarrow \;\; \frac{1}{2} \;\; -\frac{1}{2} \right) \\ \Delta_T f(x) & \longleftrightarrow & \left(\frac{1}{2} \;\; -\frac{1}{2} \;\; \rightarrow \;\; -\frac{1}{2} \;\; \frac{1}{2} \right) \end{array} \tag{1.26}$$

By averaging on the spin direction, the last two functions vanish unless the nucleon target is polarized in some direction. This means that, in order to study the helicity and transversity related phenomena, the polarized DIS reactions should be investigated.

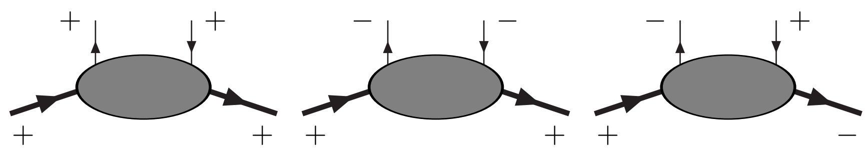

Figure 1.3: The three quark-nucleon helicity amplitudes.

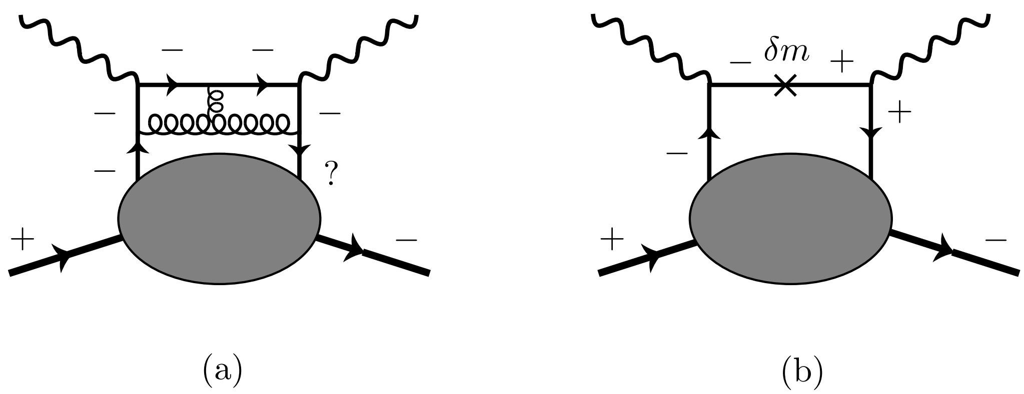

Figure 1.4: Why $\Delta_T f(x)$ decouples from DIS. (a) A typical perturbative contribution to DIS. The chirality of the propagating quark is not changed by the coupling to gluons or photon, so it cannot be reabsorbed to form the outgoing nucleon. (b) A mass insertion (marked with an $\times$) can flip chirality but gives a contribution suppressed by $\mathcal{O}(1/Q^2)$.

In particular, transversity is proportional to the "helicity flip" channel[4] which is dummy in inclusive DIS at the leading order. The third channel in 1.26, cannot be generated by a single quark distribution or fragmentation (as it is shown in figure 1.4) unless a mass insertion breaks the symmetry at higher twist[5].

This suggests (as it will be discussed in the next sections) that transversity can't be directly measured in a polarized DIS reaction.

[4]This behaviour w.r.t. the helicity is sometimes in literature expressed as a mathematical property (odd chirality) of function $h_1(x)$ but the meaning is unchanged.

[5]The term twist strictly describes the parameter t in the kinematical coefficient Q^{-t+2} extracted from the hadronic tensor. From the experimental point of view, the twist represents the level at which some effects appear in the cross-sections. Throughout this text, the expression twist two or leading twist are taken as synonym of leading order.

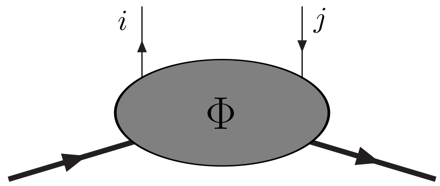

Figure 1.5: The quark-quark correlation matrix Φ.

1.3.3 The QCD quark-quark correlation matrix

In figure 1.5 it's shown the conceptual meaning of the correlation matrix Φ which connects an incoming quark in a state i to an outgoing quark in a state j:

$$\Phi_{ij}(k,P,S) = \int d^4\xi\, \mathrm{e}^{\mathrm{i}k\cdot\xi}\, \langle PS|\bar{\psi}_j(0)\psi_i(\xi)|PS\rangle\,. \tag{1.27}$$

Here, we recall, i and j are Dirac indices and a summation over color is implicit. The parton distribution functions are calculated as integrals over k of traces of the form:

$$\mathrm{Tr}(\Gamma\Phi) = \int d^4\xi\, \mathrm{e}^{\mathrm{i}k\cdot\xi}\, \langle PS|\bar{\psi}(0)\,\Gamma\,\psi(\xi)|PS\rangle\,, \tag{1.28}$$

where Γ is a Dirac matrix structure, generally expressed as linear combination of the Dirac basis:

$$\Gamma = \left\{1,\ \gamma^\mu,\ \gamma^\mu\gamma^5,\ \mathrm{i}\gamma^5,\ \mathrm{i}\sigma^{\mu\nu}\gamma^5\right\}, \tag{1.29}$$

The complete tree level result for equation 1.27 is well described in [3] and it'll be revisited in the next section. Neglecting all the contributions above the leading twist, one symbolically gets:

$$\Phi(x) = \frac{1}{2}\left\{f(x)\,\not{P} + \lambda_N\,\Delta f(x)\,\gamma_5\,\not{P} + \Delta_T f(x)\,\not{P}\,\gamma_5\,\not{S}_\perp\right\}\,, \tag{1.30}$$

where $f(x)$ is the coefficient of the unpolarized term, $\Delta f(x)$ is the coefficient for the helicity-dependent term and $\Delta_T f(x)$ is the coefficient for the transverse spin component.

1.3.4 The Parton Distribution Functions (PDF)

In particular, working in the light-cone frame and applying the time reversal invariance[6] to eq. 1.28, the projection on γ^+,$\gamma^+\gamma_5$ and $\sigma^{1+}\gamma_5$ retrieve[7] the leading twist PDFs introduced in section 1.3.1:

$$\begin{aligned}
\Phi^{[\gamma^+]} &= \quad f_1^{(R)} + f_1^{(L)} \quad &&\equiv f(x) \propto F_2/2x \\
\Phi^{[\gamma^+\gamma_5]} &= \quad f_1^{(R)} - f_1^{(L)} \quad &&\equiv \Delta f(x) \propto \lambda g_1, \\
\Phi^{[i\sigma^{1+}\gamma_5]} &= \quad f_1^{(\uparrow)} - f_1^{(\downarrow)} \quad &&\equiv \Delta_T f(x) \propto S_T^i h_1
\end{aligned} \tag{1.31}$$

By convention the functions traced with a vector matrix (γ^μ) are called $f_{..}$; those traced with an axial vector matrix ($\gamma^\mu\gamma_5$) are called $g_{..}$ and finally those traced with the second rank tensor ($i\sigma^{\mu\nu}\gamma_5$) are called $h_{..}$. The subscript $'1'$ tags the twist-two functions.

Going further in the formalism, one succeeds to trace the relation between two of the three leading order PDFs appearing in eq. 1.31 and the hadronic tensor appearing in the cross-section:

$$W_{\mu\nu}^{(\mathrm{S})} \propto F_2(x)/2x = \frac{1}{2}\sum_a e_a^2\left[f_a(x) \ + \ \bar{f}_a(x)\right] \tag{1.32}$$

$$W_{\mu\nu}^{(\mathrm{A})} \propto g_1(x) = \frac{1}{2}\sum_a e_a^2\left[\Delta f_a(x) + \Delta\bar{f}_a(x)\right] , \tag{1.33}$$

In figure 1.6 the measurements of F_2 and xg_1 by the first and second generation of DIS experiments are presented. As it has been already said, because of the intrinsic nature of transversity, $h_1(x)$ doesn't play any role in inclusive polarized DIS and must be measured through different channels.

[6]This property can apply because the quark-quark correlation functions refer to the target structure independently from the collision (which breaks the time reversal invariance).

[7]The involved Dirac matrices are re-defined from the light-cone axis.

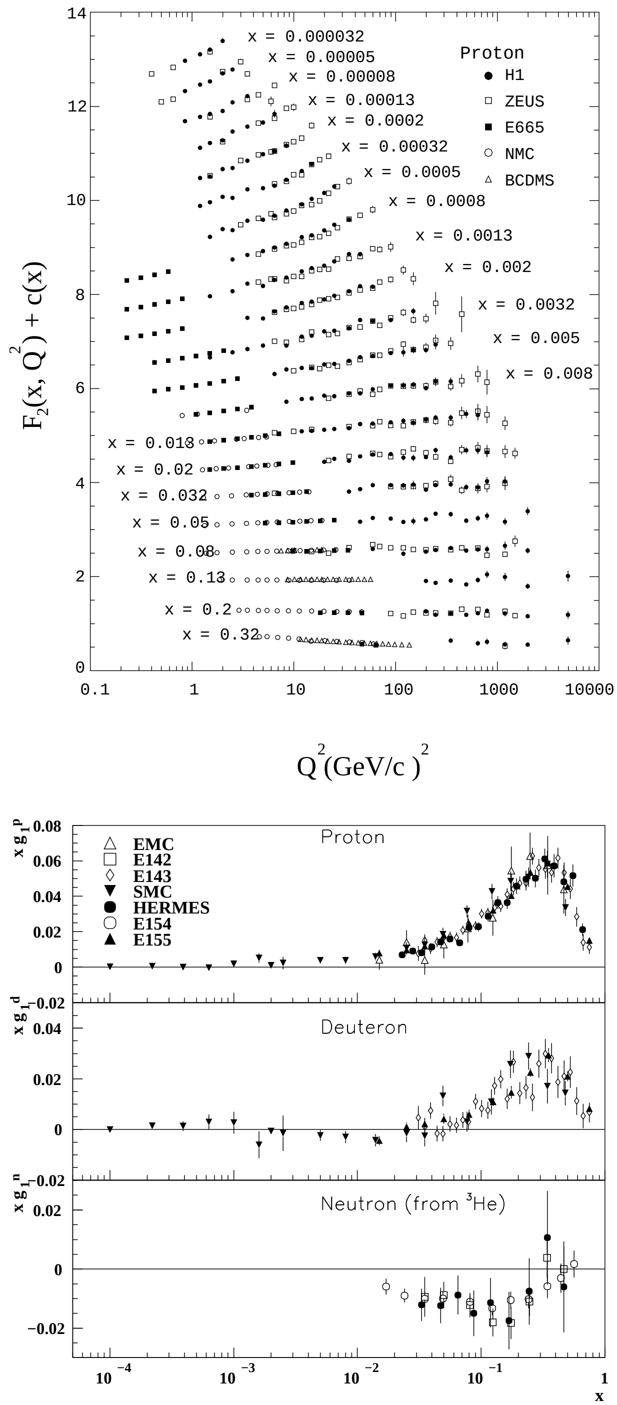

Figure 1.6: Measurement of F_2 (proton) as function of Q^2 and $xg_1(x)$ (for proton, neutron and deuteron) by the first and second generations of DIS experiments.

From theoretical physics we know that this observable obeys to the following relations:

verifies the Soffer bound:

$$|h_1(x)| \ \leq \ (f_1(x) \ + \ g_1(x))\,; \tag{1.34}$$

has non-relativistic limit:

$$h_1(x) \ = \ g_1(x)\,. \tag{1.35}$$

In the following sections the channel offered by semi-inclusive DIS to measure transversity will be presented.

1.4 Transversity in semi-inclusive DIS

1.4.1 The role of quark fragmentation function

At variance with the inclusive case, in semi-inclusive DIS, the quark-quark correlation matrix isn't sufficient to fully describe the reaction.

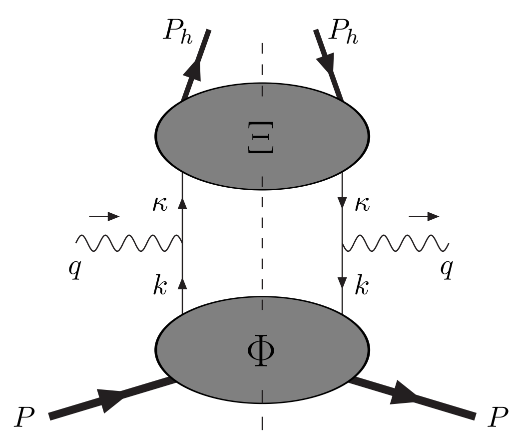

Figure 1.7: Diagram contributing to semi-inclusive DIS at LO.

Figure 1.7 shows the conceptual scheme of a reaction in which a quark of momentum k is emitted and reabsorbed by the nucleon (of quark-quark correlation matrix Φ), fragments into a hadron of momentum P_h and correlation matrix Ξ.

The hadron production is a time reversal non invariant phenomenon involving the quark fragmentation functions defined as:

$$\Delta_{ij}(P_h, S_h; k) = \sum_X \int d^4x\ e^{ik\cdot x}\,\langle 0|\psi_i(x)|P_h, S_h; X\rangle\langle P_h, S_h; X|\overline{\psi}_j(0)|0\rangle \quad (1.36)$$

$$= \int d^4x\ e^{ik\cdot x}\,\langle 0|\psi_i(x)a_h^\dagger a_h\overline{\psi}_j(0)|0\rangle\,, \quad (1.37)$$

where an averaging over color indices is implicit and $a_h^\dagger$ and a_h are the creation and annihilation matrices operating on the vacuum to produce the states $|P_h, S_h; X\rangle$ where P_h and S_h are the momentum and spin vectors of the produced hadron.

Developing the same formalism that in section 1.3.3 led to equation 1.28, it is possible to project the fragmentation function 1.37 on the Dirac basis:

$$Tr\big(\Gamma\Delta(z, \mathbf{k}'_T)\big) = \int d^4\xi e^{ik\cdot\xi}\,\langle 0|\,\psi(\xi)a_h^\dagger a_h\overline{\psi}(0)\Gamma|0\rangle\,. \quad (1.38)$$

The arguments of the functions are the lightcone momentum fraction z and the transverse momentum $\mathbf{k}'_T$, which is the perpendicular momentum of the hadron h with respect to the quark momentum.

In particular, projecting to γ^-, $\gamma^-\gamma^5$ and $i\sigma^{i-}\gamma^5$, the following functions are found:

$$\Delta^{[\gamma^-]}(z, \mathbf{k}'_T) = D_1(z, \mathbf{k}'^2_T) + \frac{\epsilon_{T\,ij}\,k_T^i S_{hT}^j}{M_h}\,D_{1T}^\perp(z, \mathbf{k}'^2_T), \quad (1.39)$$

$$\Delta^{[\gamma^-\gamma_5]}(z, \mathbf{k}'_T) = G_{1s}(z, \mathbf{k}'_T) \quad (1.40)$$

$$\Delta^{[i\sigma^{i-}\gamma_5]}(z, \mathbf{k}'_T) = S_{hT}^i\,H_{1T}(z, \mathbf{k}'^2_T) + \frac{k_T^i}{M_h}\,H_{1s}^\perp(z, \mathbf{k}'_T) + \frac{\epsilon_T^{ij}k_{Tj}}{M_h}\,H_1^\perp(z, \mathbf{k}'^2_T). \quad (1.41)$$

In the above expressions we have used the shorthand notations G_{1s} etc. standing for;

$$G_{1s}(z, \mathbf{k}'_T) = \lambda_h\,G_{1L}(z, \mathbf{k}'^2_T) + \frac{(\mathbf{k}_T\cdot\mathbf{S_{hT}})}{M_h}\,G_{1T}(z, \mathbf{k}'^2_T). \quad (1.42)$$

Consistently with the quark-quark correlation matrix treatment, the decaying functions traced with a vector matrix (γ^μ) are called $D_{..}$, those traced with an axial vector matrix ($\gamma^\mu\gamma_5$) are called $G_{..}$ and finally those traced with the second rank tensor ($i\sigma^{\mu\nu}\gamma_5$) are called $H_{..}$. A subscript $'1'$ is given to the twist-two functions, subscripts $'L'$ or $'T'$ refer to the connection with the hadron spin being longitudinal or transverse and a superscript $'\perp'$ signals the explicit presence of transverse momenta with a non contracted index.

The twist-two functions have a natural interpretation as decay functions, $\Delta^{[\gamma^-]}$ being the probability of a quark to produce a hadron in a specific spin state (characterized by the spin vector S_h).

Indeed, as we will see in section 1.4.2, the function $D_{1T}^{\perp}$ is a purely interaction-dependent function.

The fragmentation functions $\Delta^{[\gamma^-\gamma_5]}$ and $\Delta^{[i\sigma^{i-}\gamma_5]}$ are differences of probabilities for quarks with, respectively, different chiralities or transverse spins to produce a hadron in a specific spin state. For the latter also a new decay function appears because of the non-applicability of time reversal invariance. A transversely polarized quark with nonzero transverse momentum can produce unpolarized hadrons, in particular it can produce spinless particles, such as pions. The relevant function $H_1^{\perp}$ is the one appearing in the single spin Collins effect [4], investigated at COMPASS and object of the preliminary results reported in this thesis.

Among the decaying functions appearing in 1.41, $D_{1T}^{\perp}$ and $H_1^{\perp}$, because of their time-reversal odd nature, have no equivalent in the quark-quark correlation functions.

1.4.2 The integrated cross section

Let's consider, first of all, the cross-sections integrated over $\vec{P}_{h\perp}$. In this case we obtain:

$$\begin{aligned}\frac{d\sigma}{dxdydz} &= \frac{4\pi\alpha_{\mathrm{em}}^2 s}{Q^4}\sum_a e_a^2\, x \left\{\frac{1}{2}\left[1+(1-y)^2\right] f_a(x)\, D_a(z)\right. \\ &- \left.(1-y)\,|\vec{S}_\perp|\,|\vec{S}_{h\perp}|\,\cos(\phi_S+\phi_{S_h})\,\Delta_T f_a(x)\, D_{1Ta}^{\perp}(z)\right\}. \qquad (1.43)\end{aligned}$$

As one can see, at leading twist, the transversity distributions are probed only when both the target and the produced hadron are transversely polarised.

From (1.43) we can extract the transverse polarisation $\vec{\mathcal{P}}_h$ of the detected hadron, defined so that:

$$d\sigma = d\sigma_{\rm unp}\,(1 + \vec{\mathcal{P}}_h \cdot \vec{S}_h)\,. \tag{1.44}$$

If we denote by $\mathcal{P}_{hy}^{\uparrow}$ the transverse polarisation of h along y, when the target nucleon is polarised along y ($\uparrow$), and by $\mathcal{P}_{hx}^{\rightarrow}$ the transverse polarisation of h along x, when the target nucleon is polarised along x ($\rightarrow$), we find

$$\mathcal{P}_{hy}^{\uparrow} = -\mathcal{P}_{hx}^{\rightarrow} = \frac{2(1-y)}{1+(1-y)^2}\,\frac{\sum_a e_a^2\,\Delta_T f_a(x)\,D_{1Ta}^{\perp}(z)}{\sum_a e_a^2\,f_a(x)\,D_a(z)}\,. \tag{1.45}$$

If the hadron h is not transversely polarised, or – *a fortiori* – is spinless, the leading-twist $\vec{P}_{h\perp}$-integrated cross-section does not contain $\Delta_T f$. In this case, in order to probe the transversity distributions, one has to observe the $\vec{P}_{h\perp}$ distributions as we shall discuss in the next sections, or consider higher-twist contributions.

The equation 1.45 represents the most favored channel to investigate transversity through, for instance, lambda production.

1.4.3 Azimuthal asymmetries

We now study the (leading-twist) $\vec{P}_{h\perp}$ distributions in semi-inclusive DIS and the resulting azimuthal asymmetries. We shall assume that the detected hadron is spinless, or that its polarisation is not observed. For simplicity, we also neglect the transverse motion of quarks inside the target. The transversity dependent term in the hadron tensor can be written as:

$$\begin{aligned} W^{\mu\nu(S)} &= 2\sum_a e_a^2\,z\int d^2\vec{\kappa}_T\,\delta^2(\vec{\kappa}_T + \vec{P}_{h\perp}/z) \\ &\quad\times\Big\{ -g_\perp^{\mu\nu}\,f(x)\,D(z,\vec{\kappa}_T'^2) \\ &\qquad -\frac{\Big(S_T^{\{\mu}\varepsilon_T^{\nu\}\rho}\kappa_{T\rho} + \kappa_T^{\{\mu}\varepsilon_T^{\nu\}\rho}S_{T\rho}\Big)}{2M_h}\,\Delta_T f(x)\,H_1^{\perp}(z,\vec{\kappa}_T'^2) \\ &\qquad + \ldots\Big\}. \end{aligned} \tag{1.46}$$

Contracting $W^{\mu\nu(S)}$ with the leptonic tensor one can write the azimuthal dependent cross-section:

$$
\begin{aligned}
\frac{d\sigma}{dx\,dy\,dz\,d^2\vec{P}_{h\perp}} &= \frac{4\pi\alpha_{\rm em}^2 s}{Q^4} \sum_a e_a^2\, x \left\{ \frac{1}{2}\left[1+(1-y)^2\right] f_a(x)\, D_a(z,\vec{P}_{h\perp}^2) \right. \\
&\qquad + (1-y)\,\frac{|\vec{P}_{h\perp}|}{zM_h}\,|\vec{S}_\perp|\,\sin(\phi_S+\phi_h) \\
&\qquad \left. \times\, \Delta_T f_a(x)\, H_{1a}^\perp(z,\vec{P}_{h\perp}^2) \right\}. \qquad (1.47)
\end{aligned}
$$

From this we obtain the transverse single-spin asymmetry

$$
\begin{aligned}
A_T^h &\equiv \frac{d\sigma(\vec{S}_\perp)-d\sigma(-\vec{S}_\perp)}{d\sigma(\vec{S}_\perp)+d\sigma(-\vec{S}_\perp)} \\
&= \frac{2(1-y)}{1+(1-y)^2}\,\frac{\sum_a e_a^2\,\Delta_T f_a(x)\,\Delta_T^0 D_a(z,\vec{P}_{h\perp}^2)}{\sum_a e_a^2\, f_a(x)\, D_a(z,\vec{P}_{h\perp}^2)}\,|\vec{S}_\perp|\,\sin(\phi_S+\phi_h)\,. \qquad (1.48)
\end{aligned}
$$

The factor (dependent on y) appearing in 1.48 is usually called depolarization factor:

$$
D_{NN} = 2\,(1-y)\,/\,\left(1+(1-y)^2\right) \qquad (1.49)
$$

The T-odd fragmentation function $\Delta_T^0 D(z,\vec{P}_{h\perp}^2)$ is defined as:

$$
\Delta_T^0 D(z,\vec{P}_{h\perp}^2) = \frac{|\vec{P}_{h\perp}|}{zM_h}\,H_1^\perp(z,\vec{P}_{h\perp}^2)\,. \qquad (1.50)
$$

The existence of an azimuthal asymmetry in transversely polarised leptoproduction of spinless hadrons at leading twist, which depends on the T-odd fragmentation function $H_1^\perp$ and arises from final-state interaction effects, was predicted by Collins [5] and is now known as the Collins effect.

The measurement of the analyzing power $\left\langle \frac{H_1^\perp}{D} \right\rangle$ appearing in eqs 1.48 and 1.50 performed at LEP by DELPHI collaboration will be discussed in section 2.3.2.

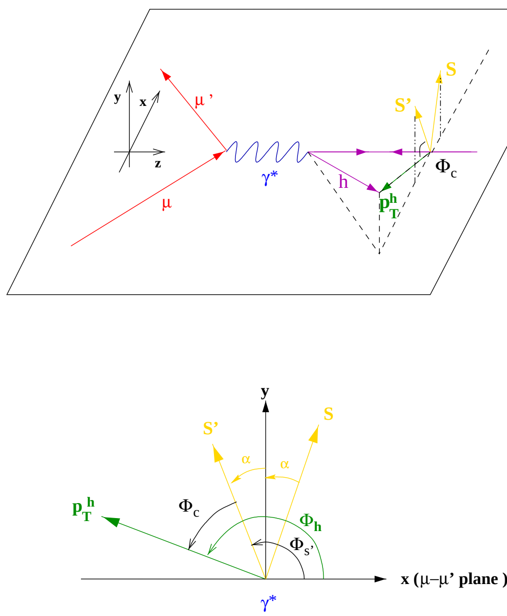

Figure 1.8: Definition of the 'Collins angle' $\phi_c = \phi_h - \phi_{S'}$ in the Breit frame: (a) perspective view, (b) front view (the γ^* points out of the page).

The Collins angle Φ_C was originally defined in as the angle between the transverse spin vector of the fragmenting quark and the transverse momentum of the outgoing hadron, i.e.,

$$\Phi_C = \phi_h - \phi_{s'} \,. \tag{1.51}$$

Since, as dictated by QED, the directions of the final and initial quark spins are related to each other by (see Fig. 1.8):

$$\phi_{s'} = \pi - \phi_s \,, \tag{1.52}$$

equation 1.51 becomes $\Phi_C = \phi_s + \phi_h - \pi$. Ignoring the transverse motion of quarks in the target, the initial quark spin is parallel to the target spin (*i.e.*, $\phi_s = \phi_S$) and Φ_C can finally be expressed in terms of measurable angles as:

$$\Phi_C = \phi_S + \phi_h - \pi \,. \tag{1.53}$$

Chapter 2

Experimental results and perspectives

2.1 Phenomenology of transversity

Since the transversity physics case is quite recent, only few experimental observations have been published in the last 10 years. Several European and American laboratories have contributed to the study of transversity via three kinds of reactions:

1. polarized hadron-hadron collisions;

2. lepton-nucleon polarized DIS;

3. $e^+ \, e^-$ collisions.

Since lepton-nucleon polarized DIS is also the method pursued by COMPASS, the results obtained in so far will be discussed in detail. Some important results which have been shown recently in the International Workshop on Spin Physics at BNL (SPIN 2002) will be added in section 2.3.1.

2.2 Lepton-nucleon DIS with a transversely polarised target

In a DIS of high energy muons off a transversal polarized target, the structure function h_1 can be determined via the following channels:

1. semi-inclusive leptoproduction of a transversely polarised hadron;

2. semi-inclusive leptoproduction of an unpolarised hadron;

3. exclusive leptoproduction of an unpolarised hadron;

4. semi-inclusive leptoproduction of two or more hadrons;

The first quantitative results have been published by SMC and HERMES collaborations looking at pion leptoproduction. The semi-inclusive leptoproduction of a transversely polarised hadron (e.g. Λ production) will be investigated at COMPASS but it's not treated in this thesis. Finally the results in the correlation of the two-mesons system in semiinclusive leptoproduction [6] haven't yet been published .

COMPASS proposes to investigate all these channels starting from the same algorithm used in the SMC paper and described in section 2.2.2.

2.2.1 The HERMES results

The HERMES results [7] refer to the data collected in 1997 when a 27.6 GeV positron beam has scattered off a hydrogen longitudinally polarized target.

The data analysis on transversity-related signals is possible making use of the kinematically suppressed (by a factor $\frac{1}{Q}$) transverse spin component of the proton target:

$$|\vec{S}_\perp| \equiv |\vec{S}| \sin\theta_\gamma \simeq \frac{2Mx}{Q}\sqrt{1-y}\,|\vec{S}|\,. \tag{2.1}$$

The HERMES results for semi-inclusive leptoproduction of positive pions

The letter published in 2000 claims the first measurements of azimuthal asymmetry for semi-inclusive pion production at HERMES experiment, DESY.

The electron beam extracted from HERA storage ring, has 27.6 GeV energy and scatters off a nuclear target.

The measurements have been performed on longitudinally polarized and unpolarized targets[1]. Both the scattered positron and the produced hadron are detected by the HERMES spectrometer inside its $0.04 \times 0.22\ rad^2$-wide acceptance.

[1] All the measurements belonging to longitudinal polarized beam scattering off an unpolarized target, also reported in the cited article are skipped.

The kinematics of the process is illustrated for the lepton-gamma frame in figure 2.1 where k and k' are the incoming and scattered muon momenta:

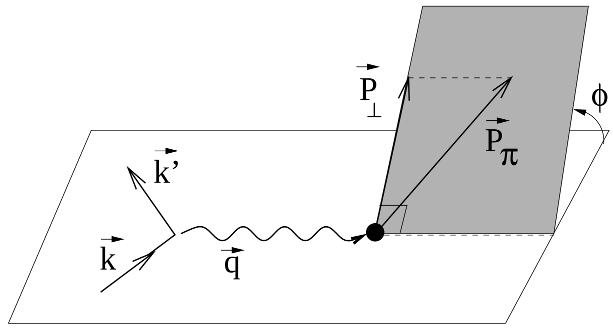

Figure 2.1: Kinematic planes for pion production in semi-inclusive deep-inelastic scattering.

The outgoing pion, emitted with an azimuthal angle Φ, has momentum P and transverse component $P_\perp$. The target spin, being parallel to the incoming lepton, lies in the scattering plane and the Collins angle coincides with the azimuthal angle Φ of the hadron. The azimuth-dependent spin asymmetry can be written as:

$$A_{UL}^{W} = \frac{\frac{L^{\uparrow}}{L_P^{\uparrow}} \sum_{i=1}^{N^{\uparrow}} W(\phi_i^{\uparrow}) \; - \; \frac{L^{\downarrow}}{L_P^{\downarrow}} \sum_{i=1}^{N^{\downarrow}} W(\phi_i^{\downarrow})}{\frac{1}{2}[N^{\uparrow} \; + \; N^{\downarrow}]}, \tag{2.2}$$

where the $\uparrow$ / $\downarrow$ denotes positive/negative helicity of the target. $N^{\uparrow/\downarrow}$ is the number of selected events involving a detected pion for each target spin state corresponding to the dead-time corrected luminosities $L^{\uparrow/\downarrow}$ and $L_P^{\uparrow/\downarrow}$, the latter being averaged with the magnitude of the target polarization.

All of these quantities are effectively averaged over the two beam helicity states to arrive at single-spin asymmetries. The weighting functions $W(\phi) = \sin\phi$ and $W(\phi) = \sin 2\phi$ are expected to provide sensitivity to the fragmentation functions discussed in chapter 1, in combination with different spin distribution functions [8] [3]:

$$\sin\phi \quad \longrightarrow \quad h_1(x) \otimes H_1^{\perp}(z) \tag{2.3}$$

$$\sin 2\phi \quad \longrightarrow \quad h_{1L}^{\perp}(x) \otimes H_1^{\perp}(z) \tag{2.4}$$

Several kinematical cuts are applied to:

	π^+	π^-
$A_{UL}^{\sin\phi}$	0.022±0.005±0.003	-0.002±0.006±0.004
$A_{UL}^{\sin 2\phi}$	-0.002±0.005±0.010	-0.005±0.006±0.005

Table 2.1: Target- and beam-related analyzing powers, averaged over x and $P_\perp$, for the azimuthal $\sin\phi$ and $\sin 2\phi$ moments of the pion production cross section in deep-inelastic scattering.

	$\langle Q^2\rangle$	π^+		π^-	
$\langle x\rangle$	(GeV^2)	$A_{UL}^{\sin\phi}$	$A_{UL}^{\sin 2\phi}$	$A_{UL}^{\sin\phi}$	$A_{UL}^{\sin 2\phi}$
0.040	1.4	0.010±0.008±0.004	-0.008±0.008±0.011	-0.004±0.010±0.004	0.002±0.010±0.008
0.074	2.2	0.028±0.009±0.003	0.007±0.009±0.012	-0.004±0.010±0.003	-0.008±0.010±0.010
0.137	3.7	0.032±0.011±0.003	-0.005±0.011±0.009	0.012±0.013±0.003	-0.007±0.013±0.007
0.257	6.4	0.041±0.021±0.005	0.005±0.021±0.009	-0.025±0.028±0.005	-0.028±0.028±0.008

Table 2.2: Target-related analyzing powers averaged over $P_\perp$, for the azimuthal $\sin\phi$ and $\sin 2\phi$ moment of the π^+ and π^- production cross section in deep-inelastic scattering as a function of x.

1. virtual scattered photon mass: $1\ GeV^2 < Q^2 < 15\ GeV^2$;
2. invariant mass of the phton-proton system: $W \equiv \sqrt{2M\nu + M^2 - Q^2} > 2\ GeV$;
3. x range[2] : $0.023 < x < 0.4$;
4. energy transfer: $y < 0.85$;
5. hadron carried momentum: $0.2 < z < 0.7$;
6. azimuthal angle: $P^\perp > 50\ MeV$.

The results integrated over x and $P_\perp$ are shown in table 2.1. The first moment $A_{UL}^{\sin\phi}$, strictly related to the Collins effect as described in chapter 1, is well above 0 (a bit less than 4 standard deviations) in case of π^+ while it is consistent with 0 in case of π^-. In the quark-parton model this effect can be caused by the bigger content of u quarks with respect to d quarks in the proton target.

The second moment $A_{UL}^{\sin 2\phi}$ is consistent with zero for both positive and negative pions.

In table 2.2 the behaviour of the two analyzing powers in function of x intervals is shown.

[2]To be far from the region in which PDF's vanish.

The HERMES results for exclusive leptoproduction of positive pions

In this new letter [9] the Collins angle has been calculated through the exclusive reaction:

$$e^+ + \vec{p} \rightarrow e'^+ + n + \pi^+ . \tag{2.5}$$

The events have been tagged requiring that the missing mass in the corresponding semi-inclusive reaction:

$$e^+ + \vec{p} \rightarrow e'^+ + X + \pi^+ \tag{2.6}$$

corresponds to the nucleon mass. Actually the results presented requires that $M_X < 1.05$ GeV. The analysis has been done applying some kinematics cuts on the:

1. virtual scattered photon mass: $Q^2 > 1\ GeV^2$;
2. invariant mass of the photon-proton system: $W > 2\ GeV$;
3. x range: $0.023 < x < 0.8$.

The azimuthal asymmetry has then been evaluated as:

$$A(\phi) = \frac{1}{|P|} \frac{N_e^{\uparrow}(\phi) - N_e^{\downarrow}(\phi)}{N_e^{\uparrow}(\phi) + N_e^{\downarrow}(\phi)} , \tag{2.7}$$

where N_e represents the yield of exclusive π^+, the superscript $\uparrow$ ($\downarrow$) denotes a target polarization direction anti-parallel (parallel) to the positron beam momentum, and P is the average polarization of the target protons.

The cross section asymmetry integrated over x, Q^2 and t is shown in Fig. 2.2. The average values of the kinematical variables are $\langle x \rangle = 0.15$, $\langle Q^2 \rangle = 2.2$ GeV^2 and $\langle t \rangle = -0.46$ GeV^2 (with 75% of the events occurring at $|t| < 0.5$ GeV^2). The data show a large asymmetry in the distribution versus azimuthal angle ϕ, with a clear $\sin\phi$ dependence. A fit to this dependence of the form

$$A(\phi) = A_{\mathrm{UL}}^{\sin\phi} \cdot \sin\phi \tag{2.8}$$

yields $A_{\mathrm{UL}}^{\sin\phi} = -0.18 \pm 0.05 \pm 0.02$ with a reduced χ^2 of 0.8. The summary of the kinematical behaviour as function of x, Q^2 and t are reported in table 2.3.

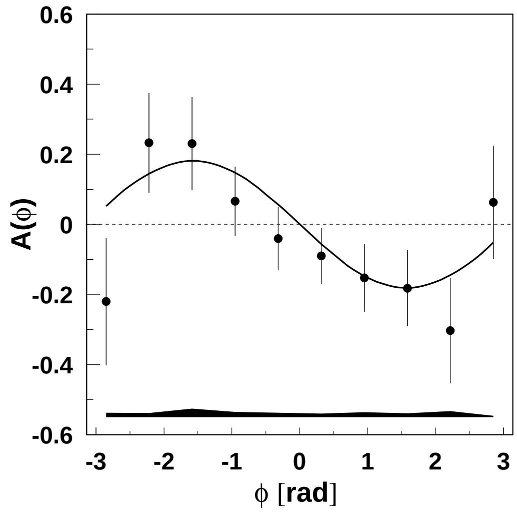

Figure 2.2: Cross section asymmetry $A(\phi)$ averaged over x, Q^2, and t for the reaction $e^+ + \vec{p} \to e'^+ + n + \pi^+$.

2.2.2 The SMC results

The SMC collaboration has looked [10] at transversity effects selecting the leading (fastest) hadron produced in DIS off a transversely polarized target (proton and deuteron) and by studying its azimuthal dependence with respect to the ϕ_c angle, defined in the Breit frame (see figure 1.8). This is equivalent to look for asymmetries in the yields of hadrons produced opposite in azimuth (weighted by sin ϕ_c)

$$\varepsilon_N = \frac{1}{< \sin\,\phi_c >} \cdot \frac{N(\phi_c) - N(\phi_c + \pi)}{N(\phi_c) + N(\phi_c + \pi)} \tag{2.9}$$

The largest effects appear for sin $\phi_c = \pm\,\pi$ (therefore left-right asymmetry w.r.t. final quark spin). The transverse single-spin asymmetry A_N is derived from the measured asymmetry ε_N as

$$A_N = \frac{1}{P_T\, f\, D_{NN}} \cdot \varepsilon_N \tag{2.10}$$

where P_T and f are the target transverse polarization and dilution factor, respectively. D_{NN} is the transverse spin transfer coefficient (or depolarization factor) in $\gamma^* + q \uparrow\to q'$ defined in 1.49. D_{NN} is large at low y and decreases with increasing y. The low y region

	$\langle x \rangle$	$\langle Q^2 \rangle$ [GeV^2]	$\langle \sin\theta_\gamma \rangle$	$A_{\mathrm{UL}}^{\sin\phi}$
x				
0.05		1.3	0.06	$-0.40 \pm 0.16 \pm 0.02$
0.08		1.6	0.10	$-0.24 \pm 0.10 \pm 0.02$
0.16		2.6	0.16	$-0.10 \pm 0.07 \pm 0.01$
0.31		3.6	0.29	$-0.04 \pm 0.22 \pm 0.02$
0.47		5.0	0.36	$0.25 \pm 0.54 \pm 0.02$
Q^2 [GeV^2]				
1.5	0.12		0.15	$-0.20 \pm 0.07 \pm 0.02$
2.4	0.17		0.17	$-0.21 \pm 0.11 \pm 0.02$
3.4	0.21		0.17	$-0.13 \pm 0.14 \pm 0.01$
5.1	0.26		0.16	$-0.07 \pm 0.17 \pm 0.01$
7.9	0.38		0.19	$-0.13 \pm 0.51 \pm 0.01$
$-t$ [GeV^2]				
0.04	0.11	2.2	0.11	$-0.04 \pm 0.08 \pm 0.01$
0.14	0.13	2.4	0.13	$-0.18 \pm 0.13 \pm 0.02$
0.25	0.14	2.3	0.14	$-0.31 \pm 0.15 \pm 0.02$
0.39	0.16	2.5	0.16	$-0.33 \pm 0.14 \pm 0.02$
1.34	0.24	2.8	0.24	$-0.20 \pm 0.12 \pm 0.02$

Table 2.3: $A_{\mathrm{UL}}^{\sin\phi}$ as a function of x, Q^2, and t.

corresponds also to the large x region, where quarks polarization is expected to be higher. Thus larger asymmetries are expected at lower y. The events have been selected requiring:

- $Q^2 > 1$ GeV^2;
- $y < 0.7$;
- $\nu > 10\,(15)$ GeV for proton (deuteron) data;

and, for the most energetic hadron in the event

- $z > 0.25$;
- $p_T > 0.1$ GeV/c and $p_T > 0.5$ GeV/c.

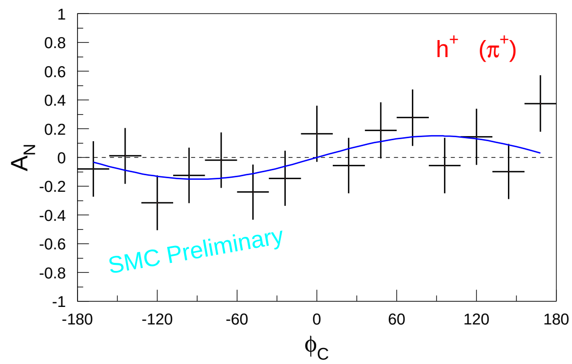

Figure 2.3: ϕ_c azimuthal distributions for positive hadrons produced off transversely polarized protons with a $(Const + A_N \sin\,\phi_c)$ fit superimposed.

About 120 K events on proton and about 250 K events on deuteron have passed these selections and have been used in the analysis. Average values of the kinematical variables for the selected sample are: $< z >\sim 0.45$, $< p_T >\sim 0.5$ GeV/c for the $p_T > 0.1$ GeV/c data and $< p_T >\sim 0.8$ GeV/c for the $p_T > 0.5$ GeV/c data, both for the proton and the deuteron target.

The target system of SMC used consisted of two cells with opposite polarizations. During the data taking, the target polarization itself was reversed several times in order to minimize systematic effects related to the apparatus acceptance and changes in efficiencies.

Figure 2.3 shows the ϕ_c azimuthal distribution for positive hadrons (mainly π^+'s) produced off the polarized proton target. This ϕ_c distribution has been obtained from the measured one (raw distribution) after weighting it with $P_T\, f\, D_{NN}$ and subtracting the unpolarized part. The superimposed sinusoidal line is a fit to the data of the form $(Const + A_N \sin\,\phi_c)$.

Figure 2.4 shows the transverse single-spin asymmetry A_N for proton and deuteron data separately. In figure 2.4a the A_N data are also separated for positive (mainly π^+'s) and negative (mainly π^-'s) hadrons. $A_N = 0.11 \pm 0.06$ for π^+'s, and $A_N = -0.02 \pm 0.06$ for π^-'s on the proton target at $< x >\sim 0.08$ and $< Q^2 >\sim 5$ GeV^2. On deuteron, A_N is small for both π^+'s and π^-'s. Figures 2.4b and 2.4c show the p_T dependence of A_N for positive and negative hadrons, respectively. The data indicate that A_N increases in magnitude with increasing p_T.

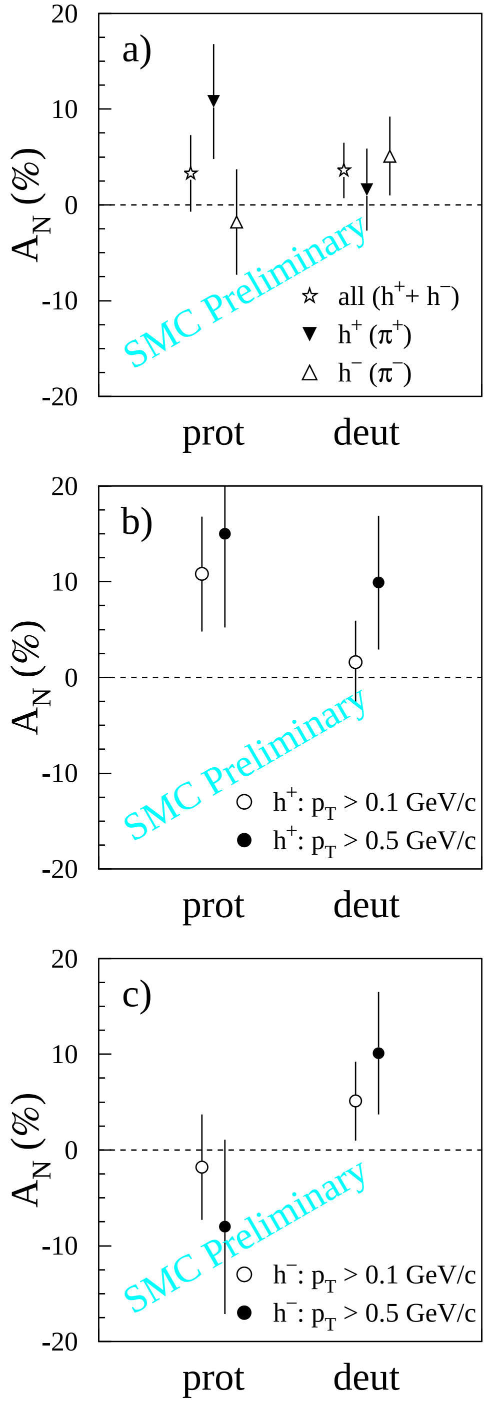

Figure 2.4: The transverse spin asymmetry A_N for proton and deuteron data. The errors shown are statistical only.

Although the statistical precision is limited indications of possible transverse spin effects are observed in the data, with an almost $2\,\sigma$ positive effect for π^+'s produced on protons.

2.3 Other channels to observe transversity

2.3.1 The preliminary results at RHIC

The Relativistic Heavy Ion Collider (RHIC, sketched in fig. 2.5) at the Brookhaven National Laboratory operates with gold ions and protons. With the addition of Siberian snakes and spin rotators, there is the possibility of accelerating intense polarised proton beams.

The spin-physics program at RHIC will study reactions involving two polarised proton beams with both longitudinal and transverse spin orientations. At the average centre-of-mass energy of 200 GeV, with a mean polarization for one of the proton beams of about 16% and an integrated luminosity of 0.2 pb^{-1}, the STAR experiment has shown at Spin 2002 conference [11] its preliminary results on transversity.

The talk dealt with the measurements of semi-inclusive π^0 production:

$$p_{\uparrow\downarrow}\; p \longrightarrow \pi^0\; X\,. \tag{2.11}$$

The analysis, which continues the one started with E704 at Fermilab, confirms the dependence of the π^0 production cross-section from the direction of the beam polarization direction. The asymmetry has been calculated as:

$$A_N = \frac{\pm 1}{< P_{beam} >}\frac{N_u - RN_d}{N_u + RN_d} \tag{2.12}$$

where $N_{u(d)}$ are the counting rates with the beam polarized in one or the opposite direction and R is a constant normalizing the luminosity of one beam w.r.t. the other.

Asymmetries growing with the pion energy and reaching the value of about 20% have been observed attesting that a signal due to transversity took place in the *pp* RHIC facility. In figure 2.6 the experimental points are compared to preliminary theoretical predictions.

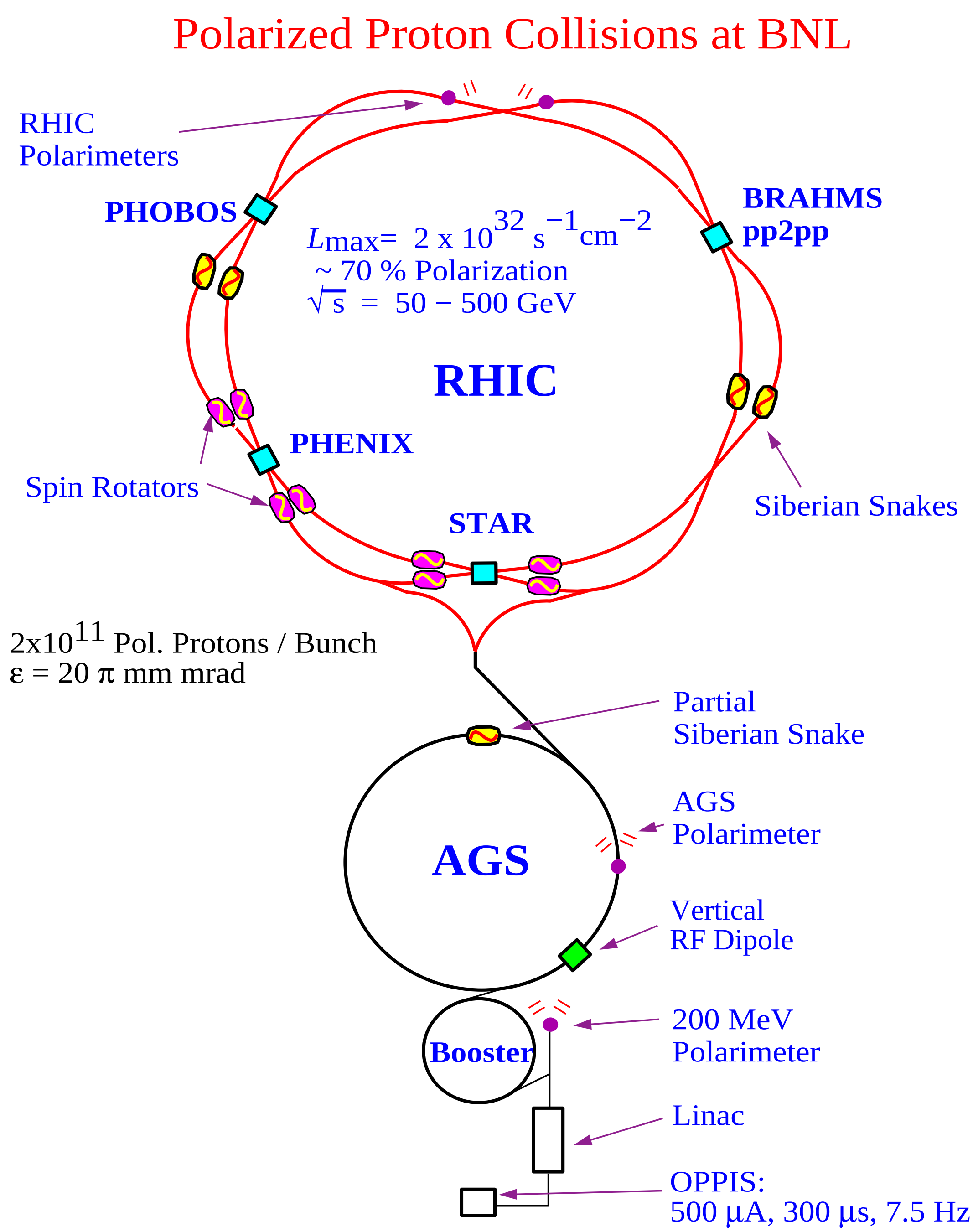

Figure 2.5: An overview of RHIC.

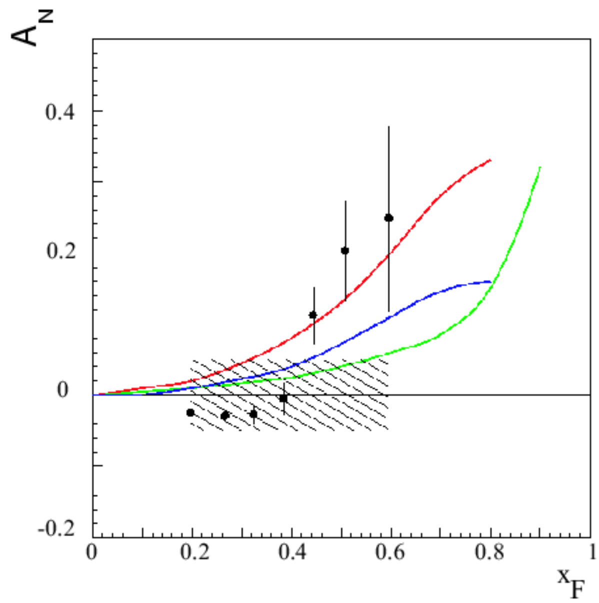

Figure 2.6: The experimental values for the asymmetry as function of x_F (E/100 GeV) compared with predictions by Anselmino for transversity (in red) and Sivers effect (in blue), and by Qiu and Sterman for twist 3 effects (in green).

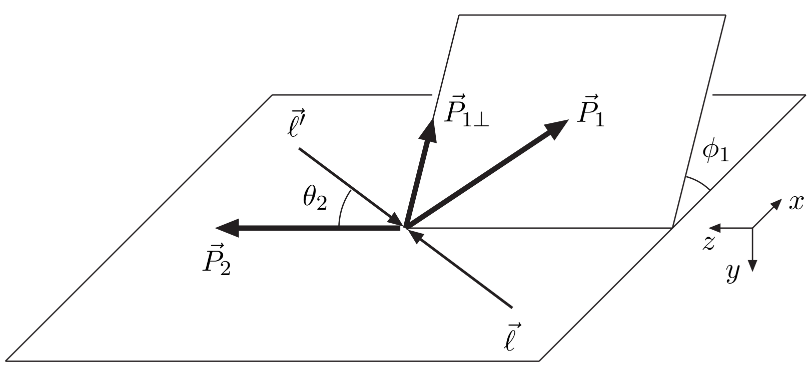

Figure 2.7: Kinematics of two-hadron production in e^+e^- annihilation.

2.3.2 Measurement of Collins analyzing power at LEP

An independent source of information on the Collins fragmentation function $H_1^{\perp}$ is inclusive two-hadron production in electron-positron collisions (see Fig. 2.7):

$$e^+ e^- \to h_1 \, h_2 \, X \, . \tag{2.13}$$

This process has been recalled by the authors of [1]. The cross-section for the angular dependence of two alike hadrons production, omitting the flavour indices and referring to Fig. 2.7 for the kinematical variables shows the following shape:

$$\frac{d\sigma}{d\cos\theta_2 d\phi_1} \propto (1+\cos^2\theta_2)\left(1 \; + \; \frac{6}{\pi}\left[\frac{H_1^{\perp(1)}}{D^{(1)}}\right]^2 C \, \frac{\sin^2\theta_2}{1+\cos^2\theta_2}\cos(2\phi_1)\right) \tag{2.14}$$

where C is a constant containing the electroweak couplings.

Thus, the analysis of $\cos(2\phi_1)$ asymmetries in the process (2.13) can shed light on the ratio between unpolarised and Collins fragmentation functions. Efremov and collaborators [12] have carried out such a study using the DELPHI data on Z^0 hadronic decays. Under the assumption that all produced particles are pions and that fragmentation functions have a Gaussian $\vec{\kappa}_T$ dependence, they find:

$$\left\langle \frac{\overline{H}_1^{\perp(1)}}{D^{(1)}} \right\rangle = (6.3 \pm 1.7)\,\% \, , \tag{2.15}$$

where the average is over flavours and the kinematical range covered by data. The result (2.15) is an indication of a non-zero fragmentation function of transversely polarised quarks into unpolarised hadrons. The same authors argue that a more careful study of the θ_2 dependence of the experimentally measured cross-section could increase the value (2.15) up to $\sim$ 13%. An analysing power of this order of magnitude would make the possibility of observing the Collins effect in the current experiments rather tangible.

2.4 Outlook

In section 2.2.1, it has been shown how a non-vanishing azimuthal asymmetry has been measured at HERMES. The interpretation of this result, however, is not unique since, in longitudinal polarization, the asymmetry generated by transversity could be accompanied by other twist-three effects. On the other hand, the vanishing of $A_{UL}^{\sin 2\phi}$ goes in the right direction of confirming the major role of h_1 w.r.t. the other PDFs contributing at that order. Several interesting updates of these measurements have been presented at Spin 2002 conference [13].

Although the SMC results (section 2.2.2) may be considered as the starting point for the observations of single spin asymmetries in hadron production from a transversely polarized target, the data are preliminary and can't be taken as conclusive measurements.

The same arguments can be stated about the preliminary STAR results on the asymmetry for π^0 production.

The last comment is about the direct measurement of the Collins fragmentation function (section 2.3.2): it should be taken as an indication for the absolute value of $H_1^{\perp}$. Many collaborations, as HERMES, now quote different absolute numbers following the same behaviour as function of z as that proposed by DELPHI.

The general impression is that, everywhere in the world, some phenomena connected to transversity have shown up and that the interpretation of such measurements is becoming more and more consistent.

Chapter 3

The COMPASS experiment at CERN

3.1 The COMPASS collaboration

The COMPASS (*COmmon Muon and Proton Apparatus for Structure and Spectroscopy*) experiment is a fixed target experiment at the CERN SPS (see figure 3.1). The acronym points to the fact that the experiment is the result of the merging of two previous proposals. In March 1995 two "Letters of Intend (LoI)" have been addressed to CERN SPSC from:

- the *Hadron-Muon Collaboration (HMC)* proposing [14] to make use of a high energy polarized muon beam to investigate the spin structure of the nucleon: this was a sort of natural evolution of the SMC experiment although a completely new apparatus was proposed;
- the *CHarm Experiment with Omni Purpose Setup (CHEOPS)* collaboration proposing [15] to perform hadron spectroscopy with a high energy hadron beam; this collaboration was gathering the physics community of the CERN OMEGA facility and the CERN LEAR experiments.

In March 1996 the two experimental groups submitted a joint proposal (COMPASS) [4] to carry on jointly a diversified physics program with hadron and lepton beams. CERN approved the COMPASS proposal in Febraury 1997. Since year 2002 COMPASS collects physics data.

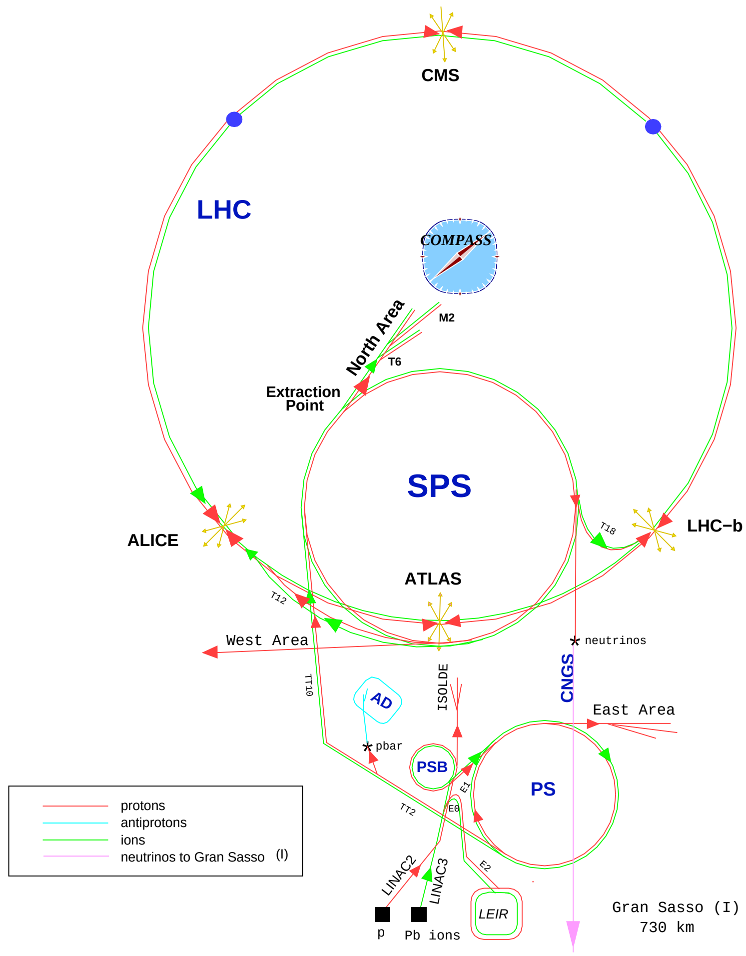

Figure 3.1: CERN accelerator complex and the COMPASS experiment location in the SPS North area area at CERN.

In his annual report to CERN Council, the General Director, prof. Luciano Maiani, remarked how, waiting for the dawn of LHC era, COMPASS is *"the only large experiment in operation"*.

3.2 The COMPASS experiment

COMPASS is a fixed target experiment with a very broad physics program to be performed using various beams and targets and a two stage spectrometer with full particle identification (PID), capable to reconstruct complex final states.

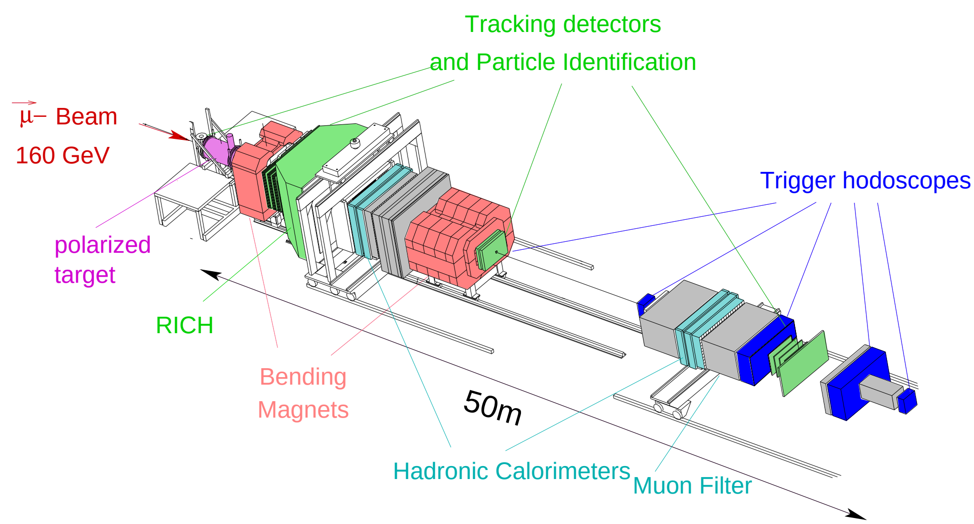

Figure 3.2: A schematic view of the COMPASS experimental set-up (2002).

After one technical run, in the year 2000, and a commissioning run in 2001, *the COMPASS experiment is now running and taking data with 160 GeV muon beam from the CERN SPS and a polarized deuterated target* [16]. The objectives of the collaboration to be achieved with priority until 2005 will deal with the measurements of:

- # the gluon polarization in the nucleon $\frac{\Delta g}{g}$ (via open charm and high p_t hadron pairs);
- # flavour decomposition of helicity PDFs.
- # the transversity - related PDF h_1 (see chapters 1 and 2).

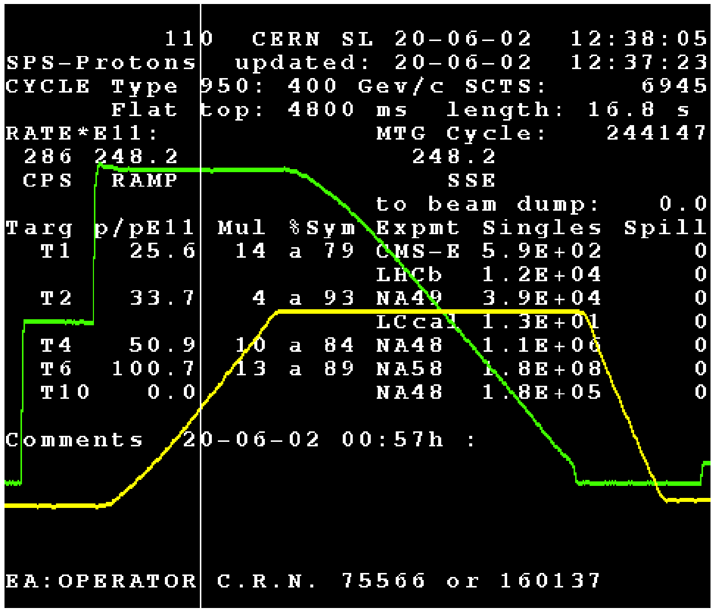

Figure 3.3: An example of SPS accelerator monitor given by the CERN Teletext page Server. A cicle of 16.8 s with a 5.1 s flat top is displayed.

In this chapter the present COMPASS beam and setup (target, spectrometer, trigger, DAQ) are described in detail.

3.3 Defining the initial state: the beam and the target

3.3.1 The muon beam and the BMS

COMPASS makes use of a high-intensity muon beam produced from SPS high energy protons (400 GeV/c momentum). An example of SPS operation cycle is reported in picture 3.3 where the yellow curve represents the behaviour of protons' flux as function of the time and the flat top represents the primary beam extraction (spill). Normally the SPS cycle had 5.1 s long spill with a period of 16.8 s.

In figure 3.4, the mean and peak intensities for 400 GeV protons is shown as function of the time for 2002 SPS proton run. These intensities in plateau reach about $3 \cdot 10^{13}$ protons/s.

The primary interactions on a 50 cm long beryllium target, yield a beam of about 2

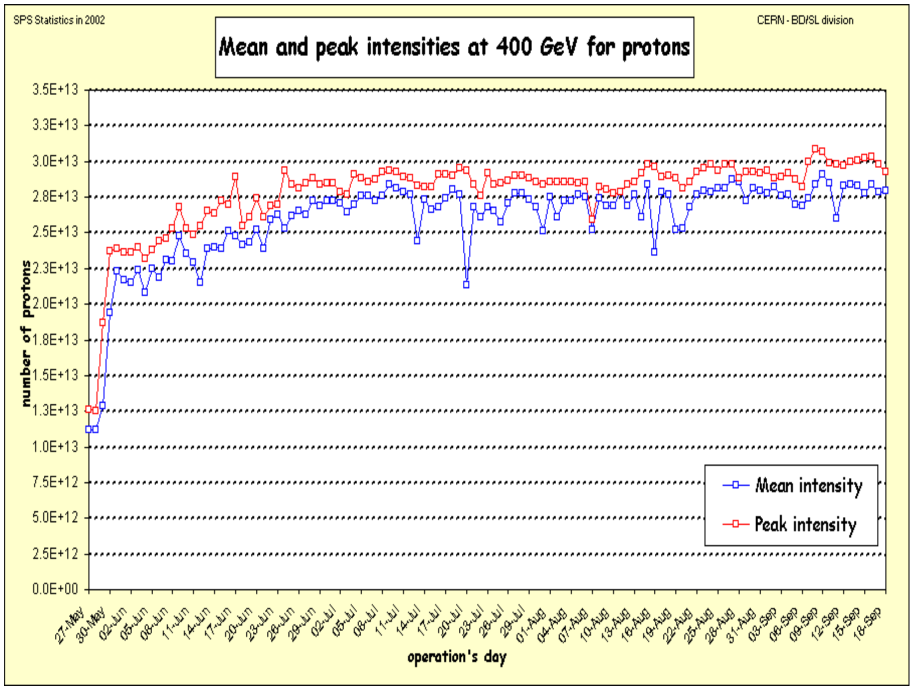

Figure 3.4: The intensity of the proton primary beam in the 2002 SPS run.

$\times\ 10^8\ \mu$ /spill ($4 \div 5 \cdot 10^7 \mu$/sec) at 160 GeV. The present system (i.e. the beam/magnet setup) allows similar intensities in the range $100 \div 160$ GeV whereas, at higher μ momenta the intensity drops very fast (exponentially).

The muon beam is generated from the weak decay of the pions in the 600 m long Hadron Decay Section. A set of absorbers is then installed to absorb the component of pions and protons. The muon beam reaches the COMPASS area following the "M2" secondary line (see figure 3.5). Several scrapers placed along the line improve the muon beam phase space and two sets of bending magnets select the muon beam momentum. The muon beam ranges from 60 to 190 GeV/c for both positive and negative charges. In so far, COMPASS used a positive beam with energy $E_b = 160$ GeV and about $\pm$ 3% in momentum spread.

The measurement of the beam momentum is done along the M2 line by the Beam Momentum Stations (BMS) which consist of two telescopes (each made by two planes) installed upstream and downstream the B6 bending magnet.

The hodoscope planes are composed of scintillator elements which are 5 mm high and 20 mm thick in the direction of the beam and which overlap by a few hundred μm. In the central region, some hodoscope strips are segmented in the non-dispersive plane in order to limit the rates in a single channel. As the beam cross section varies from one plane to the other the sizes of the hodoscopes vary as well. The time resolution of this detector is about 260 ps [17].

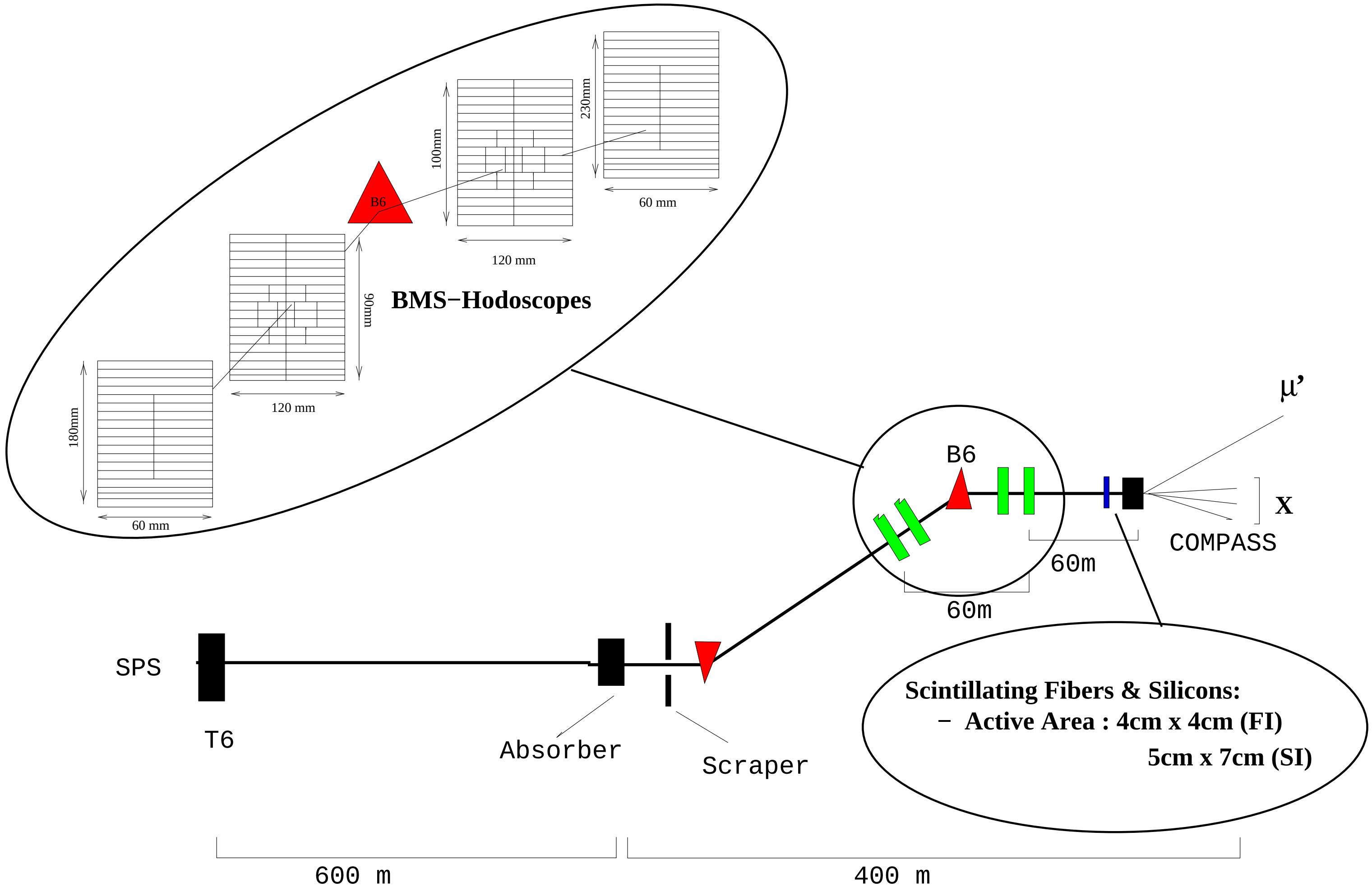

Figure 3.5: The BMS set-up along the M2 muon beam line.

3.3.2 The polarized target

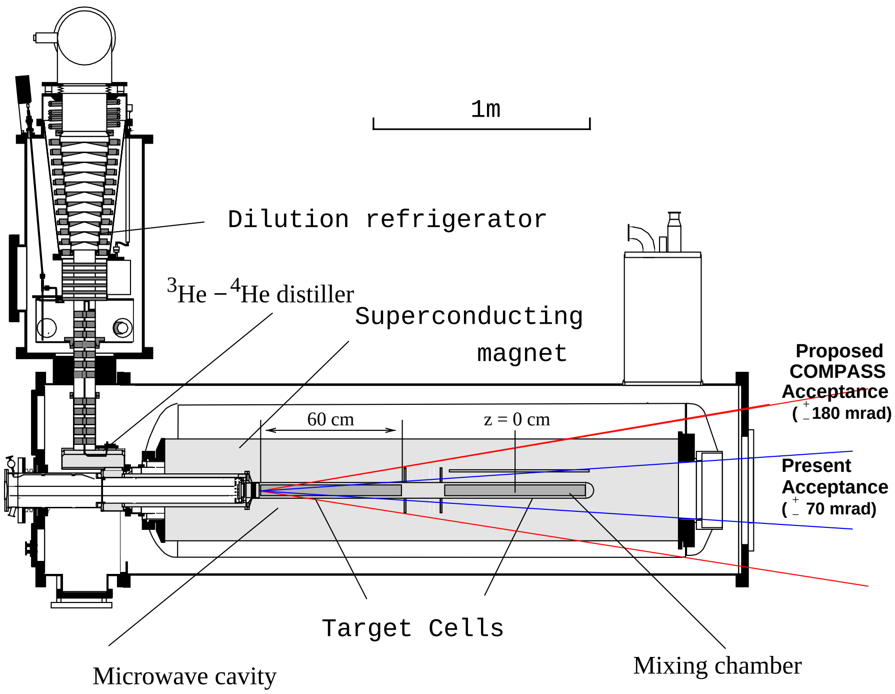

Figure 3.6: The target system used for COMPASS muon runs.

COMPASS uses solid targets containing polarized protons or deuterons. These targets are obtained, by a mechanism known as Dynamic Nuclear Polarization (DNP), on appropriate materials. The target system is composed (see figure 3.6) by:

- the target cells;
- the dilution refrigerator;
- the superconducting solenoid;
- the dipole magnet.

The target material is splitted into two individual cylindrical cells (separated by 10 cm), 60 cm long and 3 cm wide. The target material is either NH_3 (to obtain a polarized proton target) or ^{6}LiD (to have a polarized deuteron target). In so far we have used only the ^{6}LiD

material		NH_3	^6LiD	
length of each cell		60		cm
distance between the cells		10		cm
cell's diameter		3		cm
thickness	ρ	61	59	g/cm^2
dilution factor	f	0.176	0.5	
typical polarization	P_T	0.89	0.5	
figure of merit	$F = \rho(P_T f)^2$	1.4	3.6	g/cm^2

Table 3.1: The main characteristics of the proton and deuteron targets in use at COMPASS.

target which, as explained below, has a figure of merit more than a factor two better than the NH_3 target.

The two cells can be polarized in opposite directions w.r.t. the incident beam making use of low temperatures and high magnetic fields. To polarize the nucleons present in the target cells, a procedure starting from the creation of molecular paramagnetic complexes which can be oriented by an external high magnet field is used. This first step is done in Bonn where the target materials are kept frozen and irradiated by the 20 MeV electron beam extracted from the LINAC.

The nucleons' spins are polarized with a procedure known as Dynamic Nuclear Polarization (DNP), based on hyperfine transitions induced by an operational solenoid field (2.5 T). The COMPASS target system permits to polarize the cells only longitudinally; once the polarization is obtained, the nucleons are kept "frozen" at 50 mK in order to obtain a thermodynamical relaxation of several weeks.

In table 3.1 the main characteristics of the COMPASS targets are listed. In particular, the dilution factor is the fraction of the events [18] scattered off the polarizable nucleons under study[1].

The figure of merit ($F = \rho(P_T f)^2$) takes into account also the material density and the feasible level of polarization: it represents the equivalent density of the material considering only the nucleons totally polarized.

[1]This number is in general function of x but at leading order can be calculated as number of nucleons present in polarizable molecules divided by the total number. In case of NH_3 only the three protons in the hydrogen atoms are polarizable (N has spin 0), so $f = \frac{3}{17} \simeq 0.176$; in the same fashion, the ^6LiD wavefunction almost factorizes as [19] (α + p + n + d), because of the singlet status of α, only the deuterons are polarizable and $f = \frac{4}{8}$ =0.5.

The cooling is provided by the dilution refrigerator which can reach temperatures of the order of tens of mK. In this system, following the suggestion given by F. London in the 50's, the cooling is obtained in the liquid mixture of ^{3}He and ^{4}He helium isotopes which undergo a phase transition at temperatures below 1 K (see the phase diagram in figure 3.7).

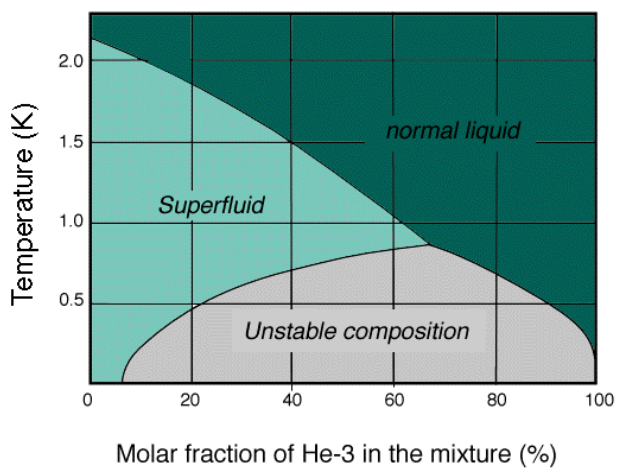

Figure 3.7: Status of ^{3}He - ^{4}He mixture as function of ^{3}He molar fraction and absolute temperature.

In the COMPASS proposal, the solenoid magnet had been designed to allow a large geometrical acceptance in the final state.

Because of the unavailability of the solenoid magnet designed at the time of proposal [4] and manufactured by Oxford Instruments, since year 2001 the old magnet from the SMC experiment has been installed on the target platform. This magnet provides 2.5 T longitudinal field over a 1.5 m long target volume with homogeneity better than 20 ppm over the target volume. Passing from the Oxford Instruments solenoid to the old SMC one, COMPASS suffers of a big reduction in its geometrical acceptance passed from 180 to 70 mrad.

By means of two saddle-shaped extra coils, the magnet can also provide a transverse magnetic field of 0.5 T. This dipole field can either be used for orienting the spin orthogonal to the beam direction, or to adiabatically rotate the spin direction from parallel to antiparallel to the beam direction (or viceversa).

In longitudinal mode COMPASS can improve the target polarization during running time (dynamic mode). When the plateau is reached, to minimize the systematics, two operations take place:

- every 8 h the target spins are rotated making use of the dipole field (0.5 T magnetic field);
- the nucleons' spins are flipped maintaining the external magnetic field constant and irradiating the target by microwaves which stimulate discrete transitions in the spins' orientation.

When COMPASS runs in transverse mode, the spins are moved transversely w.r.t. the incident muon direction by the dipole and maintained in such configuration. Since the holding field is different than the one used to polarize, there is no possibility to improve the polarization in transverse mode: in such a case one builds up the polarization in longitudinal mode, then rotates the field and profits of the long relaxation time of the nucleons' spin (frozen mode). In this case the nominal beam line[2] is moved to compensate the bending effect of the dipole and keep the beam along the nominal beam axis in the spectrometer.

All the possible COMPASS target configurations are sketched in picture 3.8.

A NMR system performs measurements about the target polarization which, during the 2001 and 2002 runs, have reached negative and positive values ranging from -45% to +51% (see chapters 6 and 7) improving the design value reported in table 3.1. Due to a power cooling problem, in year 2002, the dipole current could be risen up to 85 % of its nominal value with a corresponding reduction in the magnetic field. No measurable polarization loss has been found under these conditions.

3.4 Defining the final state: the spectrometer

The COMPASS spectrometer (sketched in figure 3.9) has been designed to reconstruct and identify all the particles over a wide angular and kinematical acceptance.

It is divided into two stages (Large and Small Angle Spectrometers) with complementary kinematical coverage built around two bending magnets, SM1 and SM2. SM1 has 1 Tm magnetic rigidity and covers an angular acceptance equal to 200 (h) mrad $\times$ 250 (v) mrad; SM2 has 4.4 Tm magnetic rigidity and an entrance window accepting all the particles emitted up to 40 mrad. COMPASS uses many tracking detectors, different in conception, manufacturing technique, active surface, and electronics. They can be catalogued w.r.t.

[2] This operation is actually done shifting the quadrupoles placed upstream the target. The first SciFi station in the spectrometer is moved as well to track the beam.

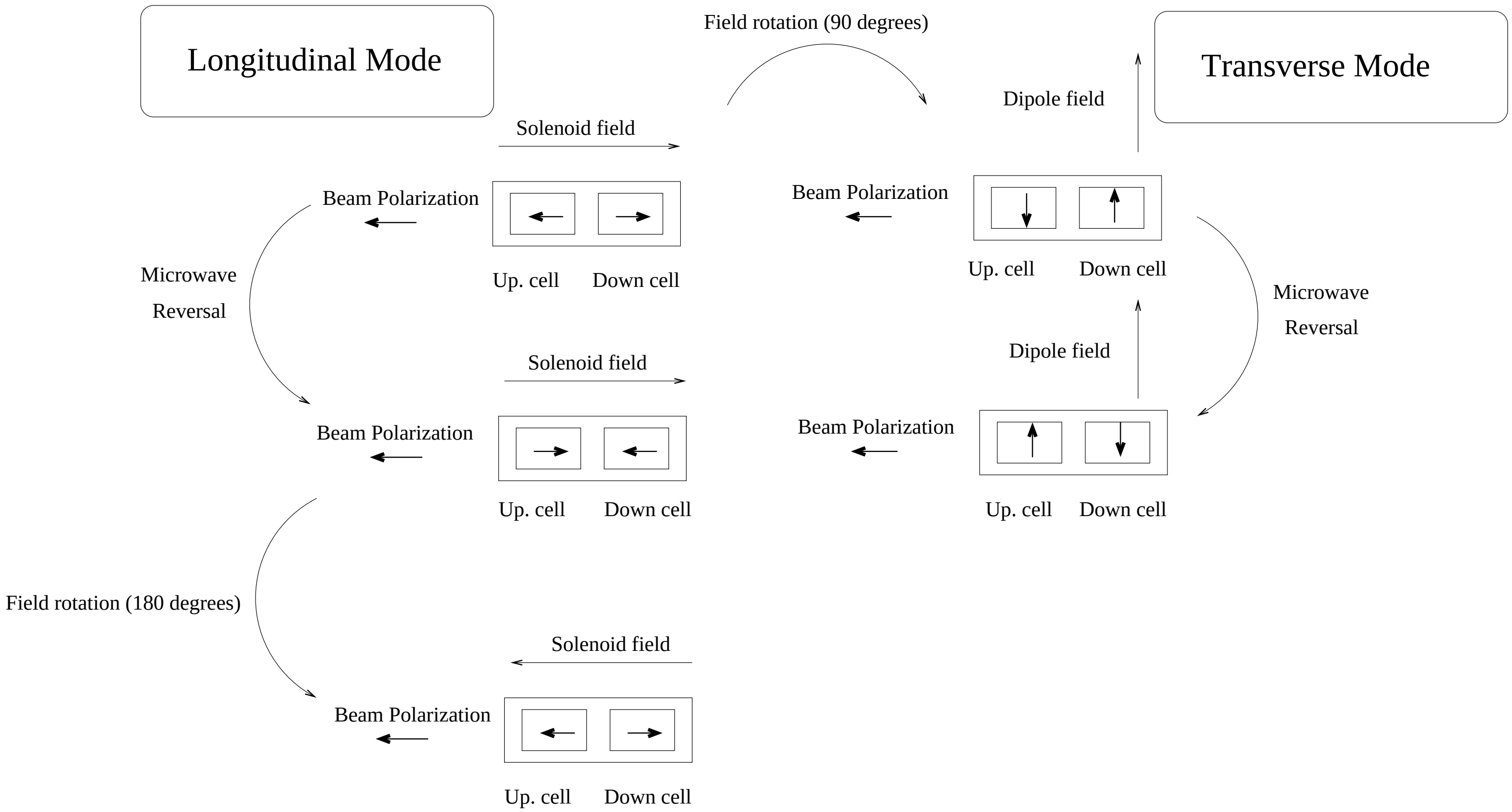

Figure 3.8: Procedures to change the target spins' orientation among all the COMPASS polarization modes.

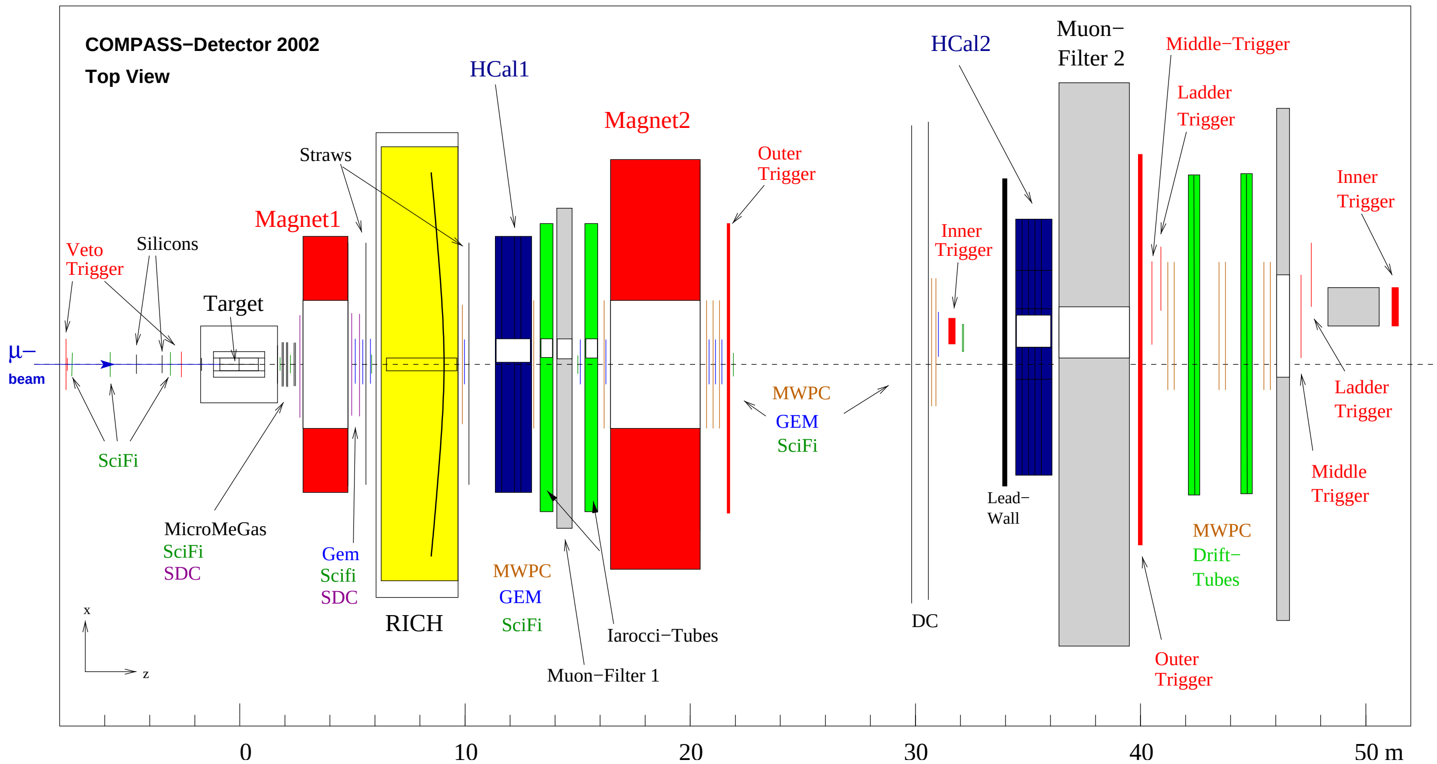

Figure 3.9: The COMPASS experimental setup in 2002.

Detector name	Detector type	Active area	Resolution (space)	(time)
SciFi (J)	VSAT	$52.5 \times 52.5\ mm^2$	$120\ \mu m$	$400 - 500\ ps$
Silicons	VSAT	$70 \times 50\ mm^2$	$14\ \mu m$	$2 - 3\ ns$
SciFi (D)	SAT	$123 \times 123\ mm^2$	$410\ \mu m$	$370\ ps$
MicroMegas	SAT	$380 \times 380\ mm^2$	$70\ \mu m$	$8.5\ ns$
GEM	SAT	$300 \times 300\ mm^2$	$50\ \mu m$	$12\ ns$
SDC	LAT	$140 \times 125\ cm^2$	$170\ \mu m$	
STRAW	LAT	$325 \times 277\ cm^2$	$200 - 300\ \mu m$	
MWPC	LAT	$150 \times 120\ cm^2$	$500\ \mu m$	
W4/5	VLAT	$240 \times 500 cm^2$	$500\ \mu m$	

Table 3.2: Trackers' conception and type. The active surface and the space/time resolutions are also written.

the active surface as Very Large, Large, Small and Very Small Area Trackers supporting more and more current loads as much as they approach the nominal beam line. By this "segmented spectrometer" the complete control on beam and hadron tracking is achieved. The Ring Imaging CHerenkov detector (RICH-1), the two hadronic calorimeters (HCAL) and the two Muon Walls (MA, MB) complete the COMPASS setup as installed in 2002 and performs particle identification (see section 3.5).

In the original COMPASS proposal [4] two large electro-magnetic calorimeters were also foreseen, one in each spectrometer stage, as well as a second RICH (RICH-2) to be positioned in the second spectrometer. They haven't yet been constructed but plans to complete the spectrometer are being finalized.

3.4.1 The tracking detectors

In COMPASS several types of detectors [20] [21] are used in order to reconstruct the particles' trajectories (see table 3.2). In both the spectrometers, Large Area Trackers (LAT) cover surfaces greater than 1 m^2 and support fluxes up to 10 KHz. LATs are the Saclay Drift Chambers (SDC), the Straws drift tubes in the first spectrometer and the MWPCs (PA/B/S). Very Large Area Trackers (VLAT) are the W4/5 (DC) drift chambers in the second spectrometer.

The Small Area Trackers (SAT) cover surfaces of the order of 40 by 40 cm^2 and support flux loads of the order of 300 KHz. SATs are the Gas Electron Multiplier (GEM) and the

MicroMegas.

Around the nominal beam line, within a distance of several centimeters, the Very Small Area Trackers (VSAT) are installed with the aim of tracking the beam and the scattered muon at very small angles. These trackers consist of Scintillating Fibers (SciFi) hodoscopes which can stand ionizing particles at fluxes of 500 MHz/cm^2.

The Scintillating Fibers

In the COMPASS spectrometer several detectors have time resolution smaller than 1 ns; among these, there are the 4 stations of Scintillating Fibers (J-SciFi) installed upstream and downstream the polarized target (see figure 3.10) and other 4 (D-SciFi) along the spectrometer.

Each of the two stations installed upstream the target is composed by two orthogonal planes (each having an active surface of 3.94×3.94 cm^2), measuring X and Y coordinates with a total of 384 channels.

The other two stations, installed downstream, measure X,Y,U (each having a surface of 5.25 $\times$ 5.25 cm^2) for 768 channels in total, the U-coordinate being rotated by 45^o around the nominal beam line.

The fibers have 0.5 mm diameter and are partially superimposed giving rise to a staggered arrangement to avoid dead areas.

These detectors have been developed, constructed and commissioned by the Japanese Nagoya/ IHEP group.

Some specific measurements (e.g. the intrinsic time resolution and the "time of the event") will be object of some dedicated studies reported in chapter 6.

The other 4 SciFi stations measure two coordinates (X, Y) and have active surface increasing from 52.5×52.5 mm^2 to 123×123 mm^2. Those stations, built in Bonn and Erlangen (D), give performances similar to those installed nearby the target. Due to the somewhat larger overlap between the fibers, the timing resolution of the D-SciFi is better than that of J-SciFi (0.37 ns vs 0.45 ns).

The Silicons

To help the fibers in the beam tracking, the silicons detectors [22], especially built for COMPASS hadron runs, have been installed in the target region.

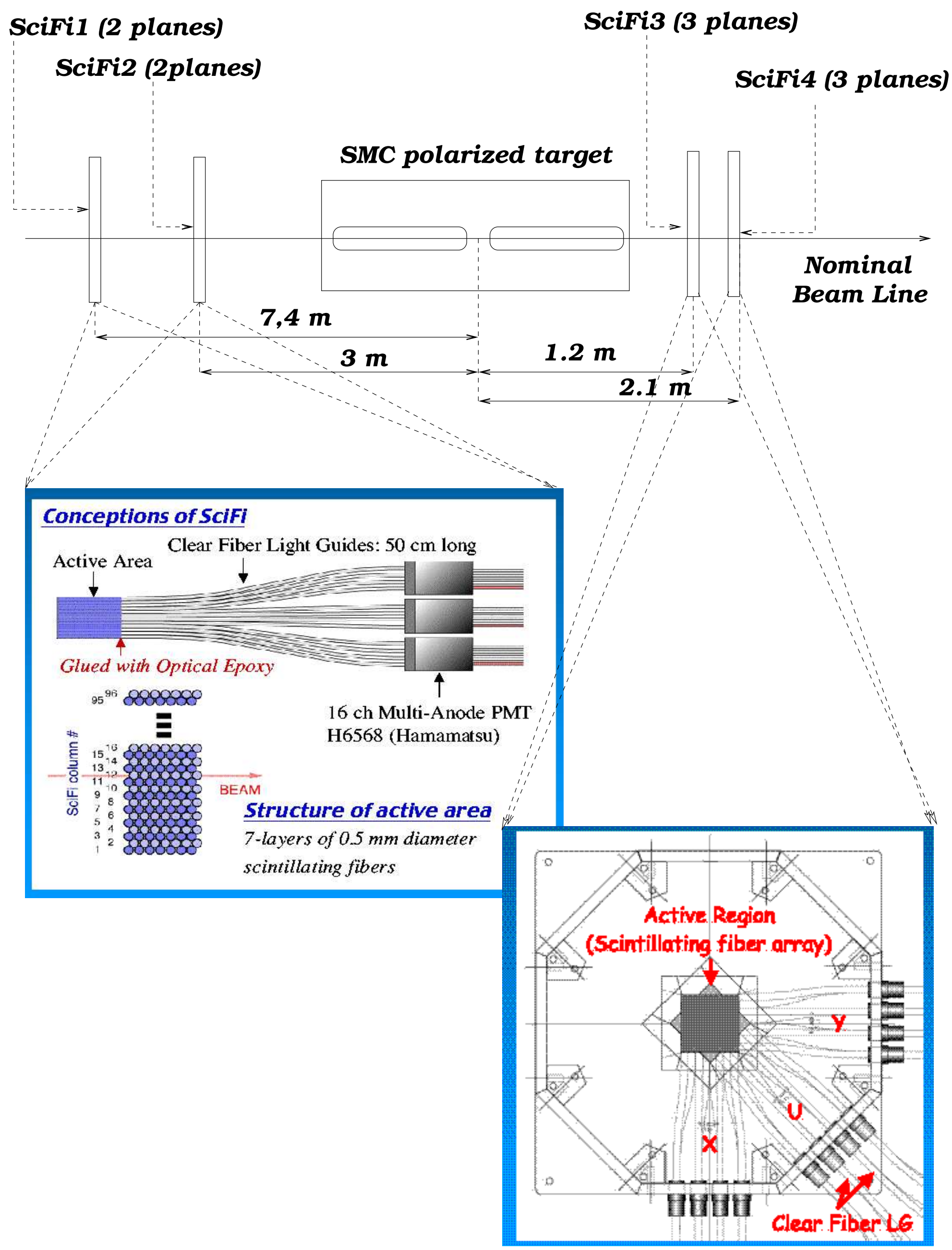

Figure 3.10: Geometrical disposition and hardware conception of fibers' stations installed nearby the target.

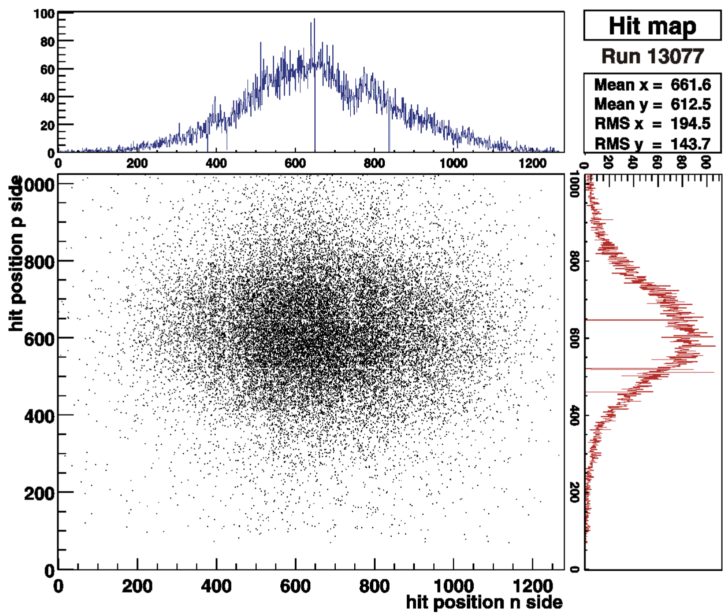

Figure 3.11: The beam profiles as measured by silicons stations.

Their active surface is about 50 × 70 mm^2 and the high spatial resolution, the best one in COMPASS ($\sigma_x \simeq 14\ \mu m$), is determined by the 50 μm strip pitch. Their time resolution, σ_t, reaches 2.5 ns.

The ionizing particles traversing the detector produce electron-hole pairs (whose production threshold is 3.6 eV for such detectors) along their tracks which are separated by an external field before recombination. The electrons drift towards the anode where the current is detected. Two independent read-out set-up's measure the two orthogonal coordinates as shown in figure 3.11.

The silicons planes are rather thin (280 μm) in order to minimize the Coulomb scattering which would reduce the spatial resolution.

The Micromegas

Micromega [23] is an acronym for MICRO MEsh GAseous Structure. These detectors (whose principle scheme is shown in picture 3.12) are parallel faces gaseous trackers composed by three electrodes: the drift electrode, the micro-mesh and the microstrips. The distance between the drift cathode and the micro-mesh plane is 3 mm while the anode plane is 100

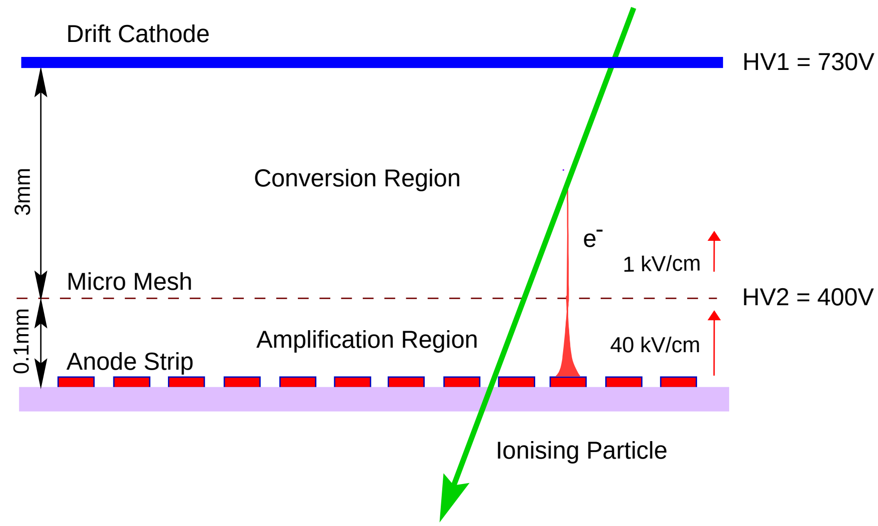

Figure 3.12: The principle scheme of the Micromegas used in COMPASS.

μm away from the micro-mesh.

A particle crossing the active zone converts in the space between the drift cathode and the micro-mesh. The ions and the electrons are decoupled by a moderate electric field of the order of 1 KV/cm. When the electrons traverse the micromesh, because of the intense field set between this electrode and the microstrips (40 KV/cm), an avalanche is generated giving raise to a signal which is read at the anode strips.

The 3 Micromegas COMPASS stations are installed between the target and the first bending magnet and operated with a mixture of Ne (80%), C_2H_6 (10%) and CF_4 (10 %). They have 40 $\times$ 40 cm^2 active zone (blind in 2.5 cm around the beam) and measure 4 coordinates rotated by 0, $\pm 45^o, 90^o$ w.r.t. the x axis. The resolution in space is about 70 μm and in time less than 10 ns while the efficiency for particle detection better than 98%.

The GEMs

The Gas Electron Multipliers (GEM), shown in picture 3.13, are parallel faces gaseous trackers as well [24]. The amplification electrode is done by 50 μm kapton foil with 5 μm metal clad on both sides.

This foil is perforated by a large number of holes (usually 10^4/cm^2) produced by photolithographic techniques and then treated by etching process. Inserted between the drift electrode and the grounded strips' face, on the foil's faces is applied 300 $\div$ 500 V tension corresponding to 50 KV/cm electric field (proportional regime).

In the GEM detectors manufactured for COMPASS, three GEM foils (corresponding to 3 amplification stages) are used and operated with a mixture of Ar (70%) CO_2 (30%). They have 30 by 30 cm active surface (with a dead zone varying in function of the covered position in the spectrometer), 50 μm space and 12 ns time resolutions and more than 97% efficiency in charged particle detection.

Three GEMS stations are installed between SM1 and the RICH, other three between the RICH and SM2 and other four (for a total of 10) between SM2 and the second Muon Wall.

The Drift Chambers

Since year 2002 one station of drift chamber is installed before SM1 and two are installed downwards of it. They are operated with Ne (45%), C_2H_6 (45%), CF_4 (10%) gas mixture which leads to a maximum drift time of 70 ns.

Each drift station provides 8 coordinates, 2 $\times$ (1h, 1v, 2 rotated by $\pm 45^o$ degrees) with a typical spatial resolution of 170 μm. The dead zone is made neutralizing a disc of 30 cm in diameter centered on the beam axis. Operating the chambers with an anodic tension of 1750 V, the SDCs have shown an efficiency in the detection of charged particles above 95%.

The Straw Chambers

The stations of STRAW [25] tubes are installed only downstream SM1. They consist of 6 double layers (see picture 3.14) measuring two space points (x, y, u) where the last coordinate is inclined by $\pm$ 10^o with respect to the vertical plane.

These are grounded aluminized kapton tubes (6 or 10 mm diameter) through which 20 μm golded tungsten wires are set at about 2000 V potential. The signal is caused by the avalanche produced by the ionizing particle whereas the impact point is calculated from the electrons' drift time.

The STRAW pitch varies from 6.04 mm (inner part) to 9.51 mm (outer part) depending on the needed space resolution. The operational gas is a mixture of Ar (74%), CF_4 (20%) and CO_2 (6%).

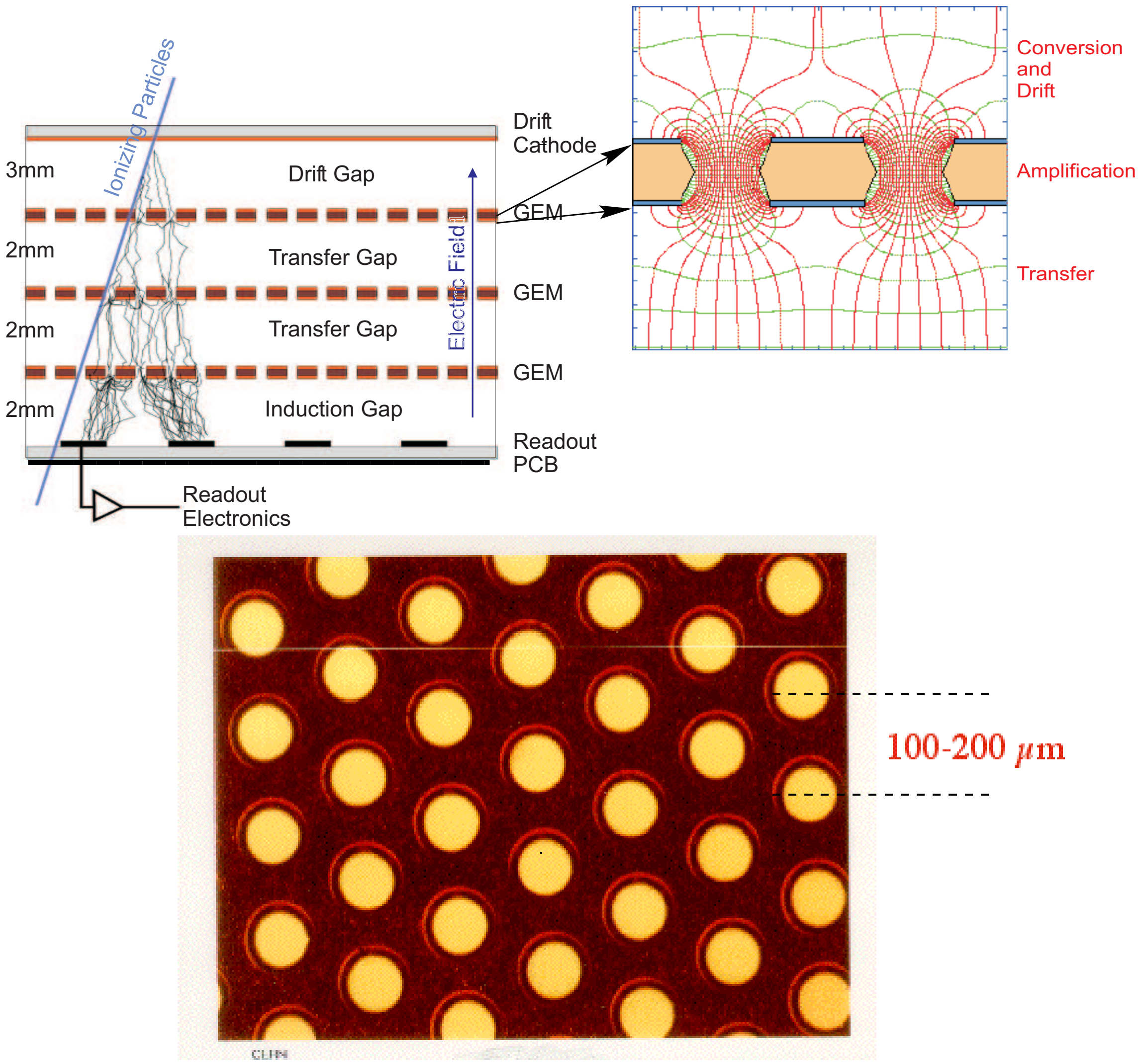

Figure 3.13: The detection principle of a triple GEM detector and the picture taken with optical microscope of a GEM foil.

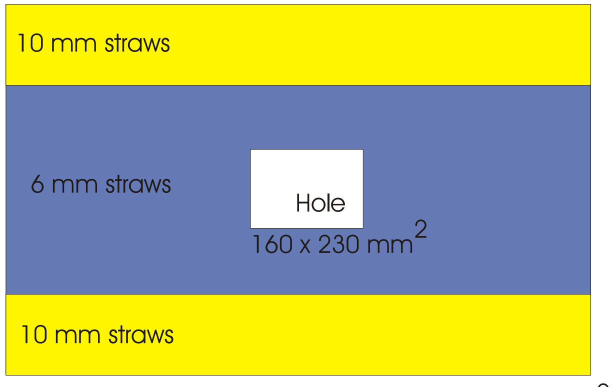

Figure 3.14: A picture for the STRAW double layers installed in the first spectrometer.

The W4/5 Chambers

The W4/5 system [26] has been installed after year 2001 run to enhance the acceptance in the high Q^2 region (see section 3.7). Two stations composed by 4 planes are presently installed between SM2 and the second Muon Wall (MB) (see section 3.6) at about 30 m downstream the target.

Each station has an active zone of 240×500 cm^2 (deactivated in the center within 50 cm diameter) and measures two pairs of coordinates (one horizontal or vertical and the other one rotated w.r.t. the vertical plane). The cathode wires are grounded, rotated by 5^o and separated by 2 mm pitch, the anode wires have 4 cm pitch and are operated with a tension of 2100 V; two neighbour anodes are separated by a potential wire hold at negative tension ($\sim$ -800 V).

A cathode plane is inserted between two anodes measuring the same coordinate whereas two (one for each orientation) are inserted between two anodes measuring different coordinates.

These chambers are inserted in the MWPC gas system and operated with Ar (70%), CF_4 (20%) and CO_2 (10%).

The MWPCs

These detectors are the main large area trackers in the second spectrometer. They consist of 14 stations for a total of 34 planes. All of them have 2 mm wire pitch and use a gas

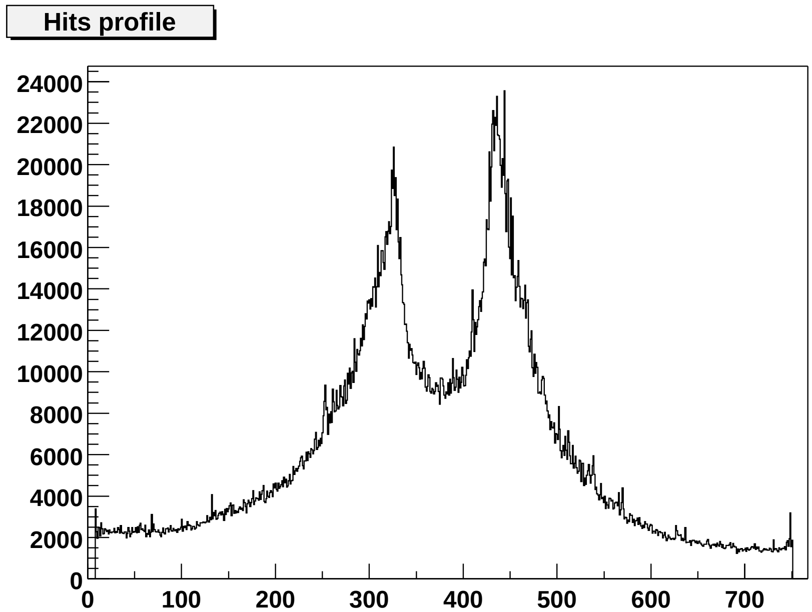

Figure 3.15: The hit profile from MWPCs.

mixture of Ar (70%), CF_4 (20%) and CO_2 (10%).

They are of three types depending on the active surface and the measured coordinates:

\# A^* (PS) $\longrightarrow 152 \times 120\ cm^2$ (x, y, u, v), 1 station;

\# A (PA) $\longrightarrow 152 \times 120\ cm^2$ (x, u, v), 7 stations;

\# B (PB) $\longrightarrow 152 \times 92\ cm^2$ (x, u) or (v), 6 stations;

The typical hit profile image is reported in figure 3.15 whereas the efficiency is about 99.29% for charged particle detection at nominal anode tension (4.25 KV).

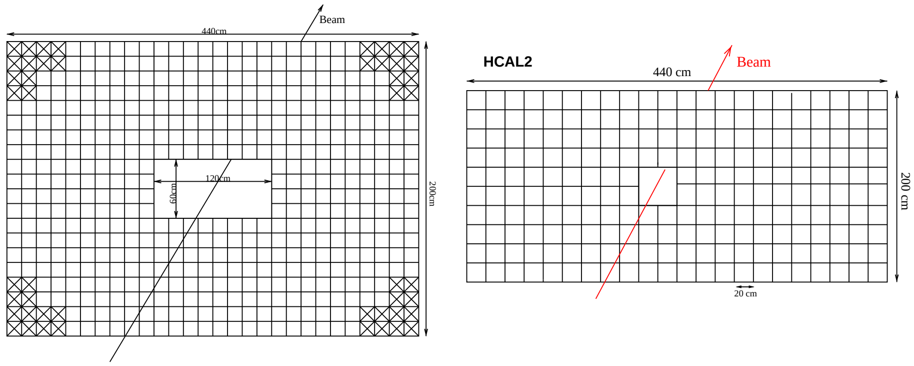

Figure 3.16: Front view of the two calorimeters installed in COMPASS. The surface is divided into the elementary cells and the beam hole is also drawn.

3.5 The particle Identification

If the momentum of a charged particle is measured in the spectrometer, one can identify such state knowing the energy (by the calorimeter) or the speed (by the RICH).

While the calorimeter needs the particle to be absorbed, the RICH represents a not invasive way of detection.

The calorimetry covers all type of particles (charged and neutral) with a very changeable resolution dependent on the energy. The RICH can identify only charged particles (via the Cherenkov effect). The principle and performances of this detector will be treated in detail in chapter 4.

3.5.1 Energy measurements and calorimetry

In the COMPASS final setup, two couples of hadronic and electro-magnetic calorimeters will be set in each spectrometer stage. Up to now, none of electro-magnetic calorimeters has been available whereas HCAL1 and HCAL2 are on track.
The hadron calorimeters are composed of cells arranged in matrices with the aim of measuring the energy of the hadron component in the radiation.

HCAL1 is composed by 480 cells ($15 \times 15 \times 100$ cm^3 each) made of iron and plastic scintillators whose thickness corresponds to 5 pion's (or 7 proton's) absorption lengths. HCAL2 is made of 216 cells ($20 \times 20 \times 120$ cm^3 each) composed by interleaved 16 mm lead and 4 mm plastic scintillator.

The energy resolution from HCAL2 is about 1.5 times better than from HCAL1 at the same energy.

	Active Area	Matrix Size	Element Size	σ_E/E	MIP deposit
HCAL1	$4.2 \times 3.0\ m^2$	28×20	$15 \times 15 \times 100\ cm^2$	$\frac{80\%}{\sqrt{E(GeV)}}$	$4\ GeV$
HCAL2	$4.4 \times 2.0\ m^2$	22×10	$20 \times 20 \times 120\ cm^2$	$\frac{60\%}{\sqrt{E(GeV)}}$	$2\ GeV$

Table 3.3: HCAL1 and HCAL2 hardware description and features.

3.6 Muon identification and Muon Walls

In COMPASS, the muon identification is done by the classical method of blocking all other charged particles but muons after the momentum measurement. So, two muon filters (MF1 and MF2) absorb the particles and the electro-magnetic radiation and leave only the muons to pass. MF1 is iron-made and 60 cm thick, MF2 is made of 2.4 m of concrete blocks.

Two stations in front and behind MF1, made up of Iarocci tubes and covering a surface of 400×200 cm^2, are named Muon Wall 1 (MA), operated by Ar (70%) - CO_2 (30%) gas mixture with the aim of tracking the muons scattered at big angle and reconstructed in the first spectrometer.

The analogous for the second spectrometer is the Muon Wall 2 (MB), made up of 3 cm diameter aliminium drift tubes and operated by Ar (75%) - CO_2 (25%) gas mixture, covers the same surface as MA.

3.7 The trigger system

The COMPASS trigger [27] [17] is a composite system made up of logical coincidences among dedicated stations of scintillators and the two hadronic calorimeters. In figure 3.17 the various families of hodoscopes are shown at their position along the spectrometer. In table 3.4, one finds the legend for the picture.

Despite the bending in the magnets, the muons interacting in the target cannot be easily disentangled from those passing through it without interaction especially if one looks at very small scattering angles as COMPASS does to measure $\frac{\Delta g}{g}$. So the trigger concept previews

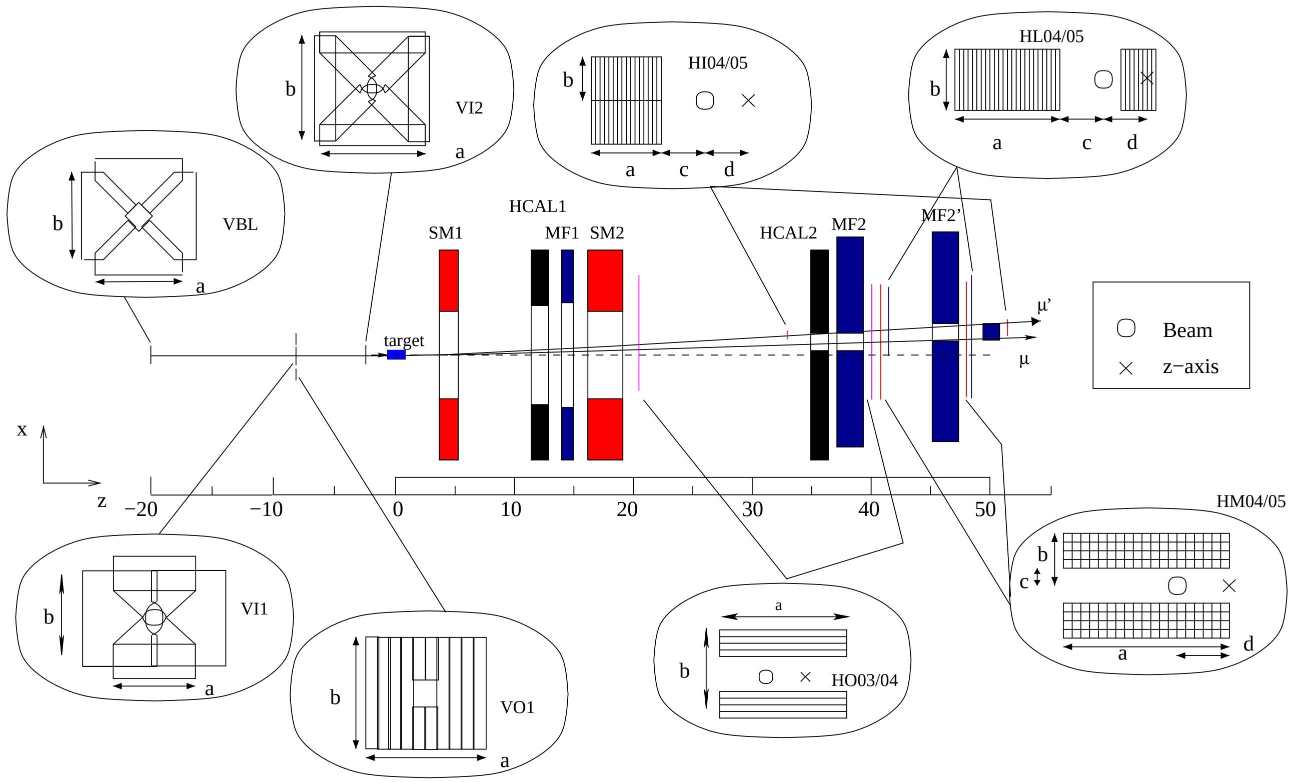

Figure 3.17: The positions and dimensions of the various trigger hodoscopes installed along the COMPASS setup.

Hodoscope name	a (mm)	b (mm)	c (mm)	d (mm)	position in z (m)
VBL	390	390			-20.0
VI1	210	250			-7.94
VO1	1464	1200			-7.69
VI2	500	500			-2.82
HI04	173.4	160	53	166	32.0
HI05	353	255	124	351	51.0
HM04	1200	510	160	240	40.3
HM05	1500	600	185	300	47.8
HL04	1282	400	295	240	40.6
HL05	1682	475	370	300	48.1
HO03	2500	1260			21.0
HO04	4800	2450			40.0

Table 3.4: Approximate dimensions of various trigger hodoscopes following the notation in picture 3.17.

two independent measurements made at different position in z in order to measure the μ' direction and filter the muons passing parallel to the nominal beam line. Furthermore to filter away the fake coincidences given by the muon halo, a minimum amount of energy left in the calorimeter by the hadrons produced in the reaction can be required (see figure 3.18). Actually a 5 GeV threshold to be deposited in HCAL1 or HCAL2 is set.

In longitudinal spin configuration, two classes of events are selected:

- quasi-real photon emission events ($Q^2 \simeq 0$);
- inclusive deep inelastic scattering events ($Q^2 > 1$ GeV^2).

To the first class belong all the triggers coming from Inner and Ladder hodoscopes which access the low-medium range in Q^2. The second class includes all the events coming from the larger hodoscopes, Middle and Outer. The coverage of the various hodoscopes in $y - Q^2$ kinematics' range is shown in figure 3.19.

In transverse mode, the Inner trigger drops and only medium-high Q^2 events are selected. A summary of the system which triggers the "events" in COMPASS is reported in table 3.5 where the request of the signal from the calorimeter and the target polarization mode are also specified.

In year 2001 run, the Outer hodoscope wasn't yet available and this caused a severe reduction in the Q^2 acceptance of the spectrometer. I performed a LEPTO based simulation in order

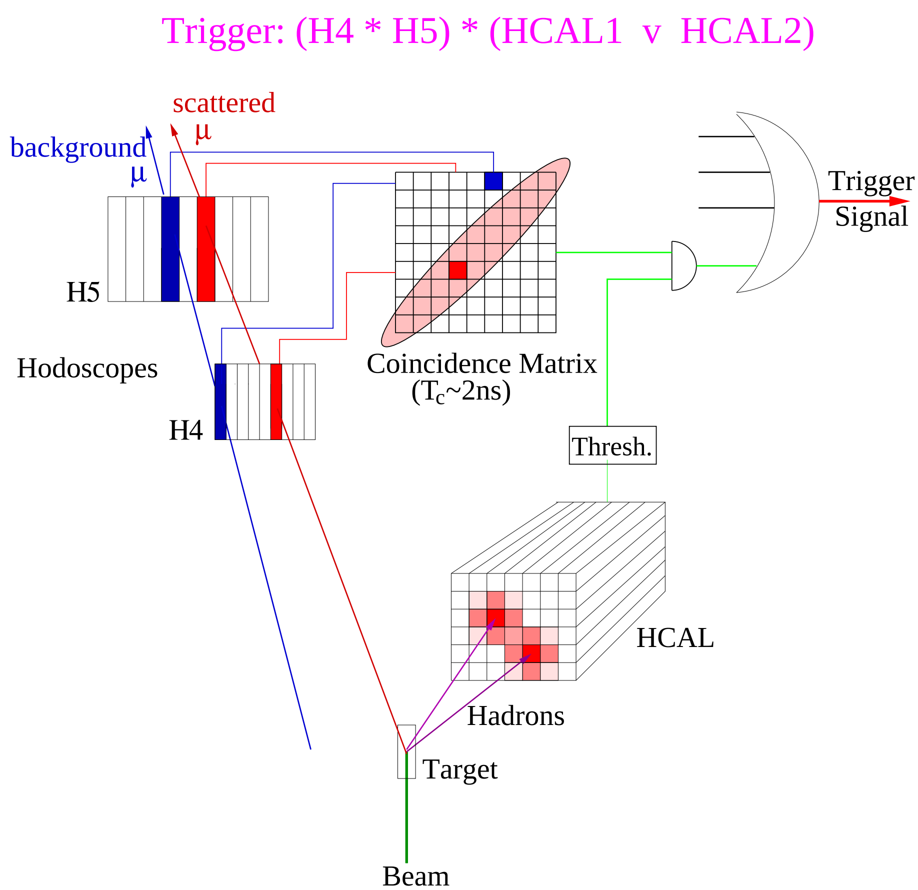

Figure 3.18: The system gives a trigger filtering by matrix coincidences and calorimeter signals the background of non interacting and halo muons.

ITC	Inner Hodoscopes + Calorimeter	Long.
LTC	Ladder Hodoscopes + Calorimeter	Long. Trans.
MTC	Middle Hodoscopes + Calorimeter	Long. Trans.
OT	Outer Hodoscopes w/o Calorimeter	Long. Trans.
inclMT	Middle Hodoscopes w/o Calorimeter	Long. Trans.
CT	Only Calorimeter	Trans.

Table 3.5: The multiple “OR” system generating the COMPASS trigger.

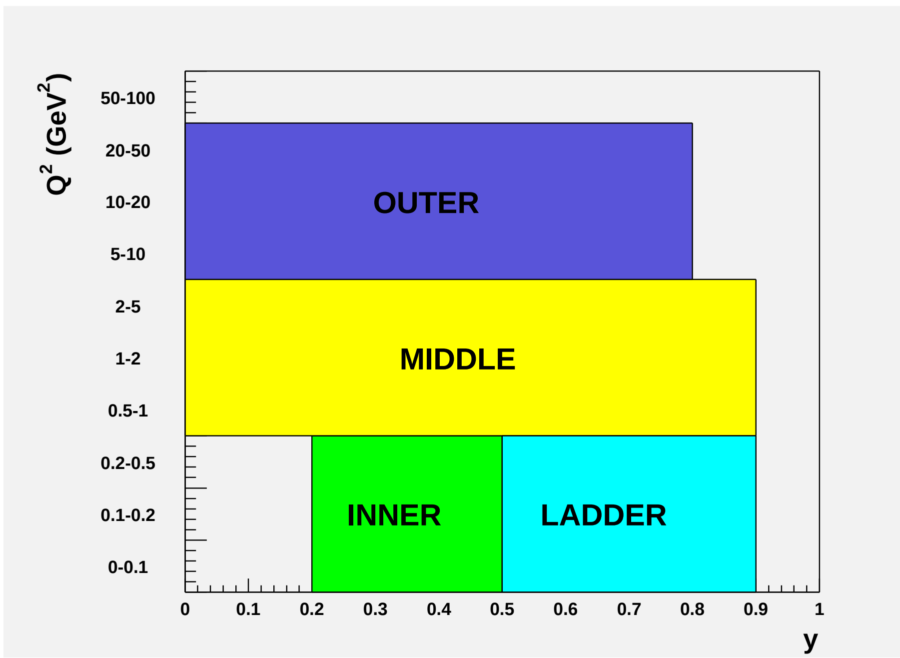

Figure 3.19: The $y - Q^2$ geometrical acceptance for the hodoscopes in the trigger system installed in year 2002.

Beam Momentum	160 GeV/c
x range	[0.01 , 1]
Q^2 range	$Q^2 > 1\ GeV^2$
Number of DIS events	10000
Number of μ' in II spectrometer	96%
Ratio of μ' in trigger T2001	37%
Ratio of μ' in W4/5	95%
Ratio of μ' in T2002	83%

Table 3.6: The kinematical variables used in the Lepto based simulation and the obtained results.

to measure the gain in geometrical efficiency which could be achieved in case a trigger hodoscope had covered the geometrical acceptance of W4/5 chambers.

In figure 3.20 the three trigger hodoscopes (T2001) used in year 2001 run are shown and compared with W4/5 geometry.

The results, shown in figure 3.21, demonstrate that, in the kinematical range reported in table 3.6, covering with a trigger hodoscope the W4/5 dimensions, the geometrical coverage passes from 37% to 95% of the total number of scattered muons (about all those reaching the second spectrometer). The goal actually achieved with the insertion of the Outer Hodoscopes (T2002) is 83%.

3.8 The Data acquisition system

In COMPASS more than 190000 channels, more than 30% of those coming from RICH front-end, are read at each event with a mean occupancy of 5% and 7% dead time in normal conditions.

Due to the bunch structure of the beam (see figure 3.3) the DAQ activity is maximum in the spill time: in year 2002, the trigger rate has approached 5 KHz whereas in COMPASS hadron runs, this value could be higher at least by an order of magnitude. Among all the high energy physics experiment running at the moment, COMPASS has one of the highest figures in event rate and data flux rate (> 30 MB/s).

Note that the LHC experiments [20] which will run after 2007, will have comparable data rate size (because of bigger number of detectors) but smaller event rate.

In figure 3.22 the DAQ concept is shown. The data coming from the detectors are

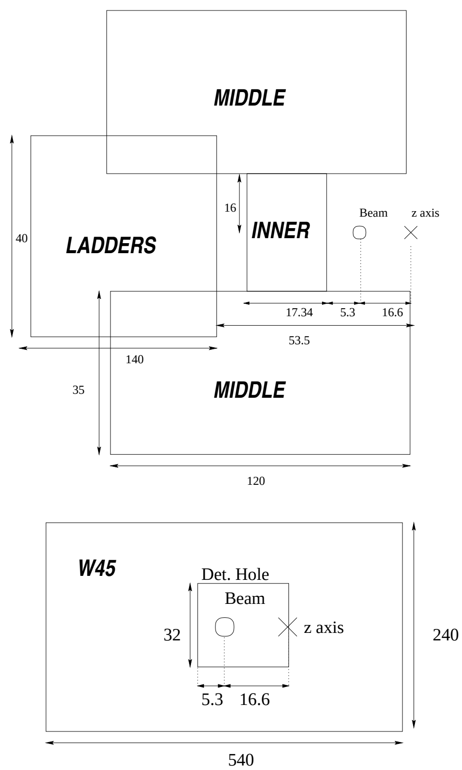

Figure 3.20: The trigger system in year 2001 (up). The W4/5 simplified geometry with a false "beam hole" reproducing the dead region of default set-up (down). Not in scale.

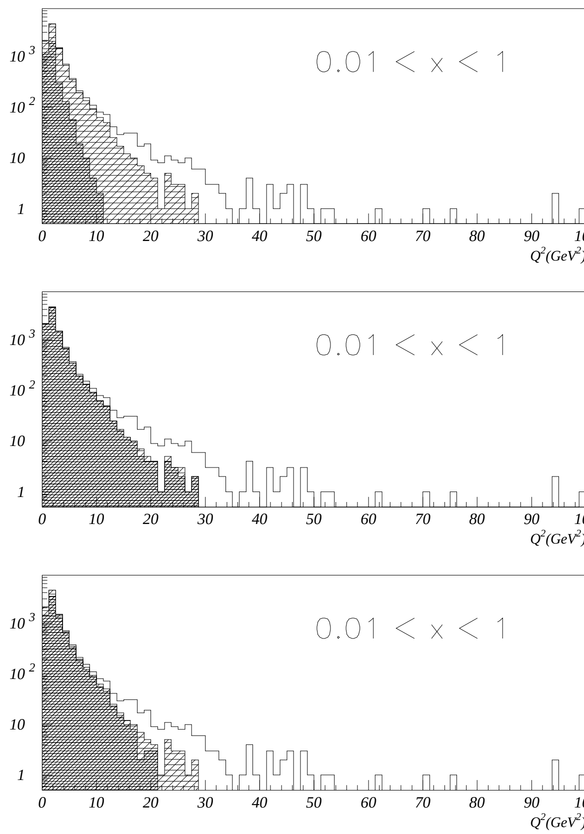

Figure 3.21: The generated distribution in Q^2 of simulated events (no fill pattern), the yield passing the first muon filter (MF1) and entering the second spectrometer (gray fill pattern) and the component geometrically accepted by trigger (dark gray fill pattern, up: T2001, middle: W4/5, bottom: T2002).

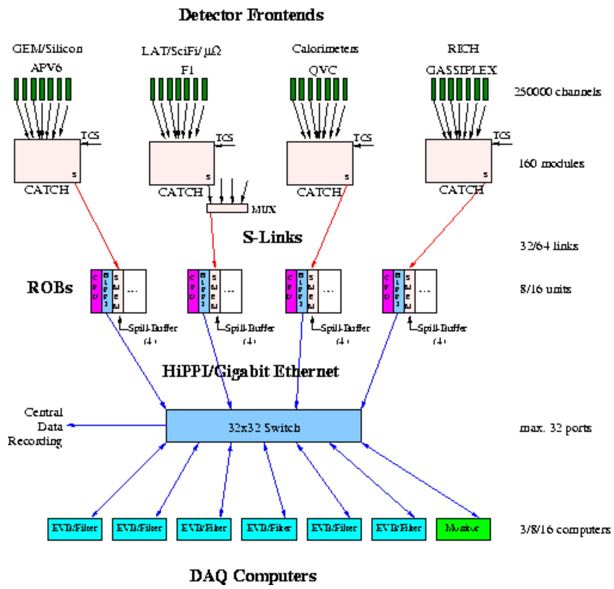

Figure 3.22: The DAQ conceptual scheme for COMPASS. Data flow from front-end cards via the drivers to the ROBs. After the intervention of the Event Builders farm, the chunck is ready to be transfered via the CDR.

digitized on the detectors front-end cards, then received by readout drivers[3], and transferred to the DAQ barrack via optical links.

Here the data are, first, collected in the so called Read-Out Buffer (ROB) PCs and then processed in the Event Building farm which stream together (from the various ROBs) the data belonging to the same event number (event building).

Once the data collected by a single Event Builder is completed because of end-of-run signal or maximum file size limit has been reached, this “chunk” is ready to be transferred via the CDR (Central Data Recording) to the CCF (Compass Computing Farm) which is located 4 Km away from the experimental zone.

Here it is temporary saved to disk waiting to be staged in the compass DataBase and stored in tapes by the CASTOR (CERN Advanced STORage Manager) system as described in chapter 5.

[3]All detectors use CATCH (COMPASS Accumulate, Transfer & Control Hardware) driver apart from GEM and Silicons which use GeSiCA (GEm and SIlicon Control and Acquisition).

Chapter 4

The RICH-1 Detector: Principle and Performance

4.1 Basics

4.1.1 The Cherenkov effect

The Cherenkov effect[1] can be studied in the context of the energy losses by charged particles in a material matter. This energy dU, from the point of view of thermodynamics, derives from the coupling of the electrical field with polarization vector:

$$dU \ = \ \vec{E} \cdot d\vec{P} \tag{4.1}$$

Phenomenologically, a charged and fast particle passing a material matter, emits energy in form of e.m. polarized radiation. The material matter is usually known as "radiator". The energy loss by unit of length and time follows the Frank and Tamm law:

$$\left(\frac{dE}{dx}\right)_{FT} = \frac{(ze)^2}{c^2} \cdot \int_{\epsilon(\omega)>\frac{1}{\beta^2}} \omega \left(1 - \frac{1}{\beta^2 \epsilon(\omega)}\right) d\omega \tag{4.2}$$

[1]The phenomenon was observed and described by Cherenvov between 1934 and 1944. The electromagnetic theory which succeeds to explain it was developed by Frank and Tamm in 1937. Cherenkov, Frank and Tamm received the Nobel Prize for Physics in 1958.

where ze is the charge of the particle, β is the speed and $\epsilon(\omega)$ the dielectric index as function of the frequency.

From optics, it's widely known that, in absence of absorption, there is a relation between the dielectric index ϵ and the refractive index n of a material:

$$n \equiv \sqrt{\epsilon(\omega)} \tag{4.3}$$

From equation 4.2 one finds the threshold in speed for this effect:

$$\beta > \frac{1}{n} \tag{4.4}$$

and, making use of the explicit expressions for the fields, one gets the so called Cherenkov equation:

$$\cos\theta_c = \frac{1}{\beta\, n} \tag{4.5}$$

relating θ_c, the emission angle as respect of motion direction, to the particle's speed and to radiator refractive index.

4.1.2 The Ring Imaging CHerenkov (RICH) detectors

The equation 4.5 provides a useful method to inspect the speed of the particles measuring the Cherenkov emission angle at their passage through a material radiator.

Different Cherenkov detectors can be built up to provide a very precise measurement of particles' speed in a given momentum range, in crowded environments and in high-rate experiments. Such detectors are naively composed by:

1. a radiator, where the Cherenkov photons are produced by charged particles at a speed above the radiator threshold;

2. a focusing optical system (absent in "proximity focusing" RICHes);

3. a set of position sensitive photon detectors, located on the mirrors focal surface in case of RICHes with focusing optical system ("imaging focusing" RICHes), characterised by good performances in efficiency and spatial resolution.

In case of proximity focusing devices, the photons produced in the thin radiator are simply projected onto the photon detectors installed inside the geometrical acceptance. In case of imaging focusing devices, a mirror system focalizes the photons onto a ring on the detectors plane installed outside the spectrometer acceptance. Integrating equation 4.2 on the radiator thickness one gets:

$$\mathcal{N} = \mathcal{N}_0 \; z^2 \; L \; \sin^2(\theta_C) \tag{4.6}$$

$\mathcal{N}_0$ is the detector's response parameter defined as:

$$\mathcal{N}_0 = \frac{\alpha}{\hbar c} \, \epsilon \; \Delta E = \; (370 \; eV^{-1} \; cm^{-1}) \cdot \epsilon \; \Delta E \tag{4.7}$$

where ϵ is the detector's efficiency convoluted by the energy interval of sensibility ΔE. Usually this product can be expressed in terms of radiator transparency, the reflectance of the mirror surface (if any) and photon detection efficiency:

$$\epsilon \; \Delta E = \int (QTR) \; dE \tag{4.8}$$

As a general comment, one can state that, fixing the interval in the photon energy where the photodetectors show a not vanishing sensibility (Q), all the RICH system must behave as a not interacting medium along the photons' path.

The Proximity Focusing RICH

In the case of a proximity focusing design (e.g. that one to be installed at the ALICE experiment at CERN), the photodetector is typically installed in the geometric acceptance of the reaction products. In such a case the RICH supplies information also on the center of the Cherenkov ring which coincides with the point in which the ionizing particle has crossed the photodetector; solid or liquid radiators are used to generate an intense Cherenkov radiation in a rather small volume of matter.

In figure 4.1 a proximity focusing optics is sketched out: a radiator of thickness D and refractive index n is followed by a transparent window (e.g made of quartz) whose thickness is d and refractive index n_q; the photosensitive detector is distant L from the window.

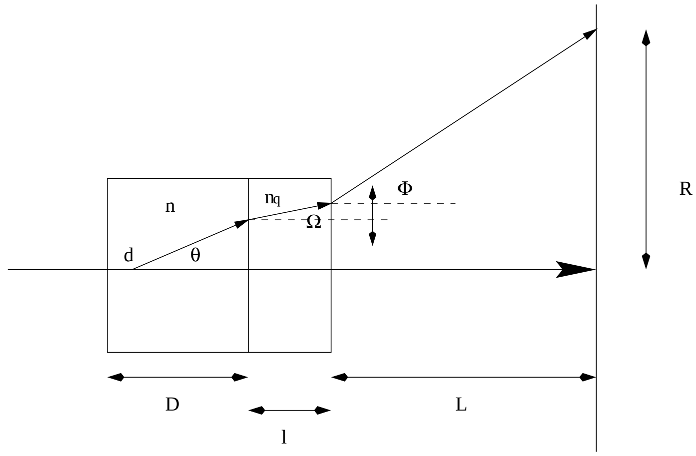

Figure 4.1: Conceptual scheme of a proximity focusing RICH.

To obtain good resolution in the impact point for the photon, it's good to set $L \gg (D + l)$. The volume between the radiator and the photodetector is filled by gas ($n_g \simeq 1$).

Computing the radius of the Cherenkov ring[2] from the impact point of a single photon and the center defined by the track, one gets:

$$R \ = \ d \ \tan(\theta) \ + \ L \ \tan(\phi) \ + \ l \ \tan(\Omega) \tag{4.9}$$

where ϕ is the exit angle of the photon from the radiator. This angle depends on the Cherenkov angle via the *Snell* law:

$$\sin(\phi) \ = \ n \ \sin(\theta) \tag{4.10}$$

The quantity $l\tan(\Omega)$, present in eq. 4.9, can be easily calculated since it depends on the refraction of the photons on the window:

$$\begin{cases} n \ \sin(\theta) \ = \ n_q \ \sin(\Omega) \ \Leftrightarrow \ \Omega \ = \ \arcsin(\frac{n}{n_q} \ \sin(\theta)) \\ \Delta R^q \ = \ l \ \tan(\Omega) \end{cases} \tag{4.11}$$

[2]The image projected by the Cherenkov photons onto the detector's surface is perfectly circular only in case the particle trajectory is perfectly perpendicular to the detector. Further distortions come from the refraction of the photons in the window's thickness.

Let's make the hypothesis that the particle is emitting the photons along its path inside the radiator with a constant probability and that this is the main source of uncertainty in the radius measurement. It follows:

$$\sigma_R^{geo} = \frac{D\ \tan(\theta)}{\sqrt{12}} \tag{4.12}$$

In case of $\mathcal{N}$ generated photons, the mean value of the radius is affected by an error of:

$$\sigma_{<R>} = \frac{\sigma_R^{geo}}{\sqrt{\mathcal{N}}} \tag{4.13}$$

Our description has skipped (for aim of simplicity) at least another source of uncertainty which should be taken into account in the calculation of $\sigma_{<R>}$.

In fact the angle θ itself, depending on the chromatic dispersion of the radiator (i.e. the dependence of the refractive index from the photon energy), is affected by an error. This error can be quoted differentiating eq. 4.5 w.r.t. n. One obtains:

$$\sigma_\theta = \frac{\frac{dn}{dE}\ dE}{n^2 \beta \sin(\theta)} \tag{4.14}$$

where the linear dependence of the uncertainty on the Cherenkov angle on the chromatic dispersion is in evidence.

The Imaging Focusing RICH

Considering gas radiators and ultra-relativistic speed:

$$\begin{cases} \beta^2 \simeq 1 \\ n^2 \simeq 1 \end{cases}$$

eq. 4.6 can be rewritten as:

$$\mathcal{N} = \mathcal{N}_0\ z^2\ L \left(1 - \frac{1}{n^2}\right) \simeq 2\ \mathcal{N}_0\ z^2\ L\ (n-1) \tag{4.15}$$

showing a linear dependence of $\mathcal{N}$ on the factor $(n-1)$.

Medium	State	$\mathcal{N}/cm$
quartz	solid	295
water	liquid	241
freon (C_6F_{14})	liquid	190
air	gas	0.31

Table 4.1: Comparison of the number of photons emitted per unit length in solid, liquid and geseous radiators.

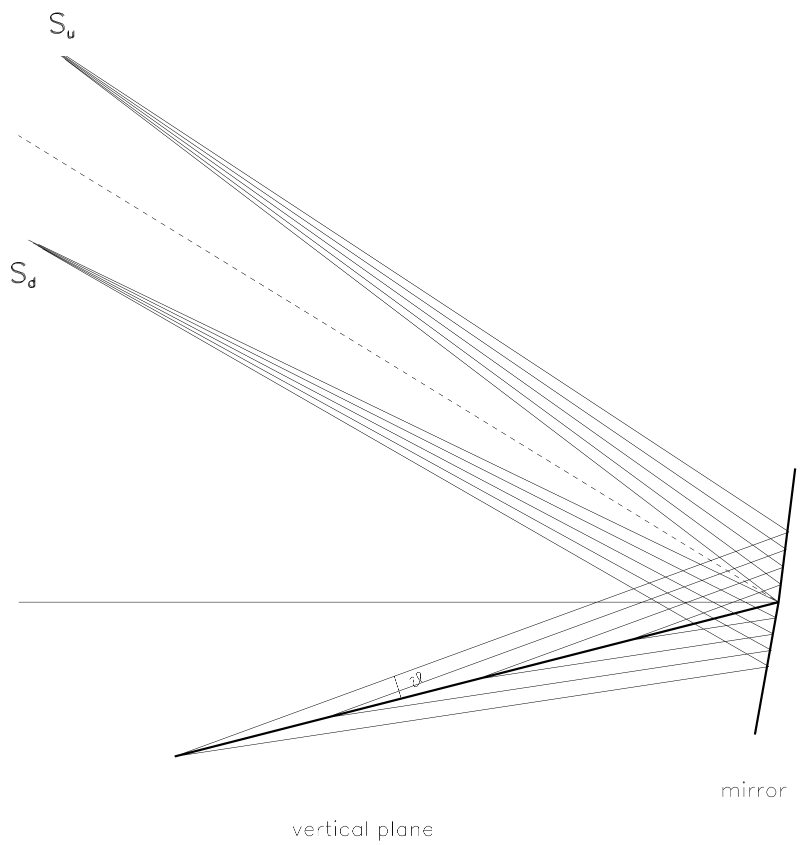

Figure 4.2: Focalization of a photon emitted at an angle θ; all the photons emitted along the path are focalized in the points S_u or S_d of the ring.

In case of gaseous media, $(n-1) \simeq 10^{-4}$, it's mandatory to have large radiator length in order to increase the amount of photons emitted by the particle. In table 4.1, in the ultrarelativistic limit, the number of photons emitted per unit length is shown for some particular cases of solid, liquid and gaseous materials.

The focalization of the photons is the base concept shown in picture 4.2 where a spherical mirror projects a photon beam (coming from the particle path) onto its focal length. If the symmetry in the azimuthal angle is taken into account, the shape of a ring appears on the photosensitive plane with radius equal to:

$$r = f \tan(\theta)$$

being f the mirror focal length. From this equation one can calculate the Cherenkov angle as:

$$\theta = \arctan\left(\frac{r}{f}\right) \simeq \frac{r}{f} \tag{4.16}$$

Each individual photon permits an independent determination of the Cherenkov angle (the only correlation is given by the measured particle trajectory which is a common piece of information used in each determination). The speed can be evaluated from the weighted mean $\bar{\theta}$ of such distribution.

$$\beta = \frac{1}{n \cos\bar{\theta}} \simeq \frac{1}{n\sqrt{1-\bar{r}^2/f^2}} \tag{4.17}$$

The resolution in β strongly depends on the error affecting $\bar{\theta}$. In the case of COMPASS RICH-1, the estimation for $\bar{\theta}$, reported in the proposal, was of the order of 200 μrad.

4.2 Present status of RICH counters

In table 4.2 the main RICH projects are grouped accordingly to the technique chosen for the photodetection. The three wide groups use:

- gas detectors with photosensitive vapours in the detector's atmosphere;

- vacuum based photon detectors;
- MWPCs with CsI Photocathodes.

In the first group, the RICHes use “TMAE” or “TEA” photosensitive vapours are included. They are mainly RICH detectors of the first generation, apart from the CLEO III's one. The wave-length interval of sensibility for such gases is mainly in the UV domain.

In the second group, standard PMTs, MultiAnode PMTs or Hybrid Photo-Diodes (HPDs) are chosen, for the wide sensitive range, the good granularity, the limited chromatic aberrations and the good rate capabilities. Working in the visible and near-UV range, they provide good resolution in Cherenkov angle detection (for example in the case of the RICH-2 designed for the LHCb experiment a resolution σ of about 0.35 mrad is expected).

The projects grouped into third section have chosen special MWPCs in which one of the cathode planes is formed by large PCBs segmented in pads and deposited by a thin (hundreds of nm) layer of CsI [28]. The CsI quantum efficiency doesn't vanish only in the far UV ($\leq 210\ nm$). From the sensitivity of CsI to the UV photons comes the need to equip the MWPCs with entrance window showing good transparency in such wavelength region. This is the case of ALICE and COMPASS which adopt quartz windows.

photodetector	project	status	notes
PHOTOSENSITIVE	CERES	ending	TMAE
GASES	CRID	ended	TMAE
	DELPHI	ended	TMAE
	OMEGA	ended	TMAE
	CAPRICE (1)	running	TMAE
	CLEO III	started	TEA
VACUUM-BASED	DIRC	started	PMTs
PHOTON	HERMES	started	PMTs
DETECTORS	PHENIX	started	PMTs
	SELEX	ended	PMTs
	AMS (2)	design	MA PMTs
	HERA-B	started	MA PMTs
	LHCb (3)	LHC era	HPDs/MA PMTs
MWPCs with CsI	ALICE	LHC era	prototype in STAR
PHOTOCATHODES	COMPASS	started	
	HADES	started	prototype : HIRICH

Table 4.2: RICH projects grouped according to the chosen photodetection technique; the project status is also indicated. (1) - balloon-borne experiment; (2) - space-borne experiment; (3) - 2 options for the photodetectors.

4.3 RICH-1

RICH-1 [29] is a large acceptance gaseous RICH using 3 m of C_4F_{10} as radiator and MWPCs with CsI photo-cathodes as UV Photon Detectors. The main characteristics of this RICH are the large acceptance and the use of far UV Photon Detectors, which implies large dimensions, UV transparencies of the elements up to the photo-cathode, and good UV mirror reflectance.

In this section the detector is described, and first results about the performances are given.

Aim of the device

The requirements for RICH-1, given by the general design of the experiment, are:

- the capability to separate π and K with momenta up to ~ 60 GeV/c in a high-intensity environment;
- the full acceptance of the large-angle spectrometer (horizontal: ± 250 mrad; vertical: ± 200 mrad);
- the minimisation of the amount of material, to preserve the tracking resolution of the small-angle spectrometer and the energy resolution of the downstream electromagnetic and hadronic calorimeters;
- the capability to register and handle high data fluxes.

As a comment about the energy range covered by this device we note that the mass of the particle, reconstructed by the momentum information of the spectrometer and by the speed information of the RICH-1 is:

$$m = p\,\frac{\sqrt{1-\beta^2}}{\beta}\,.$$

This gives a relative resolution on the mass of

$$\left(\frac{\sigma_m}{m}\right)^2 = \left(\frac{\sigma_p^2}{p^2}\right)^2 + \gamma^4\left(\frac{\sigma_\beta^2}{\beta^2}\right)^2$$

which means that, for high speed particles (being $\beta \simeq 1$ and $\gamma^2 \gg 1$), the contribution in speed is dominant as respect of momentum's. Our detector is measuring (in the ultrarelativistic range up to 60 GeV) the speed with a very high precision; taking the expected

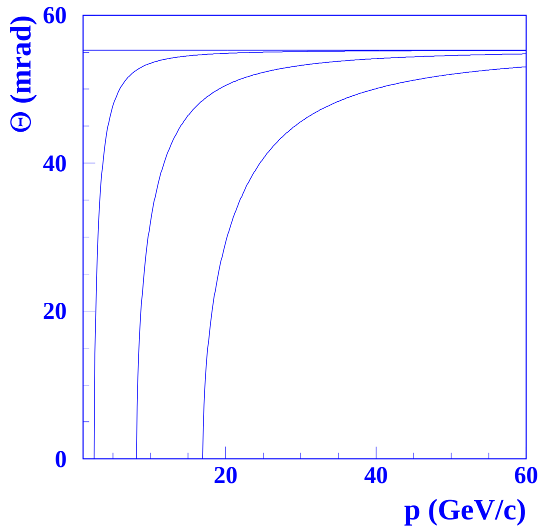

Figure 4.3: RICH1 resolution

resolution given in the proposal:

$$\frac{\sigma\beta}{\beta} \simeq 8.8 \cdot 10^{-6}\,. \tag{4.18}$$

For example the relative error in the mass measurement for 40 GeV pions and kaons are:

$$\frac{\sigma_m}{m} \simeq \gamma^2 \frac{\sigma_\beta}{\beta} \quad \begin{cases} \simeq 287^2 \cdot 8.8 \cdot 10^{-6} \simeq 0.73 & \text{for pions} \\ \simeq 81^2 \cdot 8.8 \cdot 10^{-6} \simeq 0.05 & \text{for kaons} \end{cases} \tag{4.19}$$

and the distance between the peaks of the two distribution is:

$$m(K) - m(\pi) \equiv 354\ MeV \tag{4.20}$$

$$\equiv 3.46 \cdot \sigma_m(\pi)\,, \tag{4.21}$$

meaning that the K signal is separated by more than 3 σ from π.

In figure 4.3 the expected Cherenkov angle as a function of the momentum for pions, kaons and protons is presented.

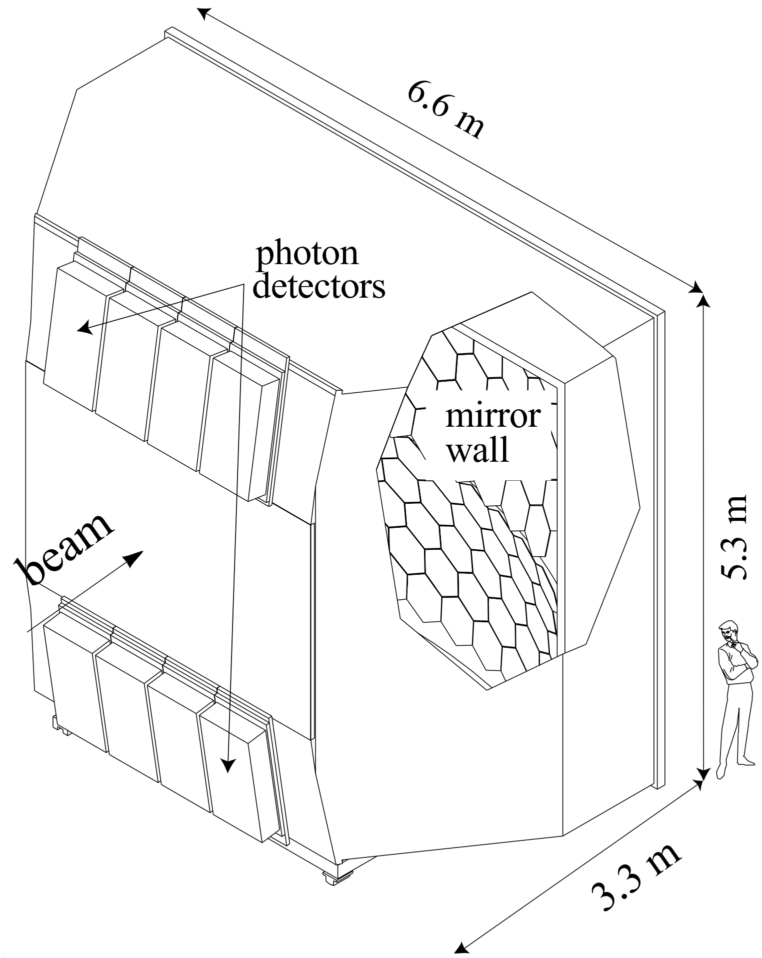

Figure 4.4: Artistic view of COMPASS RICH-1.

These requirements resulted in the design sketched in figure 4.4 and in the following achieved parameters:

RADIATOR (section 4.3.1): A 3 m long C_4F_{10} radiator at atmospheric pressure [30], with a contamination of oxygen and moisture kept below 5 ppm, to have a transmittance higher than 80 % for 165 nm photons, for a typical path length of 4.5 m.

For the radiator vessel ($\sim$ 80 m^3) non polluting materials were used, mainly aluminum. Input leakage rate is $\sim$ 3 Pa×l/s.

MIRRORS (section 4.3.2): The mirror system [31] consists of spherical mirrors, radius of curvature 6.6 m, segmented in 68 hexagonal and 48 pentagonal pieces covering a total area

> 20 mm^2. Two spherical surfaces focalise the Cherenkov photons onto two sets of photon detectors placed above and below the acceptance region. These mirrors have: local deviation of the shape from the spherical $\sigma_\theta < 0.2$ mrad; maximum deviation from the radius of curvature $\delta_R/R = 0.5$ %, reflectance $> 80\%$ down to 165 nm.

PHOTON DETECTORS (section 4.3.3): Taking into account the large area to be instrumented (5.3m^2) and the need for pixel size ~1cm, our choice was to use MWPCs with segmented CsI photo-cathodes, i.e. the UV photon detector developed in the context of RD26 [28] and, later, for the ALICE HMPID project [32], adopted for several other projects [33, 34]. RICH-1 is equipped with 8 identical chambers, each one having an active surface of 576×1152 mm^2. Two 576×576 mm^2 double-layer PCBs, each segmented in 5184 8×8 mm^2 pads, coated with CsI form the photo-cathode planes (for more details about the coating technique see [35]). Fused silica windows ($600 \times 600 \times 5$ mm^3) separate the radiator from the photon detectors. Detail about photon detector design and construction, CsI handling and tests of the small and full-size prototypes can be found in reference [36].

FRONT-END ELECTRONICS (section 4.3.4): The total of 82944 channels, equipped with analogical readout electronics, sums up to about one third of the total number of channels of the experiment. The heart of the read-out system are the large front-end BORA boards [37], housing the front-end chip and local intelligence.

MATERIAL BUDGET: The two major contributions to the material budget in the acceptance are the radiator (10.5% of X_0) and the mirrors (5.5% of X_0 for the substrates, 2.5% of X_0 for the mechanical supports); the front and rear vessel windows are sandwiches of two thin Al foils and a layer of rigid foam, resulting in ~2 % of radiation length per window. The total radiation length is 22.5% of X_0. In table 4.3 the updated list of material budget per component is reported.

4.3.1 The gas radiator

The radiator gas and its transparency

In table 4.4 there are listed the chemical and physical characteristics which have suggested to choose perfluorebutan (C_4F_{10}) as gas radiator for RICH-1.

The high number of photons, the intrinsic transparency and the low chromatic dispersion in the UV permit to use this radiator coupled to solid state photocathode-equipped chambers.

Component	Radiation length ($\%X_0$)
Gas Radiator	10.5%
Mirrors	5.5%
Upstream window	2.0%
Downstream window	2.2%
Mirror mechanics	2.3%
Total	22.5%
Total (beam line)	1.6%

Table 4.3: Material budget of RICH1

The low emission threshold ($\gamma_{th} \simeq 18$) fulfils the requests of particle ID down to momenta of some GeV/c.

The effective transparency depends on the amount of O_2 and H_2O inside the vessel because of the high absorption cross section of these molecules in the UV region.

The RICH1 gas radiator		
chemical formula		C_4F_{10}
volume		$\sim 90\ m^3$
length		$3\ m$
weight		$\sim 10\ q$
density	$\bar{\rho}$	$\simeq 11\ Kg/m^3$
boiling temperature		$-1.7^o\ C$
(n-1) at 7 eV		$1530 \cdot 10^{-6}$
cromatic dispersion at 7 eV	dn/dE	$\simeq 53 \cdot 10^{-6}$
number of photons	N_{ph}	34
Cherenkov max angle		$55.3\ mrad$
threshold for π	p^{π}_{th}	2.5 GeV/c
threshold for K	p^{K}_{th}	8.9 GeV/c
threshold for p	p^{p}_{th}	17.0 GeV/c

Table 4.4: Radiator's main charateristic.

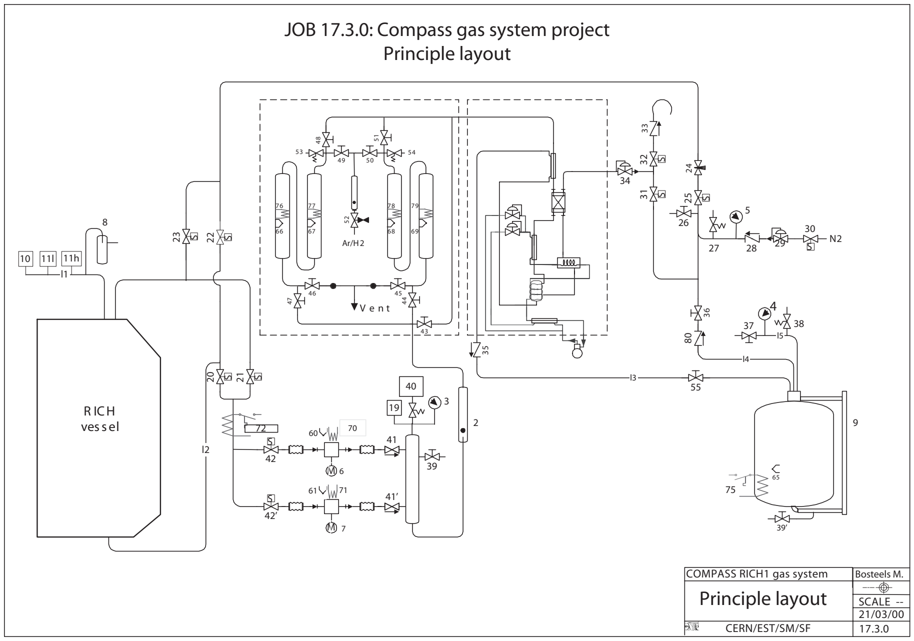

Figure 4.5: Schematic diagram of the COMPASS RICH-1 gas system

The gas system

The RICH-1 gas system (fig. 4.5) follows a basic design [38] already used for other RICH detectors (HERA-B [39], CAPRICE [40]). Its main task is to provide, during detector operation, well controlled pressure conditions, within small limits, in the RICH vessel ($\sim$80 m^3) to purify the radiator gas from oxygen and water vapour contaminations and to perform the filling of the vessel and the C_4F_{10} recovery. Its main components are two oil-free compressors[3], working in parallel, a pressure sensor installed on top of the radiator vessel, a pneumatic valve. The system is complemented by filtering cartridges and a cooling system for N_2 and C_4F_{10} separation. The relative pressure in the vessel is kept constant controlling the input flow by the pneumatic valve which is regulated according to the pressure sensor response. The compressors, aspiring the gas from the vessel, run at constant frequency. They are heated (typically at 50^0 C) to prevent C_4F_{10} condensation in this section of the gas system, where the pressure can reach 500 kPa. The control of the system is performed via a Programmable Logic Control (PLC).

[3]Haug SOGX 50-D4

The choice to regulate the pressure of the gas radiator vessel relatively to the atmospheric pressure is dictated by the two thin vessel walls required in the spectrometer acceptance region. Operational conditions foresee 200 Pa at the upper side of the larger thin wall (corresponding to a relative pressure of 700 Pa at lower side and to 100 Pa on top of the vessel). An upper limit of 300 Pa and a lower limit of -200 Pa for the relative pressure on top of the vessel have been set accordingly to the thin wall structure and the overall vessel mechanical design. If the relative pressure exceeds these limits, the forces generated by the thin wall deformation could induce deformations of the vessel structure, to which the mirror wall is fixed, thus generating mirror misalignment. For pressure values further from the allowed range, the thin walls risk to be damaged. Moreover, in all operational conditions, only a pressure difference of at most 1000 Pa between the vessel and the photon detector volume is allowed to avoid mechanical stresses on the fused silica plates: this is guaranteed regulating also the photon detector pressure relatively to the atmospheric one. The relative vessel pressure is kept constant within 10 Pa over months of operation. The avoid accidental pressure values outside the allowed range, for example in case of a long power failure, a safety-bubbler, mounted on top of the vessel, will release gas to the atmosphere or let air enter in the vessel.

The radiator gas is circulated at a rate of 3 to 5 m^3/h through a filter[4], to prevent building up impurities due to leaks: the global, i.e. vessel and gas system, rate of air input is $\sim$3 Pa$\times$l/s. Two filter cartridges, mounted in parallel, ensure to have at least one operational filter at all times. They can be regenerated in situ.

Before filling and during long shutdown periods, the vessel is flushed with nitrogen. N_2 and C_4F_{10} separation during filling and recovery is based on the different boiling points of the two gases and provided by a cooling system with heat exchangers operating at -35^0 C. During filling and emptying, the pressure in the separator section is kept at 400-500 kPa: nitrogen vented out thus contains $\sim$4-5% residual C_4F_{10}.

The system operation has been stable over periods of months. It is also quite easy, thanks to the simple design principle.

[4]BASF-Catalyst R13-11 by BASF AG, 67056 Ludwigshafen, Germany

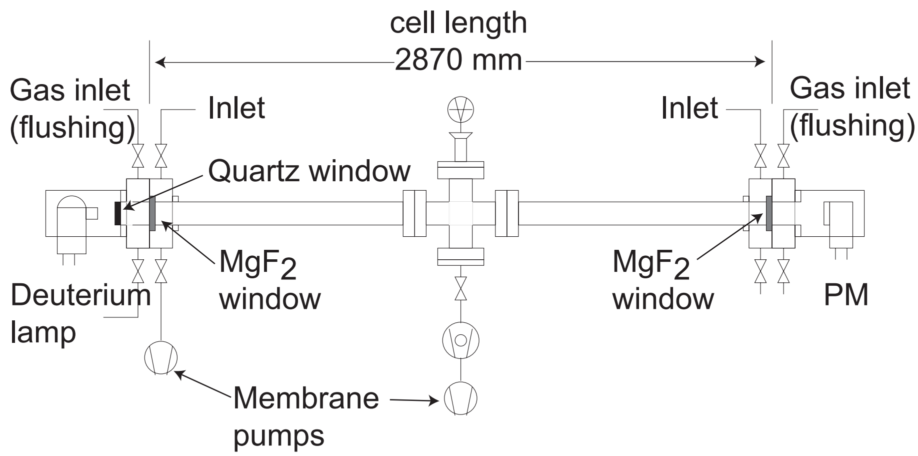

Figure 4.6: Schematic drawing of the UV integral measurement setup.

Gas quality measurements

The gas system is complemented by monitoring instrumentation, including commercial instrumentation (a hygrometer, an oxygenmeter and a binary gas analyser), a sonar to determine the gas composition by measuring the speed of the sound in the gas [41] and a setup for transparency measurements. This setup allows to perform an integral measurement over the range from 160 nm to 210 nm. The system consists of a stainless-steel transmission cell of 2870 mm length (fig. 4.6); at one side a deuterium lamp[5] is attached and on the other side there is a solar-blind photomultiplier tube[6] reading the intensity of the transmitted light. A fused silica window is installed along the light path to match the sensitivity of this measuring system with that of the photon detectors. The measuring cell can be evacuated down to 10^{-3} Pa for normalisation measurements. Alternatively, normalisation can be obtained by flushing the measuring cell with nitrogen.

Radiator gas cleaning

C_4F_{10} is intrinsically transparent in the UV region of interest for RICH-1, but in the commercially available material strongly UV absorbing contaminations are present. Therefore

[5]Hamamatsu L2D2 lamp, type L7295
[6]Hamamatsu type R7639

gas cleaning is needed before injecting it in the RICH gas system. It is clear from experience that the amount and nature of polluting material traces varies in the different production and delivery batches.

A cleaning system was put in operation in year 2000 and also used in year 2001. Liquid C_4F_{10} is circulated permanently through the filters in a closed loop. This cleaning system has a direct connection with a cell, 51 mm long, closed by CaF_2 windows, mounted in the vacuum chamber of the CERN reflectometer [42], which has been modified to allow light transmission measurements for COMPASS and ALICE experiments. The UV light transmission through the liquid (corresponding to more than 7 m of gas path length at atmospheric pressure) can be measured. The normalisation of the measured transmission is performed flushing the cell with clean nitrogen. This set-up makes it possible to monitor on-line the material transparency during cleaning procedure.

In a first stage, different filter materials have been tested: silica gel, activated carbon, 13X molecular sieves and Cu-catalyst, the last one resulting to be the most efficient for the material used during this test phase and it was adopted. It has allowed to obtain light transmission $\geq$80% down to 165 nm (fig. 4.7) with material loss of 7%. Later, depending on the different material samples, the same light transmission has been obtained with material losses up to 50%. The large variation of loss rates is related to the different amount and nature of contamination impurities: ideally, the choice of the best filter should be sample dependent.

A second cleaning system has been put in operation in year 2002. The material is circulated in closed loop in gas phase through activated carbon filter and 13X molecular sieve, later replaced by 5A molecular sieve. Oxygen is removed in a cool section (T $\sim$-60^{0}C), where C_4F_{10} condensate and the liquid drops back to the bottle, while gas component is vented out. Typical material loss is $\sim$20%.

4.3.2 The mirror system

The RICH-1 optical system is formed by two UV reflecting spherical surfaces (total area $\sim$21 m^2) with centres vertically displaced, up and down, by 1600 mm with respect to the beam axis, so to focalise the image outside the spectrometer acceptance. The two surfaces are a mosaic type composition of spherical mirror units: 68 of them are regular hexagons (side length 261 mm) and 48 are pentagons of six different size, to avoid saw-teeth patterns on the surface borders. The clearance left between adjacent mirrors results in a 4% loss of

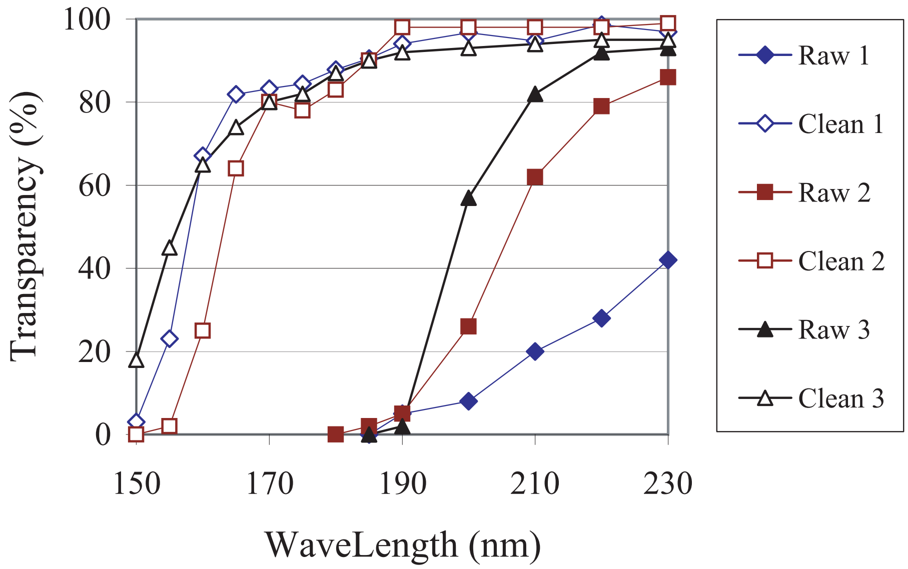

Figure 4.7: UV light transmission through 51 mm of liquid C_4F_{10} scaled to 5 m of gas, 100 kPa, for three different samples. Raw material and clean material transmission are shown.

reflecting surface (fig. 4.8).

The main design parameters of the mirrors are:

- radius of curvature, R = 6600 mm, ±1%
- "spot diameter" D, i.e. the diameter of the smallest circle containing 95% of the power associated with the image of a point-like source, < 3.5 mm
- roughness, r.m.s. < 1.6 nm
- reflectance r > 80%, for wavelengths in the interval 160-200 nm
- substrate thickness: < 6% of radiation length (minimum material is required also for the mechanical structure of the mirror wall).

The mirror substrates are borosilicate glass, 7 mm thick; their stiffness is confirmed by a F.E.M. calculation [43].

The 126 (10 spare units) substrate, produced by IMMA [44], have been visually inspected and individually characterised by measuring the radius of curvature, R, and the "spot diameter", D [45]. For the 126 substrates, the average values are: R_{av} = 6606 mm ± 20 mm and

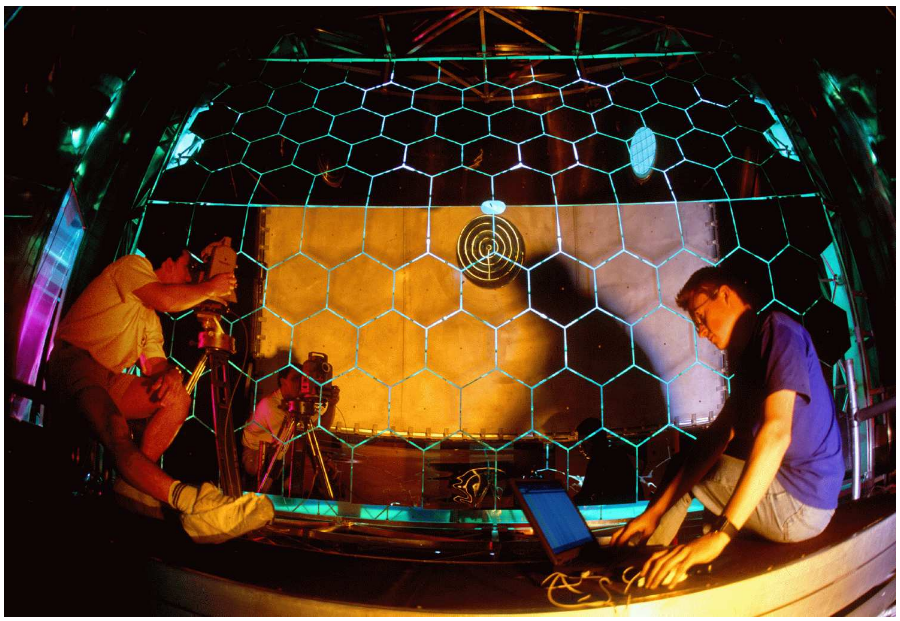

Figure 4.8: COMPASS RICH-1 mirror wall; the picture has been taken during mirror alignment procedure inside the RICH vessel.

D_{av} = 1.65 mm ± 0.45 mm. The roughness of the polished surfaces has been checked on a sampling base: the measured roughness r.m.s. was in all cases < 1.6 nm (average value: 1.26 nm± 0.11 nm). The substrates have a 6 mm diameter hole at their centre, to allow an extra fixation, by a nylon screw, of the mirrors on the first element of their mechanical support, a stesalite disk, 46 mm diameter, glued on an annulus of 290 mm^2, at the centre of the mirror substrates, rear face.

UV mirror coating

To obtain a good reflectance in the UV region the reflecting layer (Al, about 80 nm) and the protective layer (MgF_2, about 30 nm) have to be deposited with a carefully tuned and controlled procedure. Some crucial requirements are: very good vacuum (10^{-7} mbar), high deposition rate (2-4 nm/s) and rapid rotation of the mirror. For the procedure tuning, feedback to the manufacturer [46] was provided by making use of the CERN reflectometer facility [42], later used to measure the reflectance of each mirror at the centre and at the edge. The coated mirrors must be carefully protected against humidity at all time.

The measured reflectance is good (fig. 4.9) (only four mirrors had to be re-coated) and the mean value of the reflectance for wavelengths in the useful interval (160-200 nm) is always in the range 83 - 87%. Repeated measurements of the reflectance after 1 and 2 years permanence in RICH vessel indicate, after the expected short term degradation, stable reflectance values above 165 nm (fig. 4.9).

Mirror tiling

The hexagons were divided into two sets, according to their R values (> or < 6607 mm). For each surface, the best mirrors (R nearest to the nominal value) were used to fill the central region, around the beam, and going further, sequences of mirrors minimising R-variation were chosen. In the case of pentagonal mirrors, the alternatives were limited by their different sizes.

The mechanics of the mirror wall

For the mechanical supporting structure of the mirror wall was chosen a net-like configuration, in which the nodal points, where the mirrors are suspended to, lay on a sphere with

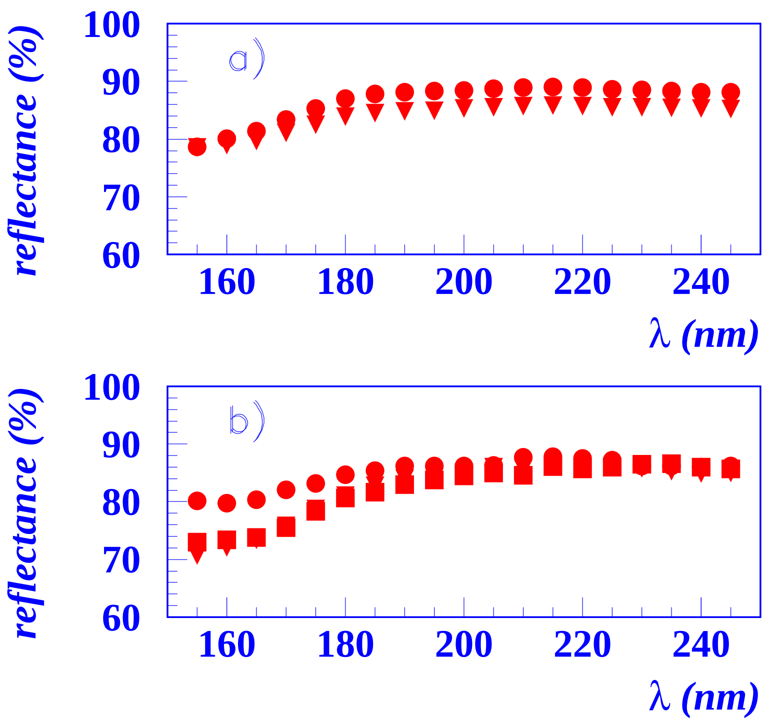

Figure 4.9: a) Mean value of the reflectance measured for the 126 mirror units at the centre (dots) and at the edge (triangles). b) Reflectance of one mirror unit immediately after production (dots), after one year (squares) and after two years (triangles) permanence in RICH vessel.

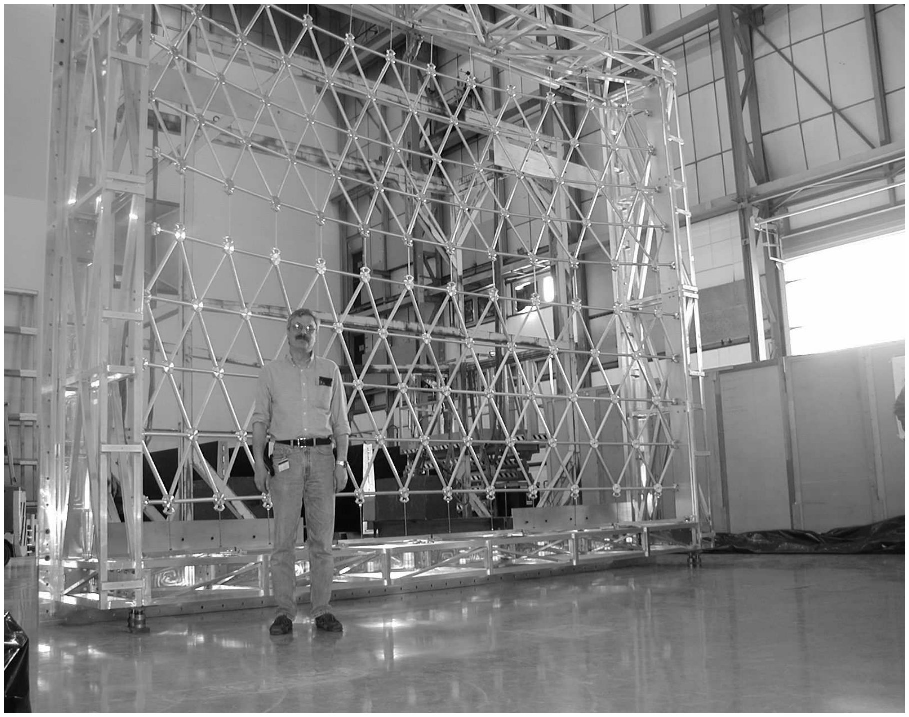

Figure 4.10: The mechanical structure of the mirror wall.

a very high mechanical precision; as a consequence, only angular adjustment of the mirror units is needed (radial adjustment is suppressed to reduce the amount of support material).

The aluminium structure (fig. 4.10) is formed by:

- a rectangular (6.05×4.85 m^2) stiff outer frame, which lies outside the acceptance of the spectrometer (stiffness checked with F.E.M. calculation) screwed on the rear flange of the radiator gas vessel;
- a double-spherical structure of high mechanical precision, with connection points to which the mirrors will be anchored (figures 4.10, 4.11);
- the joints, i.e., mechanisms connecting the mirrors to the above mentioned structure and allowing for mirror alignment, rotating around two orthogonal axes(fig. 4.11); they permit angular adjustments via converting the translational push (or pull) of a micrometric screw (pitch 0.5 mm) against one end of a rigid bar (200 mm long) into a rotation at the other end of the bar constrained to a pivot anchor; the angular

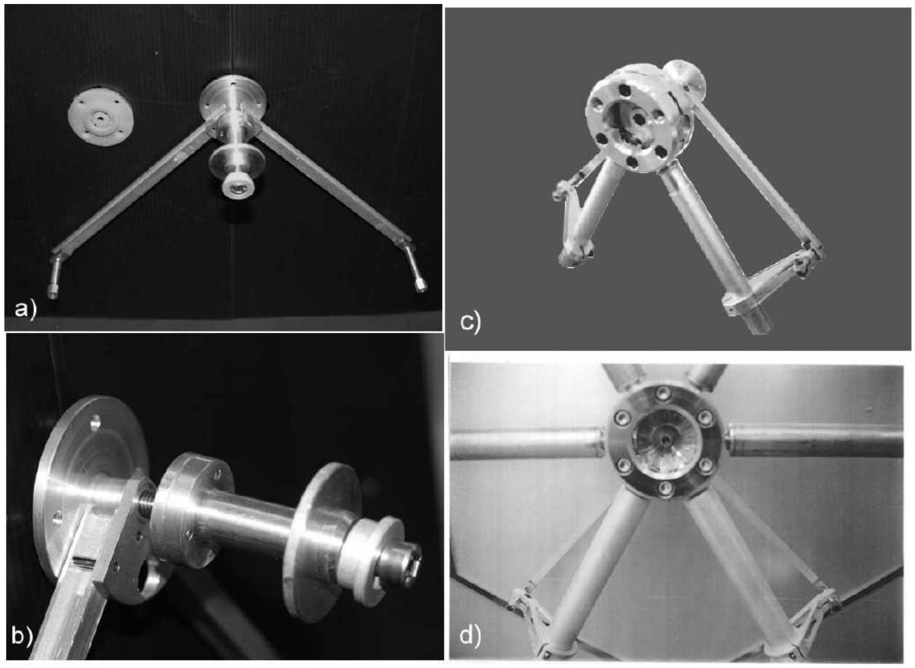

Figure 4.11: a) and b) A mirror joint (see text); c) the mirror joint mounted on a prototype portion of the mirror supporting structure; d) a mirror (rear face) monuted on the supporting structure.

resolution is 2.5 mrad/turn with very good linearity, practically no hysteresis and a negligible (0.01 mrad) cross-talk. Their unit weight is 112 g.

For the assembling of the spherical surfaces a dedicated mould was manufactured using a five-axis miller. After assembling, the mirror-wall support has been carefully surveyed and found to be fully satisfactory: the centres of the front faces of the 'nodes' actually lie, within ± 1 mm, at the designed positions on two spherical surfaces. The equivalent thickness of the mirror supporting wall, including the joints, is 2.5 % of a radiation length.

Mirror mounting and alignment

Mirror mounting and alignment took place within the RICH vessel; during operations the air was continuously filtered and dried (humidity between 10 and 30 % was measured, varying with the presence/absence of operators inside). First, each mirror was equipped with its support and regulation joint and then mounted at its own place on the mirror-wall. After mounting all the mirrors onto the supporting wall, they were aligned. As the loci of the centres of the spherical surfaces are outside the vessel volume, the following alignment procedure was adopted: the coordinates of the two sphere centres are known in the vessel reference frame, the coordinates, respect to the same reference frame, of a theodolite are measured and its axis oriented along the straight line joining the centres of the sphere and of the theodolite (reference line). If the mirror which is just in front of the theodolite is perfectly aligned, the normal to the mirror surface, at the intersection point with the reference line, will also lie along this line. If it is not aligned, the normal and the reference line will be at an angle, and the image from the mirror of a reticle will be seen displaced: the mirror is rotated to make them coincide. At the end, the residual misalignment angle of the mirror is measured and accepted if it is less than 0.1 mrad, the precision with which is defined the “reference line”. To allow the positioning of the theodolite in front of every mirror, special scaffoldings, minimising vibrations, have been built inside the vessel and removed at the end of the alignment exercise.

4.3.3 The photon chambers

RICH-1 is equipped with 8 identical chambers (see in exploded view, fig. 4.12 and in section, fig. 4.13), each one has an active surface of 576×1152 mm^2. The photocathode planes are formed by two 576×576 mm^2 double-layer PCBs. Anode wires, 1260 mm long, are supported at mid length by insulating MACOR [47] bars. The fused silica (quartz) windows are formed by 2 identical fused silica plates ($600 \times 600 \times 5$ mm^3) glued onto Al frames via an intermediate FPM 75 frame. Gas tightness is obtained with FPM 75 o-rings. The use of nonmetallic materials has been minimized in the design. The Alcoa Alca Plus Al alloy [48] is used for all the chamber frames.

Great care is devoted to the handling of the PCBs with CsI layer to ensure that they are never exposed to atmospheres with more than 100 ppm air contamination: We have built a cathode PCB transport system with closed circulation of filtered N_2 and dedicated glove boxes for assembling and for maintenance interventions.

During detector construction, all mechanical parameters are checked and, when necessary, corrected by hand. The goal is to keep anode cathode gaps at nominal value ± 50 μm and wire tension at nominal value $\pm 5\%$.

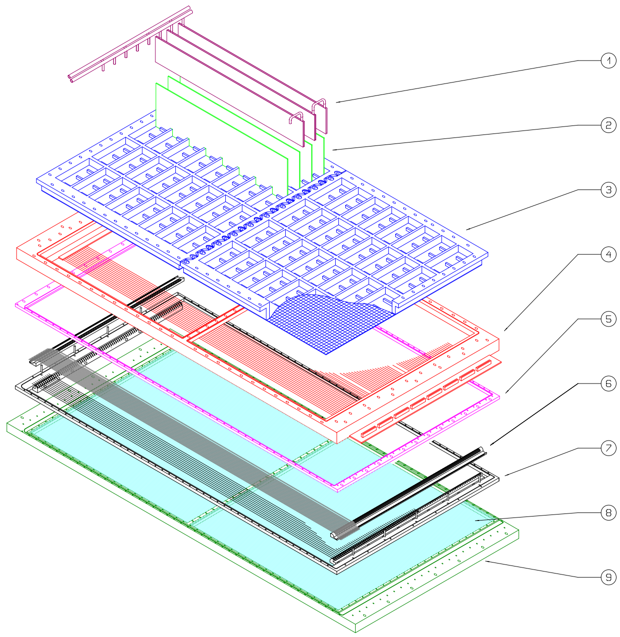

Figure 4.12: One of the photon detectors of COMPASS RICH 1: 1) cooling plates, 2) readout boards, 3) CsI photocathode boards, 4) anode wires, 5) distance frame, 6) cathode wires, 7) collection wires, 8) fused silica plates, 9) fused silica frame.

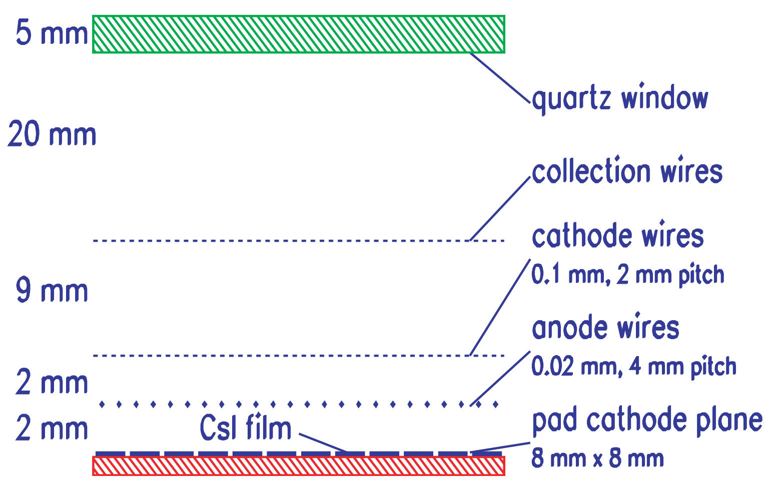

Figure 4.13: Section of the RICH-1 photodetectors.

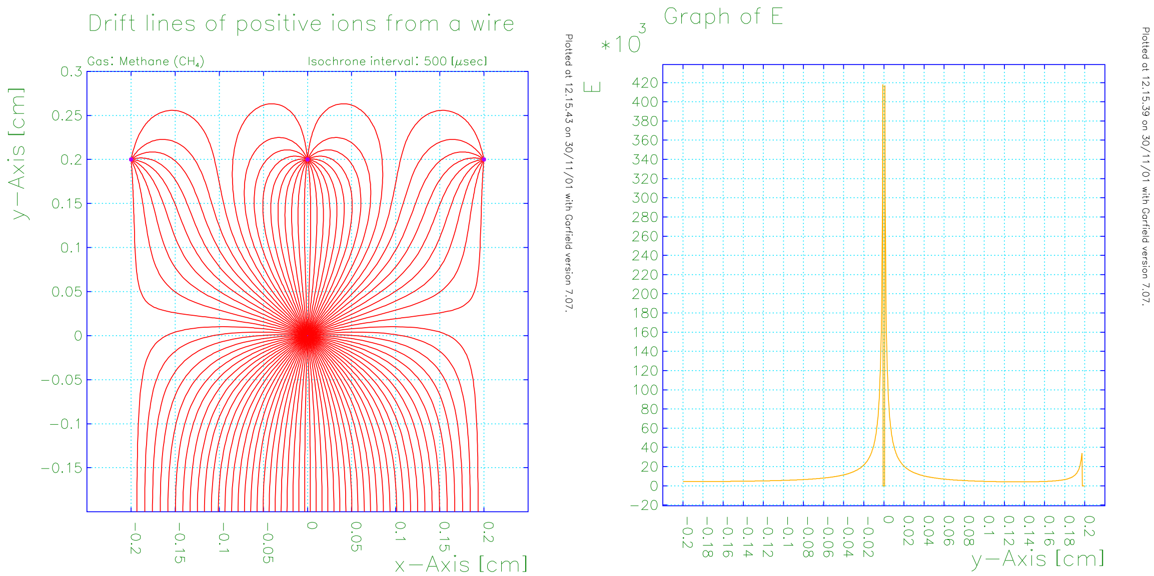

Figure 4.14: Field lines (a) and electric field (b) for a 2000 V biasing voltage

Principle of operation

The photon chambers are MWPC's with a peculiar cell geometry, chosen to minimize the ion drift time. The field lines for a 2000 V applied biasing voltage are shown in figure 4.14(a) as a result of a garfield [49] simulation; the field going from the pad-cathode to the wire-cathode and passing through the anode wire is shown in figure 4.14(b). The pad cathodes are deposited with a thin film (< 500 nm, with a $\sim 10^{11}$ Ω/cm resistivity) of Cesium-Iodide (CsI). The threshold for the photoelectric effect on CsI is 6 eV, corresponding to 210 nm wavelength of the incident photons. The choice of CsI as solid UV photocathode is due to the highest quantum efficiency between all the alkali halides and the exceptionally large electron escape length, which is 16 nm for 1 eV incident photons.

Pure CH_4 is used as chamber gas, since the use of noble gasses like Ar results in sensible losses of photoelectrons due to the large backscattering effect, decreasing the photoelectric yield. In addition CH_4 shows a quite an excellent UV transparency, attractive to avoid losses of primary photoelectrons even if it makes the contribution of feedback photons not neglegible.

The quartz windows, which divide the radiator region from the photon detectors, have a good transparency for photons in the energy region of interest at a limited cost, compared

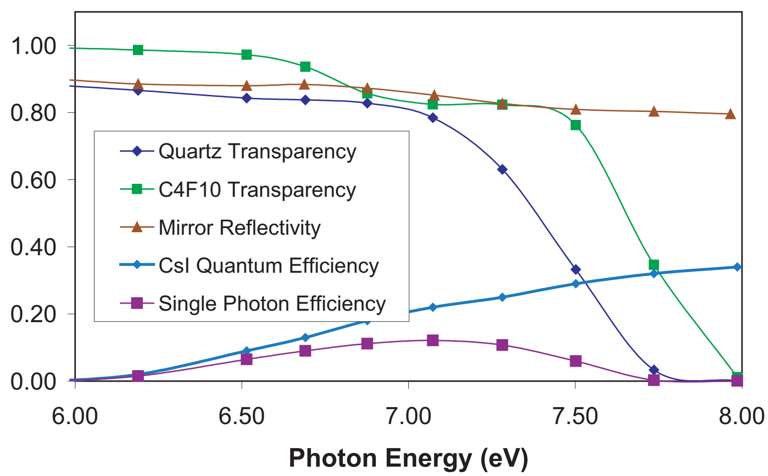

Figure 4.15: Single electron efficiency as a function of the photon energy, together with all the elements contribution to it, except the chamber gain.

to the large surface needed. The cut off wavelength of the fused silica plates is 165 nm, which overlaps with the cut off given by the radiator itself; figure 4.15 shows the the overall efficiency to create photoelectrons as a function of the photon wavelength. The gain of the detectors in pure methane has been calculated between 1500 and 2500 volts, without taking into account the effect of photon feedback at the photocathode, which increases the gas gain by photoconversion of photons emitted in the avalanche. For the calculation of the Towndsend and attachment coefficients we have used two simulation programs MAGBOLTZ [50] for fields below 20 kV/cm and IMONTE45 [51] by the same author for higher fields. In order to avoid extrapolations close to the wires the coefficient calculation was clearly extended above the maximum of the electric field.

The result of the gain calculation is shown in figure 4.16 and is in good agreement with the points measured by using a ^{106}Ru source which prevalently emits β electrons with a mean energy of 3.541 MeV. The range of stable operation for this kind of detector is between a gain of 10^4 (low level for full efficiency) and 10^5, after which we start to become too sensitive to photon feedback. The fact that here we notably exceed this limit is due to the fact that there was no deposit of CsI on the pad cathodes used here.

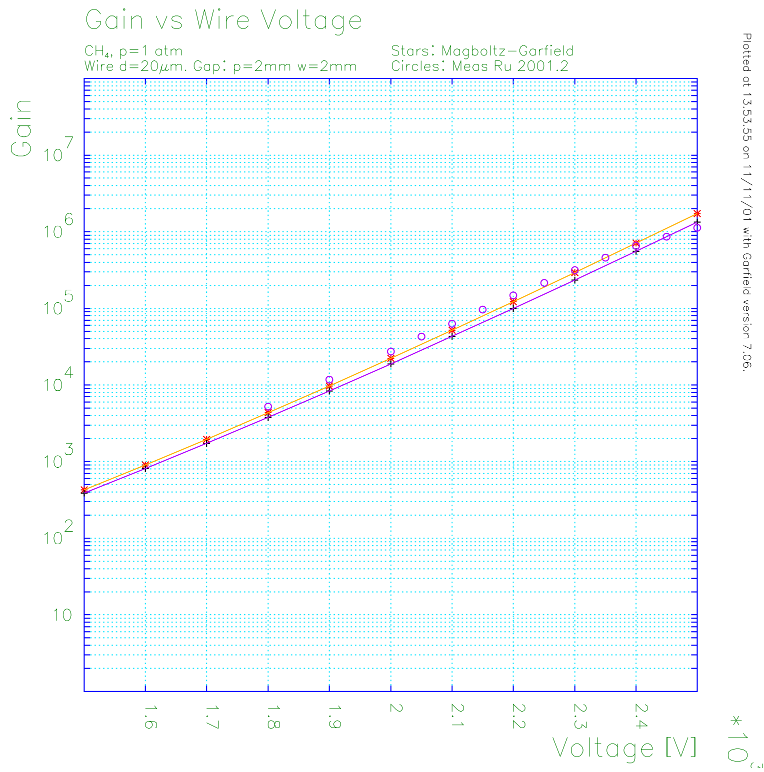

Figure 4.16: Measured (open points) and calculated (cross) photon detector gain between 1500 and 2500 volts.

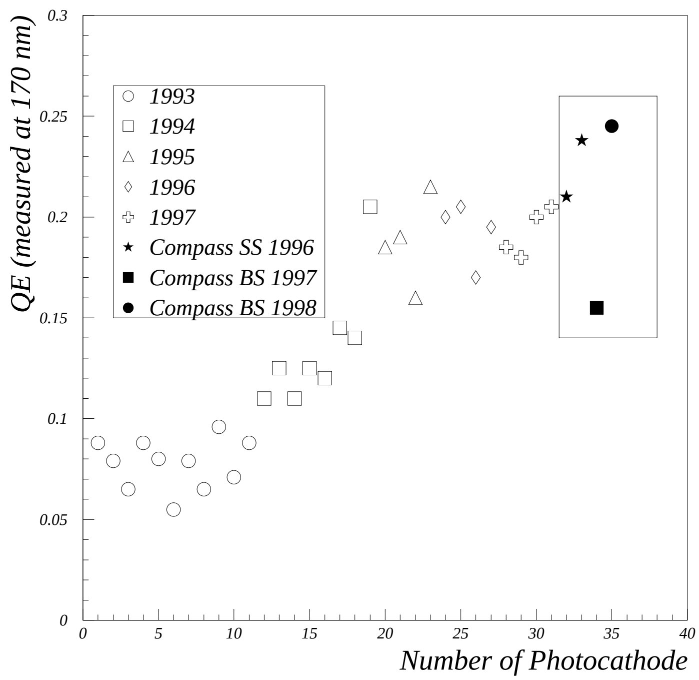

Figure 4.17: Measured Quantum Efficiency for the Big Surface (BS) and Small Surface (SS) CsI photocathodes deposited at CERN until 1998.

Detector performances

Starting in 1996, we have tested a small-size prototype of MWPC with CsI photocathode (20×20 cm^2), a full-size prototype and the first of the 8 final chambers. All the tested chambers are electrically very stable and exhibit dark current < 10 nA up to at least 200 V above the working HV value. Gas tightness is also good (O_2 level < 10 ppm fluxing the chambers at the rate of one volume per hour). The effective quantum efficiency of the 5 photocathodes has been measured in the RD26/ALICE set-up with proximity focusing geometry and 10 mm C_6F_{14} radiator, and it is similar to the values measured by RD26 and ALICE [32]: effective quantum efficiency [52] at 170 nm ranges between 0.16 and 0.24 (see fig. 4.17).

During the 2001 run, six out of eight photon detectors have shown electrical instabilities at the nominal voltage of 2000-2050 V. These instabilities were both rate and voltage

Figure 4.18: Tip induced discharge observed at the microscope

dependent. The behaviour was showing a stable chamber for some hours followed by a trip due to an over-current lasting for more than 0.1 s. Studies done using the power supply as a current source, showed that the discharge was self sustained even at the lower voltage (about 1400 V) given by the current limit, and only the decrease of the voltage below 1000 V was able to stop the phenomenon. After a discharge, it was not possible to raise the chamber at the nominal voltage; only after hours, or even one full day, the chamber was behaving like before. Since two photon detectors were working fine, the problem was not intrinsic of the technology used, but most likely connected with local defects, identified in small tips on the anode wire (they can increase locally the electric field and therefore the gain, resulting in a locally higher flux of ions towards the photo-cathode which can charge the photo-cathode and end in a Malter effect [53] induced discharge [54]; the memory effect is the result of the very large amount of charge generated during the discharge). Local defects of the anode wires have been hunted by reversing the chamber bias voltage. A detected discharge is shown in fig. 4.18; the tip is clearly visible, together with the feeble light generated. Defects like this were found on about 1/3 of the LUMA [55] wires [7], which have been replaced, resulting in a better electrostatic behaviour. The anodes of two photon detectors showing a very bad behavior under this test have been rewoven completely using 20μm gold-plated tungsten OSRAM SYLVANIA wires [56], where defects like the one shown in the figure were

[7] Gold-plated type 860 20μm tungsten wire, with $\sim 3\%$ of Rhenium(Re).

absent, at least in the long region observed at the microscope.

4.3.4 The read-out system

RICH-1 has 82944 channels of analogical read-out. The RICH-1 read-out system processes the signals coming from the pixels. These signals are amplified, filtered, digitized in 10 bits, and temporarily stored at every asynchronous trigger. Threshold subtraction is performed and, for all channels above threshold, the amplitude values, together with the channel identification, are packed into a data frame and transmitted to the global data acquisition (DAQ) system. The read-out system is also capable of measuring pedestal and noise of every single channel, and setting its corresponding threshold. Sparse sample events can be acquired, independently of the global DAQ system, for monitoring purposes. The experiment foresees an average asynchronous trigger rate of at most 100 kHz and a maximum expected pixel occupancy of 20%, which generates a data transmission rate of about 6.64 Gbytes/s (presently the maximum data rate from RICH experienced in the experiment is of the order of 0.4 Gbytes/s). In the following section, we describe the general architecture of the RICH-1 read-out system, and we give architectural details of the main boards as well as the functional description of them.

The General Architecture

The RICH-1 read-out system is based on 192 identical large front-end boards, called BORA [57]. These boards are plugged on the external side of the photocathodes and connected to the pixels of the detector. There are 24 BORAs per chamber and each BORA handles 432 analog channels. Each board is identified by setting an 8-bit dip switch, where three bits identify the chamber and the remaining five bits identify the BORA within the chamber. This identification corresponds to a precise geographical position in the RICH-1. The overall operation of BORA is controlled and supervised by a 32-bit DSP (ADSP-21065L [58]). The board also has an FPGA (VIRTEX XCV100 [59]) that acts as a parallel co-processor of the DSP. The DSP configures the FPGA at reset time, and can reconfigure it at any time. The BORA board communicates with the outside world through two optical fibers and through a dedicated DSP network. One optical fiber is used to receive event triggers, and the other one is used to transmit data to subsequent processing stages of the acquisition system. The DSP network provides a slow connection with a PC (the RICH Control PC) where a high level control application software runs. This application software allows reconfiguring the FPGA and reprogramming the DSP. Programs, commands and data are transmitted through the DSP network between a BORA and the RICH Control PC. The whole RICH-1 has eight DSP networks working in parallel, one for each chamber. The RICH Control PC has a dedicated multiprocessor board, called DOLINA, to handle these networks. DOLINA has 8 on- board DSPs. The 24 BORA DSPs of a chamber and 1 DOLINA DSP form each network. All BORAs are optoisolated from DOLINA through eight specific optoisolating boards, one for each DSP network, avoiding this way grounding interference between the PC and the detector. Figure 4.19 shows the general physical architecture of the read-out system. In the RICH-1 box the eight chambers are displayed, each of them with its 24 connections (one per BORA) to an optoisolator board. The optoisolator boards are close to their corresponding chambers in the experimental area, and they are connected to DOLINA completing the eight DSP networks. DOLINA also distributes synchronization signals to the BORAs, like start of run (SOR), end of run (EOR), start of burst (SOB) and end of burst (EOB).

Noise reduction

The noise calibrations for the 2001 COMPASS run have shown an average noise level (figure 4.20(a)) of 2.14 ADC channel (1 ch. $\sim$ 1000 ENC), a factor of two higher than the design value. A more detailed analysis has shown that a large contribution to this was coming from the pads in correspondence to the walls of the grid used to reinforce the photo-cathode PCB (figure 4.20(a), filled histogram). To solve this problem 18 new ground connections were introduced between each BORA board and the photo-cathode supporting frame. The noise level after the improved grounding is shown in figure 4.20(b).

4.3.5 The Data Analysis

The analysis of RICH-1 is based on the code RICHONE [60]. RICHONE is the pattern recognition and PID code for the RICH-1 detector, and the pattern recognition method used is based on a recipe for the Cherenkov angle reconstruction from literature [61]. The method assumes that the particle trajectory is known at the RICH entrance. The raw data are first reduced by a clustering procedure; then, in two consecutive steps, the ring recognition and then the PID, based on χ^2 or on Likelihood selection, known the particle

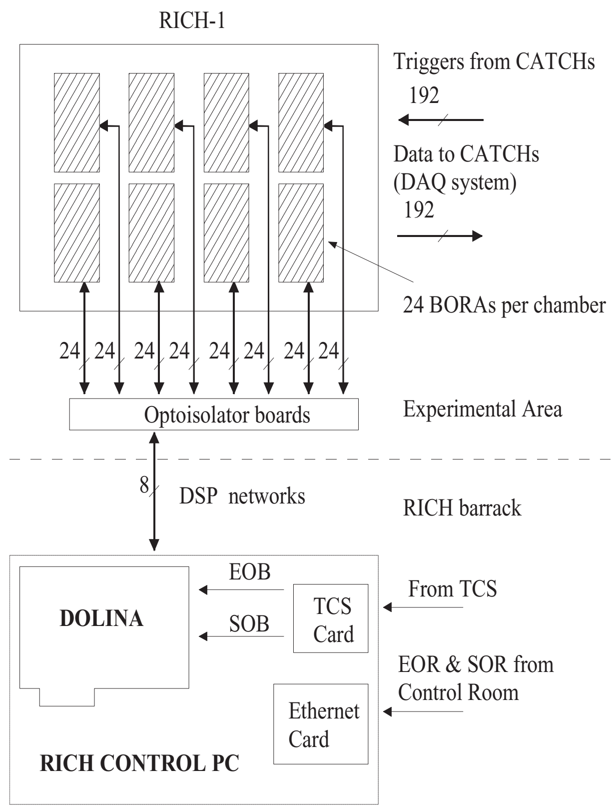

Figure 4.19: The RICH-1 read-out concept and its components.

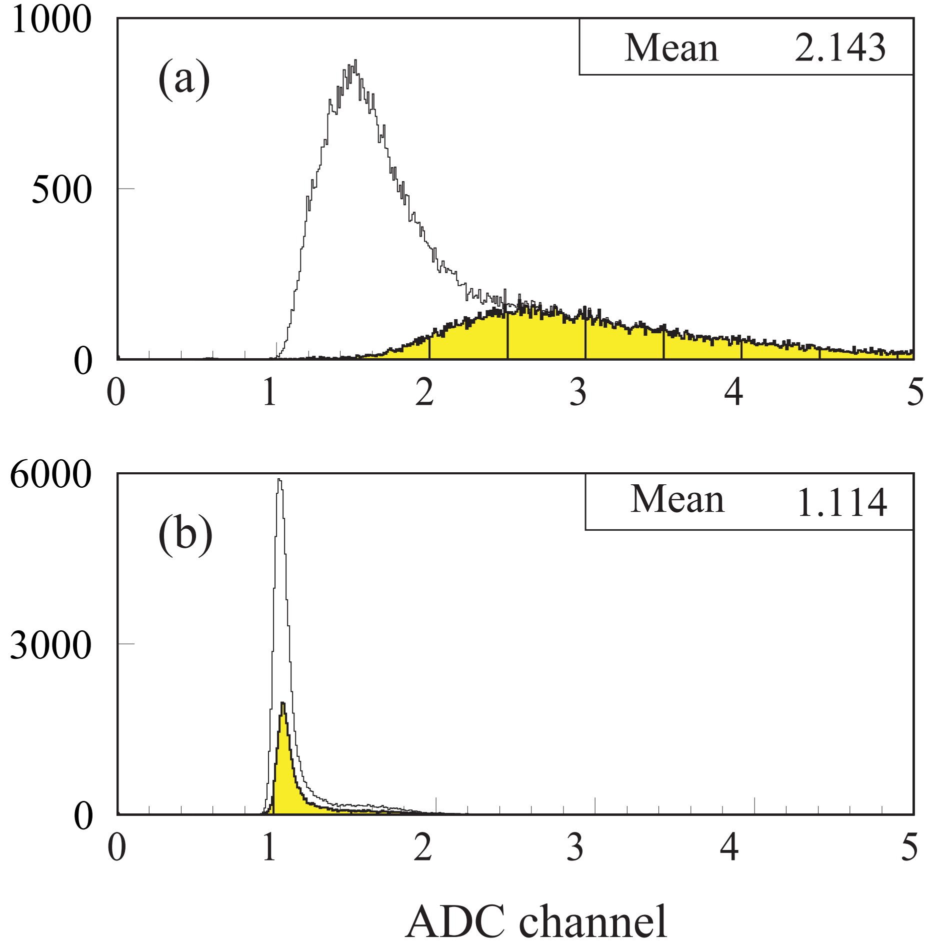

Figure 4.20: Noise gain due to improved grounding: (a) Sigma of all the channels for the 2001 run; (b) same for 2002.

momentum, are performed. The whole code has been developed and optimised with Monte Carlo data.

Preliminary information are presented. First of all rings where clearly visible in the online display of the experiment; figure 4.21(top) shows a nice multi-ring event, while a blowup of one ring is shown in figure 4.21(bottom). The bias voltage of the photon detectors is 2050 V for these images.

The upper plot in fig. 4.22 shows the distribution of the difference between the measured angles Θ_{photon} (on the reconstructed *ring*) and their *ring* average value (Θ_{ring}) (mrad), after a best-fit to a circle; the standard deviation σ is 1.37 mrad; to be compared with the proposal expectation of 0.78 mrad. The discrepancy can be well accounted by the fact that the RICH geometry (mirrors and photon detectors) has not yet been calibrated. The lower plot in fig. 4.22 shows the distribution of the number of photons per reconstructed *ring* (after clusterization); this number is in reasonable agreement with the expected one, taking into account the reduced fraction ($\sim$ 80%) of C_4F_{10}, the RICH-1 design radiator gas, present in the RICH vessel and the lower efficiency of the photon detectors. Figure 4.23 shows the distribution of the reconstructed Θ_{ring}, together with the estimated background (top) and the signal after background subtraction (bottom).

Figure 4.24 is an example of the monitoring of the refractive index of the radiator gas, a parameter which has to be extracted from data.

The particle mass distribution as reconstructed from the measured Cherenkov angle and the particle momentum is shown in fig. 4.25; the amount of background, in particular under the kaon peak is still relevant, but all the analysis is very preliminary; note that the mass values are correctly reconstructed. The nice separation among pions, kaons, and protons is also visible in the two-dimensional plot of particle momentum versus measured θ_C (fig. 4.26, low intensity data).

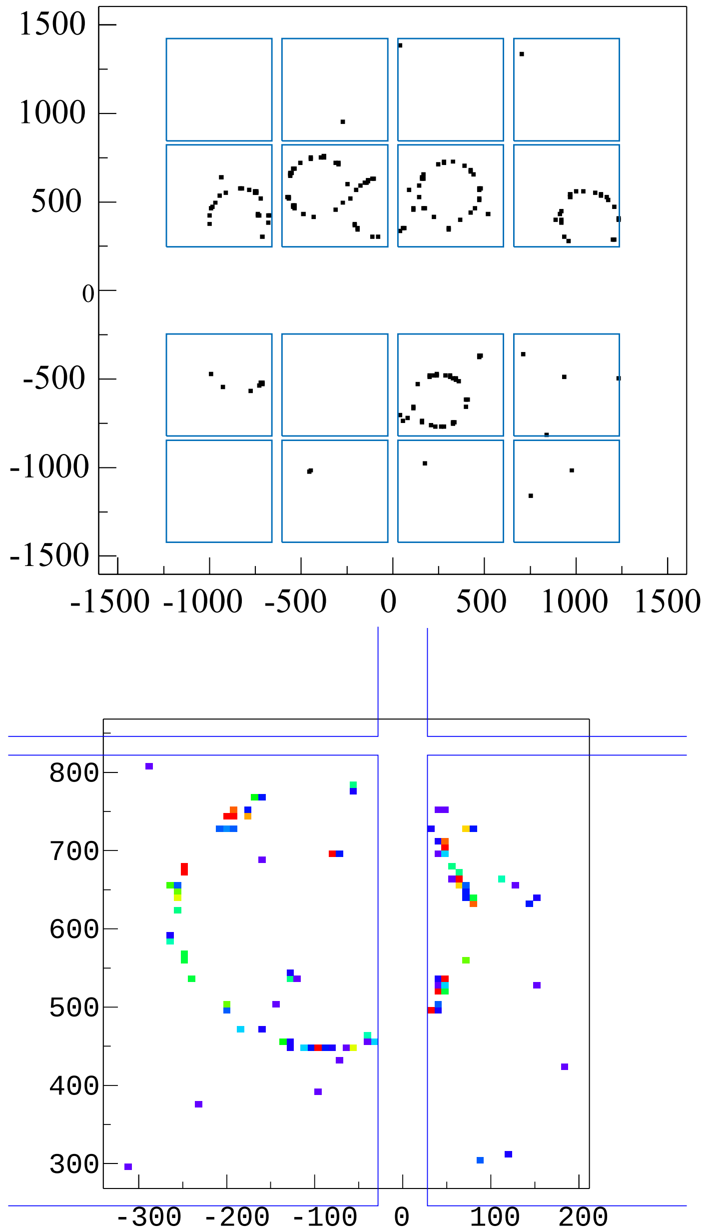

Figure 4.21: (top) On line display of one event: the boxes correspond to the frames of the 16 photo-cathodes. (bottom) On line display of one ring of a mip shared between two photon detectors (blue lines).

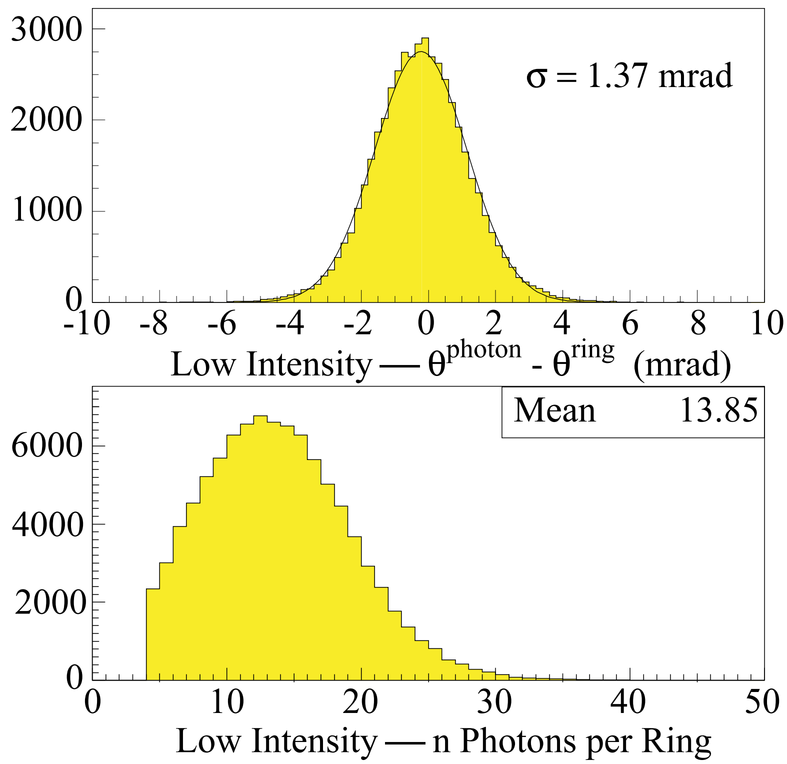

Figure 4.22: The upper plot shows the photon Cherenkov angle accuracy for photons belonging to reconstructed *rings*. The lower plot shows the distribution of the number of photons per reconstructed *ring* (after clusterization).

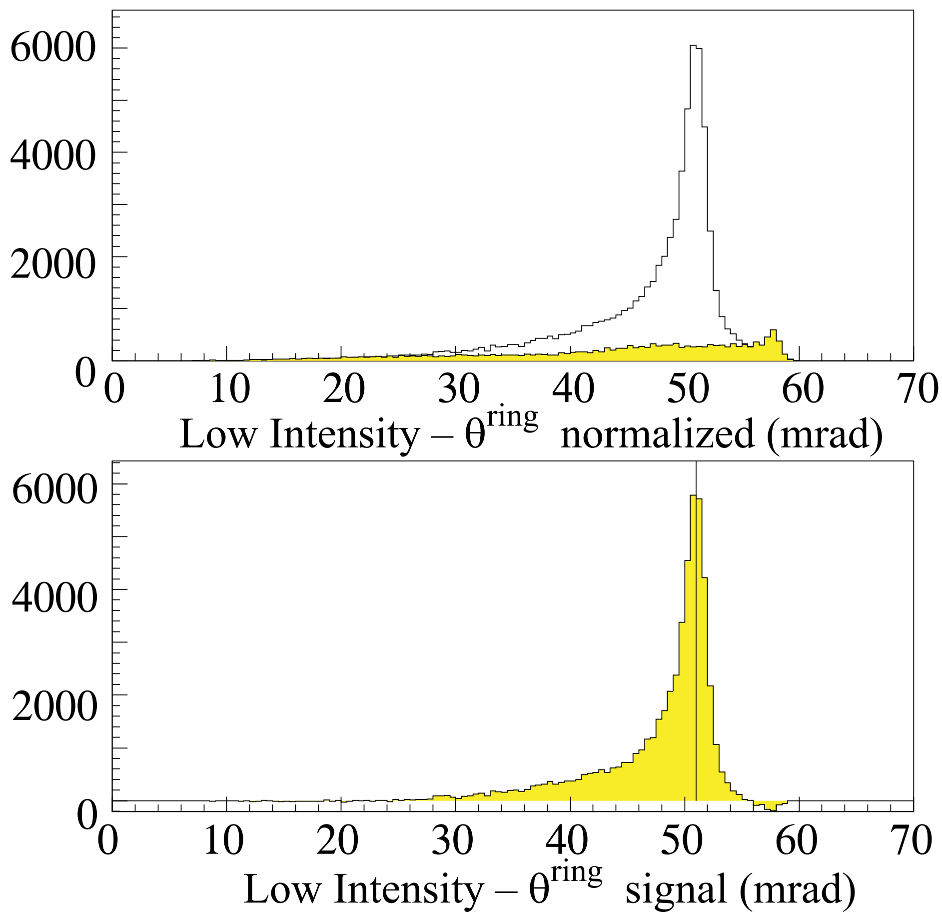

Figure 4.23: The plots show the distribution of the Θ_{ring} for the reconstructed *rings*; in the upper plot, Θ_{ring} and normalized background distributions are presented; in the lower one, the signal distribution after background subtraction is given. In both plots, no particle momentum selection is applied.

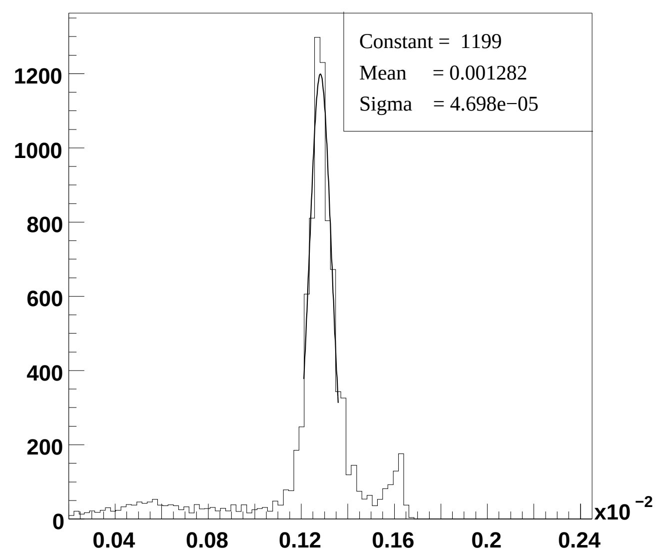

Figure 4.24: Example of monitoring of the refractive index (n-1) of the radiator gas using high momentum particles at large angles.

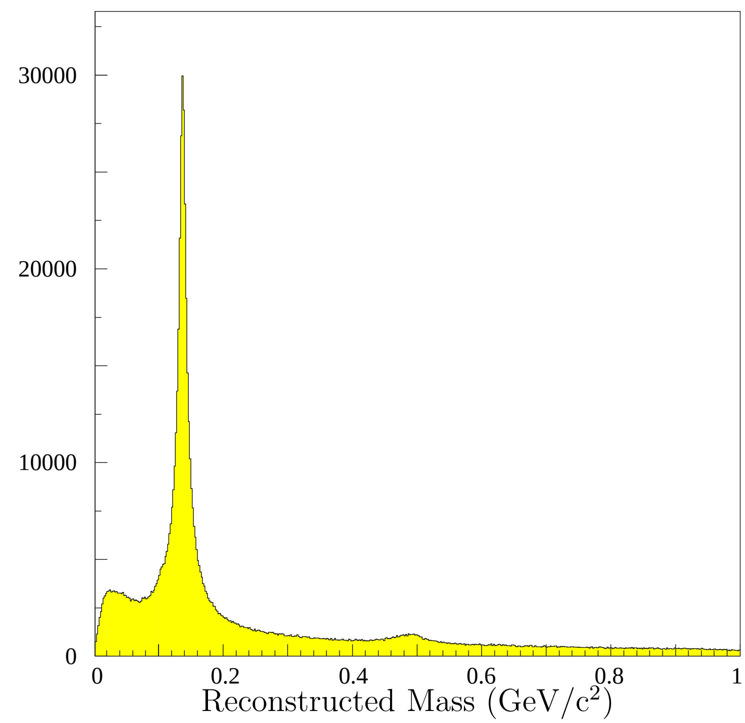

Figure 4.25: The particle mass spectrum computed from the measured Cherenkov angle and the particle momentum; in the upper part, the total spectrum; in the lower, the K mass region enhanced.

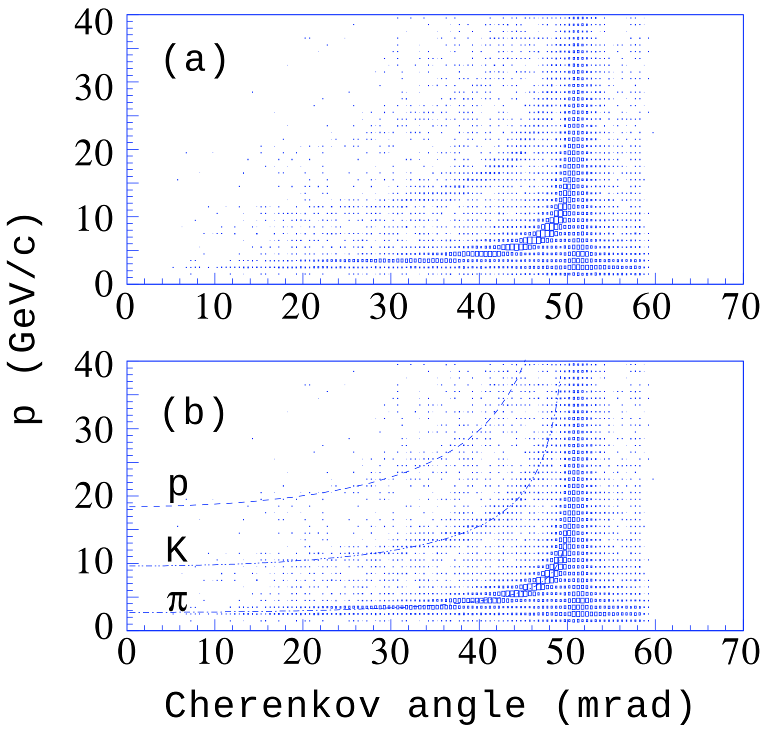

Figure 4.26: (a) Distribution of the particle momentum versus the reconstructed ring Cherenkov angle. (b) Same than a but with the kinematical curves corresponding to π, K and p masses superimposed for comparison.

Chapter 5

The data handling in COMPASS

5.1 The Compass data structure organization

5.1.1 The COMPASS DataBase (DB)

COMPASS uses an Object Database Management System (ODBMS) to define the final off-line format of the data, and to store and access them. The commercial product Objectivity/DB has been used to provide the data base functionality, while the data management of disk and tape resident data is provided by CASTOR, a storage manager system developed at CERN.

5.1.2 Objectivity/DB

Objectivity/DB is an object oriented data base system, which conforms to the guidelines of the ODMG group (`http://www.odmg.org`): the main idea is to allow object-oriented languages (like C++) to store/retrieve objects from a data base as opposed to the standard approach originally used in the relational data base world, where the quantities to be stored were sets of values without an associated structure.

The main features of Objectivity/DB used in COMPASS are [62]:

- The quantities which can be entered in the data bases are "objects" and not set of scalar quantities like in a relational data base. This means that the objects handled by the reconstruction and analysis program (CORAL, see section 5.2) program can eventually become persistent (i.e. stored in a data base) at any time. The syntax to manipulate these objects is the C++ one. In the relational data base, on the contrary, operations like preparing the data to be stored, and the data retrieving are done by a specific language (SQL) different from the one used in the reconstruction libraries.

- The system was selected by CERN as working prototype to store data for the LHC experiments. It can on paper address many PetaBytes (10^{15} Bytes) of data and effectively multi TeraBytes (10^{12} Bytes) data sets (over 260 TB during 2002 COMPASS data taking).

- The storage of multi TB data sets cannot be efficiently done on a single file system. Since a single machine cannot nowadays have such a large installed disk set, and ordinary network filesystem like AFS (Andrew File System, by Transarc) and NFS (Network File System, by Sun) are limited in performance, a distributed data storage is needed. Objectivity/DB provides a network layer to access data across the network; this access is done by separating the physical location of the data bases (host machine and file name) and their logical identifier. Applications deal only with the latter, allowing the physical files to be moved anytime.

The insertion of new objects into Objectivity/DB follows these steps:

- The object eligible to be stored should inherit (in the C++ sense) from "the" persistent object provided by the Objectivity/DB package, called ooObj.

- Once a new class is detected, a "schema" is generated, which is the layout of the class object in memory, to allow to write and read events on disk.

- Every persistent object in the program behaves as a normal object. The only action is in the object construction (in the C++ sense, via an overloaded new operator), to choose in which data base section it will eventually be stored. After that the persistent object behaves like a normal object and the Objectivity/DB infrastructure will make it persistent at a given time (normally at the end of the program execution, in the COMPASS scheme).

The COMPASS implementation, since it handles with the Objectivity/DB only via interfaces, hides completely these details and all the Objectivity/DB from the normal users and developers of other components.

This allowed CORAL from the very beginning to access data in DATE (file based) and Objectivity/DB (data base) format transparently (via run-time options). In recent times, an interface to the future store based on Oracle 9i has been provided along the lines of the previous implementation.

5.1.3 CASTOR

Theoretically, the Objectivity/DB storage can be a standalone system, taking care of both internal organisation of the data and physical location of the data bases. In reality, the available disk space is much smaller than the total amount of data (for economical reasons). Therefore a system to take into advantage the availability of tape storage (typically 1/10 less expensive than the disk space) is needed.

The most elegant solution is provided by CASTOR (CERN Advanced STORage system), developed at CERN. CASTOR is a Hierarchical Storage Manager (HSM): this means that it is a system which provides the following features:

- All files are seen in a file system structure for adressability by name (the user refers to a file as /castor/cern.ch/userlambda/storage/data.dat)
- Standard replacements for open/write/read/close functions are provided to the user, conforming to the POSIX standard.
- A file instance can exist in two forms: disk and tape.
  - When a file is in use, a disk image in a service disk pool is used;
  - When a new file is created or modified, the disk instance is asynchronously copied to tape without preventing successive reading;
  - Since the disk pool is not infinite, files with a valid instance on tape, might be removed from the pool by the system to allow other files to be created or retrieved from tape;
  - To access existing files, the system checks for the presence of a valid disk instance. If this is not the case, a disk instance is created by copying the tape instance while keeping the client (for a example a reading program). In either case, the client will only read/write disk files.

The only difference with the normal disk access is therefore the latency of the time for the tape reload.

The Objectivity/DB network layer uses these features. This has been made possible by developing (at CERN) a modified version of the network server of Objectivity/DB. In practice, these servers have been interfaced to the CASTOR library, in a way that the data base clients do not need to be changed: it is the backend of the network server that deals with all the complications of the tape access described above, delegating CASTOR to store/retrieve data in the tape system.

5.1.4 Central Data Recording

COMPASS decided from the beginning to implement the scheme of the Central Data Recording (CDR): the CDR idea is to avoid to write the data on tape at the experiment and transfer the tapes physically to an off-line computer centre. The data transfer is done via network directly to the computer centre, to be written to tape with the same infrastructure needed for off-line analysis (see figure 5.1).

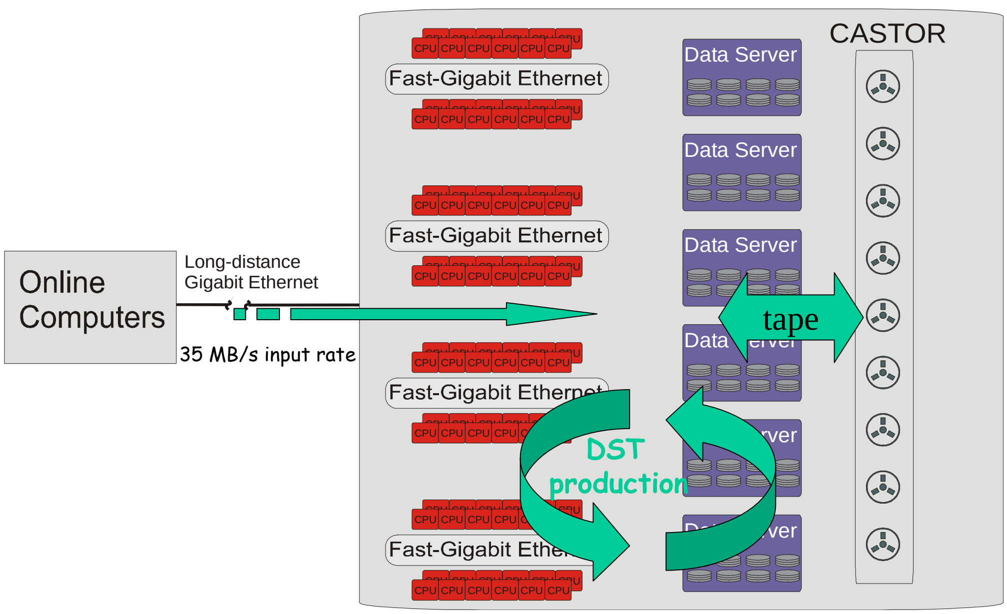

Figure 5.1: The data transfer from building 888 to the CCF via the Central Data Recording (CDR).

This is one of the main goal of the COMPASS Computing Farm (CCF), in particular of the machines called data servers (PC with typically 500 GB disk space each; in 2002, 20 of these machines were operational).

Once a run (typically 30 minutes) is finished, all the files are closed and marked for transfer. The CDR system detects these files (typically 100 files, known as chunks, for a total of about 100 GB) and transfer them to the CCF via the RFIO protocol (the standard at CERN for network data transfer). Successfully transferred files are marked as deletable and they will be deleted (in chronological order) when disk space is needed. Aborted transfers are restarted automatically.

At the receiving end (from the CCF data servers), new data are processed as soon as the transfer is finished and put in the data base and then registered into the CASTOR name space. From this moment onwards, CASTOR has full control on the files (Data base files). From this moment the data are visible (and already on disk) for possible reuse.

All these operations are basically performed in parallel from all event builder (12 in run 2002) and on the 20 CCF data servers.

The main principle is that the two stages are basically asynchronous and with no feedback, to avoid heavy operations like each machine contacting all the others to be able to perform the next step or take any action. The main exception is the monitor system which collects info from all CCF servers (CPU load and disk status) and answers to the event builder daemon to distribute the load and choose the disk with the most free space.

5.1.5 The data in the Objectivity/DB structure

When a data file (in DATE format) is entered in the data base, two objects are created from each event:

1. the RAW event buffer is encapsulated in a object and stored;
2. a header object is created to hold some minimal information (event number, trigger mask (see section 7.4) and alike) plus a data base "pointer" to the corresponding event.

The data base system allows also to check the presence of the data on disk or on tape before actually accessing it (mixing the functionalities of Objectivity/DB to identify the file and of CASTOR to query its status). The headers data bases sit permanently on disk, whilst the data have the tape system as primary repository (see figure 5.2).

On top of this hierarchy sits the run data base, which holds few critical information for each run and other data bases, keeping special events (the data acquisition produces a few

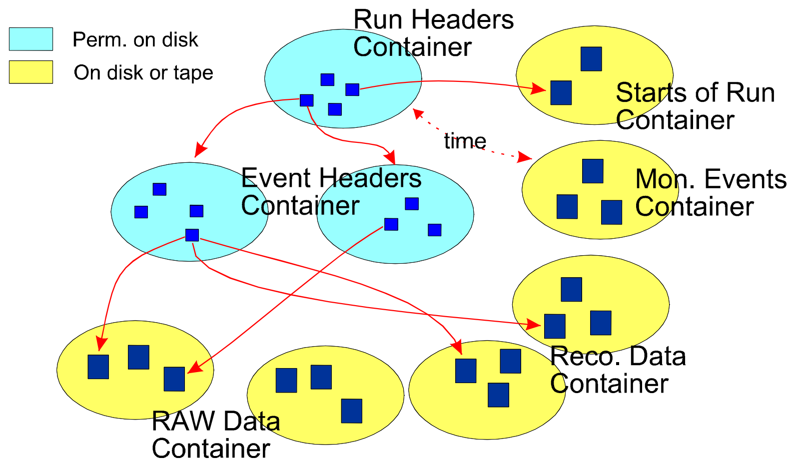

Figure 5.2: The various components of the data structure handled by Objectivity/DB.

events a run to hold general information like data acquisition configuration).

The whole data taking period is divided into slices less than 2 weeks long: for each of these periods, a DataBase Federation is built up. All the Runs objects belonging to the same time slice are handled by the same Federation. The naming scheme, discussed in detail in chapter 7 reproduces the SPS activity periods.

5.2 CORAL

The COmpass Reconstruction and AnaLysis project (CORAL) is an Object-Oriented (OO) software organized in a set of C++ class libraries implementing all the tools needed to reconstruct and analyze the COMPASS data.

The same name is used to refer to the data reconstruction program.

5.2.1 Why Object-Oriented (OO) programming

G.Booch stated [63]:

"In object-oriented analysis and design one should model software systems as collections of cooperating objects, treating individual objects as instances of a class within a hierarchy

of classes".

Compared to more traditional approaches (splitting the program execution in a series of actions namely subroutines)[1], the OO programming paradigm looks more abstract and moves the complexity of the development to the first step i.e. the definition of classes and relations: each of these classes is responsible of its behaviour *vis à vis* the other entities. A complex data structure can evolve by keeping constant its interfaces and letting the classes' internal structure to change (encapsulation).

These characteristics strongly enhance the maintainability of elaborated software, in particular when developed by many authors (as in the case of COMPASS collaboration). This methodology becomes convenient when the complexity of software increases, whereas the traditional approaches are preferable for less complicated problems.

The COMPASS collaboration needed to move to this complex programming methodology because the software requirements has crossed the line where object-oriented becomes convenient.

5.2.2 Why to use C++

The most wide-spread programming languages whose mechanisms support the object-oriented programming style are C++ and Java[2]. One of the main reasons of the C++ success is its backward compatibility with the C language, the most used language in the past: for instance, many operative systems, like UNIX and Windows 2000, are written using C. This also means that, all available C written libraries can be easily used within a C++ program and, above all, C codes can be directly used or smoothly converted to C++ codes.

COMPASS adopted C++ and, more generally speaking, the whole off-line environment following the CERN IT division suggestions and projects. At the time of the proposal, ANAPHE (formerly called LHC++) project started. Its aim is the replacement of the CERNLIB software libraries, including PAW and HBOOK. It will provide all the generic functionality which experimental high energy physicists require to build their software tools, store and analyse their data, for the LHC era and beyond.

[1] These techniques, also known as "top-down" or "structured", have been used from the dawn of the High Energy Physics experiments until LEP era and only recently some collaborations (e.g. BaBar at SLAC, CDF at Fermi Lab and the new (and forthcoming) CERN experiments) have moved to OO.

[2] Java is a pure object oriented programming language, in the sense that it does not allow different programming techniques. Being newer than C++, it has taken experience from the latter's limitations allowing a more clean object-oriented implementation of software.

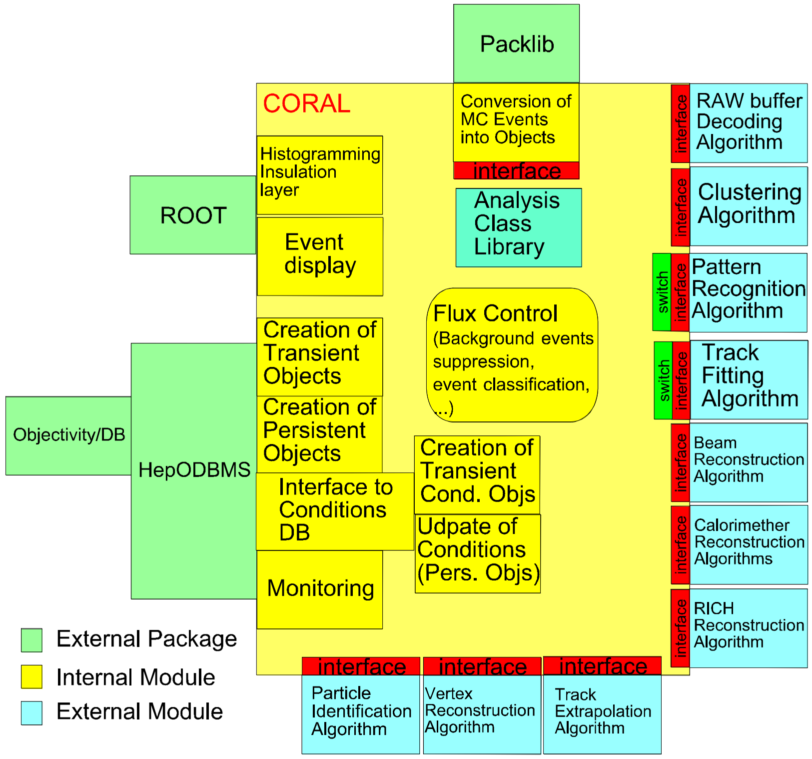

Figure 5.3: The CORAL's architecture.

Since CORAL makes use of part of this analysis environment, COMPASS has been chosen to be a "pilot experiment" driving CERN to LHC era. The result is that today we have an OO working software written in C++ which results modular (in the sense that some packages and performances can be easily enabled or disabled following the user's necessities) and flexible as it can reconstruct the data not being dependent on the way they are stored.

5.2.3 The CORAL architecture

The CORAL's architecture is shown in figure 5.3 where the core (in yellow) is interfaced to independent, selectable modules (in cyan) and to external libraries and services (in green).

Because of its OO and multipurpose nature, it's difficult to draw a flow chart for CORAL. Anyhow, in picture 5.4, the usual operations performed by CORAL to reconstruct the events are shown.

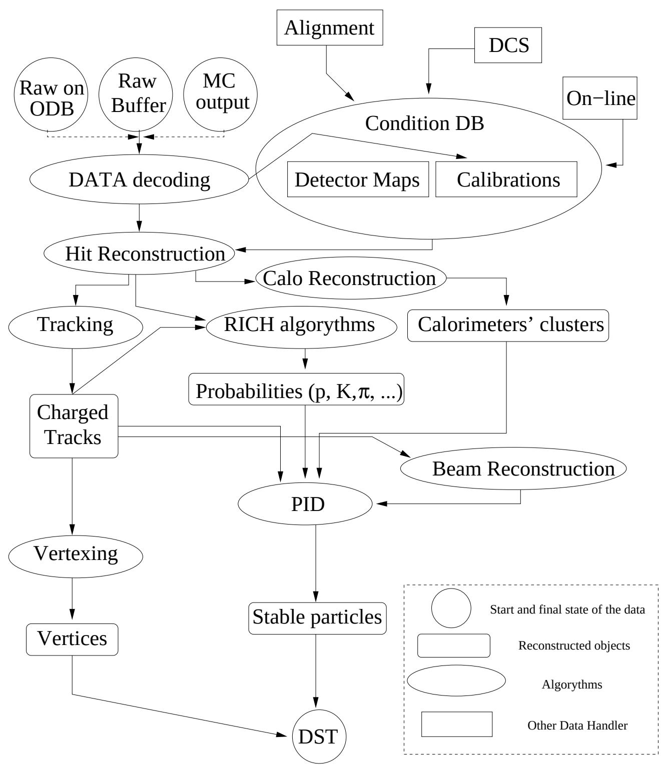

Figure 5.4: The CORAL's flow-chart.

The starting point (on the top-left) is the Data Raw Buffer collected and stored during run-time. This is decoded making use of mapping, calibration and the alignment table[3] information handled by the Condition Data Base and previously generated by dedicated tasks.

Once the data stream is interpreted, the hits belonging to different kind of detectors (trackers, RICH and calorimeters) are reconstructed and can be used by:

- the Tracking package to sort out the aligned clusters and build up the tracks;
- the RICH ring reconstruction package to associate a probability to each charged track;
- the Calorimetry reconstruction package to build up the calorimeters' clusters.

These tasks are performed by external packages which can be enabled or disabled in CORAL. The user can select to reconstruct the events making use of one package instead of another. A brief description of the packages available in CORAL at the time being is reported in 5.2.4.

Once the packages have reconstructed the event, the PID algorithm just makes use of the available information to generate a new class of "tagged" states, the stable particles produced in the event.

The tracks are used by the Vertex package which looks for the interaction's space-points and generates the vertices.

Particles and vertices are the most relevant objects stored into the DST, old and misleading acronym for Data Summary Tape which corresponds to the compact and meaningful (physical) information which can be extracted from the Data Raw Buffer.

This procedure (discussed in section 5.3) directly accesses the ODBMS creating a new Data Base made up by the CORAL persistent objects.

In the Objectivity/DB format adopted for COMPASS, up to 3 different DSTs can be related to the same run: for example there is the possibility to make 2 DST productions and compare them event by event.

The association are stored into the run header (see figure 5.5) and the reader can select the DST to load via the logical parameter known as slot number.

[3] The alignment table reports the position and the orientation w.r.t. the COMPASS reference frame of each detector (tracking stations, RICH, calorimeters) and its components (modules, submodules, calorimeter cells, RICH mirrors, etc.).

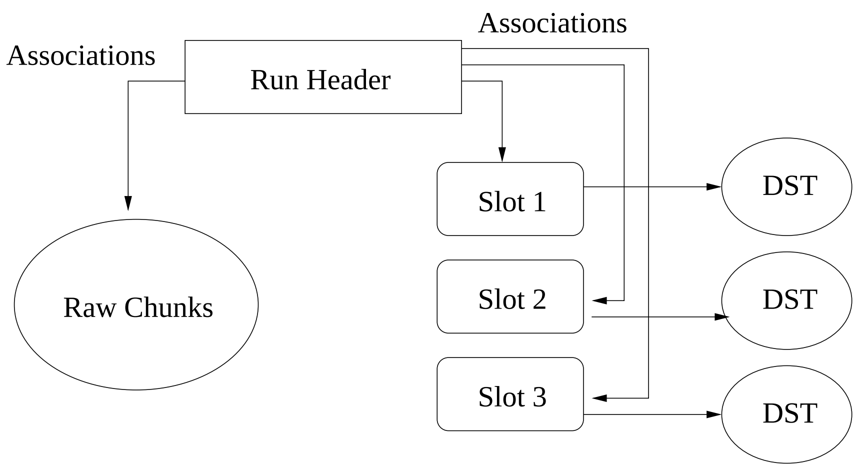

Figure 5.5: The shape of the logical association in the Objectivity/DB run header.

5.2.4 The external packages used in CORAL

Tracking

The default package [17] for the track reconstruction is called TRAFFIC (TRAck Finding and Fitting in COMPASS). For the purpose of tracking the spectrometer is divided into zones, in which the tracks are assumed to be straight: this is a very approximate assumption especially for the large angle tracks selected in the first spectrometer, due to their low momenta and to the high fringe field of SM1.

The track reconstruction is generally divided into three steps called pre-pattern, bridging and fitting. During the pre-pattern step straight track segments are searched separately for each zone and separately for each available projection. The candidates from the various projections are then combined to fit the ones consistent in all projections, again this is done separately for all zones. This procedure suppresses the so-called ghost tracks, which arise from wrong combinations. During the bridging step track pieces from different zones are combined taking into account magnetic fields or multiple scattering e.g. in the Muon Filter. Finally in the third step the global fit to the actual hit positions takes place yielding the track parameters.

Apart from the TRAFFIC package there are two other packages using slightly different approaches.

One of them is TRAFDIC, which is a TRAFFIC derivative. The main difference with

TRAFFIC lies in the bridging step. In this step TRAFFIC extrapolates track candidates from one zone through a magnetic field and checks for matching tracks in the neighbouring zone. TRAFDIC uses a dictionary of possible hit combinations on both sides of the field, obtained from Monte Carlo simulations. It also has a slightly modified pre-pattern step, using an iterative approach. During the first iteration TRAFDIC looks for matching hits applying strict cuts. In a second iteration on the remaining sample of hits a pre-pattern step with less strictly applied cuts is performed.

The third tracking approach is implemented in the RECON package. It has been especially tailored to the large angle spectrometer, which is of great importance for the detection of decay products from charmed mesons (e.g. the slow pion in D^* decay) and therefore for the gluon polarisation measurement. In this part of the spectrometer the fringe field of the SM1 plays an important role and ignoring it by assuming straight track segments introduces a bias against low momentum tracks and RECON tries to avoid this bias by an iterative procedure. From one iteration to the next the cuts selecting the hits are relaxed and also different subsets of detector planes are used, only in the final iterations the full setup of the first spectrometer stage is used. In this way the more straight tracks are found first and later on with looser cuts the tracks with larger curvature. The fine tuning is still on going using the data collected in year 2002.

Comparing the performances of the three packages, the COMPASS off-line group has selected TRAFDIC for the 2002 DST pre-production[4] which started in August.

PID

The key objects, built up from the bridged tracks, are commonly known in CORAL as "helices". These objects have a defined (vector) momentum and an electric charge. A dedicated routine, taking into account the magnetic fields present along the spectrometer, can extrapolate the helix to any point in the spectrometer.

Once a helix is built up by the tracking package, CORAL uses the PID algorithms (beam identification, muon identification, hadron identification) to associate this object to a "particle". This particle can be SPECIAL (in case it has passed beam or muon identification) or ORDINARY (in all the other cases). To the charged particles CORAL associates the

[4] The term pre-production is here used to distinguish the DSTs analyzed after the 2002 DAQ from those the Collaboration is going to officially release in the beginning of next year.

calorimeter cells closest to their direction. If there are calorimeter cells which can't be associated to any helix, new (neutral) particles are created. To the charged particle is associated a probability (if any) coming from the RICH package to be identified as a known particle.

The results obtained by the RICH software package have been already described in section 4.3.5. Let's only remind [64] that the reconstruction line can be divided into two steps :

the recognition of a "ring", associated to a measured particle trajectory, via the selection of the Cherenkov emission angle θ_C starting from the track parameters;
To this purpose the trajectories of the particles which enter the RICH are expected to be measured with good accuracy; in particular the position and the direction of the particle trajectory at (or extrapolated to) the RICH entrance window and the position of the particle trajectory at (or extrapolated to) the exit window are needed.
To reconstruct the "ring" the active pad positions on the RICH photon chambers are used, together with the pad Pulse Heights (PH); a clustering procedure is used to better estimate the photon impact points;

the identification of the mass m of the particle for which a *ring* has been reconstructed. To this purpose the particle momentum p has to be well measured.

Vertex reconstruction

The purpose of the vertex package is the reconstruction of the primary and the secondary interaction points. This is generally done in two steps. The first step is to give a first estimate of the vertex coordinates and a set of tracks assumed to originate from that vertex. This pre-filtering is done by selecting track candidates according to geometrical and kinematical criteria. The average point of closest approach then serves as estimate for the vertex position. In the second step the method of the inverse Kalman filter is used, where all the track candidates obtained from the prefilter are included in a global fit. After this step some individual tracks can be excluded if their contribution to the total χ^2 exceeds a certain value. After each step the global fit is repeated. The output of the vertex procedure are the vertex coordinates, the total χ^2 and the fitted parameters (with their full covariance matrix) of the tracks associated to the vertex.

Period	Processed Runs
P2B: 31/7/2002 $\longrightarrow$ 6/8/2002	114
P2C: 8/8/2002 $\longrightarrow$ 12/8/2002	102

Table 5.1: The two periods processed by CORAL during autumn 2002.

5.3 The DST production

As it has been already stated in section 5.2, the CORAL program has been written with the final aim of being a DST/builder. The DSTs are the hearth of any analysis which requires high statistics collection as in case of COMPASS.

For the data collected in year 2001, no mass production has been done. About 10% of the data collected has been processed in order to make tests and dedicated studies on the spectrometer. Chapter 6 will deal with the analysis of these data.

In this context, a detailed description of the DST production done upon the data collected in year 2002 is reported. I have personally been involved in the processing of the runs collected in transverse polarized target configuration.

The work has been devoted to about 220 good runs collected in transverse mode for a total DAQ elapsed time of about 11 days (see table 5.1). The selection of "good runs" have been done by the help of the on-line database (mySQL) which saves some relevant information related to each run such as:

the title (physics, detector studies, DAQ test, etc.);

the number of recorded spills;

the sign of the polarization in each cell of the target;

the electrical current in the magnets;

the on-line monitoring detectors' histograms.

The DSTs have been produced only for the "good runs" collected with physics trigger. These runs are featured by:

- a reasonably big number of spills;

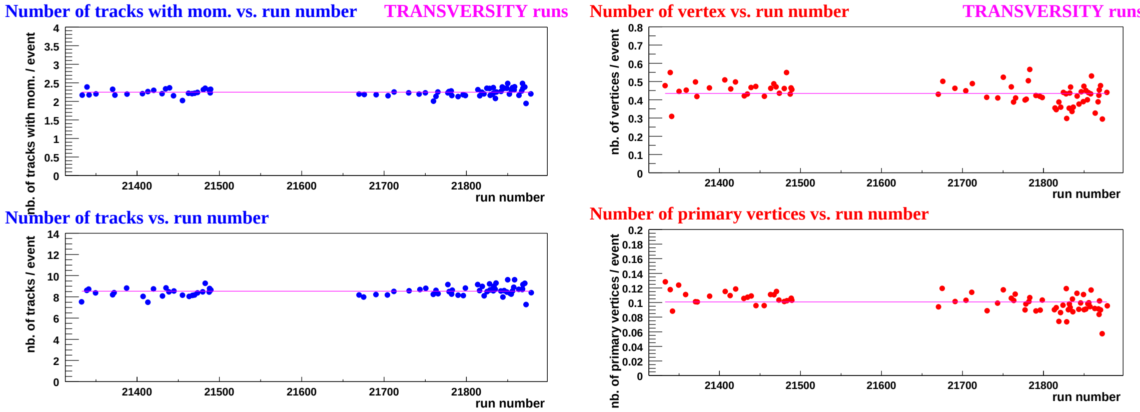

Figure 5.6: The stability check for P2B and P2C federations to find out the good runs. The mean nuber of tracks w/ and w/o momentum, the mean number of vertices and mean number of primary vertices are plotted as function of the run number.

- a correct timing information from BMS (see section 3.3.1);
- stable distributions in the number of vertices and tracks (see figure 5.6 [65]).

5.3.1 The production procedure

For the DST production, one makes use of an auto-consistent frozen CORAL world made of:

- a set of calibration and decoding maps;
- the alignment file (detectors.dat) optimized for the period to be processed.
- a statically compiled CORAL executable.

Run by run, the procedure consists in:

- asking the DB Federation the list of (N) chunks the run consists of;
- creating N new DataBases associated 1 by 1 to the raw chunks;
- storing into the Run header the list of detectors used in production.

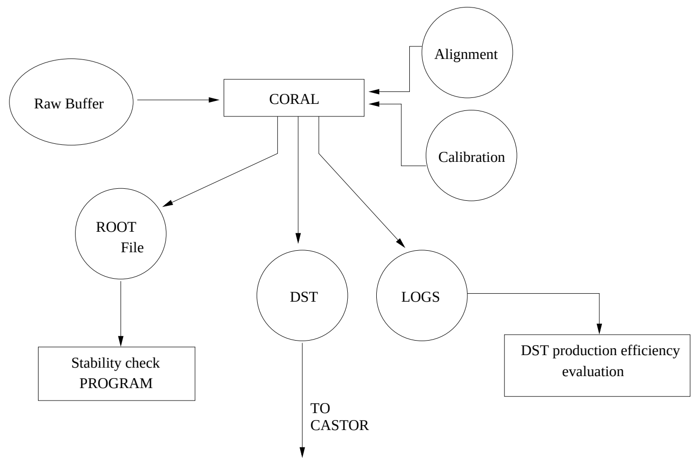

Figure 5.7: The conceptual scheme of a production job.

One by one, N independent jobs are sent to the Loading Sharing Facility (LSF)[5]: in these jobs, CORAL fills the new DST DataBases created so far. To monitor the production, the batch job, in addition to the new DST stored in the Federation, produces (see figure 5.7):

- a log file containing all the messages printed by the Objectivity/DB, LSF (unfound libraries, failure reports, etc.), CORAL (exceptions, skipped events), the End of Job statistics printed at the end of the production by the various packages (tracking, vertex reconstruction, RICH) running in the CORAL session;

- a set of standard monitoring histograms (contained in a ROOT file) from which the performances of the apparatus and the "hardware" changes in the experimental set-up (displacement of detectors and/or beam direction, fall down of detection efficiency in some planes, etc.) can be checked. An example of stability checks based on this output will be shown in chapters 6 and 7.

Since the DST production procedure makes use of many informatics' tools and services[6], its success is affected by their inefficiencies. In "plateau" conditions these inefficiencies lead to about 5% of failures.

[5]Distributed by Platform Computing Corporation (PCC).

[6]We list just three, the most relevant, of these external contacts: LSF, the Objectivity/DB's Lock and AMS servers and CASTOR.

An automatic procedure identifies all the warnings, exceptions, failures and fatal errors from the log files and fills a DST production job summary. Since the failures are mostly related to momentary failures of some services, the failed chunks can be anyhow reprocessed. In figure 5.8 the number of jobs and the CPU consumption as function of the time show how the activity of COMPASS in the DST pre-production has reached the same order of magnitude of recent ATLAS and CMS MC mass production.

The final behaviour of the production efficiency is shown in figure 5.9 and summarized in table 5.2.

Period	Total	♯RUN	♯RUN	♯RUN	♯RUN	♯RUN
		100% chunks good	90% -99% chunks good	70% -89% chunks good	50% -69% chunks good	$\leq$ 50% chunks good
P2B	116	65	35	7	3	6
P2C	101	35	52	8	4	2

Table 5.2: Summary of the DST production efficiency for periods P2B and P2C.

5.3.2 The DST size and content

A COMPASS Run is made of about 90-100 chunks, for a total amount of more than 2 M events. The DSTs are smaller than the corresponding raw because of the reduction of information to store.

Presently, this size is about 6% of the corresponding raw (1.2 GB $\longrightarrow$ 70 MB). Shorter the size, more disk space is saved, shorter is the retrieving of the DSTs from CASTOR and faster is the analysis: all the time consuming operations (decoding, tracking and vertex reconstruction) are not repeated in reading mode. As a net result the mean value spent by CORAL to reconstruct an event passes from about 0.7 s to 0.002 s.

Anyhow the physics analysis is based on the information available in the DSTs, therefore one has to compromize between these two conflicting requirements, reducing the data size and keeping the essential information.

In table 5.3 it's reported the list of the variables available in the version "3" of COMPASS DSTs. Actually, the COMPASS mass production, previewed for Febraury 2003, will use the new version "4" containing more information such as the incident beam flux, the covariant matrix of the vertices, etc.

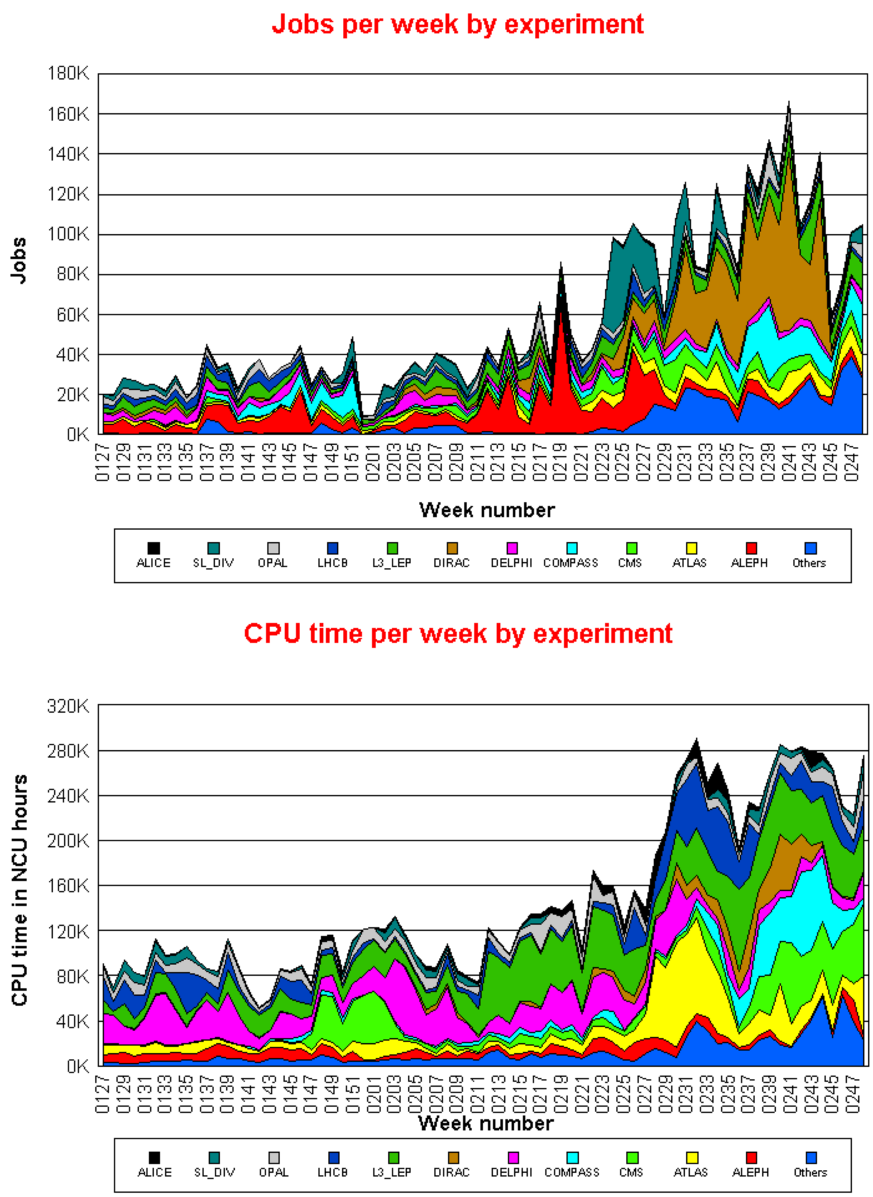

Figure 5.8: The amount of jobs and the CPU consumption for the various experiment along the 72 weeks before December 6^{th} 2002.

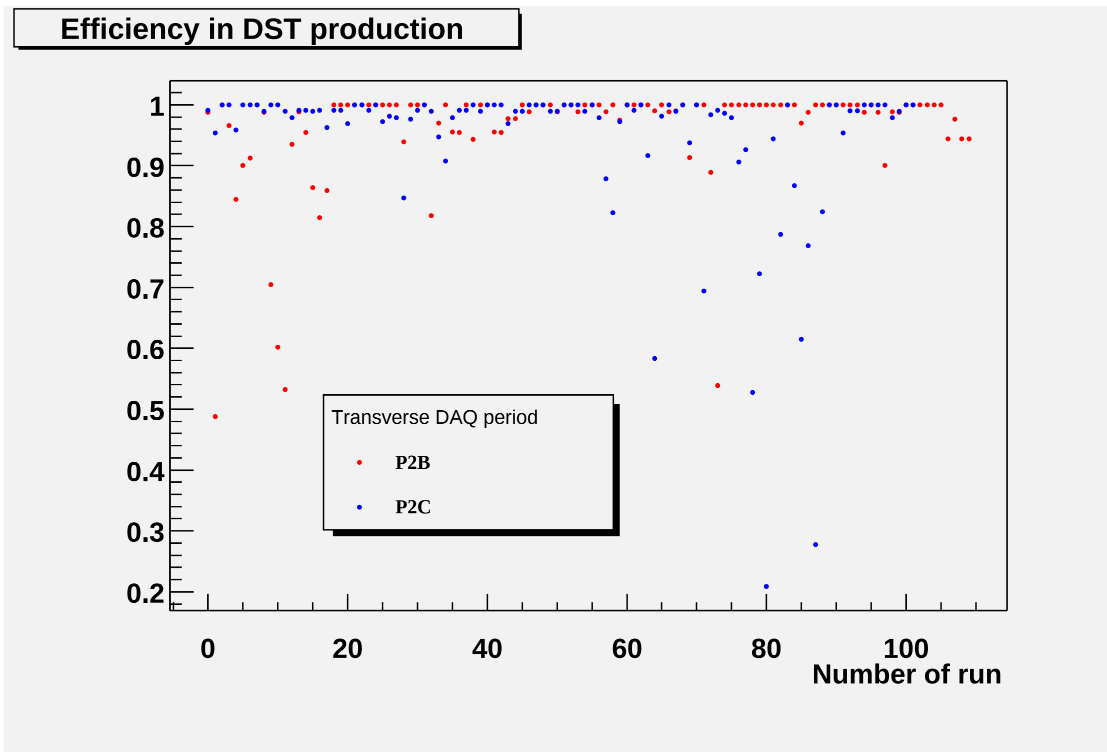

Figure 5.9: The efficiency in production for part (P2B and P2C periods) of the data sample collected in transverse mode during year 2002 run.

VArray of CALORIMETER OBJECTS
$E \pm \Delta E$ $X_{cl} \pm \Delta X_{cl}$ $Y_{cl} \pm \Delta Y_{cl}$ $Z_{cl} \pm \Delta Z_{cl}$
VArray of TRACKS OBJECTS
track quality: χ^2 time rich probabilities of being a given particle number of associated helices number of associated vertices number of associated calorimeter objects expected fired detectors bitmap fired detectors bitmap
VArray of TRACKS WITH MOMENTUM OBJECTS (HELICES)
track position: X, Y, Z track direction: dX/dZ, dY/dZ, Q/P (i.e. charge/momentum) Error Matrix: $\sigma_i \cdot \sigma_j$ particle PDG code (PID) particle type (any, μ or μ') theta Cherenkov: θ_C
VArray of VERTICES
vertex position: X, Y, Z vertex quality: χ^2 Error Matrix: $\sigma_i \cdot \sigma_j$ type (primary, secondary)

Table 5.3: The DST (version “3”) content of information.

Chapter 6

A first look at the data

6.1 The 2001 run

The objectives of the examples reported in this chapter were the study of the spectrometer and the development of the various analysis tools on the first real data collected by COMPASS[1].

The data collected during year 2001 commissioning run have been used for this aim. In 2001 SPS beam time for COMPASS started on July 12th and ended on October 23rd (110 days). The spectrometer (see figure 6.1) was still incomplete especially in the tracking[2] but the presence of 50% of the electronical channels coming from the detectors' front-ends represented a real "load" test for the DAQ system.

Most of the run time has been dedicated to detector set-up and commissioning and only the last 20 days have been used to collect physics data. The behaviour as function of the time for the data collected and transferred to the DB in the last 20 days of DAQ is shown in figure 6.2. At the end of the run time, COMPASS had more than 25,000 good raw data files corresponding to about 15 TB i.e. about 300 runs and $3.4 \cdot 10^8$ triggers [17].

The large majority of these runs have been collected with the target set in longitudinal polarization (see section 3.3.2) whereas a small fraction (less than 1%) has been taken in transverse mode.

[1]The previous work was always based on MC simulations.

[2]At that time, only 6 planes (over 12) of MicroMegas, 1 (over 3) SDC station and only half a module of Straw tubes were available. Big hardware problems affected the RICH and the calorimeters which weren't calibrated. The muon identification was a quite difficult task for the absence of Muon Walls.

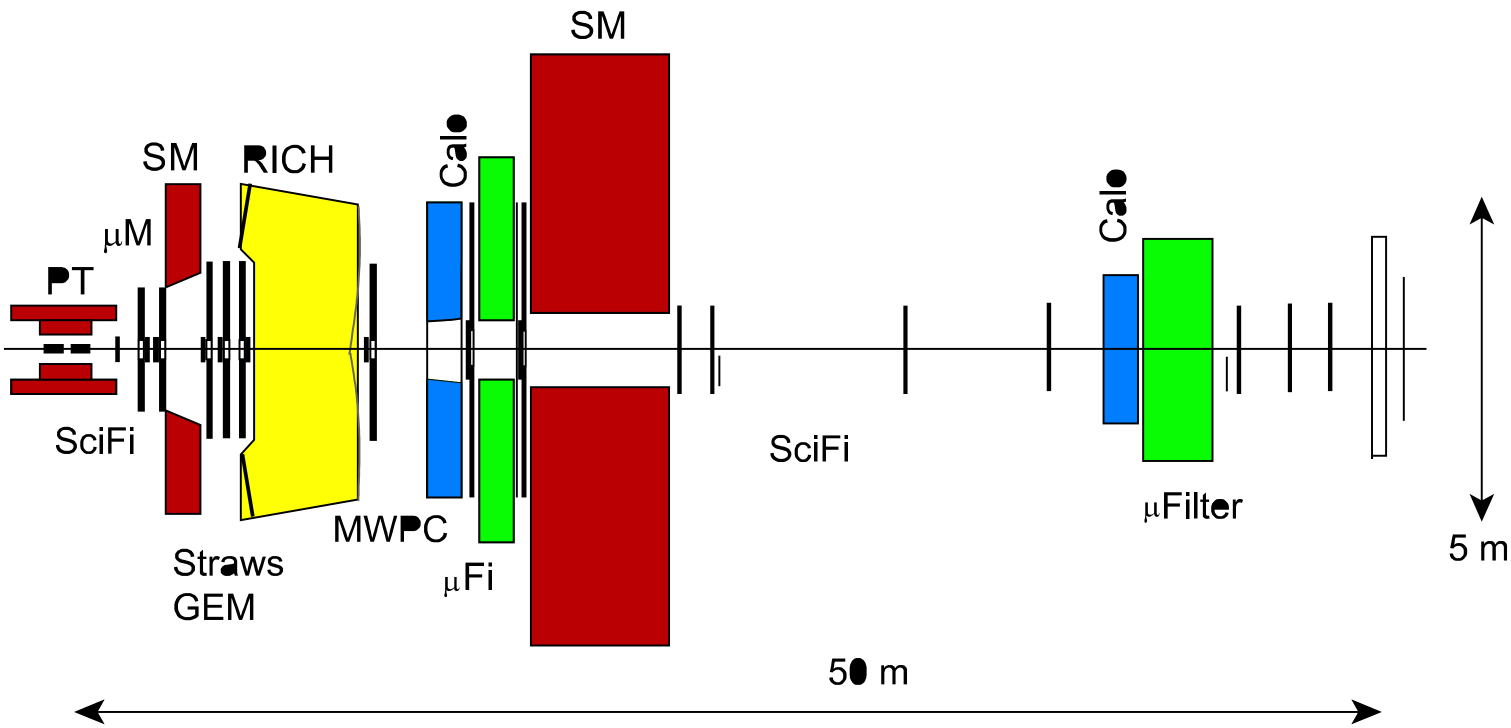

Figure 6.1: The COMPASS set-up installed in year 2001 run.

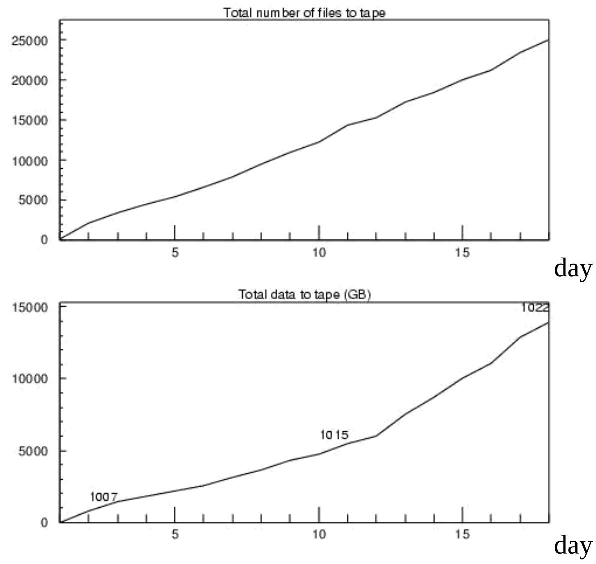

Figure 6.2: The total number of files and the total size of data stored to CCF as function of time during the last time slice of year 2001 COMPASS run.

6.2 First example: measurement of the "time of the event"

6.2.1 Aim of the job

In this section the analysis' results from a sample of data collected by fibers' stations 1-4 (see section 3.4.1) are presented. Because of their good time resolution, the fibers can be used to define the "time of the event".

An algorithm has been developed to choose, on each fiber plane, the clusters belonging to the same track. The time got from these "good combinations" has been used to compute the time of the event.

Due to the high intensity of the incident muon beam, sometimes more than one incoming track is measured both in the SciFi's before the target (which measures the μ direction) and in the BMS (which measure the μ momentum, see section 3.3.1). Having a better definition of the "time of the event" than that given by trigger time, will allow to look at the BMS in a shorter time window and thus to reduce the accidentals.

In this way the efficiency in some relevant observables' calculation, such as the incident muon momentum, is enhanced. AS a result of this analysis, both the spatial and the time resolution of the SciFi stations near the target could be determined[3].

6.2.2 The data processing by CORAL

The data have been processed by CORAL using some runs collected with different triggers and beam intensities[4].

In table 6.1, taken from the on-line logbook, the DAQ information related to each of the runs are reported.

Run	Time	Trg/spill	Spills	μ/spill ($\cdot\ 10^8$)	Trigger condition
12788	Oct 17 0-8h 01:26	8300	100	1.9	ITC, MTC, LTC
12803	Oct 17 0-8h 05:28	8000	100	2.0	ITC, MTC, LTC
13172	Oct 22 8-16h 12:54		13	3.0	Random
13203	Oct 22 16-24h 0:20	13000	50	$4.3 \cdot 10^{-2}$	Alignment (Beam Trigger)

Table 6.1: Online logbook information for the runs analyzed by CORAL. The meaning for the acronyms used to specify the trigger conditions are explained in table 3.5.

The alignment run has been taken with low intensity and Beam trigger, the Physics runs have been collected adding all the triggers coming from Inner, Ladder and Middle hodoscopes.

The analysis' routines look for hits upon the 4 fibers' stations and fill an ntuple in the ROOT output file, handled by CORAL. Clusters are defined as succession of neighbour hits within a time window of 5 ns. The detector proper time is defined as the average of the times of each list.

The time associated to clusters is then taken as the difference between the detector proper time and trigger time:

[3]This work was carried on in parallel and largely independently of the corresponding effort in the Off-line group to characterize and calibrate the SciFi hodoscopes for the data analysis.

[4]The SPS cycle length can vary for different periods (Proton physics/LHC tests/Heavy Ions). For the 2001 run, there was 5.1 s long spill every 16.8 s. There is however a difference between the effective spill and the flat top (extraction). While the latter is the nominal 5.1 s the effective spill length can be about 4 s only due to intensity variations. The rate corresponding to $2.2 \cdot 10^8$ μ/spill intensity can vary between $4 \cdot 10^7$ and $5 \cdot 10^7$ μ/sec.

$$t(cluster) \;=\; T(proper) - T(trig) \tag{6.1}$$

6.2.3 General observation

Beam profiles

The Scintillating fibers have a good spatial resolution which can be as good as 0.15 mm for the stations before the target. The spatial response has been checked looking at runs taken by "alignment" and "random" triggers and it's monitored routinely using the reconstructed straight tracks in the spectrometer.

In figure 6.3 two examples of beam profiles (from a run taken with random trigger) are shown. The shape of these views are compatible with the measurements done during the M2 line commissioning in 1999. As it can be seen, not all the beam is seen by the stations installed before the target. During M2 line commissioning in 1999 the measured standard deviation was 0.78 cm at target center position which is roughly compatible with our results if one uses the expected beam divergence [66].

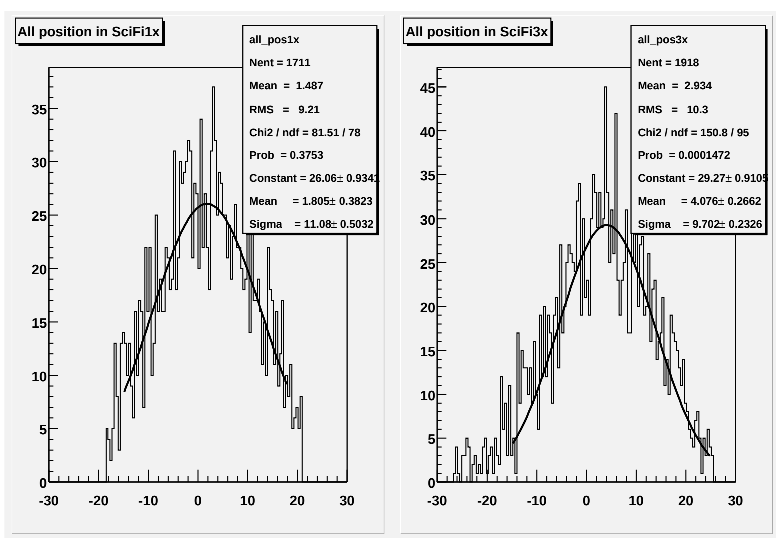

Figure 6.3: Y distribution of the clusters' centers in the upstream (SciFi1x) and downstream (SciFi3x) planes. From stations 3 and 4 the whole beam profile can be seen. The fitted beam standard deviation goes from 0.9 to 1.1 cm.

Clusters size, center, multiplicity and time

The cluster center is defined as the mean value of the abscissae of the fired fibers the cluster is built of. The cluster size is defined as the number of fibers the cluster is formed by. The knowledge of cluster's size allows to correctly compute the error in space associated to cluster center.

Typical distributions for alignment and physics runs (see figure 6.4) show that the cluster size differs from 1 only for a few per cent and, as expected, doesn't depend on the trigger conditions:

The typical time distribution from all the clusters is shown in figure 6.5. The cluster multiplicity is defined as the number of clusters found in the same detector plane in the chosen time window, it depends on the width of the time window and gives rise to the tracking complexity once somebody wants to associate all the clusters related to the same track.

In pictures 6.6 and 6.7 it's shown the behaviour of cluster multiplicity as function of the time window width and the trigger type.

The default cut is set at $\pm\ 2 \cdot \sigma_t(cluster)$. This corresponds to $\pm$ 2 ns in case of physics runs and $\pm$ 3 ns in case of alignment[5].

The probability to have events with no cluster in this time window is about $10 \div 11$ % for physics trigger and $11 \div 13$ % for beam trigger. The correlation study upon these empty events is presented in the next section.

Only for the events with 1 cluster in the first two stations, a single incident track can be reconstructed without ambiguity due to the minimal setup used in 2001.

[5] This is mostly to be addressed to the fact the t_0 calibration [17], has been optimized for runs far from this alignment one and consequently less compatible for such a case.

a)

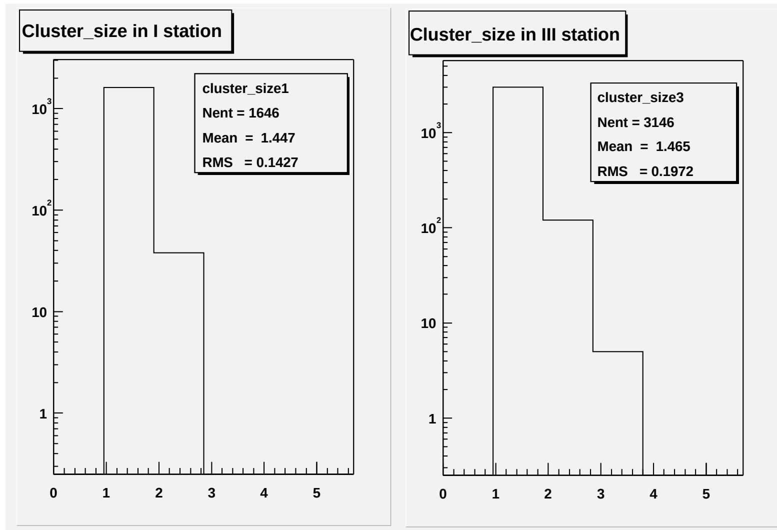

b)

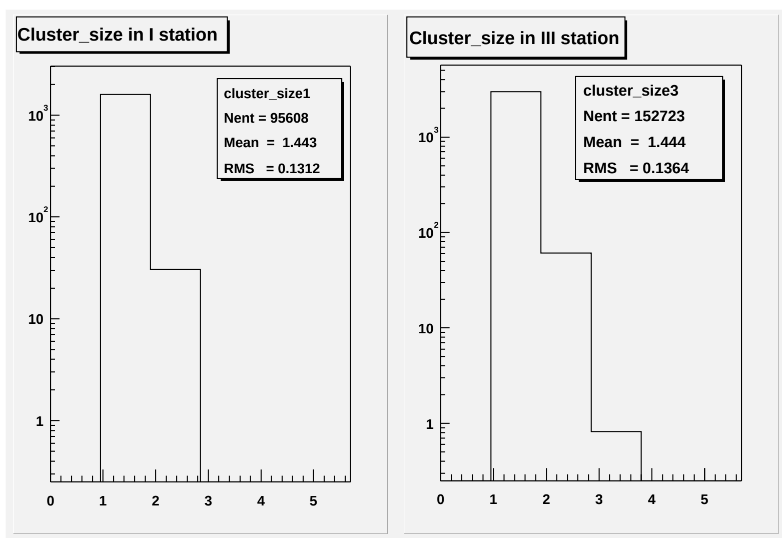

Figure 6.4: Cluster size distribution without any cut in time for physics (a) and alignment run (b). No dependance from trigger type is shown.

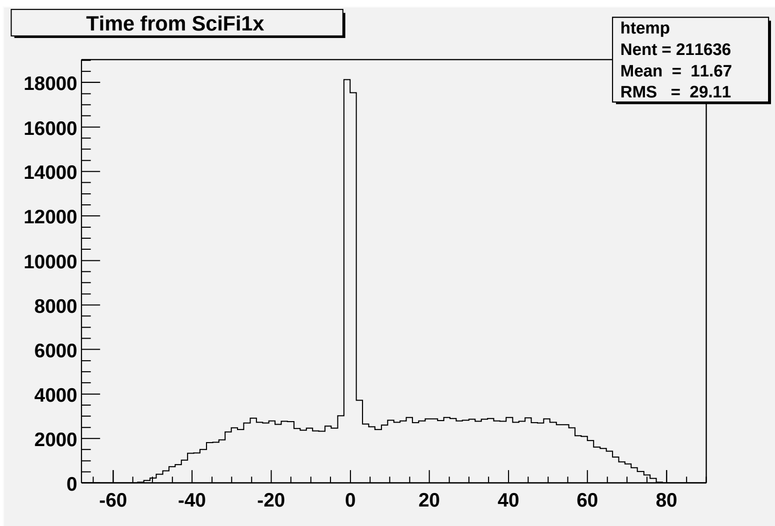

Figure 6.5: The typical time distribution from all the clusters in SciFi1x for a high intensity physics run.

a)

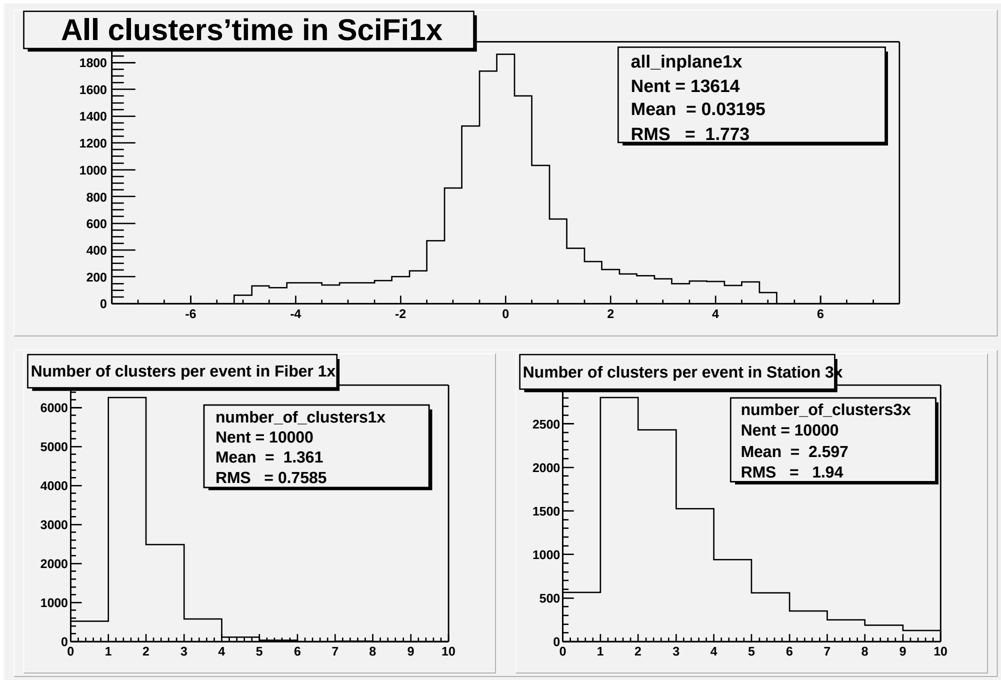

b)

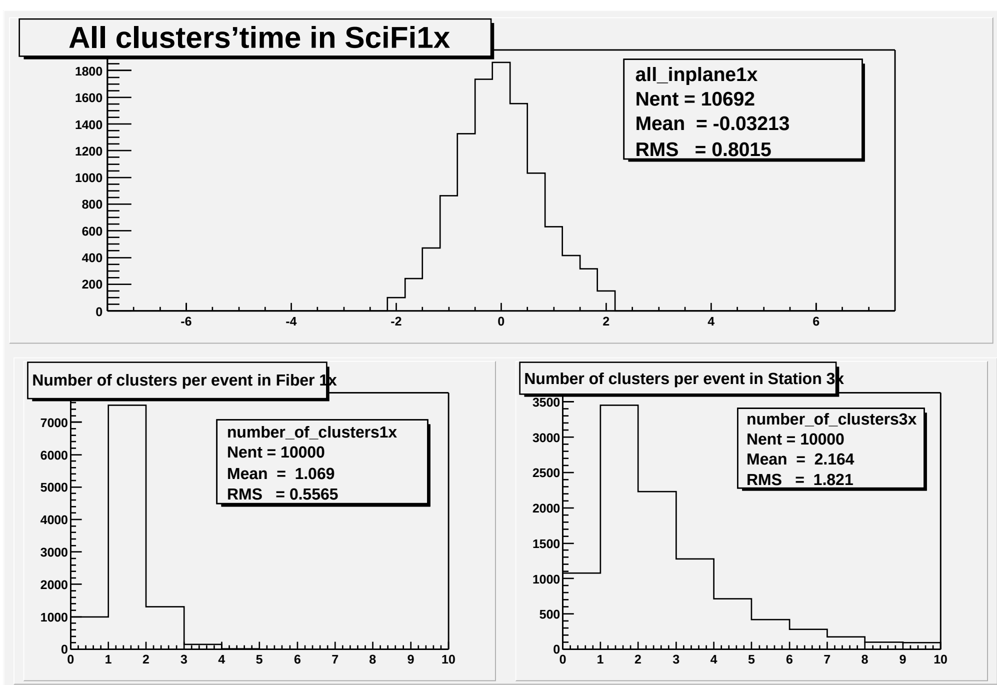

Figure 6.6: Typical distribution of clusters/event (cluster multiplicity) for physics runs in upstream and downstream planes. In (a) time window is ± 5 ns, in (b) it's ± 2 ns.

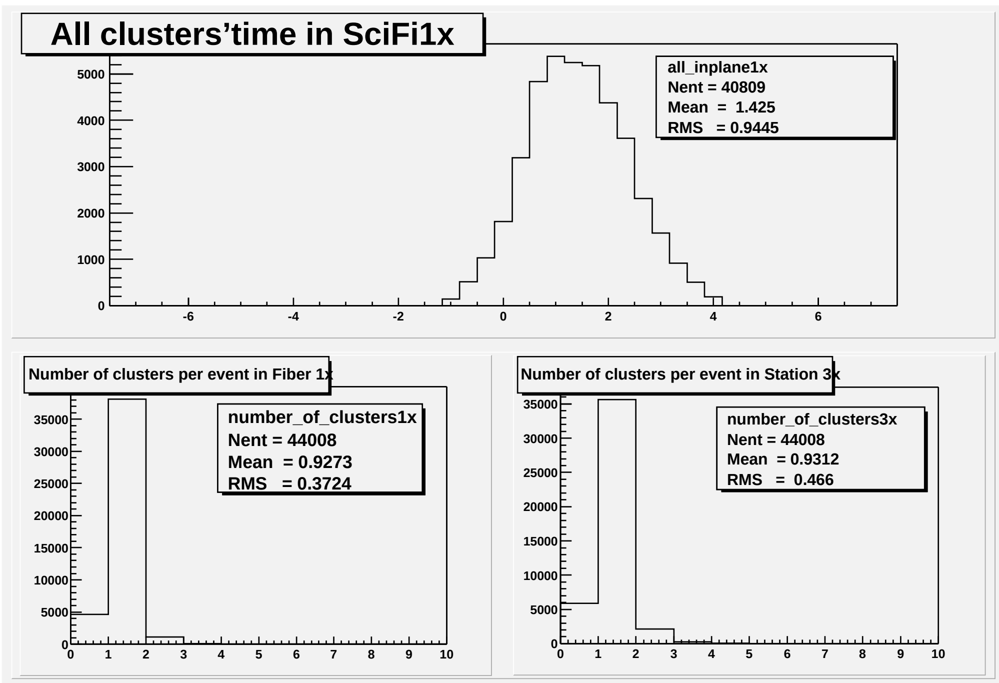

Figure 6.7: Same plot as in figure 6.6 for the alignment case. Time window is 6 ns wide. No rescaling of the trigger time makes the distribution not to be centered in 0.The multiplicity is much lower with respect of physics run case because of the intensity factor and because one triggers on non-interacting muons (this explains the loss of clusters in the downstream stations).

Coincidence of empty events

One should ask if the high number of events without cluster (see figures 6.6-6.7) is compatible with the flux intensity passing through the fibers.
Analyzing the run taken with random trigger, one can state (from interval distribution) that the probability to have an event in a time window Δt is:

$$P_1 = \frac{1}{\tau}\int_0^{\Delta t} \exp -\frac{\Delta t}{\tau}\, dt = 1 - e^{-\frac{\Delta t}{\tau}} \tag{6.2}$$

where Δt is the trigger gate and $I = \frac{1}{\tau}$ is the beam intensity.
The complementary probability, not to have clusters, is:

$$P_0 = 1 - P_1 = e^{-\frac{\Delta t}{\tau}} \tag{6.3}$$

Some measured combinations of empty events in the zy projection are:

```
1) No cluster in 1 & 2 = 0.817
2) No cluster in 3 & 4 = 0.786
3) No cluster in (1 & 2) or (3 & 4) = 0.844
4) No cluster in 1 & 2 & 3 & 4 = 0.758
5) No cluster in 1 or 2 or 3 or 4 = 0.922
```

The conditions (1-3) correspond to the following[6] linear system:

$$\begin{cases} P_0 + (1-P_0)(1-\epsilon_{12})^2 & = 0.817 \\ P_0 + (1-P_0)(1-\epsilon_{34})^2 & = 0.786 \\ P_0 + (1-P_0)(1-\epsilon_{12})^2 + (1-P_0)(1-\epsilon_{34})^2 & = 0.844 \end{cases} \tag{6.4}$$

being ϵ_{ij} the geometrical efficiency of the planes' pairs. Solving this system one finds:

[6] An approximation has been done taking identical the geometrical efficiency of the fibers' pairs placed upstream and downstream the target.

$$\begin{cases} P_0 = 75.9\% \\ \epsilon_{12} = \quad 67\% \\ \epsilon_{34} = \quad 51\% \end{cases} \tag{6.5}$$

These results satisfy conditions (4-5) within 15% error.

Using equation 6.3 one obtains for the intensity a value which agrees with the one written in the shift logbook and already reported in section 6.2.2:

$$I = \frac{1}{\tau} = -\frac{\ln P_0}{\Delta t} = 6.8 \cdot 10^7 \mu/s \simeq 3\,. \cdot 10^8 \mu/spill \tag{6.6}$$

Since the detection efficiency of this kind of detectors is very high ($\epsilon \simeq 100\%$), this means these empty events correspond to beam tracks not passing through the SciFi's. This category of events have been studied in depth for the 2002 run. They turn out to be due to the non 100% purity of the trigger system which sometimes triggers on events which are not associated to a beam particle entering the target.

6.2.4 The analysis results

Finding correlation by geometrical χ^2 criterium

As we have already said, the multiplicity is a source of ambiguity when one wants to correlate the clusters belonging to the same track.

Naively speaking, in a given time window, the clusters arise from both particles' signals and noise. In picture 6.8 a particle interacts, is scattered inside the target and gives the trigger while another one passes without deflection.

An example of combinatorial is given in the table 6.2 where the columns are filled by the position and time information taken from fibers' planes event by event.

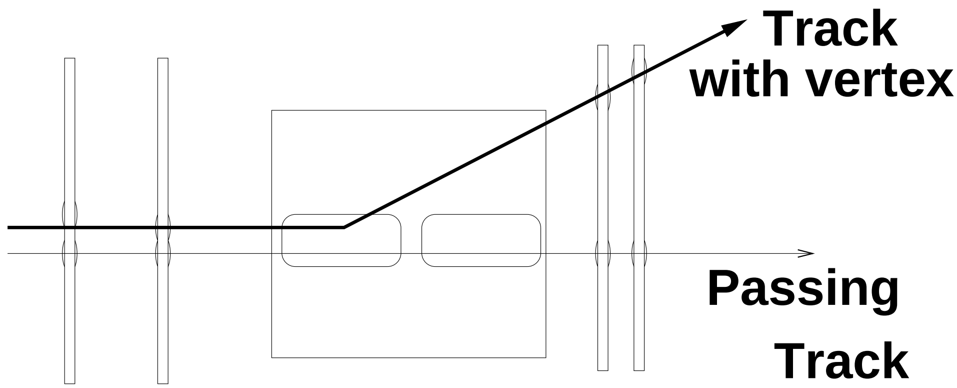

Figure 6.8: One particle interacts and shows a vertex while the other passes through the target without deflection. They can be detected in the same event if they are close enough in time.

event nb	station 1		station 2		station 3		station 4		χ^2
	pos	time	pos	time	pos	time	pos	time	
1	0.21	-0.80	-0.001	-1.22	-25.92	-1.77	1.14	-0.48	30442
1	0.21	-0.80	-0.001	-1.22	-14.85	-0.32	1.14	-0.48	10489
1	0.21	-0.80	-0.001	-1.22	0.72	-0.54	1.14	-0.48	20
2	-9.62	-1.59	-8.20	-1.27	NONE	NONE	NONE	NONE	REJECTED
3	-0.60	-0.10	-2.46	-0.17	-23.05	-0.01	-21.20	1.03	4371
3	-0.60	-0.10	-2.46	-0.17	-23.05	-0.01	-14.43	0.005	6410
3	-0.60	-0.10	-2.46	-0.17	-23.05	-0.01	-0.90	0.68	20010
3	-0.60	-0.10	-2.46	-0.17	-23.05	-0.01	-0.08	-0.06	21242

Table 6.2: Example of cluster combinations in zx plane and calculated χ^2. In the 1^{st} event, there are 3 clusters in station 3, in the 3^{rd} event 4 clusters in station 4.

For each combination a χ^2 analysis is performed as explained below. When, at least one plane has no cluster in the time window, the event is rejected from analysis.

Since the through-going tracks give rise to hits which are geometrically aligned and have correlated clusters' time, this χ^2 analysis permits to access the time resolution of the fiber's planes. The tracks are fit by usual straight line equations in both projections:

$$\begin{cases} y = mz + q \\ x = rz + s \end{cases} \tag{6.7}$$

The line's parameters are calculated from the measured positions making use of standard formulas:

$$
\begin{aligned}
m &= \frac{N \times (\sum y_k^m \; z_k) \; - \; (\sum y_k^m) \; (\sum z_k)}{[N \times (\sum z_k^2) \; - \; (\sum z_k)^2]} \\
q &= \frac{(\sum y_k^m) \; (\sum z_k^2) \; - \; (\sum y_k^m \; z_k)(\sum z_k)}{[N \times (\sum z_k^2) \; - \; (\sum z_k)^2]}
\end{aligned}
\tag{6.8}
$$

N being the number of measurements (4 for each projection), y_k^m the center of measured clusters and z_k the position of the submodule. Analogous equations have been used in the other projection for r and s.

The distribution of probability has been taken uniform in the cluster width[7]. The standard deviation of such a shape is:

$$
\sigma \;=\; \frac{width}{\sqrt{12}} \simeq 0.11 \; mm \qquad width = cluster\ size \times pitch; \tag{6.9}
$$

The pitch is equal to 82% of one single fiber diameter (0.5 mm). This is because of fibers' overlapping in the staggered structure of the plane as explained in section 3.4.1. The χ^2 has been calculated by:

$$
\chi^2 = \sum_{k=1}^{4} \frac{(y_k^m - y_k^{comp})^2}{\sigma^2} \tag{6.10}
$$

The aim of this analysis is to set a cut in χ^2 in order to disentangle the clusters generated by a passing track[8] (with good χ^2) from those arisen by a particle diffused at non-zero angle (with bad χ^2).

In figures 6.9 and 6.10 the number of combinations survived after different χ^2 cuts is shown. In the alignment case, because of the low intensity beam, even with no χ^2 selection,

[7] Many discussions have been made during the progress of this work about the shape of this probability and the subsequent value of the error to associated. It seems clear that our choice is not the best in case of cluster size equal to 2. In this case, in fact, the particle is supposed to pass in the spatial region where the fibers overlap. This width is equal to 0.17 mm and leads to an error of 0.05 mm, smaller by a factor of 2 w.r.t. the general case. Anyway, from figure 6.4, the amount of such clusters is rather small.

[8] It's clear that a further analysis should be done elsewhere (looking at trigger masks, other detectors, etc.) to establish if the passing track is interesting (e.g. if it derives from a $Q^2 \simeq 0$ event) or not (just beam tracks uncorrelated with trigger).

the mean number of cluster combinations is less than 1. This is not the case for physics triggers when just 1 combination survives only with $\chi^2 < 150$.

alignment run

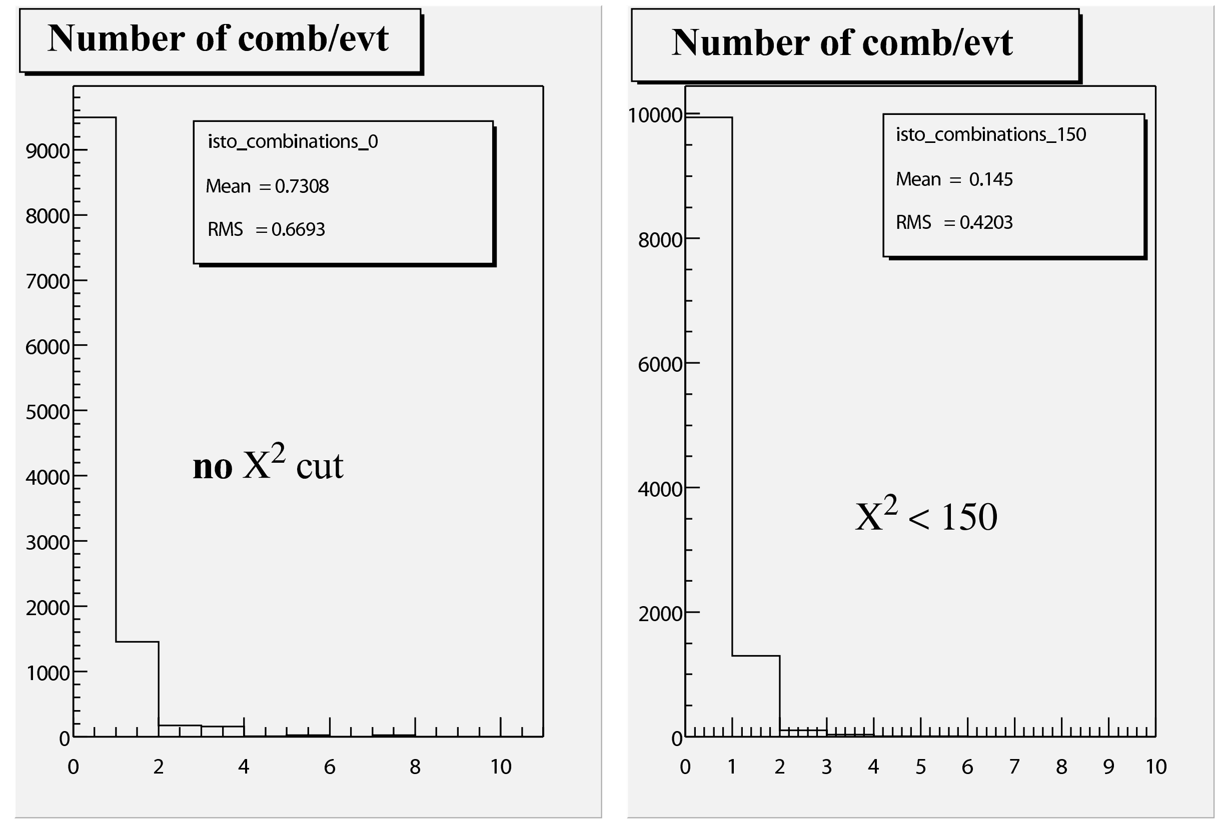

Figure 6.9: Number of cluster combinations in zx projection (in the orthogonal one, the results are analogous) for different χ^2 cuts. In the alignment run, without cuts, the mean value of 0.2 cluster/event is seen.

physics run

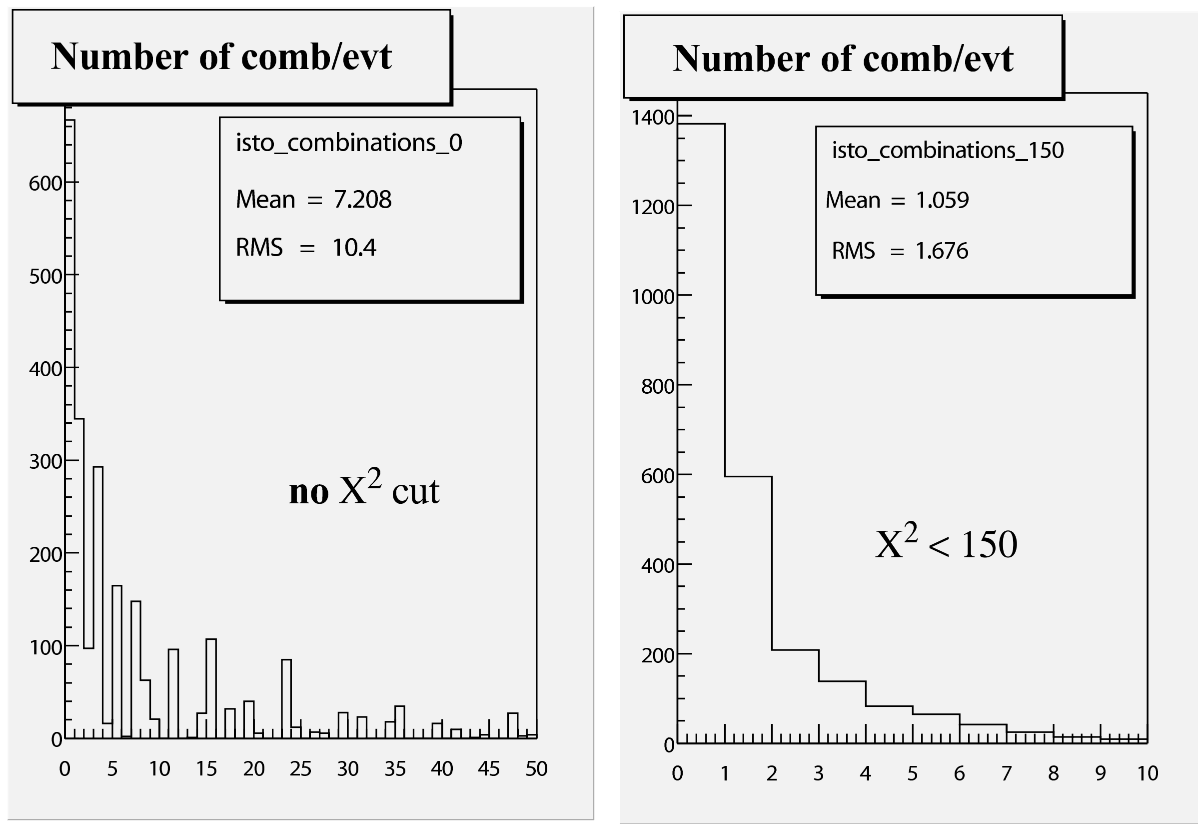

Figure 6.10: In physics runs, setting the cut at $\chi^2 = 150$, we get almost 1 combination/event while, if no cut is set, a mean of 7 combination/event are seen.

Measuring space and time resolution

The χ^2 distributions are shown in the left plots of figure 6.11. In case of alignment triggers, since only passing tracks are collected, the expected behaviour (an exponential with a negative slope) of a 2 degrees of freedom χ^2 is found. For physics triggers, instead, the χ^2 shape is destroyed by the contribution of the events which are not straight lines.

Let's concentrate on the results from alignment. For a 2-dof χ^2 distribution the slope of the exponential corresponds to $\frac{1}{<\chi^2>}$ which is equal to $\frac{1}{2}$ in case of well estimated errors. From our fit the errors' value (see equation 6.9), corresponding to the fibers' resolution in space, seem to be under-estimated. According to our analysis, one could set the errors to:

$$\sigma_{fit} \;=\; 1.31 \times \sigma \simeq 0.16\ mm \tag{6.11}$$

Next to the χ^2 distribution, it is plotted a combination of time information from fibers. Namely the following variable is plotted:

$$\tilde{t} = \frac{1}{4} \cdot (t_1 + t_2 - t_3 - t_4) \tag{6.12}$$

The difference between two groups of an even number of planes is the only way to get rid of trigger time (see eq. 6.1) and be able to access the time resolution of a single plane. From equation 6.12, assuming equal resolution for each plane:

$$\sigma(t_i) = 2 \cdot \sigma(\tilde{t}) \tag{6.13}$$

From the alignment and random trigger runs, one gets $< \sigma(t_i) >\simeq 600\ ps$. This figure can be improved using only the first two stations: one finds a slightly better resolution[9] (500 ps) got from the standard deviation of the distribution in figure 6.12. Performing the same algorithm on physics runs, one can only reach $< \sigma(t_i) >\simeq 850\ ps$ showing that geometrically aligned clusters are not always correlated in time.

In the next section another algorithm of preselection is developed to find the correct combinations in case of physics' triggers.

[9]This effect derives from the fact that the SciFis installed upstream the target have shorter light pipes which are the main source of the fibers' spread in time.

alignment run

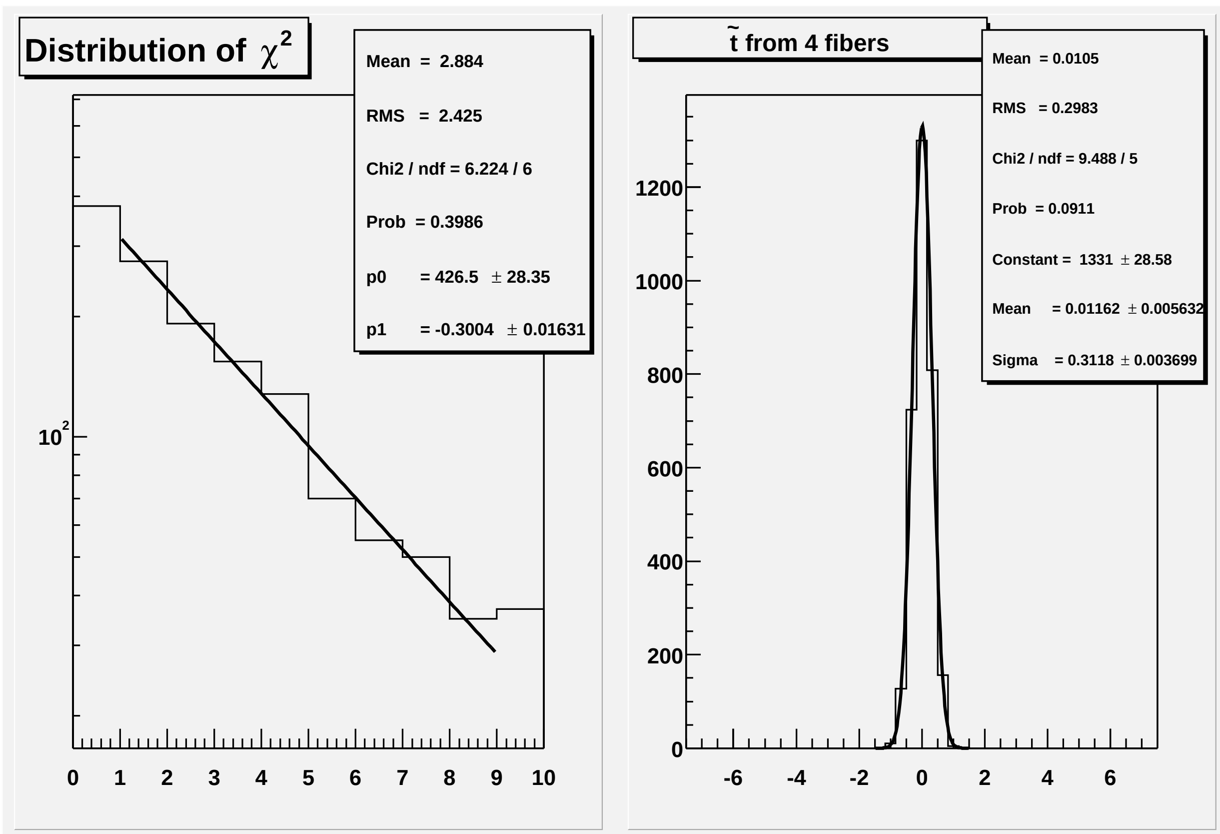

physics run

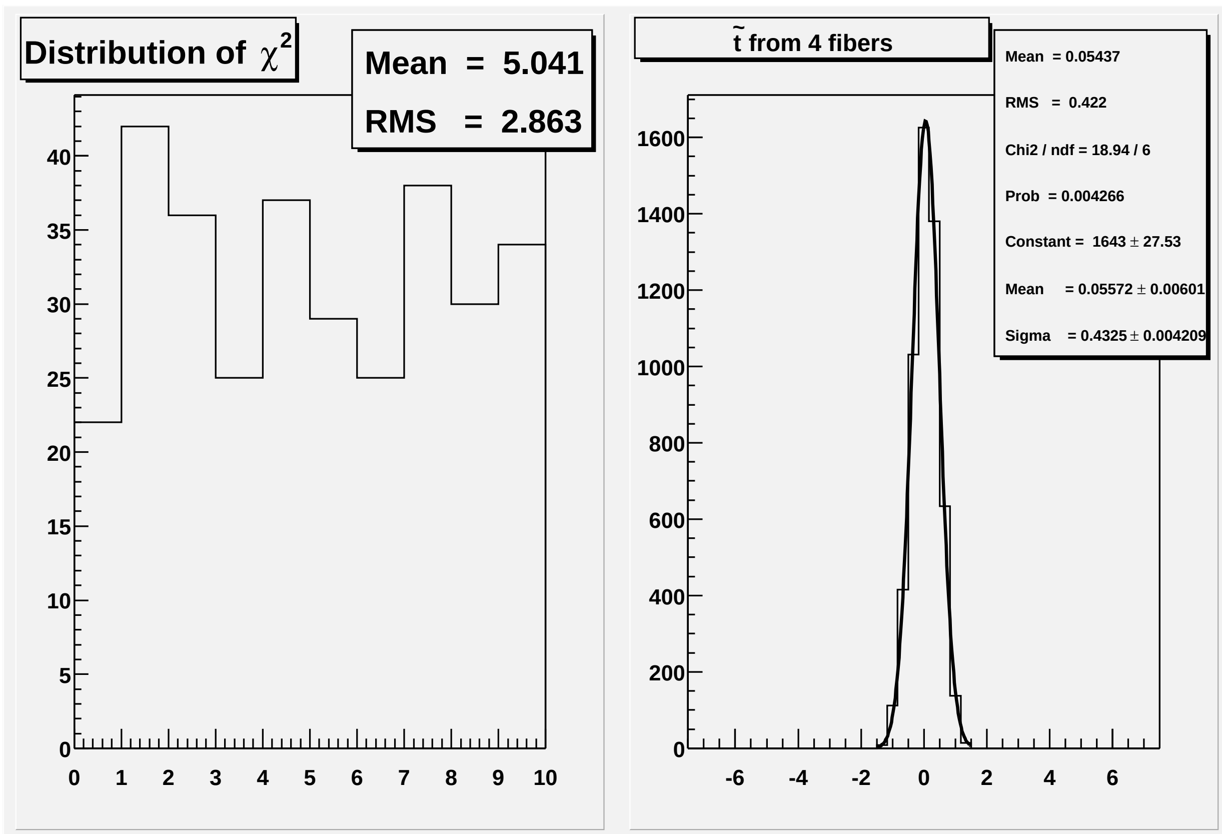

Figure 6.11: χ^2 distribution for all combinations (zoom to first 10 channels) and related $\tilde{t}$ histogram from each event in zx projections for beam (previous page) and physics triggers.

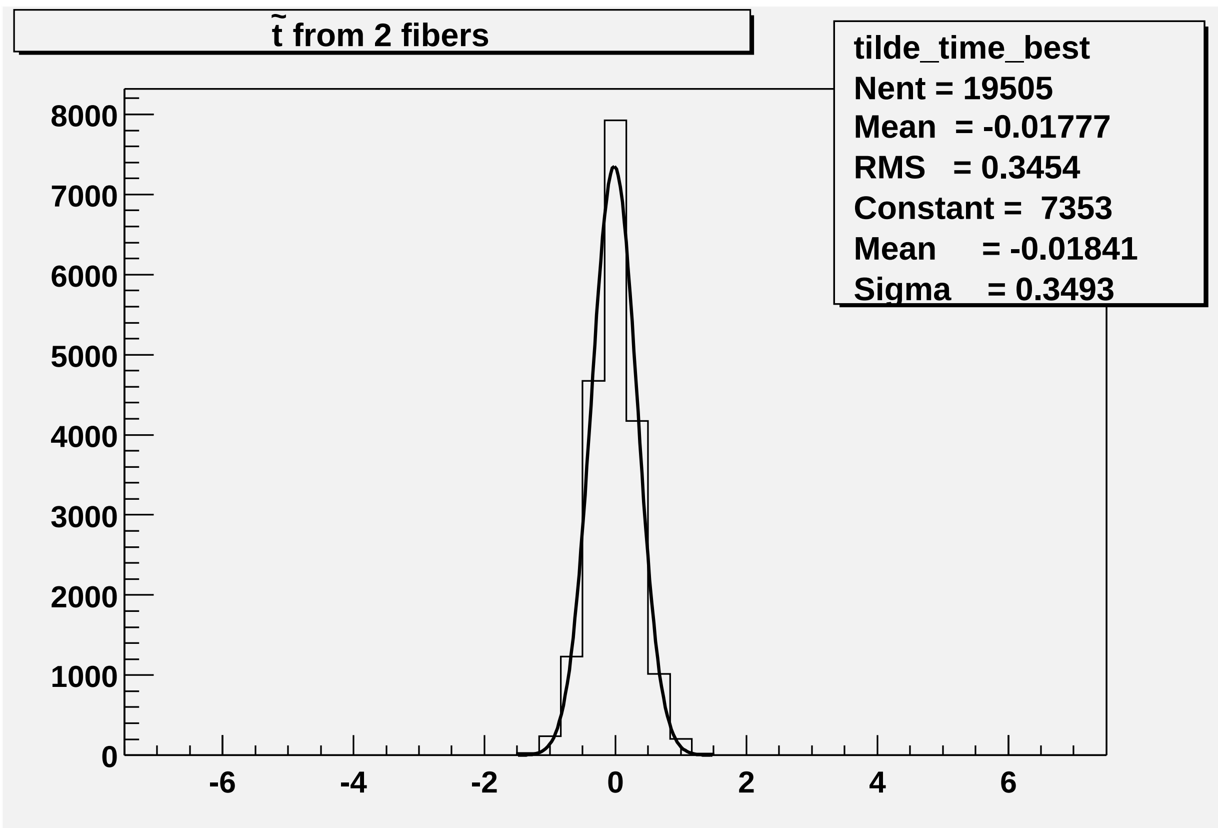

Figure 6.12: The plotted distribution is half the difference between first two planes (upstream the target), namely $\tilde{t}_{12} = \frac{(t_1 - t_2)}{2}$. The standard deviation corresponds to 500 ps time resolution.

Finding the scattered tracks using the rotated planes

In the previous section, we have seen that a naive χ^2 analysis can't distinguish between passing and scattered particles in the physics runs, i.e. it's not possible to select clusters by a χ^2 cut involving all the fibers' planes.

For physics triggers the only solution is to select the clusters associated with a track indipendently in I and II telescope (see figure 6.13): a straight line can be determined using only the stations installed downstream the target both in the case of scattered and passing tracks making use of the inclined planes.

It's clear that, in this fashion, the incident track is just a straight line joining two points in the space and there is no way to check it. Anyway the small multiplicity in the upstream stations reduces the ambiguity to few cases (see figure 6.6-6.7).

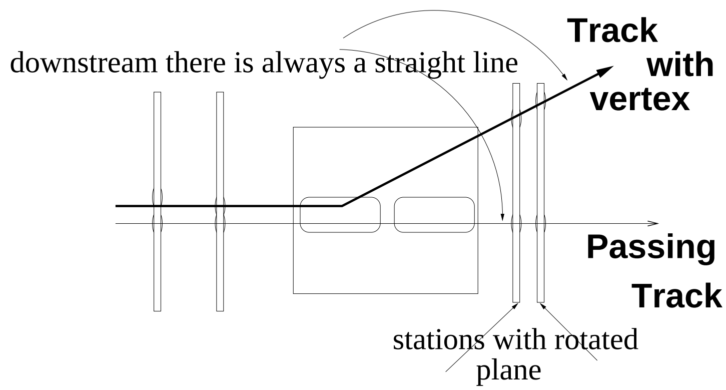

Figure 6.13: A straight line can be fitted using only the stations installed downstream the target in both the case of a scattered and passing tracks.

A χ^2 analysis has been done computing the residuals of the track on the inclined planes.

$$\chi^2 = \frac{1}{\sigma^2}\left[Residual_3 \ + \ Residual_4\right] \begin{cases} Residual_3 = & (u_3^{meas} - u_3^{comp})^2 \\ Residual_4 = & (u_4^{meas} - u_4^{comp})^2 \end{cases} \tag{6.14}$$

The χ^2 distribution is plotted in figure 6.14. The combinations with $\chi^2 < 10$ (up to where the curve is clearly exponential) have been chosen and selected. They can refer to passing or scattered tracks. It must be stressed that the χ^2 cut selects the correct clusters in station 3 and 4 (i.e. correct space points on the stations) but doesn't help in choosing the correct association among them.

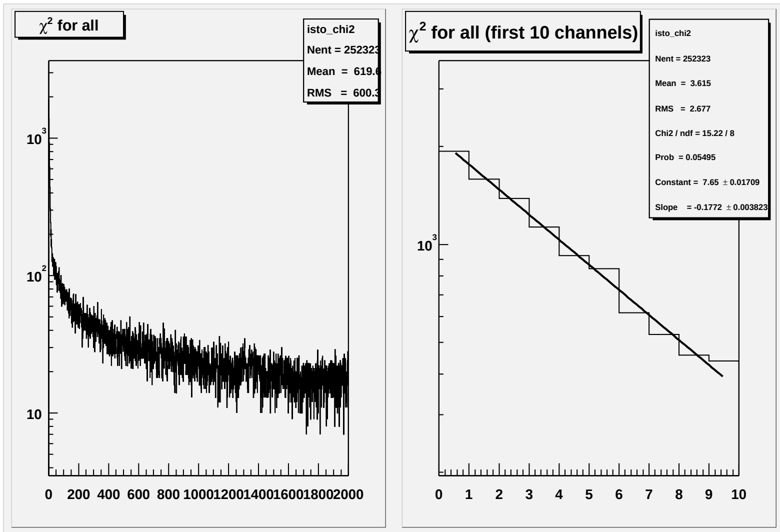

Figure 6.14: χ^2 distribution for all the combinations. The first 10 channels are fitted by negative exponential and replotted.

Selecting the events with only 1 cluster in each plane of station 1 and 2 one can compute the scattering angle θ.

Since θ is function of gaussian distributed variables, it should follow a gaussian distribution i.e. its squared value should behave as an exponential with negative slope. Analyzing the alignment runs, from scattering angle distribution (see figure 6.15), the standard deviation for θ due to fiber angular resolution has been measured. From the fit we get:

$$\sigma_\theta = \ 0.32 \ mrad \tag{6.15}$$

This is compatible (within 12%) with the value naively calculated as fraction between the fibers' error in the space (from equation 6.11) and the distance between the closest stations (III and IV):

$$\sigma_\theta = \frac{\sigma_{fit} \cdot 2}{\Delta z} \simeq 0.35 \ mrad \tag{6.16}$$

where the factor 2 is inserted to get the resolution in space.

The contribution from Coulomb Multiple Scattering in the target is not relevant since, in the COMPASS target, its angular standard deviation θ_{CMS} is of the order of 0.05 mrad, a factor 6 smaller than the angular resolution.

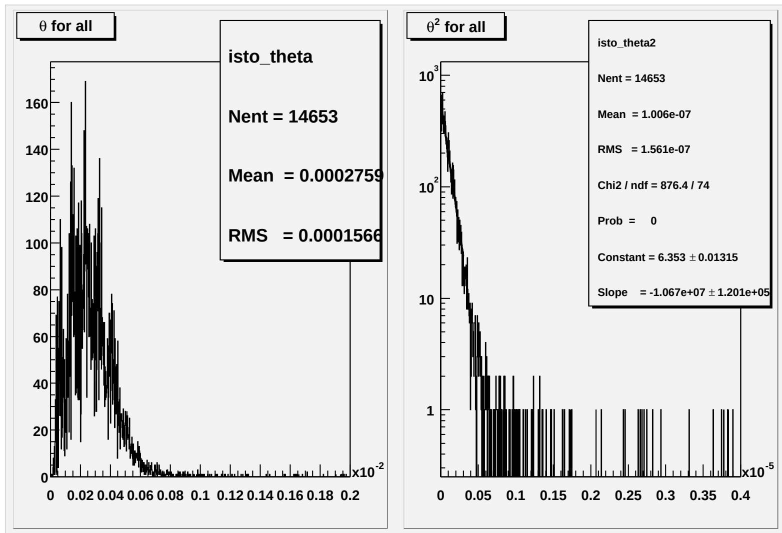

Figure 6.15: The θ and θ^2 distributions (in *radiants*) after χ^2 selection. In the latter an exponential behaviour is found.

Accepting only the tracks scattered at $\theta > 5$ $mrad$ we reduce the uncertainty due to limited angular resolution of fibers and, in case of physics triggers, we can check if the vertex can be reconstructed inside the target. We can look for the intersection between incident and scattered tracks in both projections.

In figure 6.16 it's shown the z distribution of the intersections between incident and scattered tracks. Apart from the image of the target, it's clear that, for several tracks in the II telescope the vertex is found inside the station 3 and 4; the peaks at $z > 800$ mm disappear when no ambiguity is left asking for cluster multiplicity equal to 1 in each plane (see fig. 6.17). Clearly these are phantom tracks related to unresolved ambiguities in the association of the clusters in station 3 and 4. To solve them in a more general case, further information from the other detectors of the spectrometer are needed. Using these extra information, the calculation of the “time of the event”, reported in the next section for the special case of cluster multiplicity equal to 1 in each plane, would be valid for the general case and could

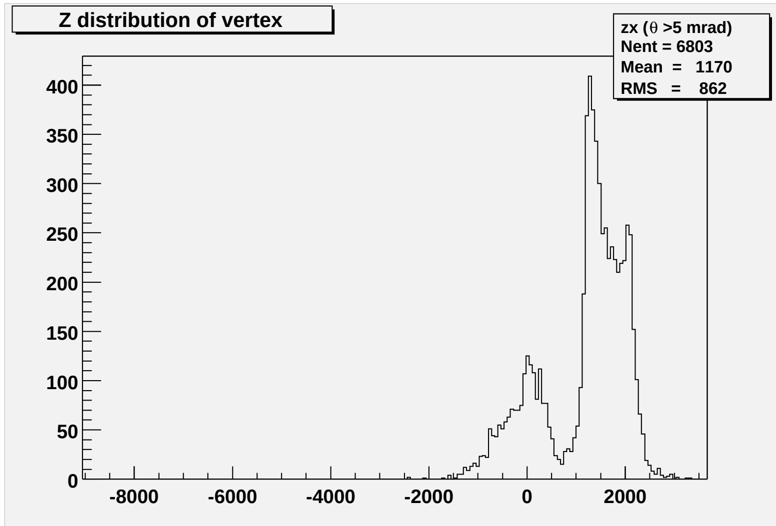

Figure 6.16: Distribution of z_v for 10^5 triggers. On the right of the target the "phantom" vertices on SciFi 3&4 are visible.

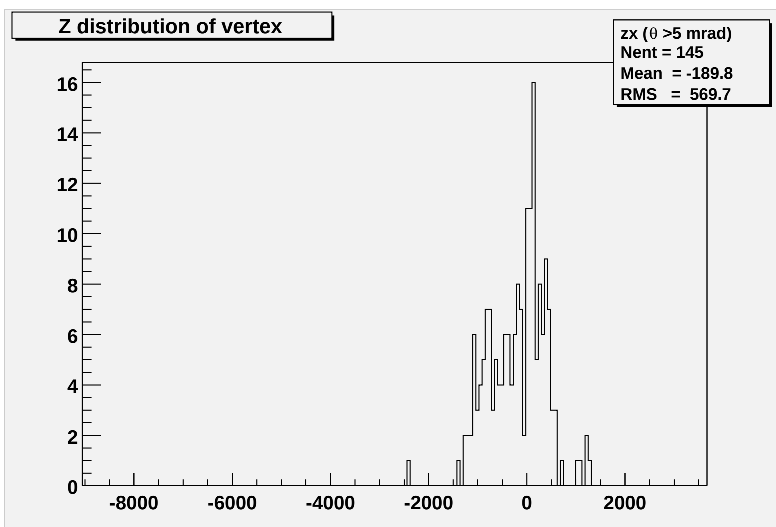

Figure 6.17: Distribution of z_v when multiplicity is 1 in every plane and there is no ambiguity. No "phantom" vertex survives and the target shape is well visible.

be used in the event reconstruction.

6.2.5 Measuring the “time of the event” in physics runs

In the previous section we have seen that the clusters, selected by χ^2 criterium calculated on residuals, give as result correlated combinations, even if the geometrical information are not sufficient and more clusters coming from other detectors are needed in order to choose the correct tracks.

The time information from these clusters is sufficient to define the “time of the event (toe)” as the difference between the upstream and downstream mean time (8 planes over 10 used):

$$toe = \frac{1}{2}[< t_{34} > \quad - \quad < t_{12} >] \tag{6.17}$$

The very good result, shown in figure 6.18, demonstrates that this variable can be measured with 240 ps uncertainty.

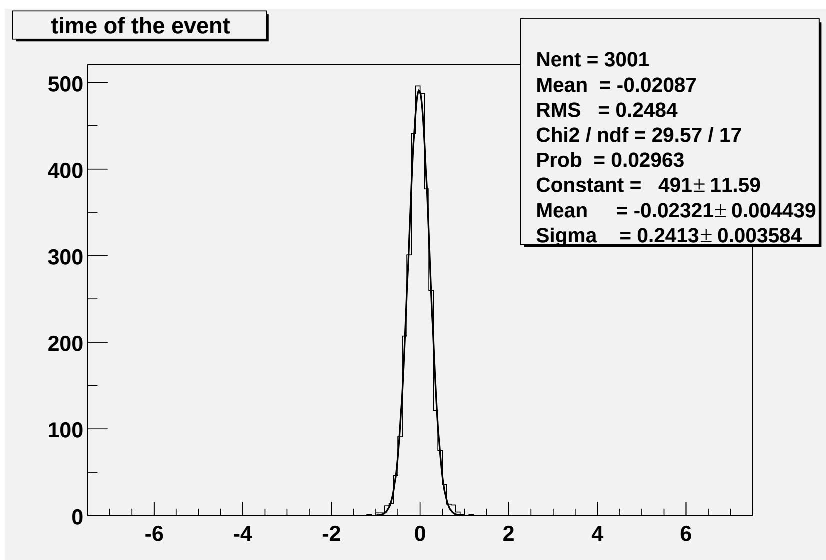

Figure 6.18: The distribution of the “time of the event” has 240 ps standard deviation.

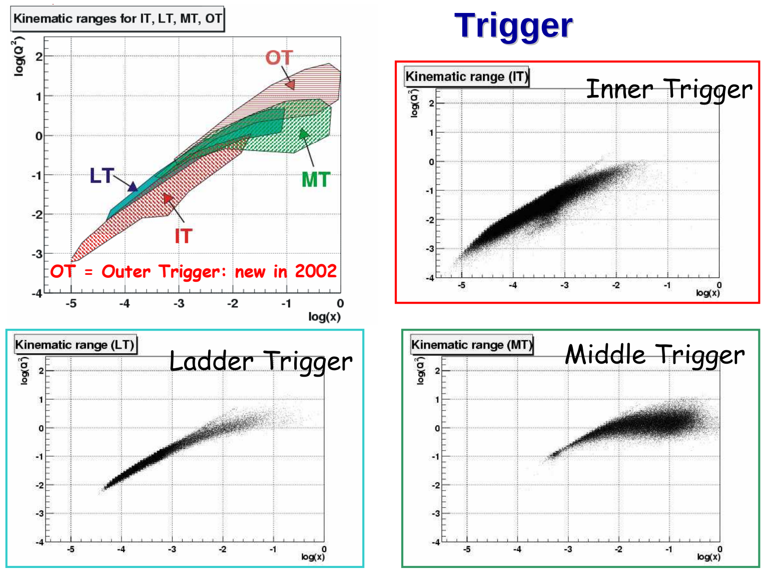

Figure 6.19: Q^2 vs x distribution of several Compass' hodoscopes forming the trigger (Inner, Ladder, Middle). On the top left the relative shapes obtained by simulation. A MC simulation for the region covered by the extra-module Outer trigger installed for year 2002 run is superimposed as well.

6.3 Second example: the primary vertex reconstruction

The vertex package (see section 5.2) implements the search for primary and secondary vertices. After the track finding, this is the second major step of the analysis, a prerequisite to the computing of the Bjorken variables.

In what follows several tests are performed to study various features of spectrometer response, both for longitudinal and transverse polarization in the target.

6.3.1 The trigger kinematical range

Making use of the PID algorithms, the incoming and scattered muon can be identified and the primary vertices ($\mu\ N \longrightarrow \mu' X$) can be reconstructed.

In figure 6.19 the Q^2 vs x distribution covered by the different trigger hodoscopes is shown in $log - log$ scale. This trigger, especially designed for Δg measurement, covers the events of photoproduction (with Inner and Ladder modules) and a small fraction of DIS (with Middle module)[10]. As apparent from the scatter plot, most of events occur at small Q^2 (quasi-real virtual photon) where the photon-gluon fusion (and consequently the charm production cross section) peaks. The DIS events are a small minority.

The final result is that COMPASS trigger accepts all the events in a surface in the plane Q^2 *vs* x going from point ($x \sim 10^{-5}$; $Q^2 \sim 10^{-3}$) to point ($x \sim 1$; $Q^2 \sim 10$).

6.3.2 The shape of the target

The two cases of longitudinal and transverse spin polarization have been analyzed. One can require to reconstruct all the primaries where, in addition to beam and scattered muons, one hadron track has been found. In the CORAL language (as illustrated in picture 6.20) this means that the primary has 3 associated tracks with momentum, one fitted by the SciFi's hodoscope mounted upstream the target (the beam muon), one pointing to the trigger modules (the scattered muon), one with associated calorimeter information (the reconstructed hadron).

In figures 6.21 and 6.22 the Z coordinate distribution and the Y vs X profiles for longitudinal and transverse polarized runs are shown.

In the z-vertex distribution, the two target cells are visible. Though the interaction probability is constant along z, they don't show a "box-shape" for the following reasons:

- the particles related to vertices found at different z cover different solid angles causing an effect of reduced geometrical acceptance. This slope is somewhat different when passing from longitudinal to transverse polarization;

- the tracking resolution is limited and the errors affect the reconstruction of the vertex coordinates, in particular the longitudinal coordinate whose error is inversely proportional to the angle between the tracks. This makes the distributions of the two cells show some shoulders at their geometrical edges and mixes somewhat the events of the two cells in the region around the target nominal centre; nevertheless the exit window of the target cryostat which is rather thin is well visible.

Comparing the figures recalled above, the first relevant difference between the runs taken in longitudinal and transverse polarization concerns the target profiles. In fact, if the transverse

[10] An extra-module has been inserted in 2002 (Outer trigger) to reach the high Q^2 region (> 1 GeV^2).

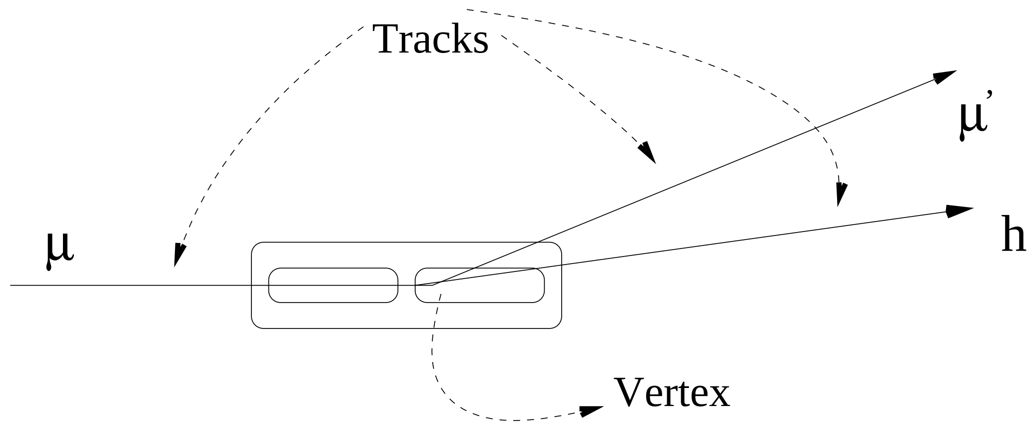

Figure 6.20: Primary vertex in case of an extra hadron has been generated.

dimensions of the target are taken as the product $RMSx \times RMSy$, one could argue that about 25% of the target isn't hit by the beam in transverse mode. Actually this is not the case since the phenomenon can differently be explained: due to the target dipole field (which is on in transverse mode), the incident beam line has been moved in order to exit the target dipole along the same direction as in longitudinal mode (no displacement of nominal beam line). Since the incident muon beam has been displaced without correcting the position of the beam trackers (namely SciFi 1X plane, see figure 6.23) a sensible loss of incoming muons is felt depopulating the target profiles in the top-right corner (see figure 6.22)[11].

In figure 6.24, the ratio for the vertices belonging to the different trigger modules are superimposed. As it can be seen most of COMPASS statistics is provided by Inner trigger while the other two elements contribute at the same level. In transverse mode the results are analogous.

[11] In year 2002 the position of the beam trackers has been optimized to cover the whole beam profile.

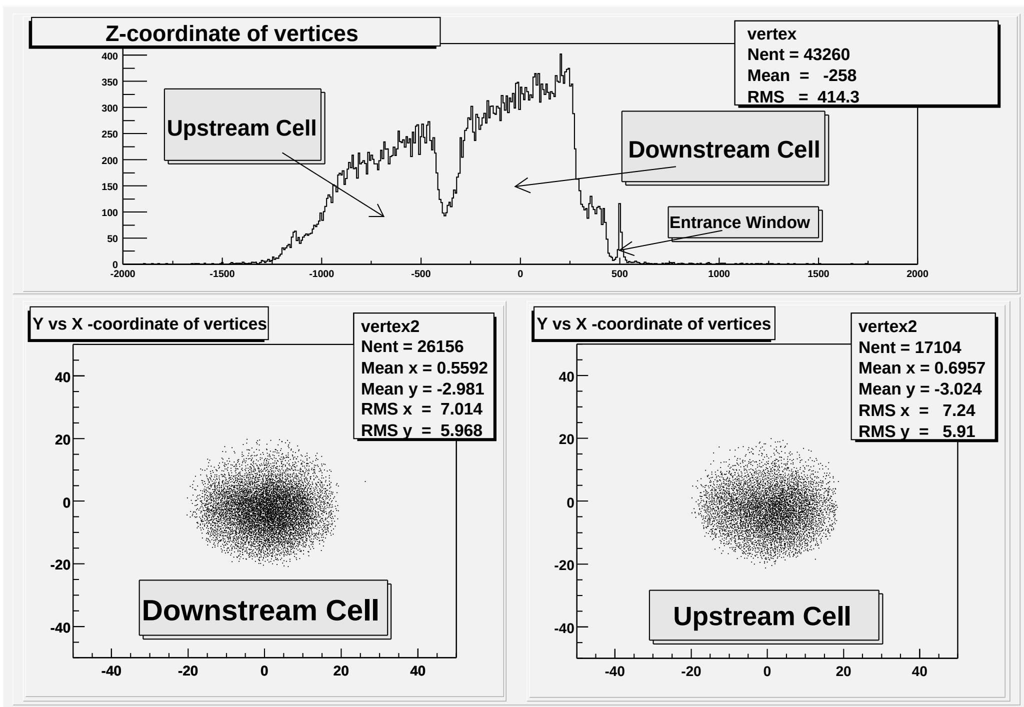

Figure 6.21: The Z coordinate distribution and the Y vs X profiles for all the primaries in which the incident, the scattered muon and only a hadron have been reconstructed. Longitudinal case. and transverse case are shown.

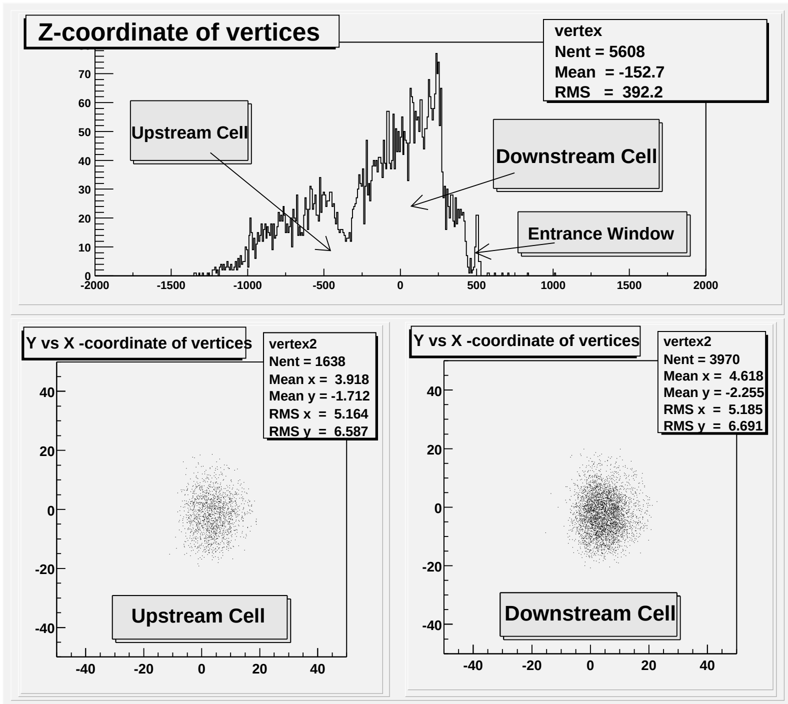

Figure 6.22: Same as previous plot but in transverse polarization.

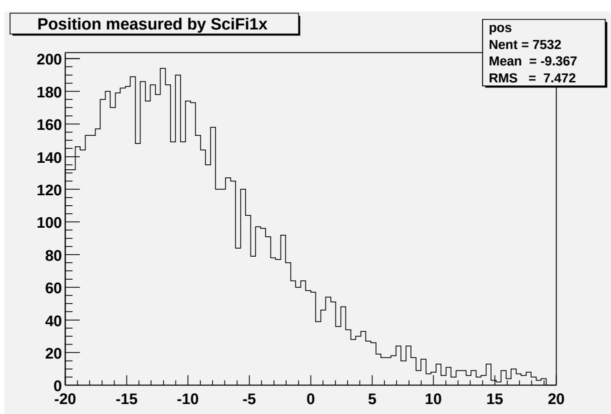

Figure 6.23: The beam profile measured by SciFi1x in the transverse runs.

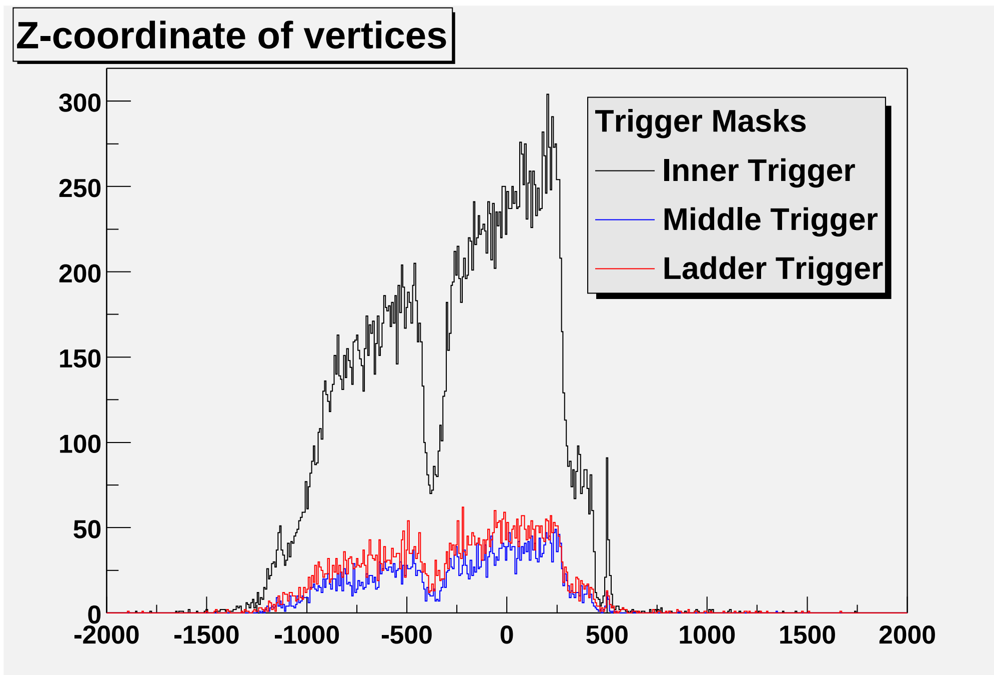

Figure 6.24: The Z coordinate distribution as function of the hodoscope which gives the trigger's signal in longitudinal runs.

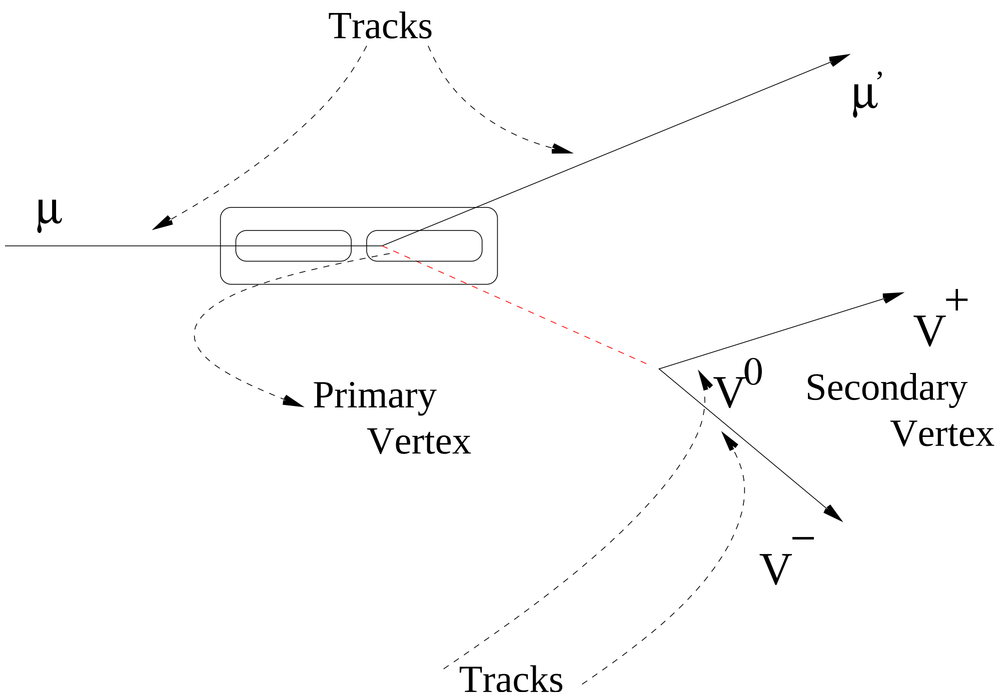

Figure 6.25: A neutral state decaying into opposite charged particles (V^0 state) is found in presence (or not) of a primary.

6.4 Third example: search for V0 resonances

The vertex package allows to look for secondary vertices. In particular, V^0's vertices can be investigated. As it's shown in picture 6.25 a V^0 vertex is a neutral state decaying into couple of opposite-charged particles. So a V^0 is found whenever a vertex with 2 outgoing tracks of opposite charge is reconstructed.

In the following section a tool to identify the V^0 particles is introduced.

6.4.1 The Armenteros-Podolanski plots

The Armenteros-Podolanski plots provide a very useful tool to identify a neutral particle V^0 into two tracks (called here + and -).

This section [67] gives a proof that in the $q_T - \alpha$ plane, V^0's corresponding to different particles will separate into distinct ellipses whose semi-axes depend on the masses of parent particle and decay products. Here $\alpha = \frac{q_L^+ - q_L^-}{q_L^+ + q_L^-}$, q_T is V^0's transverse momentum, $q_L^\pm$ and $q_T^\pm$

the longitudinal and transverse components of the decay products. Let V^0 have velocity β with respect to the lab frame. Denoting all quantities in V^0's rest frame by an asterisk we have:

$$
\begin{aligned}
q^*_{L+} &= |q^*|\cos\theta^* &(6.18)\\
q^*_{T+} &= |q^*|\sin\theta^* &(6.19)\\
E^*_+ &= \sqrt{|q^*|^2 + m_+^2} &(6.20)
\end{aligned}
$$

In the lab frame:

$$
\begin{aligned}
E^{lab}_+ &= \gamma E^*_+ + \beta\gamma q^*_{L+} &(6.21)\\
q^{lab}_{L+} &= \gamma q^*_{L+} + \beta\gamma E^*_+ = \gamma|q^*|\cos\theta^* + \beta\gamma E^*_+ &(6.22)\\
q^{lab}_{T+} &= q^*_{T+} = |q^*|\sin\theta^* &(6.23)
\end{aligned}
$$

and, as $q^*_{L-} = -q^*_{L+}$:

$$q^{lab}_{L-} = -\gamma|q^*|\cos\theta^* + \beta\gamma E^*_- \tag{6.24}$$

Hence by subtracting 6.24 from 6.22:

$$q^{lab}_{L+} - q^{lab}_{L-} = 2\gamma|q^*|\cos\theta^* + \beta\gamma(E^*_+ + E^*_-) \tag{6.25}$$

and, by conservation of momentum:

$$q^{lab}_{L+} + q^{lab}_{L-} = q^{lab}_{V^0} = \beta\gamma m_{V^0} \tag{6.26}$$

Therefore, by definition of α and dividing 6.26 by 6.25:

$$\alpha = k\cos\theta^* + \lambda \tag{6.27}$$

where $k = \frac{2|q^*|}{\beta m_{V^0}}$, $\lambda = \frac{E^*_+ - E^*_-}{m_{V^0}}$. So:

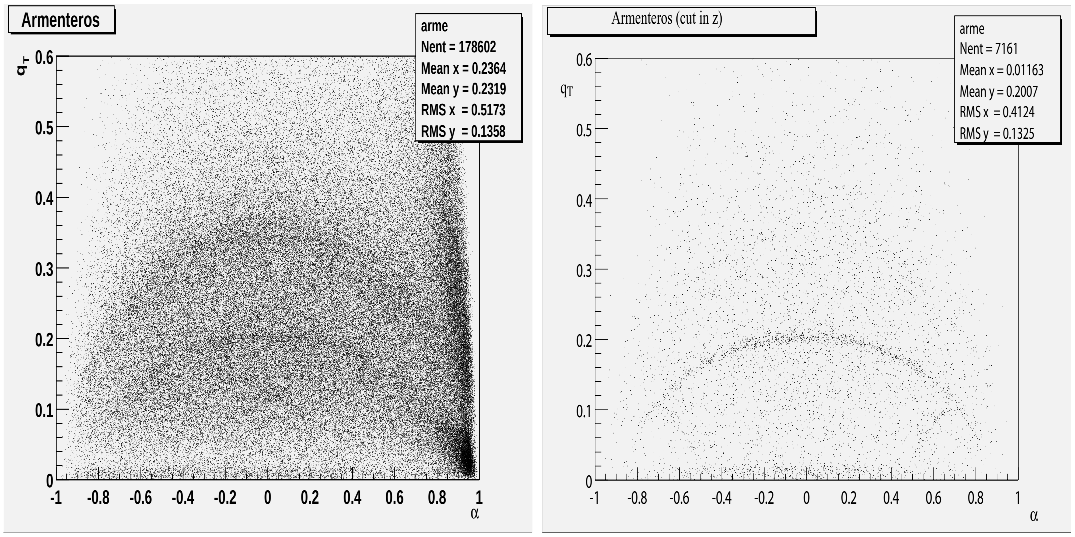

Figure 6.26: The Armenteros-Podolanski plots for a sample of V^0's from year 2001 COMPASS data. In the plot on the left no cut is imposed and the K_S^0 and ρ ellipses can be seen. In the plot on the right, a cut on the kinematical variables makes evident the K_S^0 ellipse as well as the ellipses belonging to Λ's and $\overline{\Lambda}$'s.

$$\cos\theta^* = \frac{\alpha - \lambda}{k} \tag{6.28}$$

$$\sin\theta^* = \frac{q_T^+}{|q^*|} \tag{6.29}$$

As $\cos^2\theta^* + \sin^2\theta^* = 1$, it follows that:

$$(\frac{\alpha - \lambda}{k})^2 + (\frac{q_T^+}{|q^*|})^2 = 1 \tag{6.30}$$

Which is the formula for an ellipse, with semiaxes $\frac{2|q^*|}{\beta m_{V^0}}$ and $|q^*|$, and center $(\lambda\ ,\ 0)$. As a factor β appears in the ellipse parameters, they aren't relativistically invariant. However, as in practice $\beta \simeq 1$ the invariance is obtained as well.

From the definition of λ, the ellipses are centered in $(0,0)$ only if V^0 decays into identical particles as in case of K_S^0 and ρ ($\longrightarrow \pi\ \pi$). Since the decay modes of Λ and $\overline{\Lambda}$ aren't symmetric ($\Lambda \longrightarrow \overline{p}\pi^+$ and $\overline{\Lambda} \longrightarrow p\pi^-$), in V^0's rest frame, $E_+^* \neq E_-^*$ and the corresponding ellipses are antisymmetric w.r.t. the α coordinate.

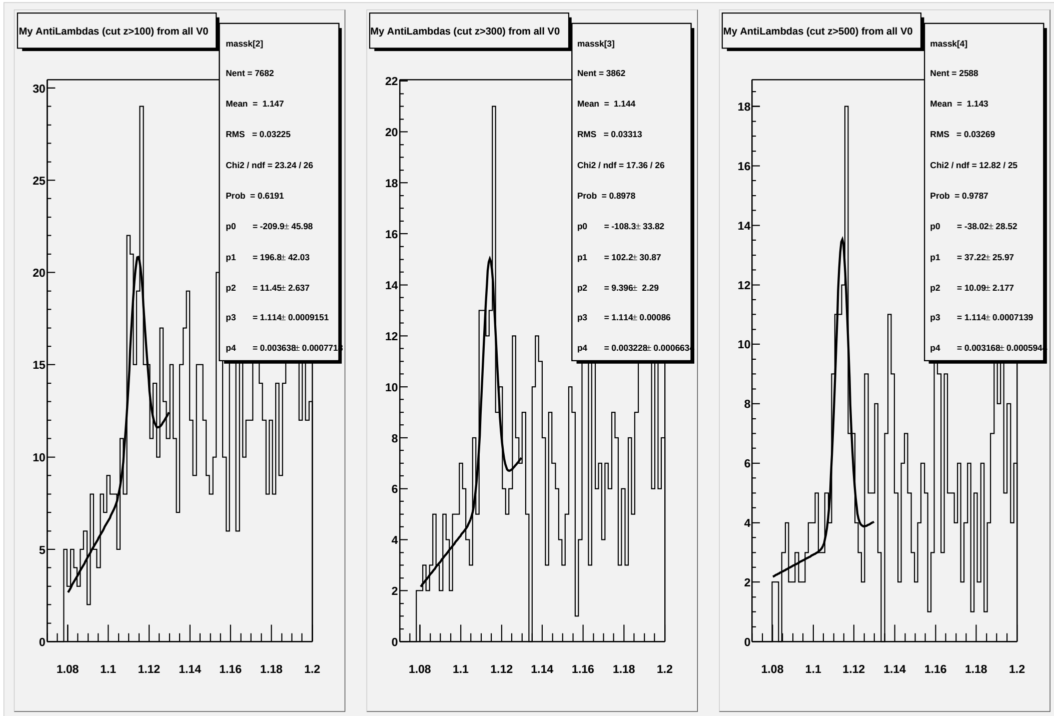

Figure 6.27: Invariant mass distribution of $\overline{\Lambda}$'s from their decay: $\overline{\Lambda} \longrightarrow p\pi^-$. A cuts on Armenteros-Podolanski's p_t variable has been done ($p_t > 10^{-2}$) to clean up the sample from electrons. Different cuts on the z-vertex (from left to right $z > 100,\ 300,\ 600\ mm$) remove part of the background. A gaussian curve peaking from a linear background has been used for the fit.

In figure 6.26 the Armenteros-Podolanski plots for the COMPASS V^0's sample is shown. The ellipses coming from K_S^0, ρ, Λ and $\overline{\Lambda}$ are clearly distinguishable.

6.4.2 The Lambda reconstruction

Performing some cuts on Armenteros-Podolanski variables, an analysis on the invariant mass has been done to find Λ's and $\overline{\Lambda}$'s in the data sample collected in longitudinal polarization.

Λ's and $\overline{\Lambda}$'s signals have been reconstructed for z-vertex coordinate greater than 100 mm (see figures 6.27, 6.28). The shape becomes more clean as much as the sample is taken far away from the target. The centers of the fitted curves have been found at 1.114 GeV which agrees with the world mean value reported by PDG (1.115 GeV).

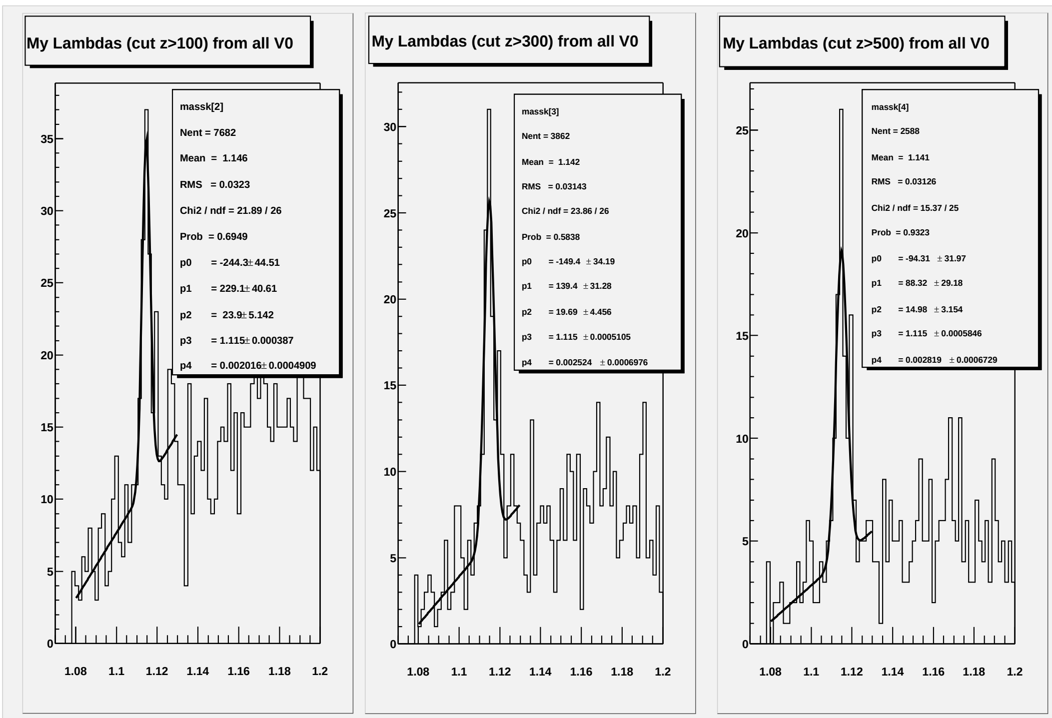

Figure 6.28: As previous plot but for Λ's.

6.4.3 The resolution for K0 mass

In figures 6.29 , 6.30 the V^0's invariant mass is reconstructed making the hypothesis that it's a neutral kaon decaying into two charged pions ($BR \simeq 68.61\%$):

$$K_S^0 \longrightarrow \pi^+ \ \pi^- \tag{6.31}$$

The data are fitted with a linear background and a gaussian signal:

$$f_{K^0}(m) = P_0 \ + \ P_1 \cdot m + \ P_2 \cdot e^{(\frac{m-P_3}{P_4})^2} \tag{6.32}$$

Some different cuts have been done on the vertex z-coordinate in order to clean up the sample. Several good results are obtained:

- the center of the gaussian (P_3) varies between 494.9 and 496.7 MeV, approaching as much the Particle Data Group (PDG) reference value (497.7 MeV) as further the sample is taken from the target;
- the resolution (P_4) varies between 6.8 and 8.0 MeV.

The latter gives a figure for COMPASS spectrometer resolution which is compatible with realistic MC predictions (retrieving about 5 MeV); the difference has to be addressed to the status of detectors' alignment and calibrations.

The good matching of figures 6.29 and 6.30 demonstrates that there is no relevant difference in the particles' reconstruction being in longitudinal or in transverse mode.

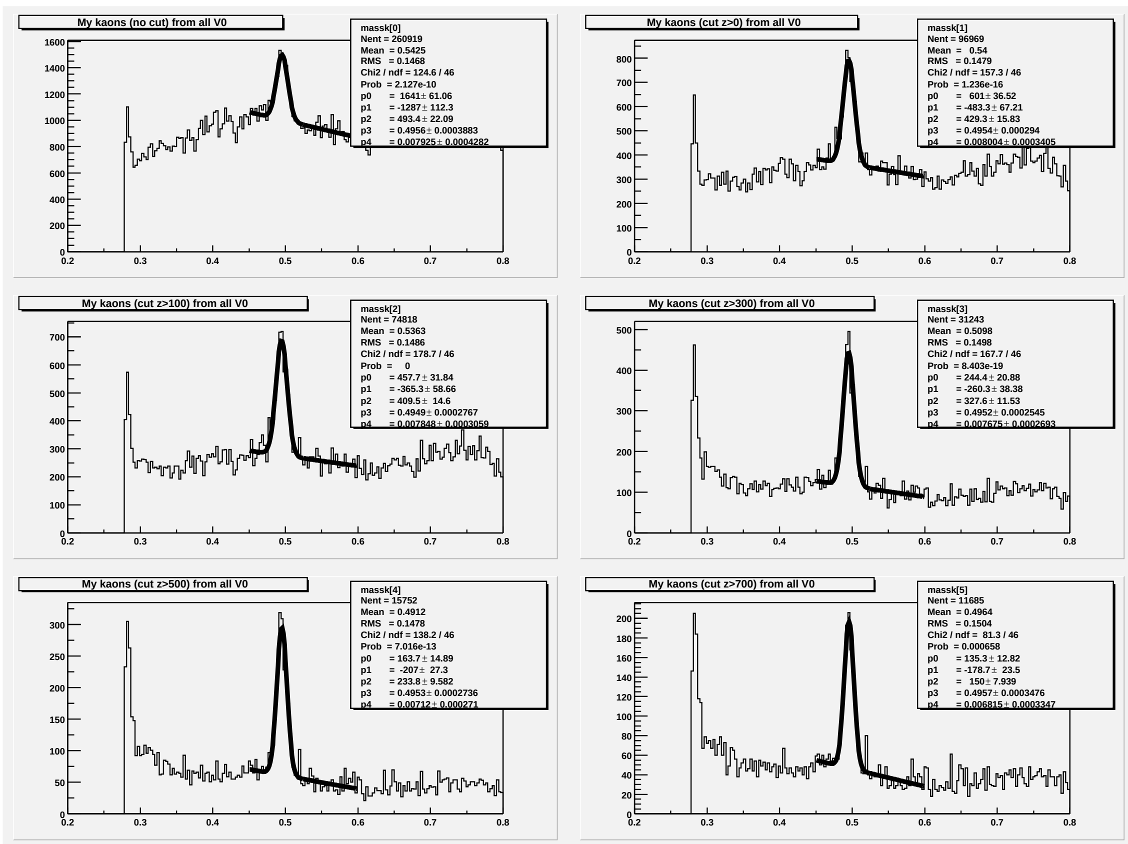

Figure 6.29: Invariant mass distribution for K_S^0's The plots refers to different cuts in the z-coordinate of the vertex. The curve used for the fit consists on a linear background and a superimposed gaussian signal.

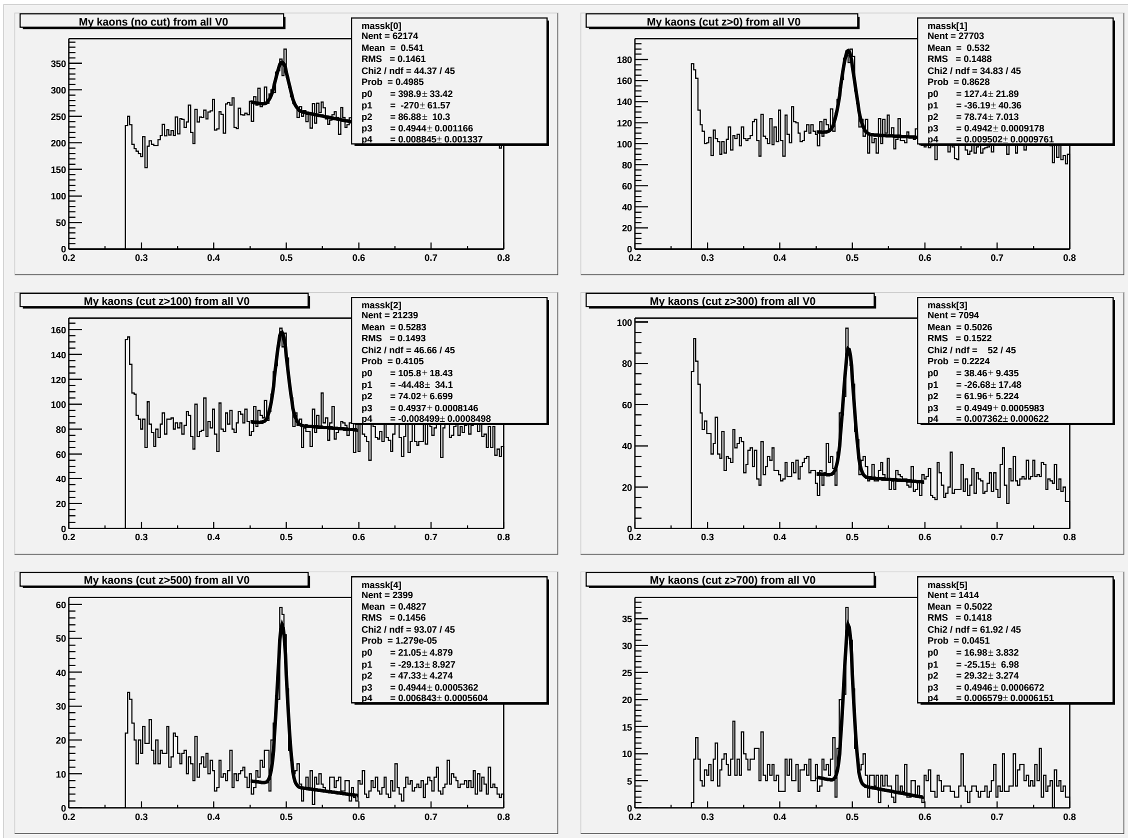

Figure 6.30: Same of figure 6.29 but in transverse case.

6.5 The stability of the Y2001 data

In order to check the stability of the data collected during the year 2001 run, an analysis on some relevant observables has been done.

Big fluctuations have been found in some statistics related to reconstruction of tracks (see figure 6.31), and vertices (see figure 6.32).

Let's call dispersion of an observable, the ratio between the width of the stability band (Δ) and its central value Y. As an example for the stability in the vertex reconstruction, keeping outside of the sample three runs which evidently show some problems in performance, the following results are found:

- the ratio of events with at least 1 vertex shows $\frac{\Delta}{Y} \sim 80\%$;
- the ratio of events with the primary vertex with and without extra tracks shows $\frac{\Delta}{Y} \sim 110\%$.

This change in the reconstruction performances has to be addressed to the work on the floor made on the detectors during the beam time.

No such fluctuations have been seen in the year 2002 data.

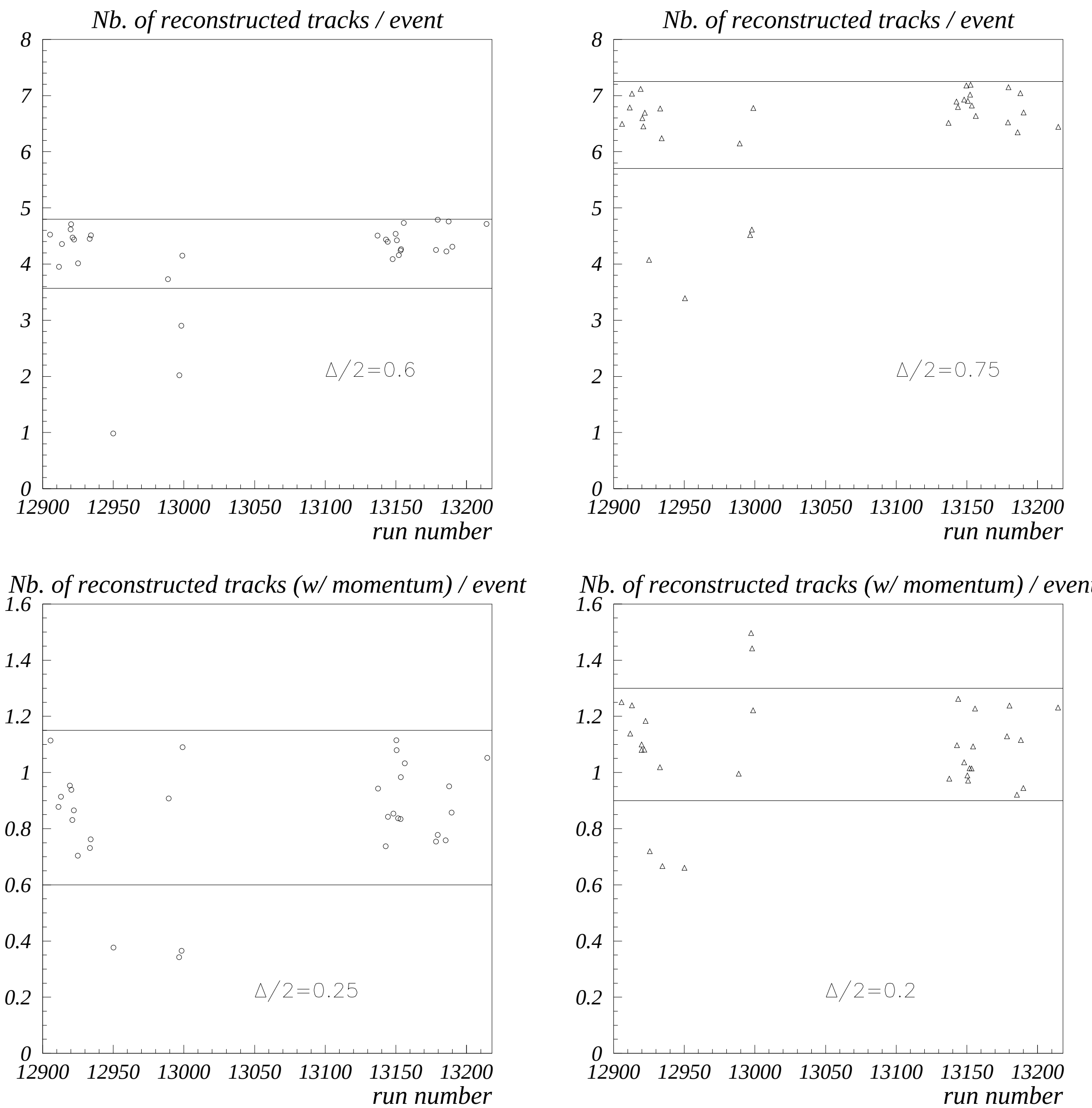

Figure 6.31: Top: Mean number of reconstructed tracks in I and II spectrometers with and without momentum as function of run number (left for the first, right for the second spectrometer); Bottom: Mean number of reconstructed tracks in I and II spectrometers with momentum (left for the first, right for the second spectrometer);.

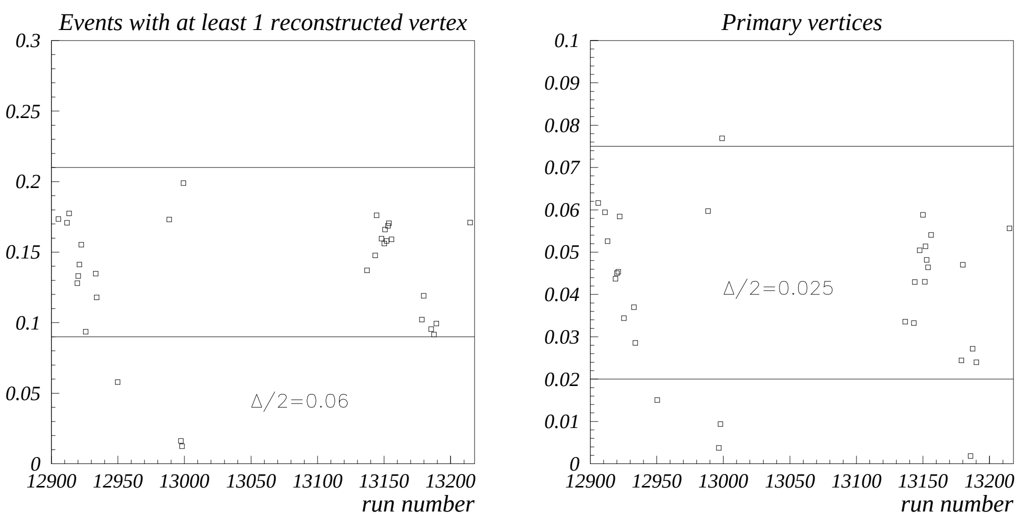

Figure 6.32: Left: Ratio of events with at least 1 vertex; Right: ratio of events with the primary vertex with and without extra tracks.

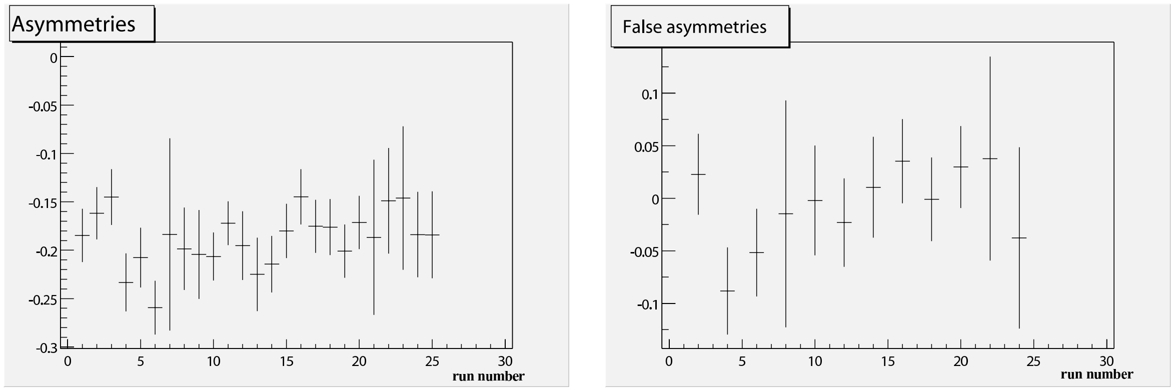

Figure 6.33: The asymmetries defined in equation 6.33 and the false asymmetries defined in equation 6.34 from year 2001 data sample.'

6.5.1 An example of asymmetry

An example of asymmetry has been computed along the whole data sample taken in longitudinal polarization, looking at primary vertices with an extra track:

The asymmetry to evaluate is:

$$\mathrm{A} = \left(\frac{\Leftarrow - \Rightarrow}{\Leftarrow + \Rightarrow}\right)_K \tag{6.33}$$

where $\Leftarrow$ is the number of vertices found in the upstream cell and $\Rightarrow$ those found in the downstream cell. This observable is widely dominated by the difference in acceptance between the two target's cells (see left plot in figure 6.21).

Dividing the data sample into runs' pairs without taking care of the spin direction (whose effect in the asymmetry is not of the leading order) one can compute the false asymmetry:

$$\mathcal{FA} = \left(\frac{\Leftarrow - \Rightarrow}{\Leftarrow + \Rightarrow}\right)_K - \left(\frac{\Leftarrow - \Rightarrow}{\Leftarrow + \Rightarrow}\right)_{K-1} \tag{6.34}$$

The result for the false asymmetries, shown in the right plot of figure 6.33, demonstrates how the data are widely inhomogeneous but still compatible for the big statistics error to be associated to each point.

6.6 Present status of the reconstruction

All in all the 2001 data have been useful to:

- study the response of single and groups of detectors;
- characterize the vertices w.r.t. to their topology (primary and secondary vertices search);
- check the resolution of the apparatus via the reconstruction of the V^0 resonances;
- to check the behaviour of the spectrometer in transverse polarization;
- develop the algorithms to verify that a sample of data is stable in the reconstruction of some general observables.

The present status of COMPASS software is much further than the results shown in this chapter. These examples have been reported in order to mention the jobs I took part in and to trace a sort of guide-line towards the preliminary physics results proposed in chapter 7 for the case of the data collected with transverse polarized target.

In this context, I'd like to add some general results obtained by the collaboration analyzing the data collected in year 2002 which demonstrate how the reconstruction has improved. In figure 6.34, the $\pi^+\pi^-$ and $p\pi^-$ are shown. For $\pi^+\pi^-$ a cut on hadron transverse momentum ($p_t > 30$ MeV/c) has been applied whilst in both the distributions the vertex is reuired to have a z coordinate greater than 45 cm. At bottom the Armenteros plot demonstrates the region populated by K_0, Λ's and $\overline{\Lambda}$'s.

In figure 6.35, the K^+K^- invariant mass distributions is shown to demonstrate the performance of RICH. All figures have been cut on transverse momentum ($p_t > 20$ MeV/c). Top figure gives distribution with pure combinatorial search. For the middle figure it is required the one of tracks to be identified. For bottom figure the identification of both tracks is required. To identify the track as a kaon the cut on the mass spectrum (computed from Cherenkov angle and track momentum) is set: if momentum of the track is higher than the RICH threshold of kaon, a further cut is applied in the region $\pm$ 100 MeV around the nominal kaon mass. In case it's lower than the RICH threshold, the track is rejected when its mass is under the pion peak ($\pm$ 100 MeV).

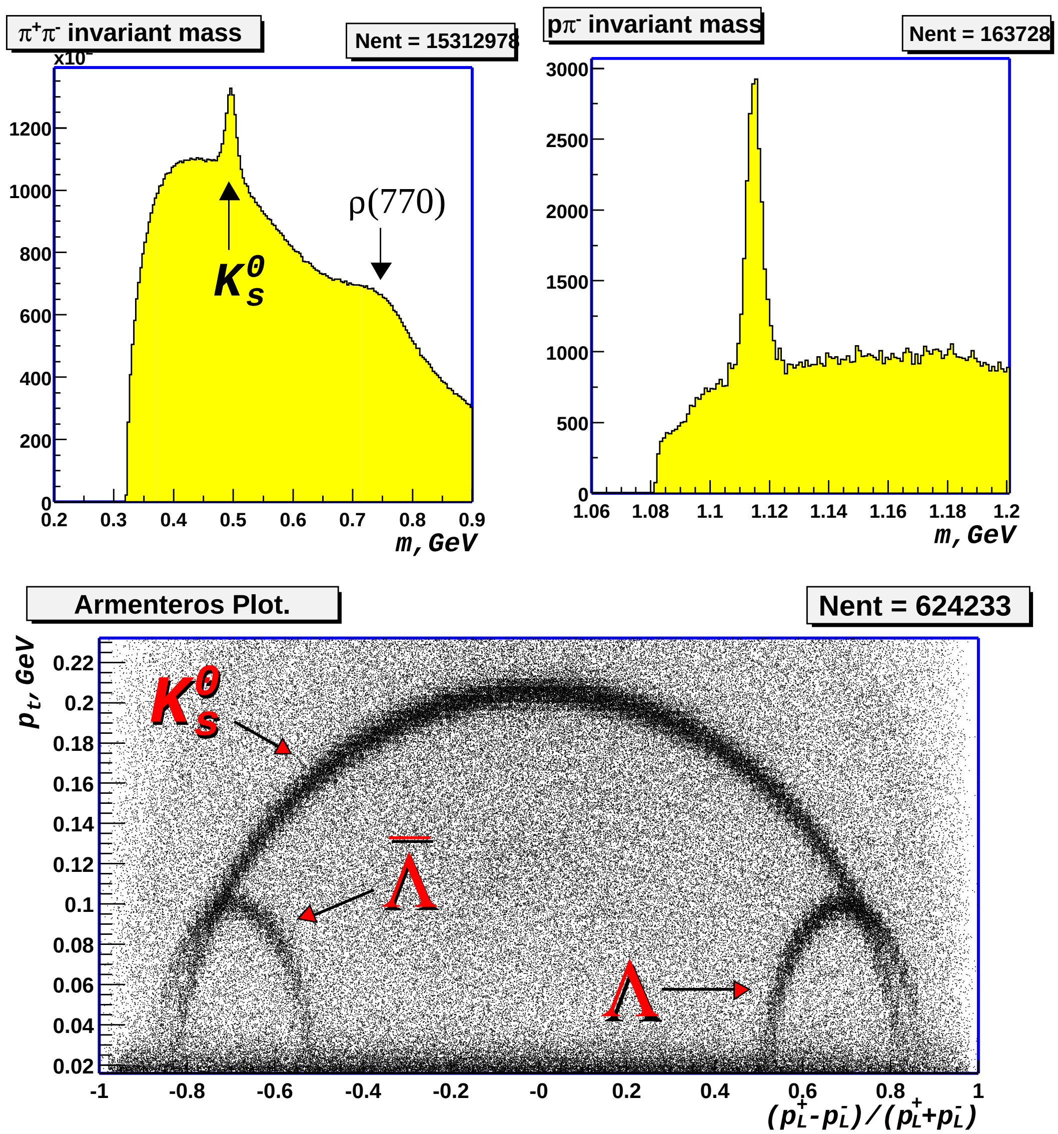

Figure 6.34: Invariant mass distribution for $\pi^+\pi^-$ and $p\pi^-$ where the clear peaks of K_0 and $\rho(770)$, $\bar{\Lambda}$'s are seen. The same resonances located in the Armenteros plot.

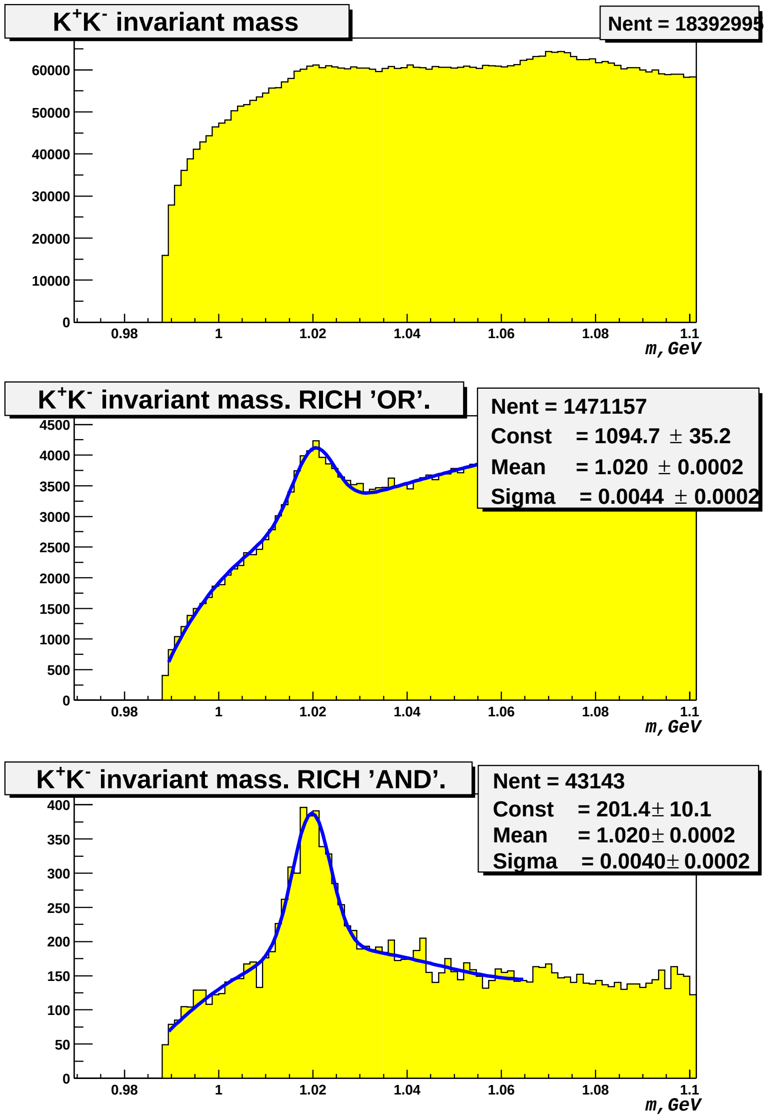

Figure 6.35: Invariant mass distribution for K^+K^- with pure combinatorial (plot on the top), requiring at least one (plot in the middle) or both the tracks (plot on the bottom) to be identified as kaons by RICH-1. The statistics corresponds of half of the day of smooth data taking.

Chapter 7

The analysis results for year 2002

7.1 The data acquisition

The data taking period started on May 27th and ended on September 18th (114 days). The data were taken in the same beam conditions of the previous year.

The data flux to tape (in GB/day and in integrated GB) is sketched in figure 7.1: the design maximum value of 3 TB to store per day has been exceeded.

This amount of data corresponds to an average efficiency in the DAQ which has approached 70% at the end of the run. This number is comprehensive of the efficiency of the SPS and target operation. The detailed behaviour of the various contributions are shown in figure 7.2 where the periods devoted to transversity measurements is also put in evidence.

The spectrometer in year 2002 has already been described in details in chapter 3. Data have been taken in both the longitudinal and transverse target directions (see section 3.3.2). In figure 7.3 the polarization of the two target cells as function of the time (in days) is shown.

The whole run can be divided into several periods. These periods are identified by the name of the Objectivity federation which handles the data. The names of the federations remind the SPS periods (e.g. P1C, P2A) but are adjusted to the physics conditions of the DAQ.

Starting on June 18th, the longitudinal polarization (periods P1B, P1C, P2A) has been held until July 31st when we switched to transverse polarization (period P2B). Due to a cooling failure of the target magnet, the polarization was lost on August 1st and rebuilt in a couple of days. On August 7th, the direction of the polarization in both cells was changed by the Microwave Reversal procedure (period P2C). Afterwards, another long period of

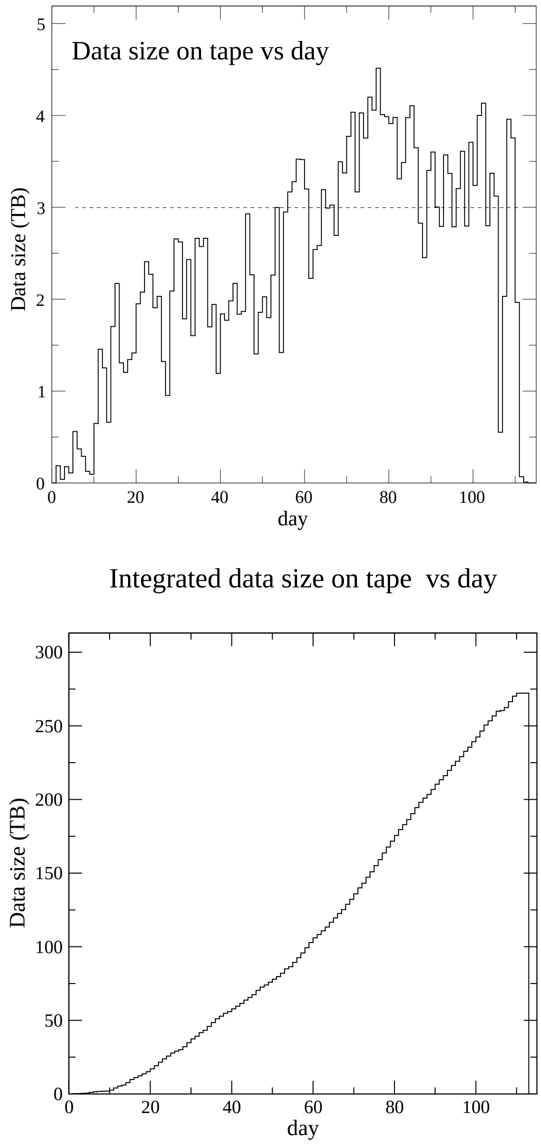

Figure 7.1: The data flux from the building 888 to the CCF as function of the time for Y2002 COMPASS run. The first plot shows the behaviour of the transfer day by day. The second plot is the integral curve of the first.

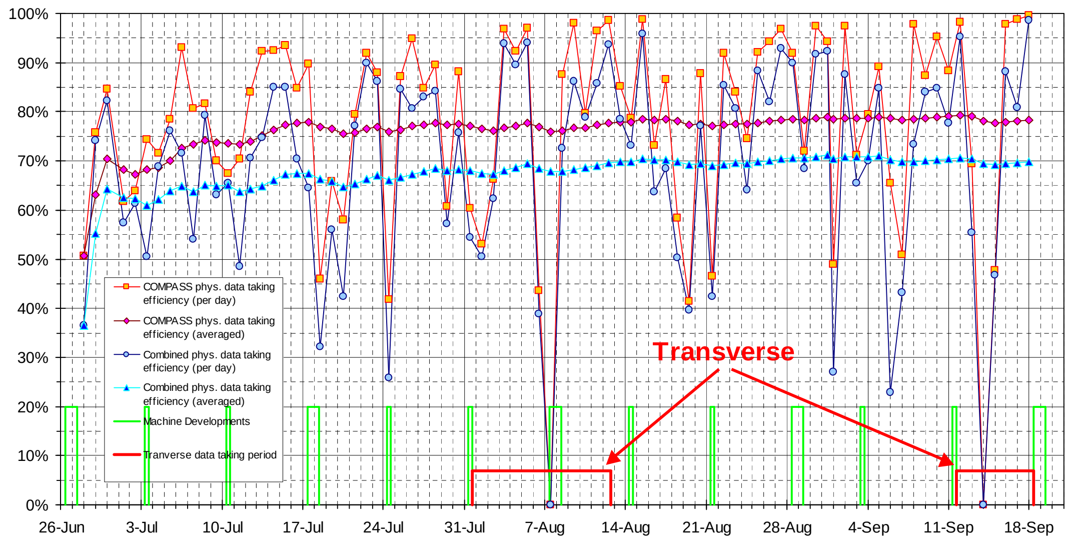

Figure 7.2: The DAQ efficiency as function of time during the 2002 COMPASS run. The meaning of the various data points are explained in the legend box.

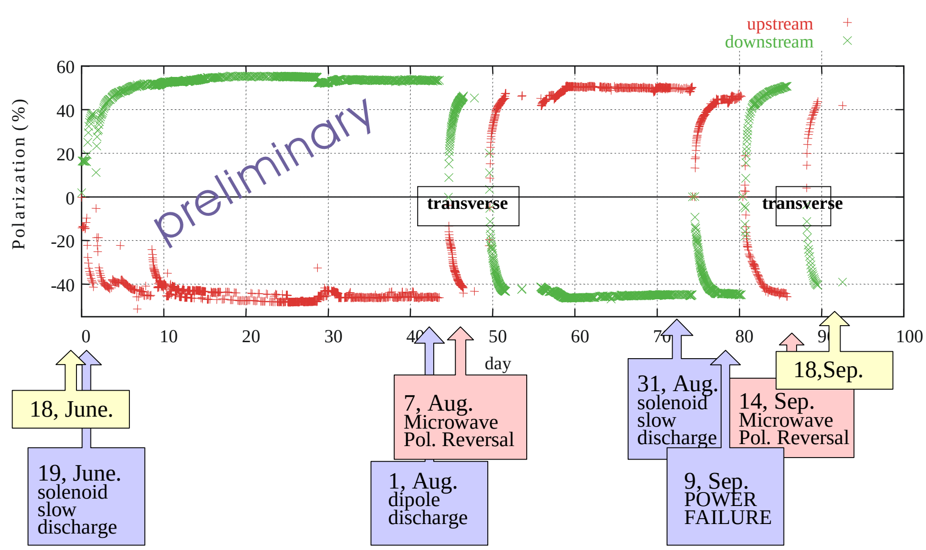

Figure 7.3: Polarization achieved in the two ^6LiD target cells during the year 2002 run.

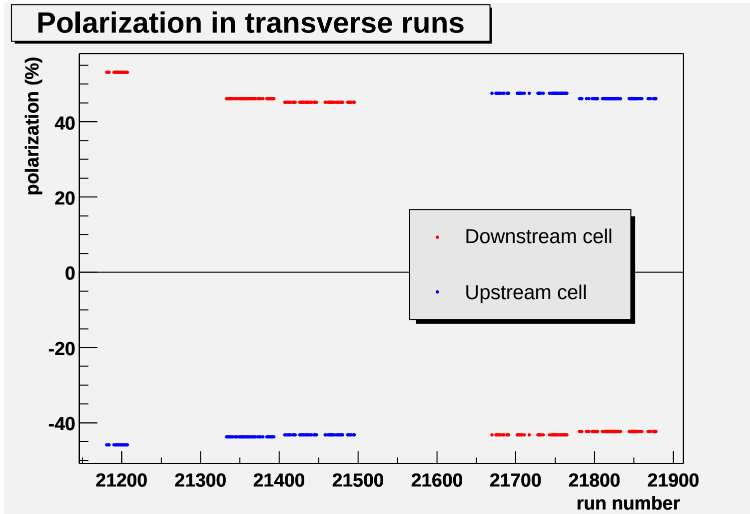

Figure 7.4: Polarization for the runs processed in the DST production.

longitudinal polarization (periods P2D, P2E, P2F, P2G) started on August 13th and ended with a power failure of the magnet on September 9th. Finally a week of DAQ has been again devoted to transversity (period P2H) with a Microwave reversal in the middle (September 14th).

7.2 The analysis goals

This chapter deals with the preliminary observation of transversity-related effects in leptoproduction for transversely polarized target in COMPASS.

As mentioned in chapter 5 the CORAL version used to produce the DSTs is still preliminary and the results coming from this pre-analysis cannot be taken as conclusive. Still this work has been extremely useful to prepare the necessary off-line tools and to identify all the problems.

The analysis reported in the following sections refer to about 2/3 of the statistics, i.e. to the first two periods listed in table 7.1. Following the procedure described in section 5.3, CORAL has produced the DSTs of about 200 runs for a total data size of about 20 TB (input) to 1.3 TB (output). The polarization of the two target cells (zooming figure 7.3 into the first two periods devoted to transversity) is reported in figure 7.4 whereas the mean

Period	Pol. UP & DOWN	Processed Runs	Mean value of Pol. UP & DOWN
P2B: 31/7/2002 $\longrightarrow$ 6/8/2002	$\Downarrow\Uparrow$	114	-43.8% 46.7 %
P2C: 8/8/2002 $\longrightarrow$ 12/8/2002	$\Uparrow\Downarrow$	102	46.8 % -42.7 %
P2H: 11/9/2002 $\longrightarrow$ 18/9/2002	$\Downarrow\Uparrow + \Uparrow\Downarrow$		

Table 7.1: Periods of DAQ in transverse polarization.

1D-histo	Number of tracks as function of event number
1D-histo	Number of tracks with momentum as function of event number
1D-histo	Number of primary vertices as function of event number
1D-histo	Number of secondary vertices as function of event number
1D-histo	Distribution of number of tracks in total and for different zones (*)
1D-histo	Total number of clusters per event
1D-histo	Total number of clusters per plane
2D-histo	Detector unique ID vs. number of clusters per event
242 $\times$ 1D-histo	Detectors' profiles
(*)	before the target, before SM1 between SM1 and SM2, between SM2 and MA after MA

Table 7.2: The monitoring histograms used for DST commissioning.

values for the polarization of each cell are reported in table 7.1 [1].

This data sample has been scrutinized to check the general performances of the apparatus as function of the run number. Having passed this stability check, the data can be treated as homogeneous and used to extract the Collins asymmetry.

7.3 The stability of Y2002 data

To monitor the performances of the apparatus, the stability of a number of observables has been checked as function of time, *i.e.* run number. The observables which are monitored are listed in table 7.2:

[1]From figure 7.4 the sample appears to be inhomogeneous in the sense that the target, before the dipole discharge, showed a stronger polarization. Waiting for the definitive NMR measurements, the figures reported in table 7.1 refer to the polarization after August 1st.

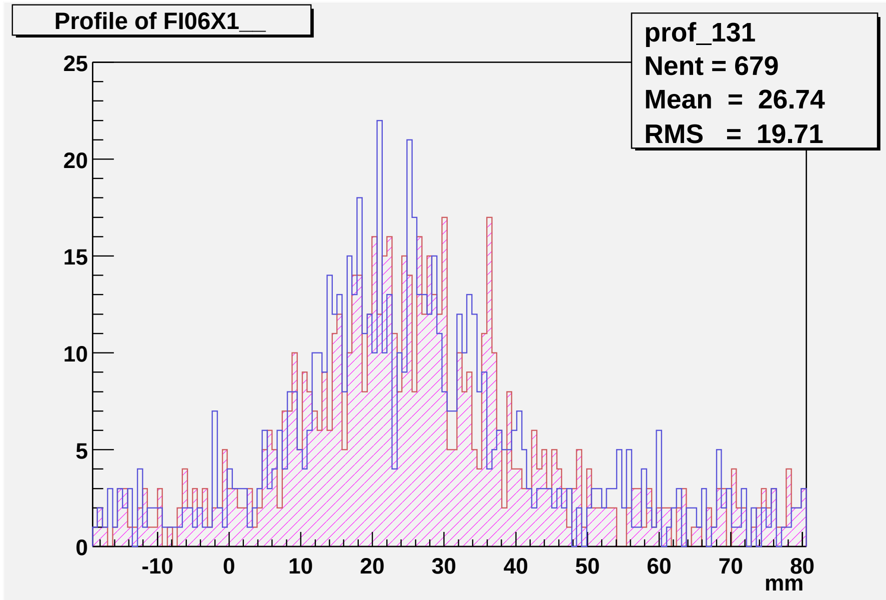

Figure 7.5: An example for the monitoring of the profiles for each tracker plane. Two profiles of SciFi6X taken from two runs have been superimposed.

The detectors profiles have been compared to a set of reference ones taken from a run which hasn't shown any anomaly. In figure 7.5 an example of such comparison is shown for the case of the plane SciFi6X.

For the other set of observables, some fluctuations have been found in the distributions of primary and secondary vertices between the first two "blocks" of runs. The fluctuations in secondaries are less strong than in case of primaries.

These fluctuations could be due to some hardware activity performed onto the detectors in the time spent to repolarize the target after the cooling failure which has killed the magnetic field of the dipole (see section 7.1). Since the alignment file has been produced from a run collected after August 1st, that hardware activity has made it less compatible with the previous configuration of the spectrometer.

Apart from specific pathologies found in several runs which have been excluded from the analysis, the data reveal an intrinsic instability in the vertex reconstruction. The drift in the vertex reconstruction efficiency seen in figure 7.6 can be due to the limited validity of the alignment table (see section 5.3.1).

The collaboration has already decided that, in the next years, more attention will be

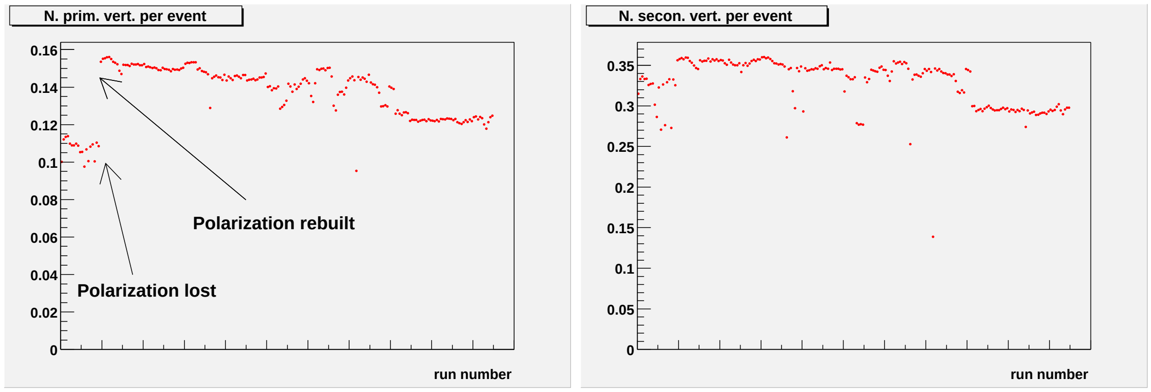

Figure 7.6: The vertex reconstruction efficiency for primaries and secondaries as function of the run number. In the primary vertex a large effect is visible after the time spent to repolarize the target. The effect in case of secondaries is much smaller.

devoted to the alignment and more alignment files will be taken within a single period.

Other jumps in the distributions are observed in the total number of clusters per event and per plane (see figure 7.7). The connection between this decrease of clusters with the pathology found in the vertex distribution is not clear. Moreover no piece of information about some noisy detector planes has been found in the run logbook which may validate such connection.

Anyhow, these hypothetical noisy front-end cards have not corrupted the tracking efficiency which appears much more stable than the vertex reconstruction (see figure 7.8). This could show how, at the level of CORAL (making use of TRAFDIC tracking package, see section 5.2.4), the vertex reconstruction is much more critical than the tracking with respect to the alignment.

What still remains unclear are the big fluctuations found for reconstructed tracks in the region upstream the target (plot in the second row, at left in figure 7.8) where the only trackers are Silicons and SciFis.

One remark is mandatory. The DST pre-production for the transverse period has started in October 2002. At that time, no mapping was available to decode the data coming from Muon Wall 1 (MA) which is crucial to identify the muons scattered at high Q^2. Furthermore the Very Large Area Trackers (W4/5) suffered of a very preliminary (and quite imprecise) alignment. Big misalignment in almost all the trackers have been found and cured by several members of the collaboration during the last months.

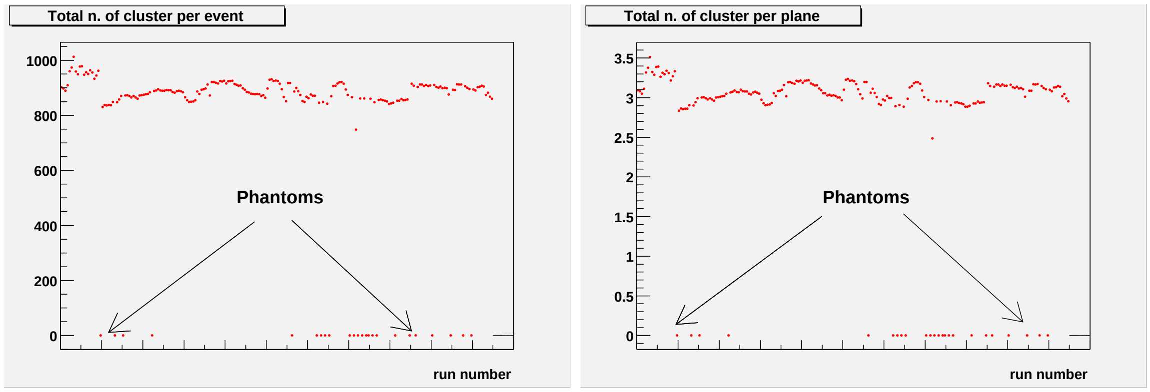

Figure 7.7: The total number of clusters per event and per plane traced along the data sample. The points at 0 don't represent empty clusters but refer to the runs processed before the implementation of the profiles' monitoring.

Although these elements shouldn't insert in the data some bias (e.g. wrong tracks and a fortiori vertices), the sample suffers of a big inefficiency in the detection of tracks scattered at large angles.

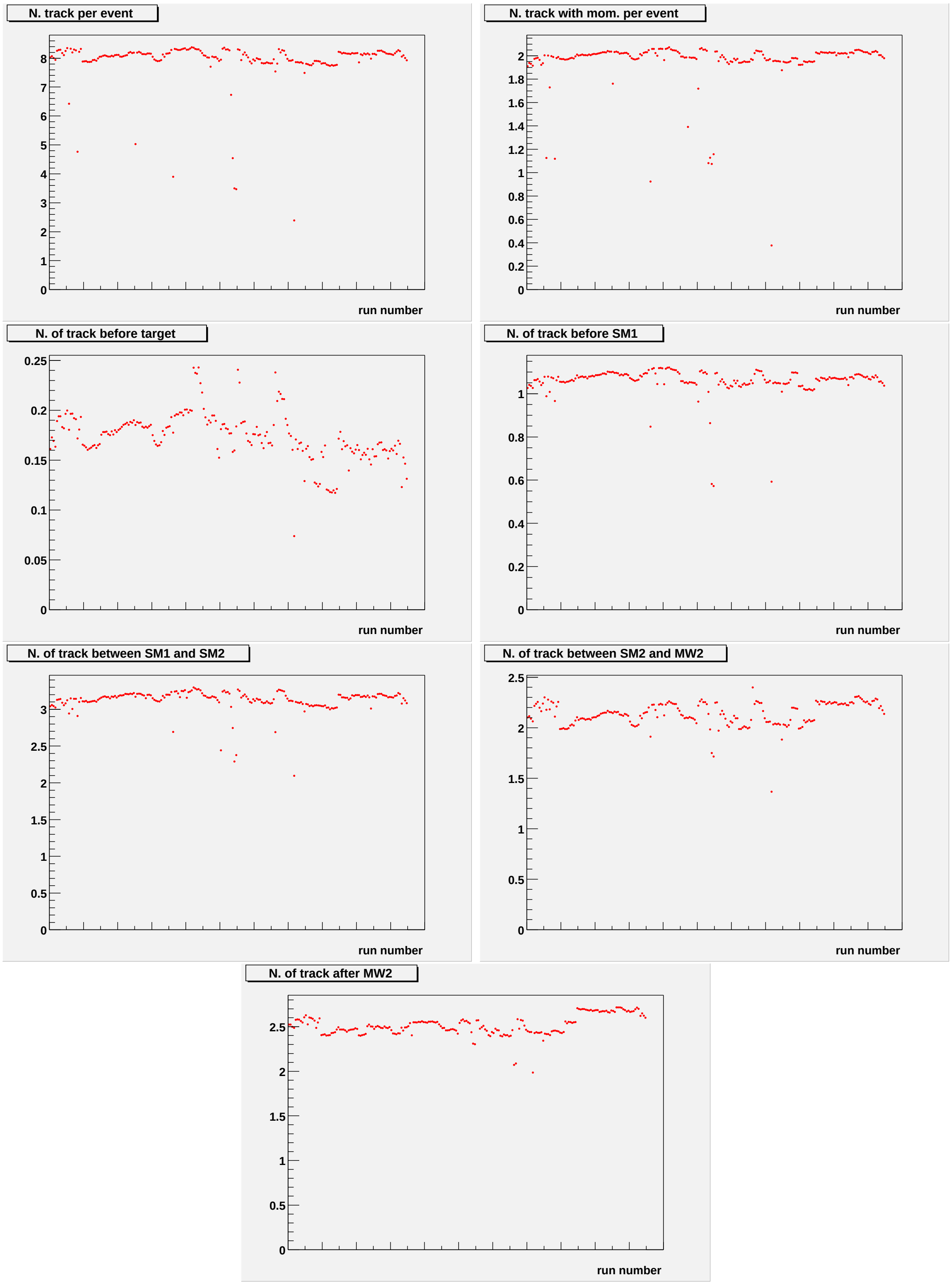

Figure 7.8: The total numer of reconstructed tracks/event with and without momentum. The number of tracks/event reconstructed in different zones of the spectrometer as specified in table 7.2.

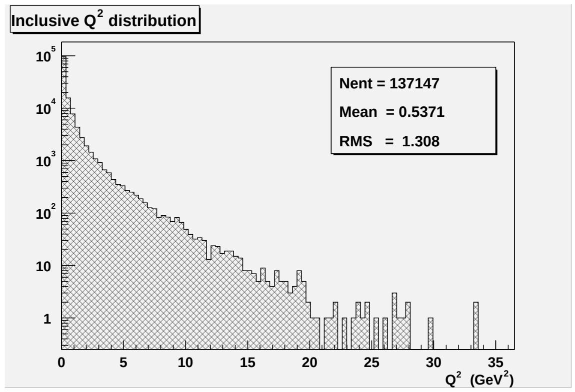

Figure 7.9: The total Q^2 distribution of the primary vertices reconstructed from the DSTs.

7.4 The kinematics

Once the DSTs have been produced and have undergone the tests described so far, a further analysis, directly done on the DSTs, can be done to reconstruct the kinematics of the events. In the inclusive reactions, the Q^2 distribution (shown in figure 7.9) can be derived from the values of the beam and the scattered muons' momenta.

The different kinematical ranges covered by the triggers' modules can be selected on the basis of the trigger mask written on the Event Headers. The "digit structure" of this experimental word (trigger mask) reflects the multiple "OR" of the trigger systems (see table 3.5). In the figures 7.10, 7.11 and 7.12 the experimental Bjorken variables reconstructed by the various modules are shown. The events triggered by simultaneous signals coming from more than one trigger subsystem have been excluded from the shown plots.

From figure 7.10, it's clear that the logical coincidence with the calorimeter cleans the ν distribution for the Middle Hodoscopes from the low energy component present without such requirement (Inclusive Middle Hodoscopes). Furthermore the Ladder Hoscopes trigger at high value of ν whereas the Outer Hoscopes trigger both the component of low and high energetic virtual photon events. From figure 7.11, one sees that the events at high x, those whose weight is more important in our measurements, mostly come from triggers given by the Outer and the Inclusive Middle Hodoscopes; in figure 7.12 the corresponding distribution in Q^2 is shown.

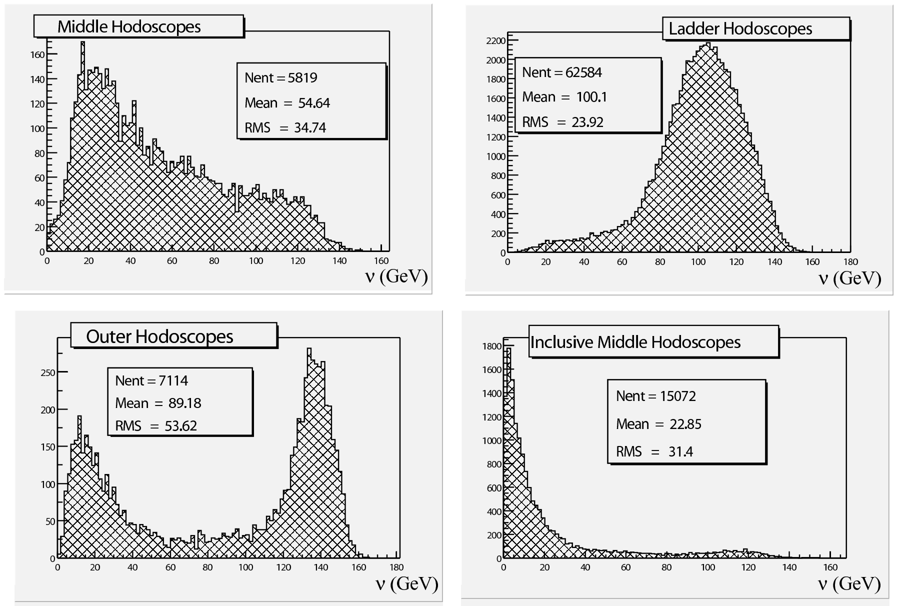

Figure 7.10: The ν variable reconstructed in the different trigger hodoscopes.

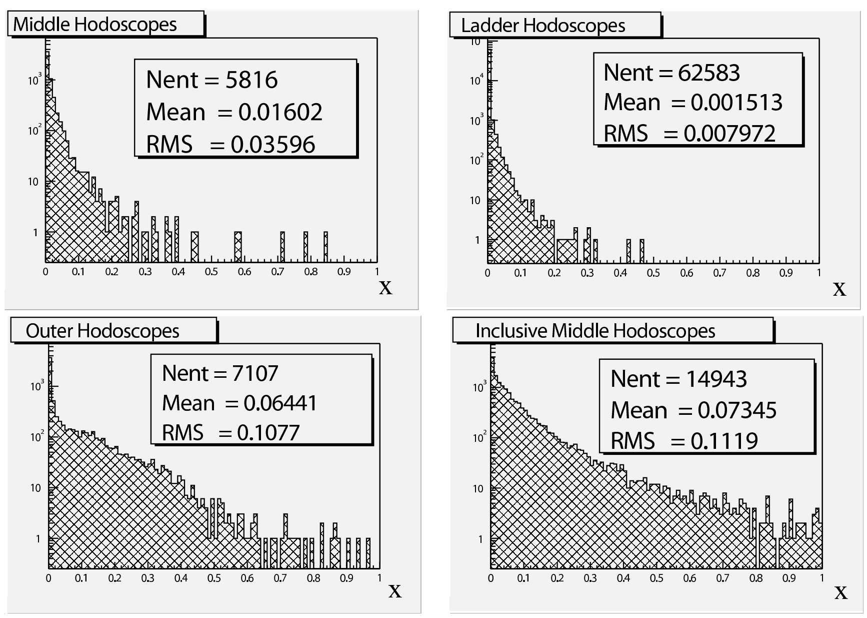

Figure 7.11: The x variable reconstructed in the different trigger hodoscopes.

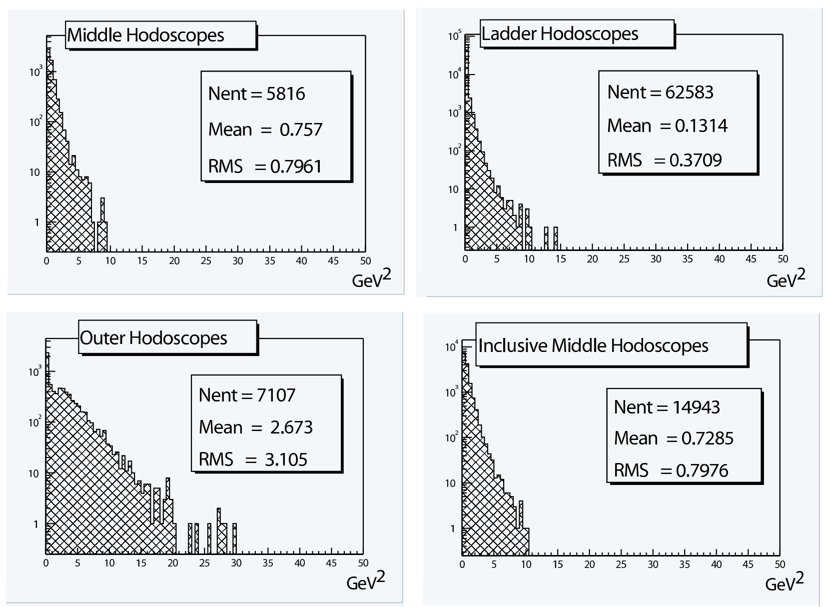

Figure 7.12: The Q^2 variable reconstructed in the different trigger hodoscopes.

7.5 The data analysis

To calculate the Collins asymmetry starting from the DSTs so far produced, one needs, first of all, to reconstruct, by mean of the program whose principle scheme is shown in picture 7.13, the semi-inclusive events: namely those in which the incoming, the scattered muon and at least one hadron have been reconstructed with momenta and their tracks point to the same vertex.

The distribution of the vertex z coordinate (analogous to that shown in figure 6.22 for the data collected in year 2001) is shown in figure 7.14.

To associate to each event a correct polarization, the events whose vertices don't fall well inside the target cells have been rejected. The vertex z coordinate distributions and the direction of the spin associated to each target cell are shown in figure 7.15.

Due to the poor trigger purity, to the misalignment of the Large Area Trackers and to the fact that the tracking algorithms are not yet well tuned, only a very small fraction of events enter the data analysis. In table 7.3 the number of analyzed events in which a primary vertex with an extra hadron track is compared to the total amount of decoded events. The conclusion is that only 2.5% of the events stored into the DSTs can be used in the analysis of semi-inclusive reactions.

	events decoded ($\times 10^6$)	events with $\mu\ \mu'\ h$ ($\times 10^6$)
P2B	177	4.4
P2C	214	5.1
Total	391	9.5

Table 7.3: The number of raw triggers in the data sample and the ratio of events useful to calculate the Collins asymmetry.

The Collins angle should not be computed for all these events because not all of them come from DIS, as apparent from figure 7.16 which shows the $x - Q^2$ range covered by the data. In section 7.5.1, the various recipes to select the interesting events are discussed.

The algorithm to transform the reference system from the lab to the Breit frame is well explained in [8] and [68]. Once this transformation is done, a routine implemented in CORAL calculates:

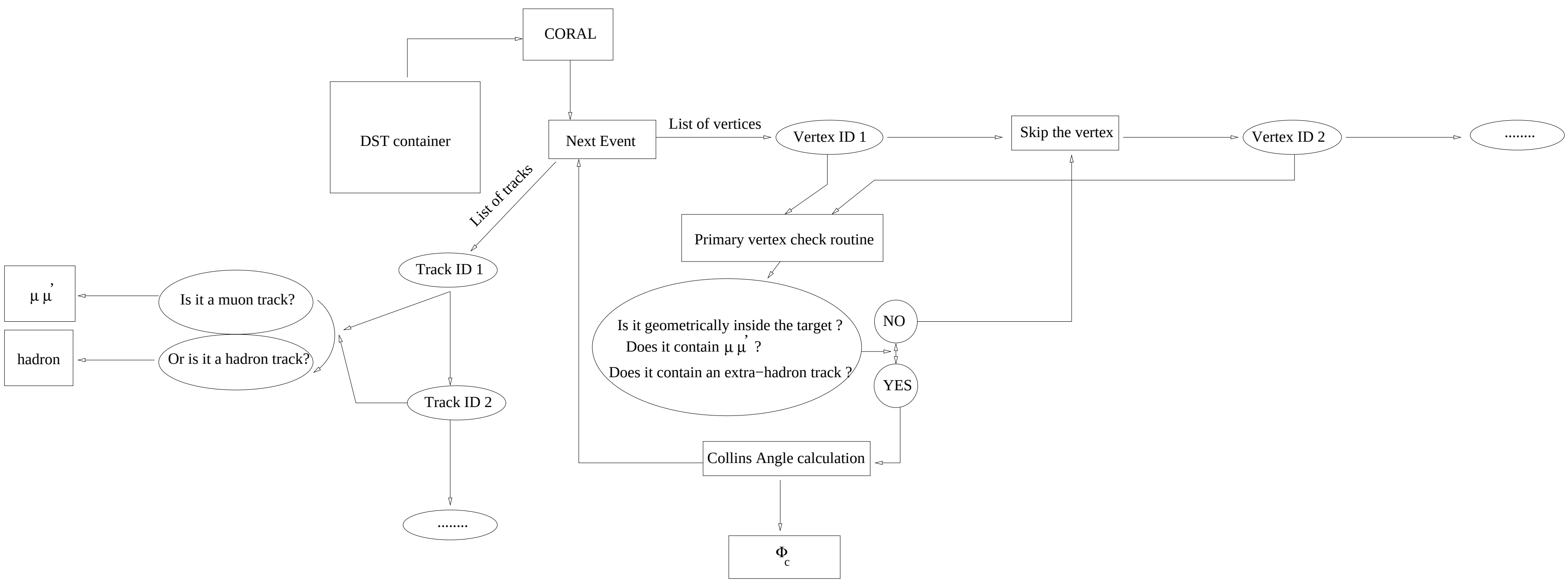

Figure 7.13: The flow-chart of the analysis program which calculates the Collins angle distribution from the DSTs.

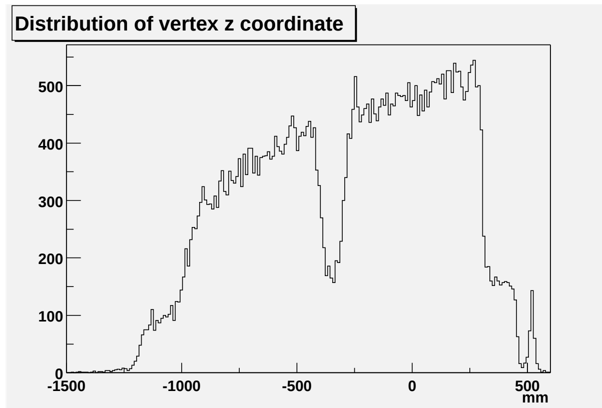

Figure 7.14: Z coordinate distribution of each primary vertex found in presence of an extra hadron track.

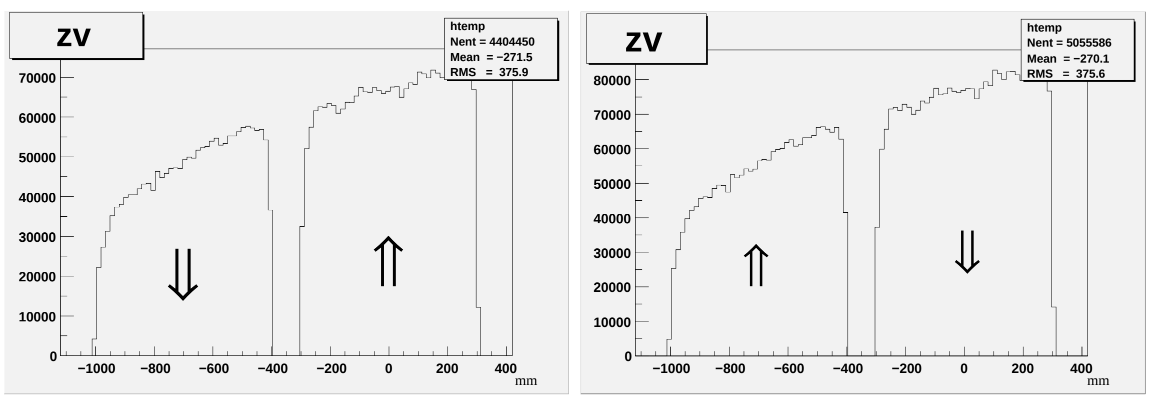

Figure 7.15: The population in the two cells and the spin orientation for both P2B and P2C statistics.

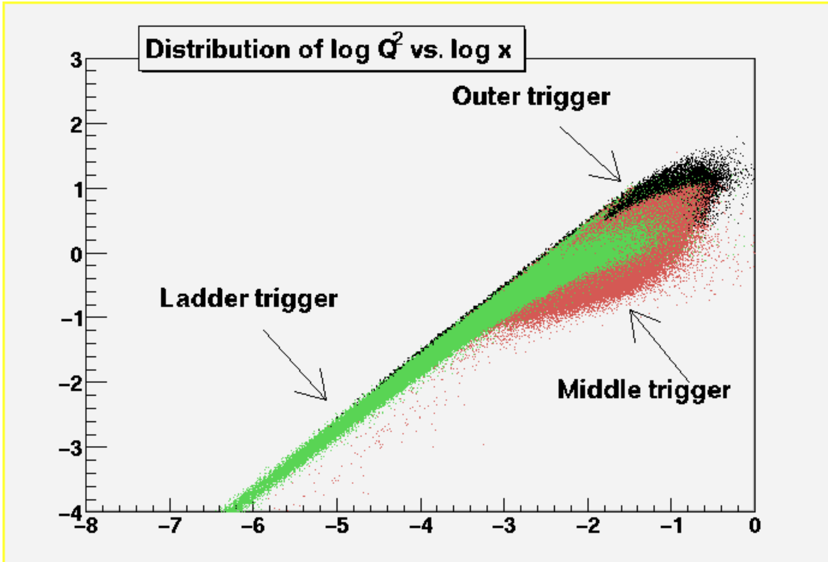

Figure 7.16: The log x - log Q^2 kinematical coverage in case of primary vertices with extra tracks for the different trigger hodoscopes.

the azimuthal angle Φ_h for the leading hadron;

the azimuthal angle of the spin vector Φ_S;

the Collins angle $\Phi_C \;=\; \Phi_h + \Phi_S - \pi$.

The result for each target cell should show an oscillation along Φ_C whose amplitude ϵ depends from transversity:

$$N_{\uparrow\downarrow}(\Phi_C) \;= N_0\,(1 \pm \epsilon \sin \Phi_C) \tag{7.1}$$

where the raw asymmetry ϵ is defined as the product of the Collins asymmetry A by the mean value of the polarization P_T, the dilution factor f and the depolarization factor D_{NN}:

$$\epsilon = A \cdot P_T \cdot f \cdot D_{NN} \tag{7.2}$$

In this thesis we will evaluate ϵ, being the studies on the dilution factor and the polarization of the target cell still in progress.

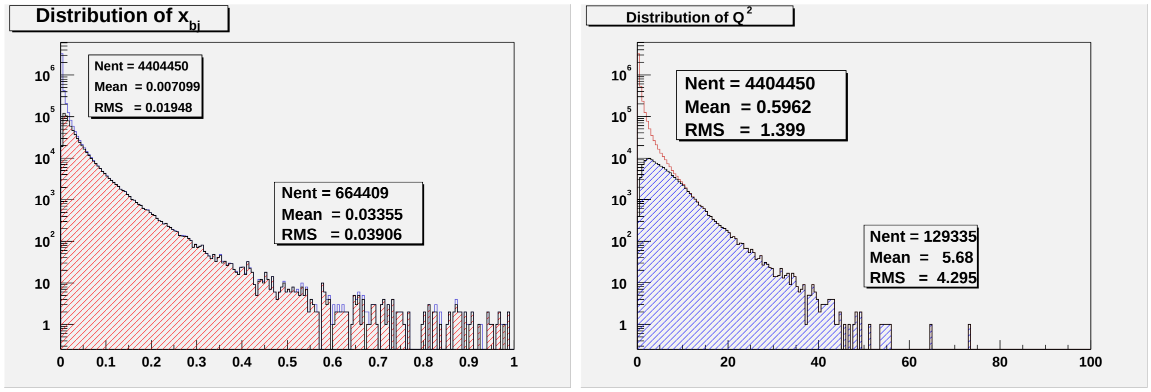

Figure 7.17: The x and Q^2 kinematical coverage in the events entering the data analysis. On the total x distribution, the events with $Q^2 > 1\ GeV^2$ are superimposed. On the total Q^2 distribution, the events with $x > 0.05$ are superimposed.

7.5.1 The Data filtering

To extract from the data the events coming from a Deep Inelastic Scattering of the virtual photon off a parton in the target, the region of $Q^2 > 1$ GeV^2 has to be investigated.

In figures 7.17, 7.18 and 7.19 the distributions in the following variables are presented:

x, and Q^2;

y and the depolarization factor D_{NN} defined in equation 1.49;

z and p_t (transverse momentum) of the leading hadron.

The complete sample and the distributions obtained after the kinematical cut (if any) specified in the figure captions are superimposed.

To have an idea of the useful statistics, the kinematical cuts described in section 7.6, have been applied to the COMPASS data and compared with SMC and HERMES (see table 7.4).

7.5.2 Systematics effects

The Collins angle can be affected by systematic uncertainties deriving from the "intrinsic" asymmetries coming from the apparatus. These asymmetries arise from the fact that both the scattered muon and the hadron aren't detected with the same efficiency at every angle.

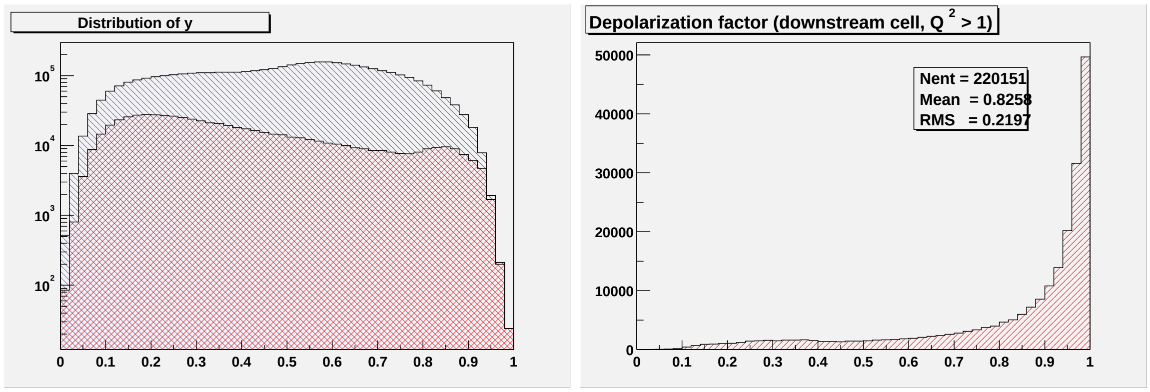

Figure 7.18: The y distribution for all the events and for the ratio passing the cut ($Q^2 > 1\ GeV^2$). For the last sample, the depolarization factor calculated on the downstream cell is also shown.

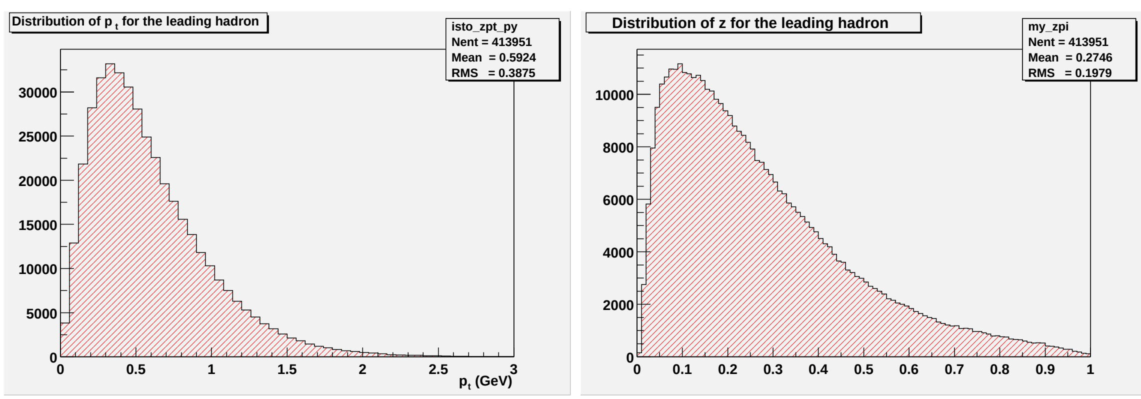

Figure 7.19: The distribution in z and p_t for the positive leading hadron.

	Hermes 2000 (*)	SMC 1999 (**)	COMPASS 2002
Q^2 (GeV^2)	$[1; 15]$	> 1	> 1
γ N invariant mass (GeV)	> 2		
photon energy (GeV)		> 10 (15)	
x	$[0.023; 0.8]$		
y	< 0.85	< 0.7	
z	$[0.2; 0.7]$	> 0.25	> 0.25
transverse hadron momentum	> 50 MeV/c	> 100 (500) MeV/c	> 100 MeV/c
Number of events		250 Kevt $(\pi^+ + \pi^-)$	343 Kevt (π^+)
$< Q^2 >$ (GeV^2)	2.2	5	2.6
$< x >$	0.15	0.08	0.045

Table 7.4: Comparison of the COMPASS kinematical coverage (after the cuts described in section 7.6) with the one of SMC and HERMES (see chapter 2).

As an example of the COMPASS spectrometer acceptance, the distribution in the azimuthal profile of the leading hadron is shown in figure 7.20. Moreover, as it has been shown in section 6.5.1, the acceptance in the upstream target is much lower ($\sim 20\%$) than downstream.

These reasons don't allow to directly use eq. 7.1 to calculate the Collins asymmetry. It has been suggested that the effects of a non uniform geometrical acceptance of the spectrometer might average out in the calculation of the Collins angle, and the Collins asymmetry could be extracted from data taken with only 1 orientation of the target polarization. A systematic study of this possibility is ongoing [69].

In this thesis we will compute the Collins asymmetry in the straightforward way, *i.e.* by comparing in each target cell the data taken with opposite polarization: we analyze the events reported in table 7.3 accordingly to their polarization, i.e. we define two independent samples of data. The two periods show some differences in the useful statistics (i.e. in the ratio of the events passing the cuts, see section 7.6) because of the difference in the number of processed events and in the efficiency of $\mu\mu' h$ vertex reconstruction.

In each of the periods again two independent samples of data can be created for the upstream and downstream target cell.

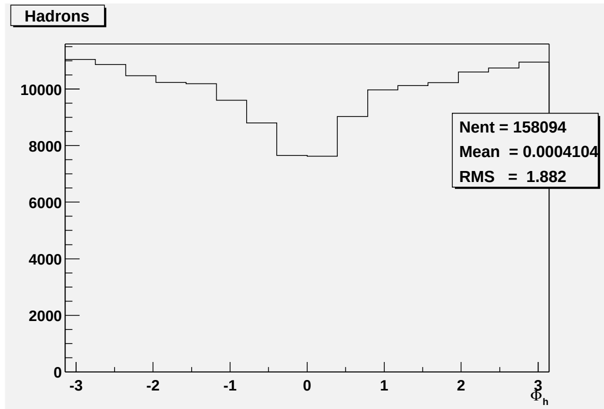

Figure 7.20: The azimuthal distribution of the leading hadron (with standard kinematical cuts, see section 7.6) in the Breit reference frame.

7.6 Is there a signal of transversity?

From now on, even if it's not explicitly said, the case of positive hadrons will be discussed. The kinematical cuts we apply are the following:

- $Q^2 > 1$ GeV^2;
- $z > 0.25$;
- $p_t > 0.1$ GeV/c.

The analysis has been performed dividing the data in the x bins listed in table 7.5 where also the relative number of events is given.

The raw asymmetries in the Collins angle have been calculated independently for each subsample from the following quantities:

$$A^d(\Phi_C) = \frac{N^d_{\uparrow\ P2B} - R^d \cdot N^d_{\downarrow\ P2C}}{N^d_{\uparrow\ P2B} + R^d \cdot N^d_{\downarrow\ P2C}} \qquad R^d = \frac{N_d^{tot,\ P2B}}{N_d^{tot,\ P2C}} \tag{7.3}$$

$$A^u(\Phi_C) = \frac{R^u \cdot N^u_{\uparrow\ P2C} - N^u_{\downarrow\ P2B}}{N^u_{\downarrow\ P2B} + R^u \cdot N^u_{\uparrow\ P2C}} \qquad R^u = \frac{N_u^{tot,\ P2B}}{N_u^{tot,\ P2C}} \tag{7.4}$$

where $R^{u(d)}$ are normalization factors given by:

Period	Upstream Cell					
	$x < 0.02$	$0.02 < x < 0.05$	$0.05 < x < 0.10$	$0.10 < x < 0.15$	$x > 0.15$	tot
P2B	25K	23K	9K	2K	1K	60K
P2C	29K	27K	11K	2K	1K	70K
P2B + P2C	54K	50K	20K	4K	2K	130K
Period	Downstream Cell					
	$x < 0.02$	$0.02 < x < 0.05$	$0.05 < x < 0.10$	$0.10 < x < 0.15$	$x > 0.15$	tot
P2B	34K	36K	19K	5K	3K	98K
P2C	40K	42K	22K	6K	4K	115K
P2B + P2C	74K	78K	41K	11K	7K	213K

Table 7.5: Useful statistics in bins of x for positive hadrons.

$$R^u = \frac{N_u^{tot,\ P2B}}{N_u^{tot,\ P2C}}\ ; \qquad R^d = \frac{N_d^{tot,\ P2B}}{N_d^{tot,\ P2C}}\ . \tag{7.5}$$

$N_{u(d)}^{tot,\ period}$ are the number of events entering the analysis for each period and reconstructed in the upstream (downstream) cell.

The distributions coming from each subsample are shown in figure 7.23 and 7.24. Each distribution, defined as in eq. 7.4 has been fitted, with a sine curve defined as:

$$A_i^{u(d)}(\Phi_C) \ = \epsilon_i \sin \Phi_C \tag{7.6}$$

where ϵ is the experimental measurement of the Collins asymmetry and the index i refers to the fitted subsample. Each fits gives an independent set of parameters ϵ^i. Three values for the asymmetry (one per target cell and the weighted mean of the first two) are associated to a single interval in x. The uncertainty of the experimental value for the raw Collins asymmetries comes from the fitting method and takes into account only the statistical errors.

In figure 7.21, the values of ϵ^i are plotted in the different bins of x.

All the experimental measurements are compatible with 0 and no clear signal of transversity is visible. Anyhow the experimental points are still compatible with the theoretical predictions recently presented about the signal of transversity from positive leading hadrons and transverse polarized deuterated targets [70], as it can be seen from figure 7.22.

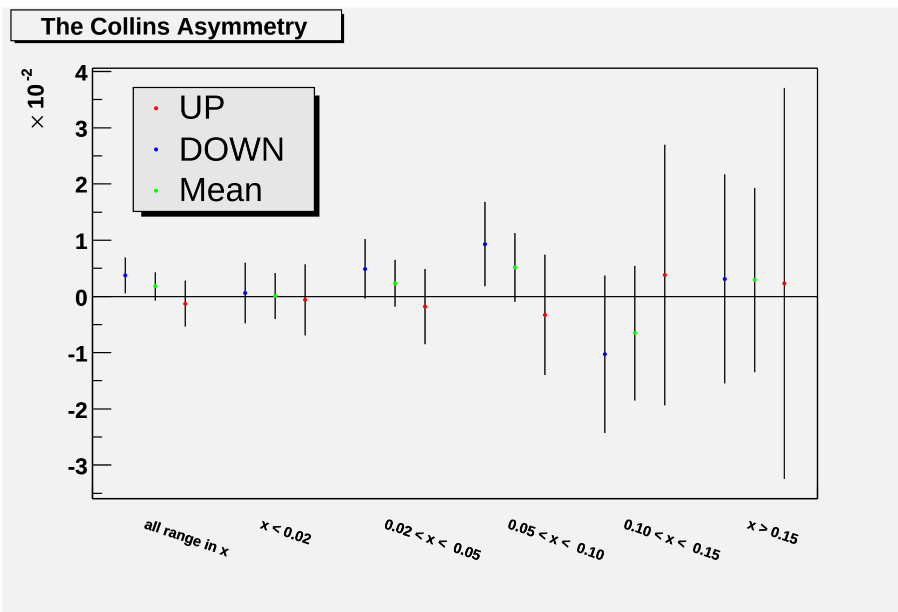

Figure 7.21: The raw Collins asymmetry in bins of x with its the statistical uncertainty.

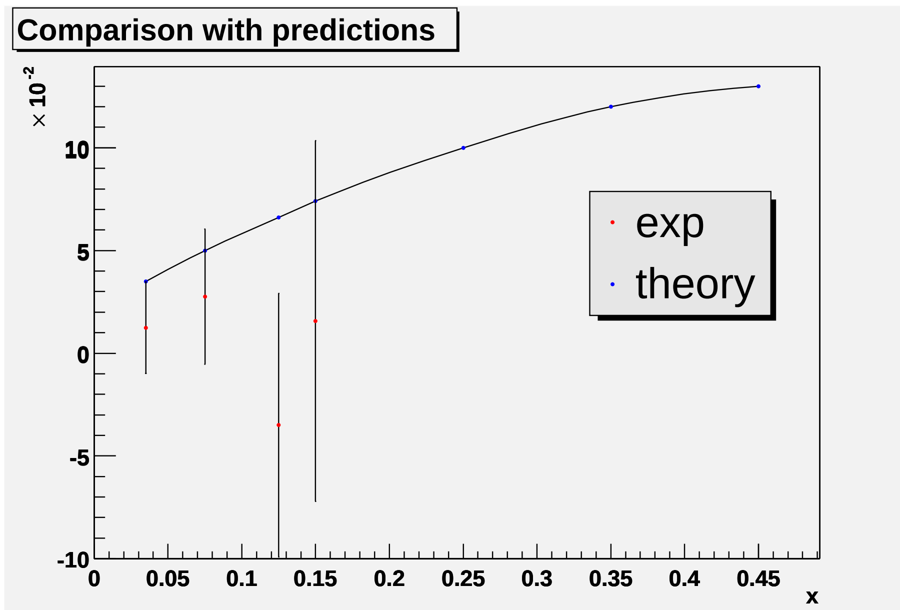

Figure 7.22: The experimental Collins asymmetry in bins of x compared with the theoretical predictions by Efremov. Several assumptions have been done on the values of the dilution factor (= 0.5), mean polarization (= 0.45) and depolarization factor (= 0.83).

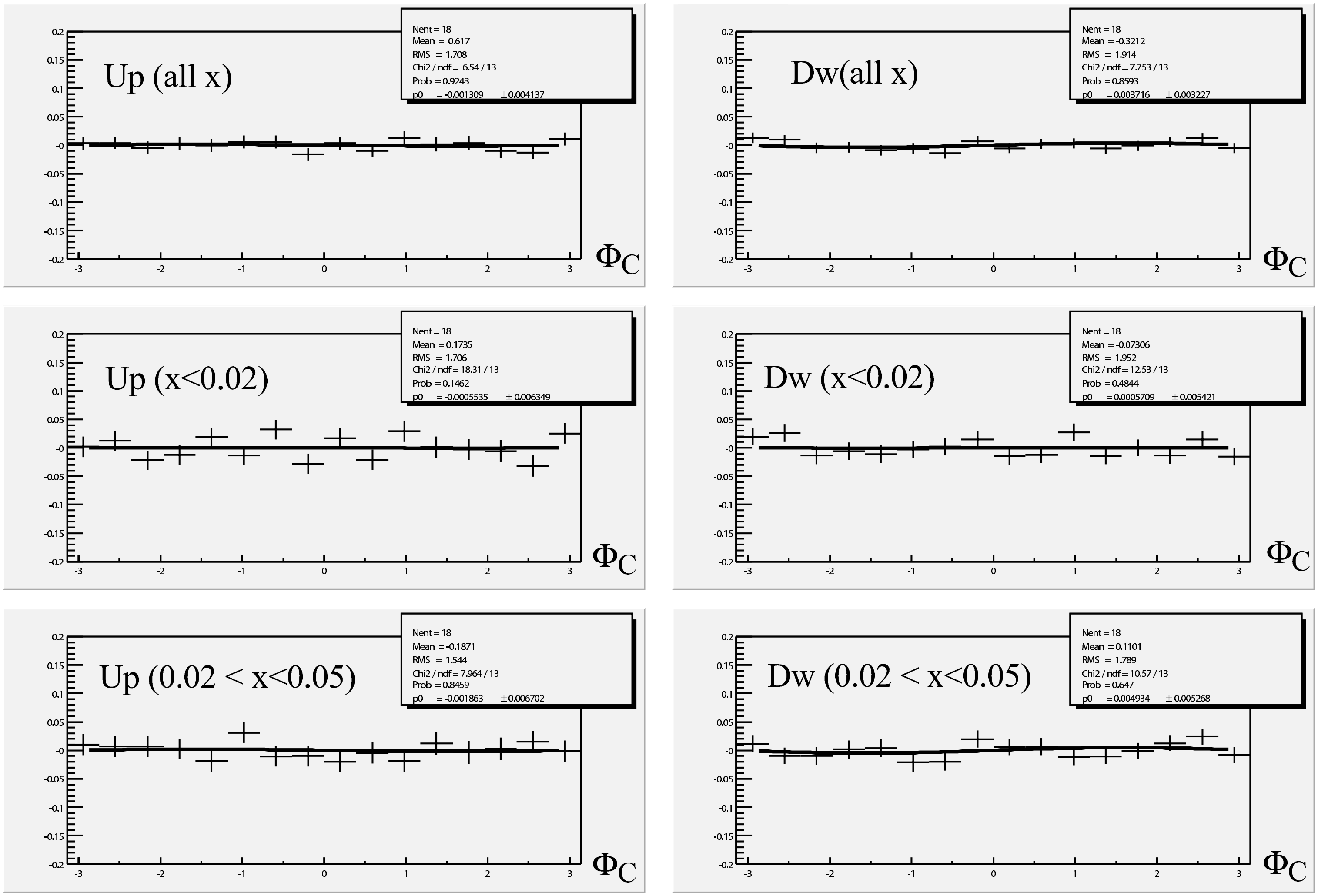

Figure 7.23: The distribution in Φ_C for the raw asymmetry calculated separately for upstream and downstream target cell and for the various subranges in x.

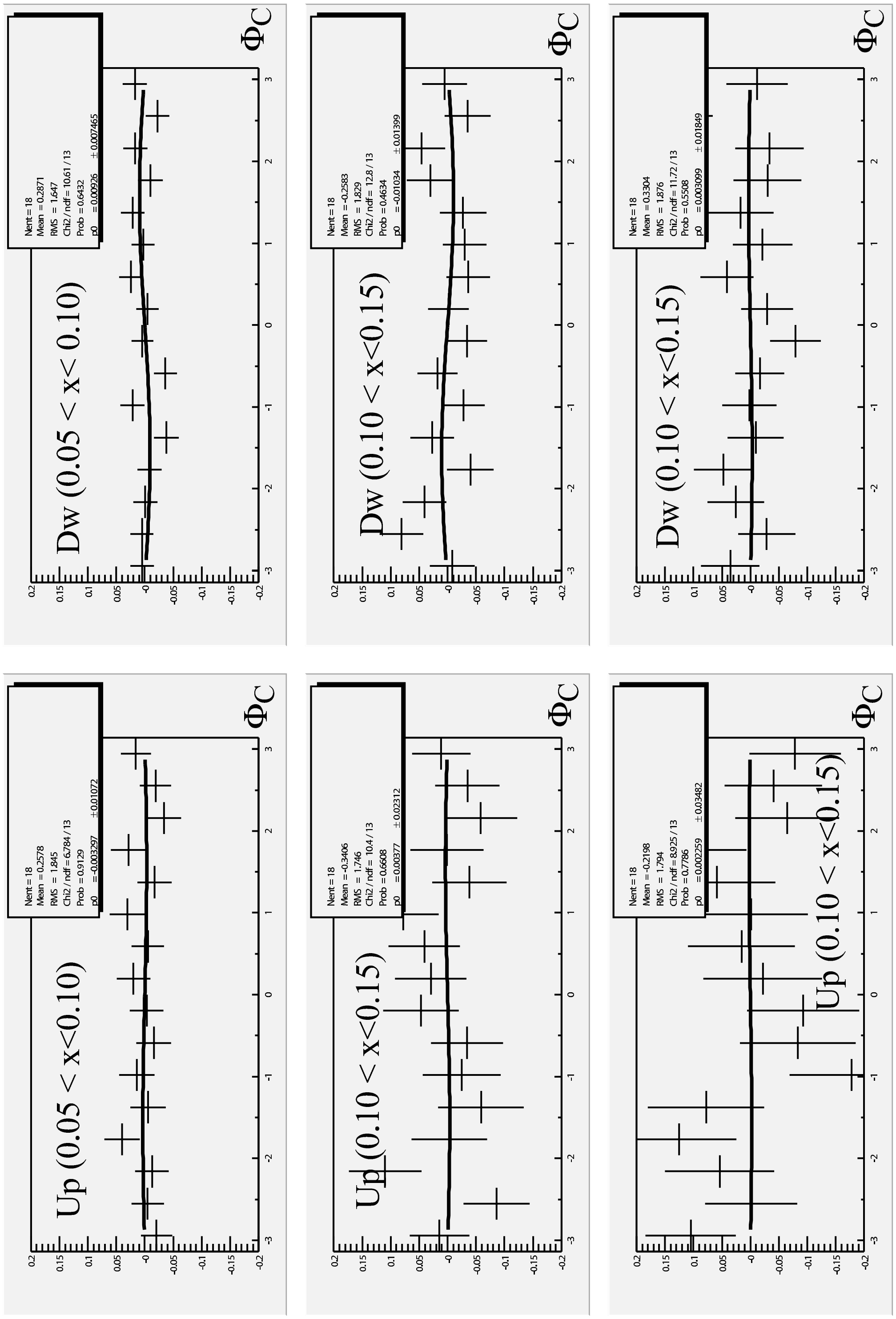

Figure 7.24: Same of figure 7.23.

7.7 Estimates of the overall reconstruction efficiency

The events analyzed in so far suffer from the inefficiencies of the tracking and trigger systems. These inefficiencies add to that coming from the reconstruction program and reduce the statistics of the data entering the analysis. In what follows, by a simple recipe, we calculate the CORAL reconstruction efficiency for semi-inclusive DIS events with the kinematical cuts and in the various bins of x described in section 7.6.

The number of expected events in the run 21472, made up of 100 spills, is given by:

$$N_i^{exp} = \Phi^{spill} \times n_{tot} \times a \times \sigma_i^{DIS} \times 100 \tag{7.7}$$

where Φ^{spill} is the muon flux reduced by the DAQ dead time, n_{tot} is the number of nucleons per unit surface present in the target, a is the combined acceptance given by the solenoid magnet and the trigger hodoscopes and σ_i^{DIS} the cross section for the SIDIS events for the different bins of x.

The number N^{exp} is related to the measured statistics N^{meas} by the following relation:

$$N^{meas} = N^{exp} \times R \tag{7.8}$$

where R is the overall reconstruction efficiency.

Taking the value of the muon flux measured at the first spill by the ionization chamber installed upstream the COMPASS set-up and supposing a DAQ dead time (see section 3.8) of 17% [2], we get an effective muon flux:

$$\Phi^{spill} = \Phi^{spill}_{mes} \times (1 - DAQ^{dt}) = 1.78 \times 10^8 \mu/spill\,; \tag{7.9}$$

from the preliminary data [71] on the weight of the target cells, neglecting all other molecules but ^{6}LiD and ^{4}He, the number of nucleons per unit surface present in the target is:

$$n_{tot} = 3.36 \times 10^{25}/cm^2\,; \tag{7.10}$$

[2]The COMPASS DAQ dead time has been set to 17% in a period of time ranging from the start of the run up to run number 21686 (P2C) taken on 8/8/2002. The run number 21472 on the base of which this calculation has been done is contained in this period. Afterwards the dead time could be lowered to 7%.

the cross section calculated by LEPTO for each bin in x, reduced by the kinematical cuts on the leading pion and by the geometrical acceptance of the solenoid magnet and of the trigger hodoscopes, is:

$$a \times \sigma^{DIS} = \begin{pmatrix} 0.21 \times 0.69 \cdot 10^{-31} \\ 0.23 \times 0.58 \cdot 10^{-31} \\ 0.25 \times 0.36 \cdot 10^{-31} \\ 0.28 \times 0.65 \cdot 10^{-31} \end{pmatrix} \qquad \begin{matrix} 0.02 < x < 0.05 \\ 0.05 < x < 0.10 \\ 0.10 < x < 0.15 \\ x > 0.15 \end{matrix} \tag{7.11}$$

Inserting these figures into equation 7.7 one finds the number of expected events:

$$N^{exp} = 1.78 \times 10^{8} \times 3.36 \times 10^{25} \times \begin{pmatrix} 0.21 \times 0.69 \cdot 10^{-31} \\ 0.23 \times 0.58 \cdot 10^{-31} \\ 0.25 \times 0.36 \cdot 10^{-31} \\ 0.28 \times 0.65 \cdot 10^{-31} \end{pmatrix} \times 100$$

$$\simeq \begin{pmatrix} 8350 \\ 8178 \\ 5172 \\ 10920 \end{pmatrix} \qquad \begin{matrix} 0.02 < x < 0.05 \\ 0.05 < x < 0.10 \\ 0.10 < x < 0.15 \\ x > 0.15 \end{matrix} \tag{7.12}$$

Taking the experimental value N^{meas} and inserting the numbers given in equation 7.12 into equation 7.8, the overall tracking and triggering efficiency results to be:

$$R_{current} = \begin{pmatrix} 7.8\% \\ 3.9\% \\ 1.9\% \\ 0.4\% \end{pmatrix} \qquad \begin{matrix} 0.02 < x < 0.05 \\ 0.05 < x < 0.10 \\ 0.10 < x < 0.15 \\ x > 0.15 \end{matrix} \tag{7.13}$$

The figures in equation 7.13 show how the efficiency for event reconstruction of the CORAL package used for the DST production is still low, and decreases in the high x range.

The strong decrease with x is mainly due to the W4/5 large area drift chambers, not properly aligned in this first analysis and to a lesser extent to the inefficiency of the outer trigger counters [72]. The tracking algorithms are presently still being improved.

A new DST has been produced for the same run 21472 making use of the "official" precompiled CORAL libraries released on 20th December 2002. Calculated from the events in the new DST, the overall reconstruction efficiency has improved following the relation:

$$R_{future} = R_{current} \times \begin{pmatrix} 1.57 \\ 1.56 \\ 1.67 \\ 1.70 \end{pmatrix} = \begin{pmatrix} 12.2\% \\ 6.1\% \\ 3.2\% \\ 0.68\% \end{pmatrix} \qquad \begin{matrix} 0.02 < x < 0.05 \\ 0.05 < x < 0.10 \\ 0.10 < x < 0.15 \\ x > 0.15 \end{matrix} \tag{7.14}$$

In the following section, on the base of this calculation, a lower limit to the possible updates to the work presented in this thesis will be discussed.

7.8 Outlook

The sample on which the analysis described in this chapter is based is not complete, in the sense that it takes into account only the signal from π^+ and 2/3 of the runs taken in transverse mode. Furthermore the low reconstruction efficiency and the misalignment of the large area detectors (still to adjust by software, see section 5.2), have reduced the analyzing power of the events entering the present analysis.

A preliminary study upon CORAL reconstruction efficiency has shown a small improvement of the reconstruction efficiency in the more recent releases of the program (see section 7.7).

Work is ongoing, in particular for the tracking at large angles where the efficiency is unaccettably low. Still, even with the small improvement already achieved, we enhance the statistical significance of the collected data.

If, for example, one takes as true the value for the asymmetry suggested by Efremov (see figure 7.22), reprocessing all the periods devoted to transversity, the statistical error decreases as:

$$\sigma \propto \frac{1}{\sqrt{N_0}} \implies \frac{1}{\sqrt{N_0 \cdot G \cdot \frac{4}{3}}} \tag{7.15}$$

where N_0 is the total amount of events already analyzed, G is the gain in the reconstruction efficiency obtained with the new CORAL release and the factor $\frac{4}{3}$ takes into account the statistics of the last period of transversity (P2H) not yet processed.

In such conditions, the statistical significance of the measured asymmetry would be about 3.5 standard deviations away from 0.

Furthermore, the signal for π^-, in case of deuteron, should exhibit about the same amplitude as for π^+ [70]. Making the hypothesis to have the same abundancy for π^+ and π^-, another factor 2 in statistics is gained looking at the combined $(\pi^+ + \pi^-)$ signal (see table 7.6), giving an overall 5 σ effect.

Of course, the gain will be much larger than the present estimate if we succeed in improving the overall reconstruction efficiency of the data at large x by the order of magnitude we aim for.

If it's true that no conclusion about the transversity can be drawn from the present analysis, but the statistics collected in 2002 is such that a final analysis should give a significant result on transversity if the signal is as large as expected.

x bin	0.02 < x < 0.05		0.05 < x < 0.10		0.10 < x < 0.15		x > 0.15		all x
	A / σ	R	A / σ	R	A / σ	R	A / σ	R	A / σ
Current (π^+)	1.4	7.8 %	1.25	3.9 %	1.01	1.9 %	1.14	0.4%	2.4
Future (π^+)	2.0	12.2 %	1.8	6.1 %	1.5	3.2 %	1.72	0.68%	3.5
Future ($\pi^+ + \pi^-$)	2.8		2.5		2.1		2.4		5.0

Table 7.6: The A / σ (signal to standard deviation) values and the overall reconstruction efficiency for the different bins in x in case of current and future Data Analysis.

Chapter 8

Conclusions

This work has been carried on in the framework of the activities performed by the Trieste group in the COMPASS collaboration during the years 2000 - 2002. It concerns one of the measurements proposed by COMPASS and approved by the CERN SPSC Committee in the fall of 1996, the measurement of Transversity.

Transversity is a relatively new topic, which has been studied theoretically only recently. Today its importance in understanding the internal structure of the nucleon has been fully recognized and many experiments are being performed to measure it.

The formalism for transverse spin I have developed in chapter 1 follows the recent works by V. Barone, A. Drago, and P. Ratcliffe [1], P. Mulders and R. Tangerman [3], R. Jaffe [2].

COMPASS can measure Transversity through a very clean channel as that offered by the Collins effect. Because of the small amplitude of the Collins azimuthal asymmetry, this effect is not easy to detect and very sophisticated experiments are needed. The COMPASS spectrometer, described in detail in chapter 3, is perfectly suited to this aim because of its capability to fully reconstruct the semi-inclusive Deep Inelastic Scattering events, and its very good acceptance to the hadrons of the current jet. The experiment had its first year of physics data taking in 2002.

At the time being, a big effort to improve the reconstruction efficiency of the CORAL analysis package is ongoing. On top, the whole data handling system is changing following the policy of CERN which has decided to dismiss Objectivity/DB and migrate all the data collected by the running experiments (as COMPASS) to Oracle 9i Data Base. The CORAL libraries providing the interfaces to the Data Base are being changed to fulfil the characteristics and requirements of the new tools.

This huge activity translates into a delay for the delivery of the new and official DSTs of the data collected in year 2002.

Analyzing the data processed by a test version of CORAL, this thesis has demonstrated that, though the signal of Transversity hasn't yet been observed, the statistics collected with transverse polarization is sufficient to detect it if its amplitude is as big as foreseen by some QCD theoretical models which embed the presently known signals of Transversity.

All in all the amount of work discussed in these pages, has let me take advantage in the knowledge of the physical phenomenon I'm studying and of the informatical tools which are needed to detect it.

Bibliography

[1] V. Barone, A. Drago, and P. G. Ratcliffe. Transverse polarisation of quarks in hadrons. *Phys. Rept.*, 359:1–168, 2002.

[2] R. L. Jaffe. Can transversity be measured? 1997.

[3] P. J. Mulders and R. D. Tangerman. The complete tree-level result up to order 1/Q for polarized deep-inelastic leptoproduction. *Nucl. Phys.*, B461:197–237, 1996.

[4] G. Baum et al. The COMPASS proposal. URL: `http://wwwcompass.cern.ch/compass/proposal/ps/proposal.ps.gz`, March 1996.

[5] J.C. Collins. Fragmentation of transversely polarized quarks probed in transverse momentum distributions. *Nucl. Phys.*, B394:169, 1993.

[6] V. A. Korotkov, W. D. Nowak, and K. A. Oganesian. Future transversity measurements at HERMES. Prepared for 8th International Workshop on Deep Inelastic Scattering and QCD (DIS 2000), Liverpool, England, 25-30 Apr 2000.

[7] A. Airapetian et al. Observation of a single-spin azimuthal asymmetry in semi- inclusive pion electro-production. *Phys. Rev. Lett.*, 84:4047–4051, 2000.

[8] A. Kotzinian. New quark distributions and semiinclusive electroproduction on the polarized nucleons. *Nucl. Phys.*, B441:234–248, 1995.

[9] A. Airapetian et al. Single-spin azimuthal asymmetry in exclusive electroproduction of π^+ mesons. *Phys. Lett.*, B535:85–92, 2002.

[10] A. Bravar. Hadron azimuthal distributions and transverse spin asymmetries in DIS of leptons off transversely polarized targets from SMC. *Nucl. Phys. Proc. Suppl.*, 79:520–522, 1999.

[11] G. Rakness. Analyzing powers for forward $p_\uparrow + p \longrightarrow \pi^0 + X$ at STAR, Sep. 2002. URL: `http://www.c-ad.bnl.gov/SPIN2002/presentations/rakness.pdf`.

[12] A. V. Efremov, O. G. Smirnova, and L. G. Tkachev. On the t-odd quark fragmentation function. *Nucl. Phys. Proc. Suppl.*, 79:554–556, 1999.

[13] D. Hasch. Azimuthal asymmetries in meson electroproduction at HERMES, Sep. 2002. URL: http://www.c-ad.bnl.gov/SPIN2002/presentations/hasch2.pdf.

[14] E. Nappi et al. The HMC letter of intend. URL: http://wwwcompass.cern.ch/compass/publications/ps/loi_hmc.ps.gz, March 1995.

[15] Yu. Alexandrov et al. The CHEOPS letter of intend. URL: http://wwwcompass.cern.ch/compass/publications/ps/loi_cheops.ps.gz, March 1995.

[16] *CERN Bullettin*, 114, August 2002.

[17] M. von Hodenberg. A first reconstruction of COMPASS data. URL: http://hpfr02.physik.uni-freiburg.de/arbeiten/diplomarbeiten/vonHodenberg.ps.gz. Master's thesis, University of Freiburg, 2002.

[18] D. Adams et al. The polarized double cell target of the SMC. *Nucl. Instrum. Meth.*, A437:23–67, 1999.

[19] N. W. Schellingerhout, L. P. Kok, S. A. Coon, and R. M. Adam. Nucleon polarization in three body models of polarized Li6. *Phys. Rev.*, C48:2714, 1993.

[20] T. Schmidt. *A Common Readout Driver for the COMPASS Experiment. URL: http://hpfr02.physik.uni-freiburg.de/arbeiten/theses/schmidt.ps.gz.* PhD thesis, University of Freiburg, June 2002.

[21] S. Dalla Torre. The COMPASS spectrometer: status and performance, Sep. 2002. URL: http://doc.cern.ch/archive/electronic/other/agenda/a021198/a021198s1t2/transparencies/dallatorre.pdf.

[22] R. Wagner. Commissioning of silicon detectors for the COMPASS experiment at CERN. URL: http://www.e18.physik.tu-muenchen.de/~rwagner/diploma/. Master's thesis, Technical University of Munchen, December 2001.

[23] D. Thers et al. Micromegas as a large microstrip detector for the COMPASS experiment. *Nucl. Instrum. Meth.*, A469:133–146, 2001.

[24] B. Ketzer et al. Triple GEM tracking detectors for COMPASS. CERN-OPEN-2002-004.

[25] M. Sans Merce. *Development of drift chambers and physics simulations for the COMPASS experiment. URL: http://wwwcompass.cern.ch/compass/publications/ps/phd_sans.pdf.* PhD thesis, Ludwig Maximilians University, Munich, October 2001.

[26] L. Cerini. Studio sperimentale di camere a deriva di grandi dimensioni per lo spettrometro COMPASS al CERN. URL: http://wwwcompass.cern.ch/compass/publications/ps/cerini.ps.gz. Master's thesis, University of Trieste, November 2002.

[27] COMPASS trigger group. Muon trigger documentation. URL: `http://wwwcompass.cern.ch/compass/detector/trigger/muon-trigger/triggerdoc.ps.gz`, June 2002.

[28] RD26 Collaboration. Status report. *CERN-DRDC*, 93-36, 94-49, 96-20.

[29] A. Albrecht et al. COMPASS RICH-1. In *RICH2002,* 4^{th} *workshop on RICH detectors*, Pylos, Greece. to be published on Nucl. Instr. and Methods.

[30] A. Albrecht et al. The radiator gas and the gas system of COMPASS RICH-1. In *RICH2002,* 4^{th} *workshop on RICH detectors*, Pylos, Greece. to be published on Nucl. Instr. and Methods.

[31] A. Albrecht et al. The mirror system of COMPASS RICH-1. In *RICH2002,* 4^{th} *workshop on rich detectors*, Pylos, Greece. to be published on Nucl. Instr. and Methods.

[32] The ALICE Collaboration. Technical design report on the high momentum particle identification detector. *CERN/LHCC*, 98-19, ALICE TDR 1.

[33] F. Piuz. RICH imaging cherenkov system based on gaseous photo-detectors: trends and limitations. In *RICH2002,* 4^{th} *workshop on rich detectors*, Pylos, Greece. to be published on Nucl. Instr. and Methods.

[34] E. Nappi. *Nucl. Instr. and Methods*, A(471):18, 2001.

[35] A. Braem. Technology of photo-cathode production. In *RICH2002,* 4^{th} *workshop on rich detectors*, Pylos, Greece. to be published on Nucl. Instr. and Methods.

[36] G. Baum et al. *Nucl. Instr. and Methods*, A(433):207, 1999.

[37] A. Albrecht et al. The COMPASS RICH-1 read-out system. In *RICH2002,* 4^{th} *workshop on rich detectors*, Pylos, Greece. to be published on Nucl. Instr. and Methods.

[38] M. Bosteels. *Nucl. Instr. and Methods*, A(371):248, 1996.

[39] D. R. Broemmelsiek. HERA-B RICH: Radiator gas system report. *unpublished*, 1997.

[40] D. Bergstrom et al. *Nucl. Instr. and Methods*, A(463):161, 2001.

[41] M.L. Andrieux et al. *Nucl. Instr. and Methods*, A(371):203, 1996.

[42] P. Baillon et al. *Nucl. Instr. and Methods*, A(277):338, 1988.

[43] J.A. Darve and R. Valbuena. Computed deformations of the spherical mirrors of the COMPASS RICH-1 detector. *CERN-EST*, Technical Note(99-09).

[44] IMMA, Ltd., Kinskeho 703, Turnov, Czech Republic.

[45] M. Laub. *Ph.D Thesis*. PhD thesis, University of Prague, 2001.

[46] SESO, Pole d'activites d'Aix-les-milles, 305, Rue Louis Arnand, 13792, Aix-en-Provence, France.

[47] MACOR by Corning Incorporated, Corning, NY, USA.

[48] Alcoa Alca Plus by Aluminum Company of America, Pittsburg, PA, USA.

[49] R. Veenhof. Garfield, a drift chamber simulation program. (Version 7), 1998.

[50] S. F. Biagi. A multiterm Boltzmann analysis of drift velocity, diffusion, gain and magnetic field effects in argon methane water vapor mixtures. *Nucl. Instrum. and Methods*, A283:716–722, 1989.

[51] S. Biagi. *Nucl. Instr. and Methods*, A(421):324, 1999.

[52] P. Pagano. Il Cerenkov a focalizzazione d'immagine dell'esperimento COMPASS. URL: `http://www.ts.infn.it/~ppagano/tesi_p.ps.gz`. Master's thesis, University of Trieste, May 1999.

[53] L. Malter. *Phys. Rev.*, 50:48, 1936.

[54] J. Va'vra. Comments on CF_4-based operation and gem-based photo-detectors. *RICH detector workshop*, 2001.

[55] LUMA METAL, Amerikavägen 5, P.O.Box 701, 39127 Kalmar, Sweden.

[56] OSRAM SYLVANIA Lighting research, 71 Cherry Hill Dr, Beverly, MA 01915, USA.

[57] G. Baum et al. BORA, a front end board, with local intelligence for the RICH detector of the COMPASS collaboration. *Nucl. Instr. and Methods*, A(433):426, 1999.

[58] Analog Devices, DSP Microcomputer ADSP-21065L.

[59] XILINX VIRTEX XCV100 FPGA.

[60] A. Albrecht et al. RICHONE: a software package for the analysis of COMPASS RICH-1 data. In *RICH2002,* 4$^{\text{th}}$ *workshop on RICH detectors*, Pylos, Greece. to be published on Nucl. Instr. and Methods.

[61] T. Ypsilantis and J. Seguinot. *Nucl. Instr. and Methods*, A(343):30, 1994.

[62] V. Duic. L'organizzazione della base di dati in COMPASS ed il problema dell'accesso remoto. URL: `http://www.ts.infn.it/acid/contrib/duicTesi020403.pdf`. Master's thesis, University of Trieste, March 2002.

[63] G. Booch. *Object-oriented analysis and design with applications.* Addison-Wesley, 1994.

[64] P. Schiavon. Trieste reconstruction software for COMPASS RICH-1. URL: `http://wwwcompass.cern.ch/compass/detector/rich/re1299.ps.gz`, December 1999.

[65] K. Kurek. private communication, Oct. 2002.

[66] L. Gatignon. Overview of M2 commissioning in 1999. URL: `http://gatignon.home.cern.ch/gatignon/m2commissioning.html`.

[67] G. Torrieri. Strangeness enhancement in heavy ion collisions at the WA97 experiment, Oct. 1999.

[68] F. Bradamante and A. Martin. A method to compute the Collins angle in transversely polarised DIS. URL: `http://wwwcompass.cern.ch/compass/notes/2002-5/2002-5.ps`, August 2002.

[69] F. Bradamante and A. Martin. Systematic effects from leading pion geometrical acceptance on the Collins angle distribution,. URL: `http://wwwcompass.cern.ch/compass/notes/2002-12/2002-12.ps`, December 2002.

[70] A. V. Efremov. COMPASS collaboration meeting, Nov. 2002.

[71] K. Gustafsson. private communication, Dic. 2002.

[72] J. Pretz. COMPASS collaboration meeting, Nov. 2002. URL: `http://wwwcompass.cern.ch/compass/collaboration/nov02/pretz.pdf`.

Errata corrige

The figures for the overall reconstruction efficiency given in equation 7.13 are not correct and the comments about the misalignment of the Very Large Area Trackers as well.

The reason for this mistake lies in the simulation program (based on LEPTO generator) used for such evaluation which contained a bug in the acceptance for the leading pion. This effect overestimated the number of reconstructable tracks emitted at large angle.

Still the evaluation of the gain obtained by the new libraries (see equation 7.14) and the extrapolation of the statistical errors reported in table 7.6 do not depend on this simulation and thus they have not been affected by this bug.